2011

Planar magneto-photonic and gradient-photonic structures : crystals and metamaterials.

Zhuoyuan Wu
Michigan Technological University

PLANAR MAGNETO-PHOTONIC AND GRADIENT-PHOTONIC STRUCTURES: CRYSTALS AND METAMATERIALS

By

Zhuoyuan Wu

A DISSERTATION

Submitted in partial fulfillment of the requirement for the degree of

DOCTOR OF PHILOSOPHY

Engineering Physics

MICHIGAN TECHNOLOGICAL UNIVERSITY

2010

This dissertation, “PLANAR MAGNETO-PHOTONIC AND GRADIENT-PHOTONIC STRUCTURES: CRYSTALS AND METAMATERIALS” is hereby approved in partial fulfillment of the requirements for the Degree of DOCTOR OF PHILOSOPHY in the field of Engineering Physics.

Department:
Physics

Signatures:

Dissertation Advisor _____
Dr. Miguel Levy

Committee Members _____
Dr. Ranjit Pati

_____
Dr. Will Cantrell

_____
Dr. Craig Friedrich

Department Chair _____
Dr. Ravi Pandey

ABSTRACT

In the field of photonics, two new types of material structures, photonic crystals and metamaterials, are presently of great interest. Both are studied in the present work, which focus on planar magnetic materials in the former and planar gradient metamaterials in the latter. These planar periodic structures are easy to handle and integrate into optical systems. The applications are promising field for future optical telecommunication systems and give rise to new optical, microwave and radio technologies.

The photonic crystal part emphasizes the utilization of magnetic material based photonic crystals due to its remarkable magneto-optical characteristics. Bandgaps tuning by magnetic field in bismuth-gadolinium-substituted lutetium iron garnet ($Bi_{0.8}$ $Gd_{0.2}$ $Lu_{2.0}$ Fe_5 O_{12}) based one- dimensional photonic crystals are investigated and demonstrated in this work. Magnetic optical switches are fabricated and tested. Waveguide formulation for band structure in magneto photonic crystals is developed. We also for the first time demonstrate and test two- dimensional magneto photonic crystals optical. We observe multi-stopbands in two- dimensional photonic waveguide system and study the origin of multi-stopbands.

The second part focus on studying photonic metamaterials and planar gradient photonic metamaterial design. We systematically study the effects of varying the geometry of the fishnet unit cell on the refractive index in optical frequency. It is the first time to design and demonstrate the planar gradient structure in the high optical frequency. Optical beam bending using planar gradient photonic metamaterials is observed. The technologies needed for the fabrication of the planar gradient photonic metamaterials are investigated. Beam steering devices, shifter, gradient optical lenses and etc. can be derived from this design.

ACKNOWLEDGEMENTS

It has been my honor and pleasure to work with Prof. Miguel Levy since fall 2005. He is an outstanding researcher, a great mentor and a close friend. He was open-minded about my Electrical Engineering background and took a risk to have me working with him in Engineering Physics field. He taught me a lot from how to contact research, solve problems to how to develop ideas and be innovative. During my PhD career, his advice helps me working on my research in the right directions; his constant encouragement helps me face all the obstacles in research with positive attitude. He is always easy to approach and opens to discussion which makes my work a lot more efficient. I would like to thank him for the opportunity to work with him and all his supports and helps in the past years.

I would like to thank my committees: Prof. Friedrich, Prof. Cantrell and Prof. Pati for their time to read my dissertation and giving me valuable suggestions.

I would like to thank my dear parents for their tremendous love, support and trust. They are always standing by my side and encourage me to pursue my dream. I know no matter what kind of career I choose for my life. They would respect my decision and be there for me unconditionally. I sincerely hope my achievement in my life so far can make them proud.

My work would not be successful without the collaborations and help from my group fellows. Dr. Raghav Vanga is the one who led me into experiments, taught me how to use most of micro-fabrication facilities and showed me the briefly ideas about how the research projects are processed in our research group. Dr. Xiaoyuan Huang is the one who taught me how to use optical test setup and also provided great suggestions and information. Dr. Ziyou Zhou is the one who collaborated with me closely in the research. She leaded me to my first research project and patiently trained me every procedure step

by step. We also stayed in the same office and had a lot of constructive discussions. Dr. Amir Jalali was always very kind and provided plenty of theoretical support to my work.

Ding, Neluka and Pradeep are very willing to help in experiments. I am very grateful to all the help from my fellows.

I would like to express my gratitude towards to Physics department and faculty members for their support, instructions and financial assistance. I also would like to thank the faculty, staff and fellow students in Department of Physics and Department of Materials Science & Engineering which provide me with detailed instructions and research facilities. In particular, Owen Mills helps on major equipments I used like FESEM and FIB; Bill Knudsen helps on maintaining the Micro-fabrication facility.

I am also very grateful to the TRD in Toyota Technical Center in Ann Arbor to give me the precious opportunity to experience industrial research environment. Especially, I would like to thank my supervisor Serdar Yonak introducing an exciting research project to me. His intelligence, guidance and attitude to research are definitely the key reasons we could succeed in the project.

Last, but not the least, I would like to thank Dr. H. Dötsch and Dr. V. Fratello for their supplies of the high-quality LPE films which are used in all my photonic device fabrications.

Zhuoyuan Wu
Aug 7, 2010

ABBREVIATIONS

BiLuIG	Bismuth-Gadolinium-substituted Lutetium Iron Garnet
BPM	Beam Propagation Method
CAIBE	Chemically Assisted Ion Beam Etching
FDTD	Finite Difference Time Domain
FIB	Focused Ion Beam
FR	Faraday Rotation
FSS	Frequency Selective Surface
GRIN	Gradient Index
GGG	Gadolinium Gallium Garnet ($Gd_3Ga_5O_{12}$)
HMDS	Hexa-methyl-dislizane
LCP	Left-hand Circular Polarized
LHM	Left Handed Metamaterial
LPE	Liquid Phase Epitaxy
MPC	Magneto-Photonic Crystal
NIM	Negative refractive Index Metamaterial
NPGS	Nano Pattern Generation System
PhCs	Photonic Crystals
PEC	Perfect Electric Conductor
PMC	Perfect Magnetic Conductor
RCP	Right-hand Circular Polarized
SEM	Scanning Electronic Microscope
SRR	Split Ring Resonator
TE	Transverse Electric
TM	Transverse Magnetic

TABLE OF CONTENTS

LIST OF FIGURES

LIST OF TABLES

CHAPTER 1

INTRODUCTION

This thesis concerns the interaction of photons with magnetic material structures and with metamaterials. Whereas electronics involves the control of electric charge, the subject matter of the present work involves the control of photons in matter, namely, photonics. In the field of photonics two new types of material structures are presently of great interest. These materials are photonic crystals (PhCs) and metamaterials. Both are studied in the present work, with a focus on magnetic materials in the former and planar-gradient metamaterials in the latter.

The major difference between photonic crystals and metamaterials is that to form a photonic bandgap the atoms and the lattice constant 'a' in the PhCs have to be comparable in size with the wavelength 'λ', $a \approx \lambda$, because the effect of the bandgap arises from diffraction. In the case of metamaterials artificial atoms (sub-units) and lattice constant have to be much smaller than the wavelength, $a << \lambda$, because diffraction should be avoided. The wavelength passing through a metamaterial has to feel only the effective parameters of the material, such as effective magnetic permeability, μ, and effective electric permittivity, ε. From the electromagnetic point of view it is the wavelength which determines if a collection of atoms or sub-units is a material. [1]

The work on photonic crystals is developed in Michigan Technological University. Based on well developed planar magneto-photonic crystal (MPCs) waveguide studies in the Research Group of Professor M. Levy, this thesis extensively studies one dimensional magnetically-controllable optical switching phenomenona in magneto-photonic crystals. Band gap and polarization control in magneto-optic films are extensively investigated and reported on. Strong optical switching is demonstrated based on magnetic control of optical transmission in optical band gap structures. Theoretical studies of the optical

response in magneto-photonic crystal waveguides are developed and presented as part of the present work. Studies on two dimensional magneto-photonic crystals are also carried out.

The work on metamaterials stems from a four-month project during the co-operative project with Toyota Technical Center, a research institution in Ann Arbor, Michigan. The goal of the project was to realize the planar gradient metamaterials in optical frequencies which can be used for optical lensing and IR imaging. We successfully design the planar gradient photonic matematerials and simulated the optical behavior passing through this planar slab. The key application of the prototypical design is to improve vehicle's night vision by IR imaging. The fabrication and test possibility are investigated.

The following sections include introductions to photonic crystals, metamaterials and spell out the organization of this thesis.

1.1 Photonic crystals

Photonic crystals, engineered periodic dielectric structures, are a new class of materials that provide novel capabilities for the control and manipulation of electromagnetic wave. In the same fashion as the phenomena of the electron in semiconductor, atomic lattices cause electrons to have energy bands and bandgaps, a periodic dielectric lattice causes photons to have frequency bands and frequency gaps in which photon can not travel through the structures. [2, 3]

The field of photonic bandgap materials started to develop dynamically after two papers of S. John and E. Yablonovitch published both in the same volume of Phys. Rev. Lett. in 1987. These two papers clearly address that in such periodic materials with varying refractive index, spontaneous emission could be suppressed and light could be localized. The propagation of light in PhCs is governed by Maxwell equation. [4,5]

Recently, photonic crystals have attracted considerable attention both from a fundamental as well as practical viewpoint, due to their unique optical properties and their potential use in optical devices. [2-5] Significant developments have occurred by realization of integrated optical circuits which produce multifunctional optical components onto a single chip. [6, 7]

By using different materials with different dielectric constants such as piezoelectric PMN-PT crystals and iron garnets and by adjusting geometrical parameters, applied external electric and magnetic field, the propagation of light can be modified in a controllable manner. The scale invariant nature of the governing Maxwell's equations enables the study of electromagnetic phenomena in the first place, without being held back by structural complexities.

There can be one-dimensional, two-dimensional and three-dimensional PhCs. Fig. 1.1 [2] shows the simple example of schematic depiction for one, two and three dimensional PhCs.

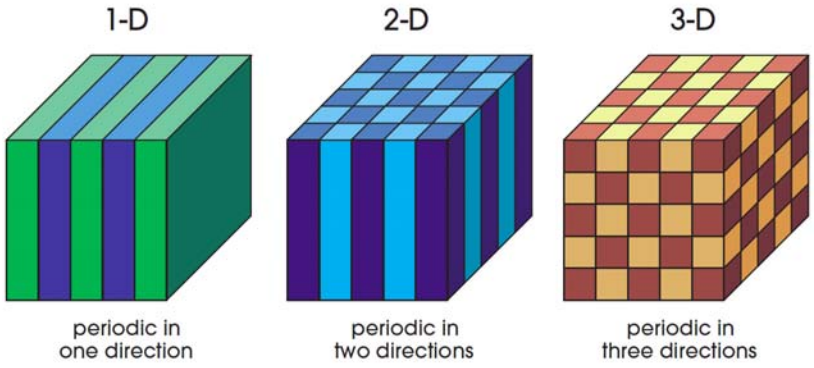

Figure 1.1 The schematic images for one, two and three dimensional photonic crystals. The different colors represents materials with different dielectric constants. Photonic crystals have the periodicity of dielectirc mateirals along one or more axes. [2]

The dimension of the photonic crystals depends on the dimension of the periodic structures. If the periodic structure exists in only one-, two- or three- direction, the photonic band gaps will show up in the one-, two- or three- direction.

The one dimensional PhCs are usually materials such as Bragg reflectors, interference filters which are generally manufactured by layer-by-layer deposition of materials with different refractive indices. Two-dimensional ones can be in the shape of dielectric pillars embedded in another dielectric material (e.g. air) or air columnar holes embedded in dielectric material [8, 9]. In my work, one dimensional PhCs are grating patterns on ridge waveguide which create multilayer material and air periodically arranged in one direction. Two dimensional PhCs are periodic air columnar holes embedded in the slab waveguide. Only the three-dimensional PhCs can have complete photonic bandgap (a direction and polarization independent). The first three-dimensional PhCs were obtained by Yablonovitch by drilling holes along their crystallographic axis of diamond in a material with high refractive index (now called Yablonovite) [10, 11]. A woodpile structure which shows the complete photonic bandgap was originally invented by Sokoulis [12]. It was miniaturized by Noda who used an advanced wafer-fusion technique to reduce the size to such dimensions that the bandgap was observed at the telecommunication wavelength ~ $1.5\,\mu m$. [13]

1.1.1 Bandgap formation

Wave optics is used to analyze these crystals. The description of light in PhCs must involve the solution of Maxwell's equations in a periodic dielectric medium. This approach is more general and elucidates the structure of light within photonics crystal.

The first step is to simplify Maxwell's equations by assuming the absence of current and sources:

$$\left\{\nabla \times \frac{1}{\varepsilon(r)} \nabla \times\right\} H(r) = \frac{\omega^2}{c^2} H(r) \tag{1.1}$$

$H(r)$ is the magnetic field of the photon, $\varepsilon(r)$ is the macroscopic dielectric constant as a function of space in the media. $1/\varepsilon(r)$ is a periodic function. The solutions of ω and $H(r)$ are determined completely by the strength and symmetry properties of $\varepsilon(r)$ as $\varepsilon(r) = \varepsilon(r$

+R_i), here R_i represents the periodicity in all three dimensions (R_i =1, 2, 3), the solutions are in a form of $H(r) = e^{i\omega r} H_{n,k(r)}$, $\boldsymbol{k}(r)$ with eigenvalues $\omega_n(k)$, where $H_{n,\boldsymbol{k}(r)}$ is a periodic envelope function satisfying:

$$\left(\nabla + ik\right) \times \frac{1}{\varepsilon} \left(\nabla + ik\right) \times H_{n,k} = \left(\frac{\omega_n(k)}{c}\right)^2 H_{n,k} \tag{1.2}$$

leading to discrete eigenvalues labeled by n = 1, 2, … over a periodic structure. These eigenvalues $\omega_{n(\boldsymbol{k})}$ are continuous functions of $\boldsymbol{k}$, forming discrete "bands" when plotted versus the latter, in a"band structure" or dispersion diagram.[14]

For a uniform one dimensional system (ε = 1), the plane wave eigensolution is $\omega(k) = ck$, as depicted in Fig. 1.2(left). The bands for $|\boldsymbol{k}| > \pi / a$ can be folded into the first Brillouin zone, as shown by the dashed lines in Fig. 1.2(left). The wave solutions with electric fields which is proportional to $e^{\pm \pi x / a}$ can be expressed as a linear combinations of $e(x) = \cos(\pi x / a)$ and $o(x) = \sin(\pi x / a)$ as shown in Fig. 1.2(inset). In the presence of such an oscillating "potential", a bandgap appears at $k = \pm \pi / a$ due to the degeneracy between $e(x)$ and $o(x)$. Given $\Delta > 0$, the field $e(x)$ is more concentrated in the higher ε as its electric field peaks in the high dielectric (n_{high}) so as to form the lower bandgap edge, while the field $o(x)$ lies more in the lower ε as its electric-field peaks in the low dielectric (n_{low}) so as to form the higher bandgap edge.(see Fig. 1.2(right)). [14] This argument explains that any periodic dielectric structure in one dimension will result in bandgaps.

The analysis of two-dimensional PhCs is similar to the one-dimensional case, except for a few additional complications. First, there are two vectors that determine the Bloch state, kx and ky. We can combine these two vectors in cylindrical coordinates, and make the Bloch state a function of kρ = kx + ky. In 2-D the Brillouin zones are area, for a square lattice, the first Brillouin zone is a square with sides of length $2\pi/a$, where a is the spacing of the lattice. The irreducible Brillouin zone is a right triangle of base and height π/a. See

Fig. 1.3. The band diagram will be a 2-D surface plot. 1-D band-diagram can be obtained by plotting the band structure only at the edges of the irreducible Brillouin zone, i.e. from Γ to X to M. Thus dispersion diagram can be used to determine the photonic band-gaps. [15]

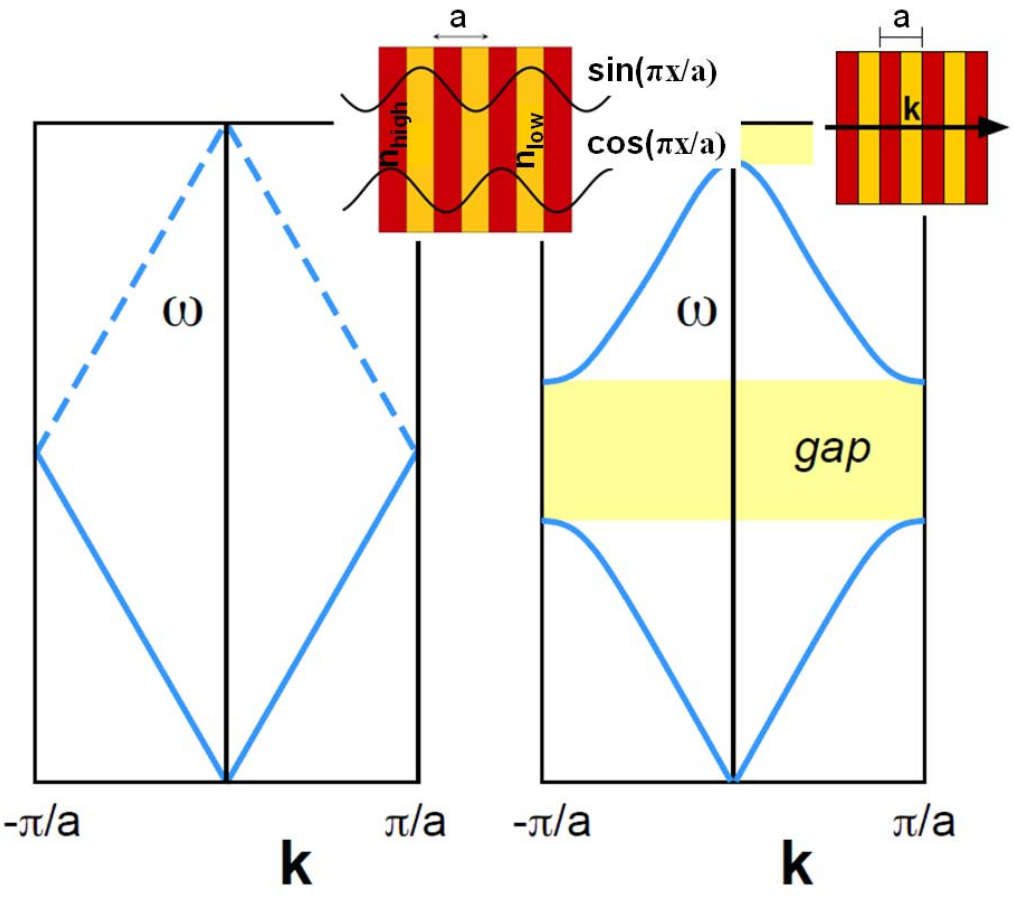

Figure 1.2 Schematic diagrams for the dispersion relation between frequency ω and wavenumber k in a one-dimensional medium. Left: a uniform medium; right: a physical periodic dielectric variation (inset) splits the band at the $k = \pm \pi / a$ Brillouin-zone boundaries, forming a photonic bandgap (in yellow). [14]

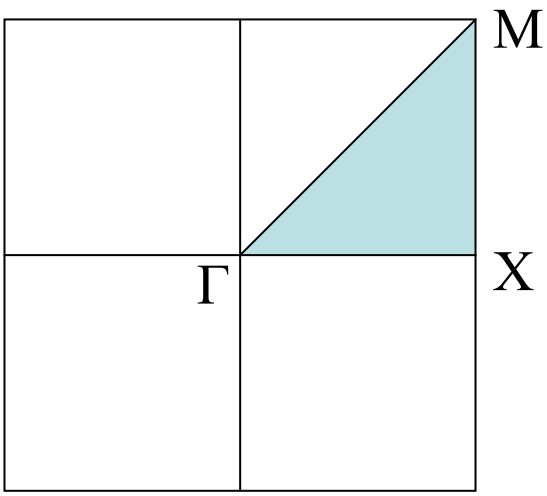

Figure 1.3 2-D Brillouin with irreducible Brillouin Zone shaded light blue. Γ, X and M are high symmetrical points at the coners of the irreducible Brilliouin zone.

In order to realize 2d photonic-crystal phenomena in three dimensions, the most straightforward design is to simply fabricate a 2d-periodic crystal with a finite height: a photonic-crystal slab, as depicted in Fig.. 1.4. Such a structure can confine light vertically within the slab via index guiding, a generalization of total internal reflection—this mechanism is the source of several new tradeoffs and behaviors of slab systems compared to their 2d analogues.

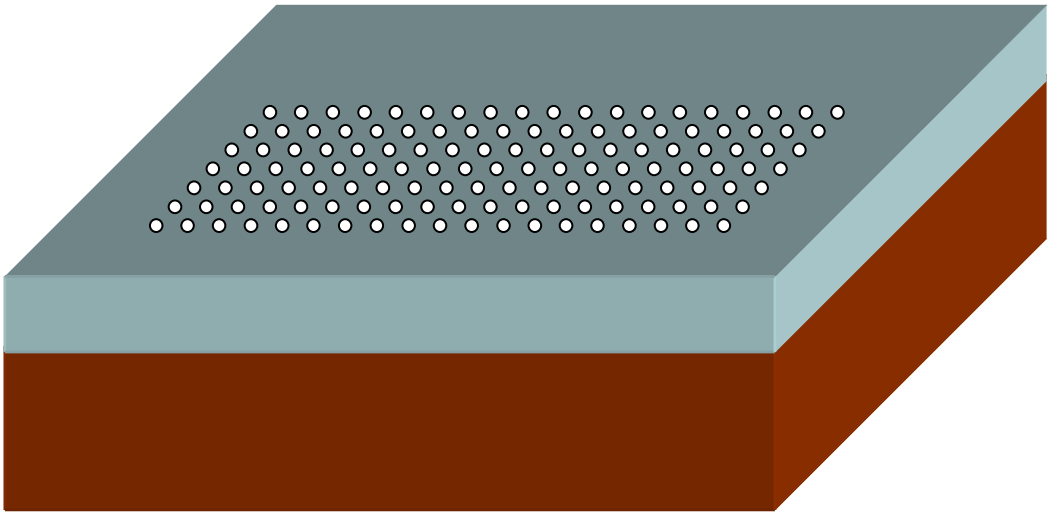

Figure 1.4 The schematic of a two dimensional photonic-crystal on a slab waveguide

If the frequency of the propagating light is in the photonic bandgaps, photonic crystals, considered as 'optical insulator' can be utilized to build ultra-compact mirrors, cavities, super prisms with the refraction angle of the incident light 100 times to 1000 times of the normal prism; optical amplifier, filter, switcher and waveguides [16-19]. On the other hand, if the frequency is outside photonic bandgaps, it can be used as wavelength division multiplexing in broadband optical communication [18], beam steering and other applications. With the improvement in the fabrication technology, more potential applications will show up [19].

Scaling down is still a challenging issue before photonic crystals are in widespread use. The current available nanotechnology is hard to achieve the photonic crystal with the size suitable for visible light application. The variation of the periodicity of PhCs by modifying structure dimensions or indices remains as a challenge especially for higher dimensional PhCs. The crystal structures built on special material can be adjusted by an external force, electric field or magnetic field. These functional PhCs can be widely used as infrared laser modulators with micro-scale sizes for remote communication such as satellite communications. They can also offer potential features leading to new devices to detect chemical reactions involving radiation of interest for chemical production, pharmaceutical development and biotechnology. [20]

1.1.2 Magneto-photonic crystals

Most of research and development in PhCs are based on metal, polymer or semiconductor materials. Not much attention was paid to the investigation of PhCs made from magnetic materials, or to the influence of external magnetic fields on photonic bandgap effects in the first decade until Inoue *et al*.[23-26] first began the study of Magnet-optical(MO) effects in one dimensional multilayer stack magneto-photonic crystals in 1996. Subsequent early work involved investigations on multi-defect and waveguide MPC structures. [21-31] All these magnetic materials based PhC structures are called as Magnetic photonic crystals or Magnetophotonic crystals, abbreviated as MPCs as follows.

The early development of MPCs up to 2003 was discussed in a review paper [32] by Lyubchanskii et al.

As the attraction of the unique magnetic-field-dependent effects such as nonreciprocity and unidirectionality[33] became widely recognized in recent years. However, there still exisit several unsolved issues in the multilayer structure MPCs. First, the high-quality films are hard to obtain as the number of layers increases. Second, it is hard to integrate the multi-layer structure into future optical integration circuit application. Last but not least, it is challenging to attain the miniaturization of external magnets in this multi-layer structure.

Some work has been reported on photonic crystals made from magneto-optic materials that allow for tunability upon changing the external magnetic field in the optical wavelength range of the incident wave [34]. Photonic crystal structures in planar magnetic film waveguides can lead to the development of on-chip magneto-optical switches, sensors and isolators for photonic device integration [35]. During the past few years, much research effort has been devoted to the investigation of one-dimensional PhCs, including significant improvement in polarization rotation in magneto-optical photonic crystal gratings on planar ridge waveguides studied by our group [36].

Our group proposed and developed MPC waveguide structures.[36, 37, 38-42] as shown in Fig. 1.5 to achieve one dimensional MPC instead of sputtering multilayer film structures. This alternative structure can obtain precise [36] control of the refractive index contrast by patterning a periodic relief structure on the surface of an optical waveguide. This structure also can easily used for integration in complex planar photonic and open up a way to connect with semiconductor based devices for optical integration circuit application. [43, 44]

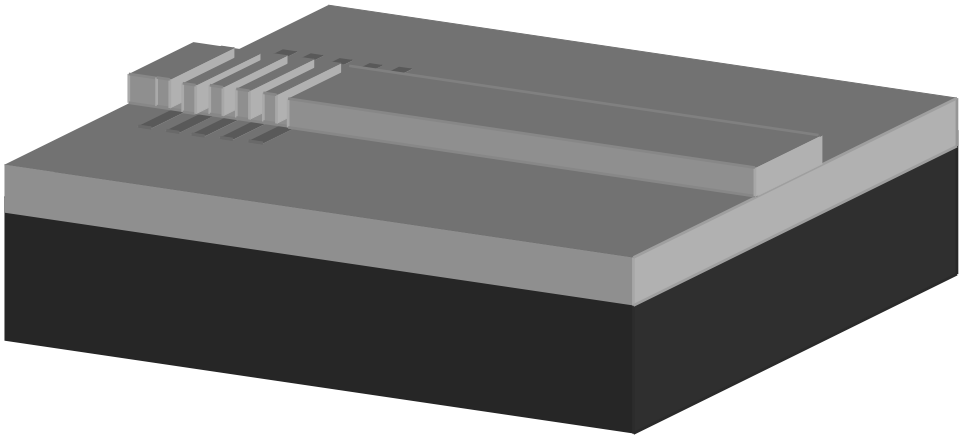

Figure 1.5 Schematic of one dimensional photonic crystal on ridge

The whole structure is based on a waveguide so that it is more suitable for the planar integration compared to stacked-film structure [36]. What's more, stacked structures do not present birefringence since the propagation is normal to the plane of the film. The presence of birefringence and waveguide modes which naturally arises in this type of planar ridge waveguide structure introduces more interesting phenomena. The involvement of birefringence in MPCs system and the mechanism between polarization rotation and waveguide scattering modes have been deeply studied both in experiment and theory by R. Li and M. Levy, as well as By A. Jalali. Several discoveries have been made. [40, 41, 45-47]

The photonic crystal part of the work presented in this dissertation concerns band gap tunability in magneto-photonic-crystal multi-mode waveguides. Specifically, it addresses the magneto-optic response of one-dimensional PhCs fabricated in magnetic garnet films. Band gap tunability and on-off switching is demonstrated in band gaps formed by mode-coupling between different-order waveguide modes. The activation of TM-TM or TE-TE mode coupling upon the application of a magnetic field results in the on-off switching of optical band gaps. This device is successfully fabricated and demonstrated. What's more, we investigate the properties of the waveguide band structure and its optical response beyond simple stack models, incorporating waveguide mode analysis and we extend this

treatment to two dimensional square lattice photonic crystal structures by simulations and experiments.

1.2 Metamaterials

As is well known, the permittivity ε and permeability μ of materials determine the response of an electromagnetic field of a system. We can classify a medium as shown in Table 1.1. Most naturally existing media have both positive permittivity and permeability ($\varepsilon > 0,\ \mu > 0$). These materials are designated double positive (DPS) media. When permittivity is less than zero and permeability is greater than zero ($\varepsilon < 0,\ \mu > 0$), media are designated as epsilon-negative (ENG) media. In the infrared (IR) and visible frequency range, noble metals like silver and gold exhibit this characteristic. Media with positive permittivity and negative permeability ($\varepsilon > 0,\ \mu < 0$) are designated mu-negative (MNG) media. Some gyrotropic materials exhibit this characteristic in certain frequency regime. A medium with both permittivity and permeability less than zero ($\varepsilon < 0,\ \mu < 0$) are double negative (DNG) medium or Negative refractive index metamaterials (NIMs). [48] The refractive index of a medium is defined by $n = \pm\sqrt{\varepsilon\mu}$.

Metamaterials which are known as electromagnetic and multifunctional artificial materials can extend the electromagnetic properties that can not be obtained with naturally existing materials [1]. They have effectively homogeneous structures whose structural average cell size is much smaller than the guided wavelength, which means this average size should be at least smaller than a quarter of wavelength. In this way, the refractive phenomena will dominate over scattering/ diffraction phenomena when a wave propagates inside the metamaterials. The structure behaves as a real material if the structure is effectively homogeneous. Thus, metamaterials are electromagnetically uniform along the direction of propagation. [49] The structure of the materials leads to the properties instead of the composition. Metamaterials have different characteristics. NIMs have attracted much attention and effort from scientific researchers. They are

characterized by simultaneously negative permeability, permittivity and index of refraction. [50] Some interesting optical imaging properties of NIM were already indicated by Veselago and later theoretically proven by Pendry [51]. The refractive index is the main parameters to characterize the electromagnetic response of materials. It is defined as $n^2 = \varepsilon\mu$. It has two components: electric permittivity, ε, and magnetic permeability, μ. A negative index is obtained by adjusting the permittivity and permeability to be negative simultaneously.

Table 1.1
The classification of a medium

Material	Permittivity ε	Permeability μ	Refractive index n
DPS Material	>0	>0	>0
ENG Material	<0	>0	>0
MNG Material	>0	<0	>0
DNG Material	<0	<0	<0

Metamaterials gave rise to new phenomena and potential applications, ranging from negative refraction [52, 53], total external reflection [54], sub-wavelength waveguides, nanocircuits, antennas, and spectrally selective filters [55–59], to cloaking devices, wave concentrators and rotators [60–64].

1.2.1 The development of metamaterials

Metamaterials can be composed of dielectric elements or structured metallic components. Traditional metamaterials are composed of continuous metallic wires and split ring resonators (SRRs) [65, 66]. Negative index metamaterials were first demonstrated for microwave frequencies. The sample consists of square copper split ring resonators and copper wire strips on glass circuit board material. The rings and wires are on opposite sides of the boards, and the boards have been cut and assembled into an interlocking lattice. [67] By measuring the scattering angle of the transmitted beam through a prism

fabricated from this material, the effective *n*, appropriate to Snell's law can be directly measured. Negative refractive index was observed.

The development of resonant metamaterials has dramatically expanded our view of electromagnetic material interactions and given rise to new optical, microwave and radio technologies. Photonic metamaterials are a type of electromagnetic metamaterials which are designed to interact with optical frequencies which are terahertz, infrared and eventually visible wavelength. As a type of metamaterials, the periodic structures are made up of single unit cell much smaller than the optical wavelength. The subwavelength period distinguishes the photonic metamaterial from photonic band gap or photonic crystal structures. This is because the special optical properties do not arise from photonic bandgaps, but rather from a subwavelength interaction with the light spectrum, which mimics atoms or ions. However, the periodic cells (meta-atoms) are fabricated on a scale that is magnitudes larger than the atom, yet smaller than the radiated wavelength. They have been designed and demonstrated to solve the materials issue at higher frequencies as terahertz and visible light. [68]

Although negative permeability can be easily obtained in the microwave frequency range and a number of successful realizations of NIMs in the microwave and terahertz regime have been presented in recent years, it is more complicated to realize NIMs in the optical (visible and infrared) regime. [69, 70]It is not easy to fabricate such structure suitable for the optical frequency range due to the size limitation from the fabrication [71, 72]. Several structures have been suggestion as optical NIMs such as nano rods, nano strips and fishnet structures. [73, 74, 75]

Engineers at Purdue University were the first researchers to create a material that has a "negative index of refraction" in the wavelength of light used for telecommunications, a step that could lead to better communications and imaging technologies. A double-periodic array of pairs of parallel gold nanorods is shown in Fig. 1.6 [73]. When normal incident light has the electric field polarized along the rods and the magnetic field

perpendicular to the pair as shown in Fig. 1.8 (a), the electric and magnetic responses both can experience resonant behavior at certain frequencies. This resonance can be considered as a resonance in an optical LC circuit. The metal rods provide the inductance L and the dielectric gaps between the rods play the role of capacitive elements C. The circular current in the pair of rods can lead to a magnetic field opposing the external magnetic field of the light above the resonance frequency. This metamaterial has a negative refractive index in the optical range. Such behavior results from the plasmon resonance in the pairs of nanorods for both the electric and the magnetic components of light. [73]

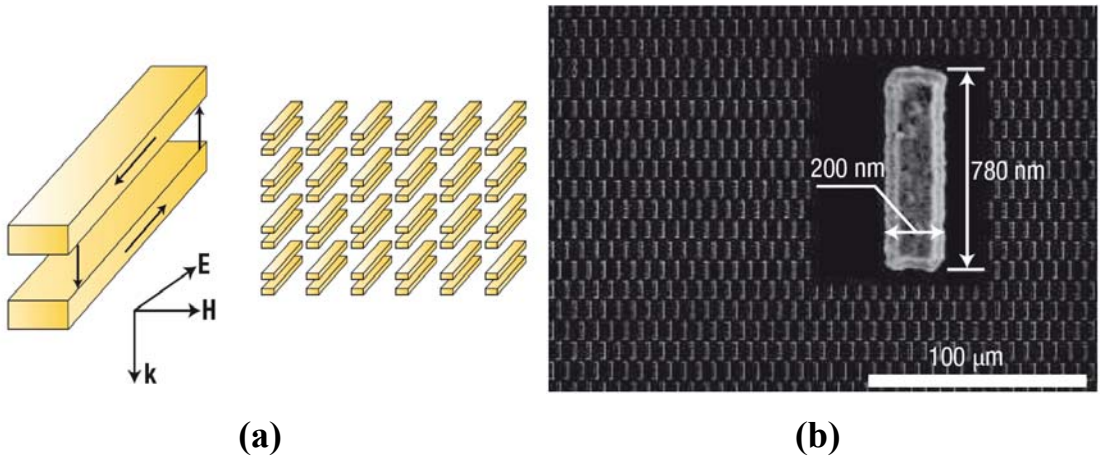

Figure 1.6 The nanorode metamaterial. (a) Schematic for the array of nanorod pairs. (b) Field-emission scanning electron microscope images. [73] See Appendix A for documentation of permission to republish this material. Printed permission by OSA

A family of coupled nanostrips with varying dimensions is demonstrated exhibiting \optical magnetic responses across the whole visible spectrum, from red to blue, which is referred to such a phenomenon as rainbow magnetism. The cross section and AFM images of this type of photonic metamaterials are shown in Fig. 1.7[74]. The experimental and analytical studies of such structures provide a universal building block and a general recipe for producing controllable optical magnetism for various practical implementations. [74] The general resonant properties of magnetic metamaterials

consisting of arrays of paired thin silver strips. The magnetism in such a structure has been discussed theoretically [76, 77].

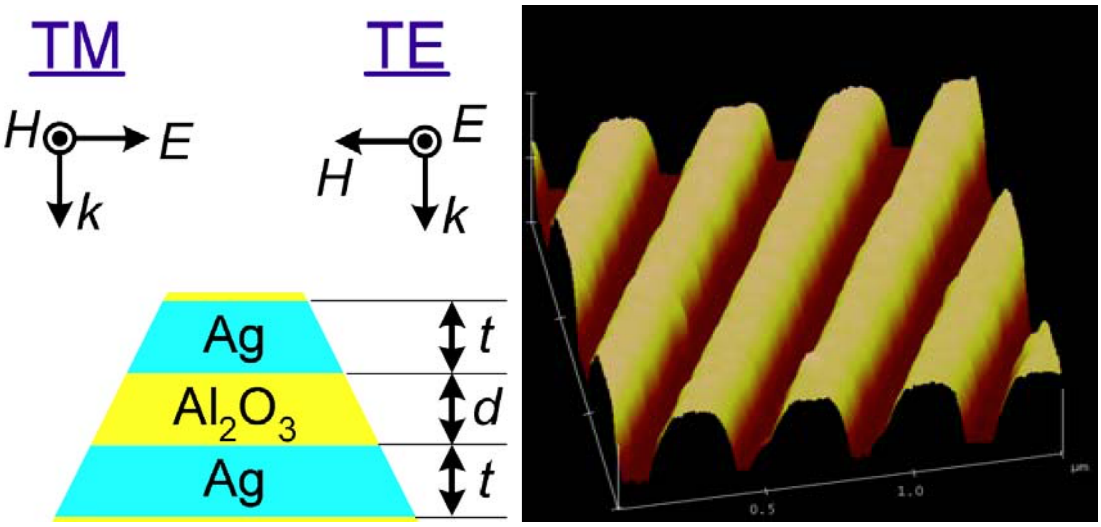

(a) **(b)**

Figure 1.7 The nanostrip metamaterial. (a) The cross-sectional schematic of arrays of coupled nano-strips; (b) The AFM image of a typical sample. [74] See Appendix A for documentation of permission to republish this material. Printed permission by OSA

The double-wire sandwich structure in which a dielectric layer is sandwiched between two metal films, popularly known as a 'fishnet', has been demonstrated in optical frequencies by creating a nano-prism in the multilayered fishnet stack to realize the negative refraction [67, 75, 78].The magnetic response originates from the antiparallel current supported by the wire pairs. When combined with long metal wires shown, this structure is shown to have negative refraction for a particular polarization at optical frequencies. [78] Three-dimensional (3D) optical metamaterials have come into focus. They open up prospects for studies of 3D optical effects and applications associated with Negative-index metamaterials and zero-index materials such as reversed Doppler Effect, superlenses, optical tunneling devices, compact resonators, cloaking device and highly directional sources [1,75]. Negative refraction of surface plasmon was recently demonstrated but was confined to a two-dimensional waveguide. Three-dimensional (3D) optical metamaterials includes the realization of negative refraction by using layered 3D

optical metamaterial cascaded ‘fishnet’ structures.A nano-prism was created in the multilayer fishnet stack to demonstrate negative refractive index at optical frequencies. [75]

1.2.2 Gradient metamaterials

Researches relative to analyzing and designing gradient index elements in conventional dielectrics have been developed since 1962 [79]. Continuously graded index structures offers an additional degree of freedom in the design of the desired characteristics compared to conventional elements with homogeneous and/or step index profile.

Most recent researches on metamaterial has been constructed from repeated unit cells containing identical elements. The averaged electromagnetic response does not vary over the structure due to the homogeneity of the structure. However, metamaterials with refractive index continuously varies in space can also be fabricated. A pattern of spatial dispersion can be introduced by a slight change in the properties of each successive element along a direction perpendicular to the direction of propagation. The averaged electromagnetic properties vary as a function of position. This forms a constant gradient index along this axis of the metamaterial, which can be confirmed by beam deflection experiments. This design increase practical usability in various applications, such as lensing and filtering. The gradient metamaterial represents an alternative approach to the development of gradient index lenses [80]. The use of metamaterial lenses instead of conventional positive index ones for the coupling with radioactive elements in high-gain antenna applications because of the reduced geometrical aberration profile in comparison to the conventional ones. [81] A gradient in the refractive index of the metamaterial is introduced by continuous tuning of a single parameter in the metamaterial element. Experimental studies of graded index metamaterials have been reported in millimeter wave and microwave. Some of these lenses make use of metamaterials operating in the positive index regime away from resonance to minimize losses. Fig. 1.8 is a picture of the gradient metamaterial slabs fabricated for millimeter wave. [1, 82, 83]

My research on photonic metamaterials combines gradient concepts with the optical fishnet structure for the purpose of extending gradient index metamaterials into the optical frequencies. We design the fishnet unit cell with optimum refractive index range by tuning the unit cell dimension. By appropriately placing these fishnet structures with different refractive indices on a planar slab, we can create gradient index on the slab. When light passes the planar slab, the deflection of light beam can be observed. This proposes the prototype for optical lensing and IR imaging.

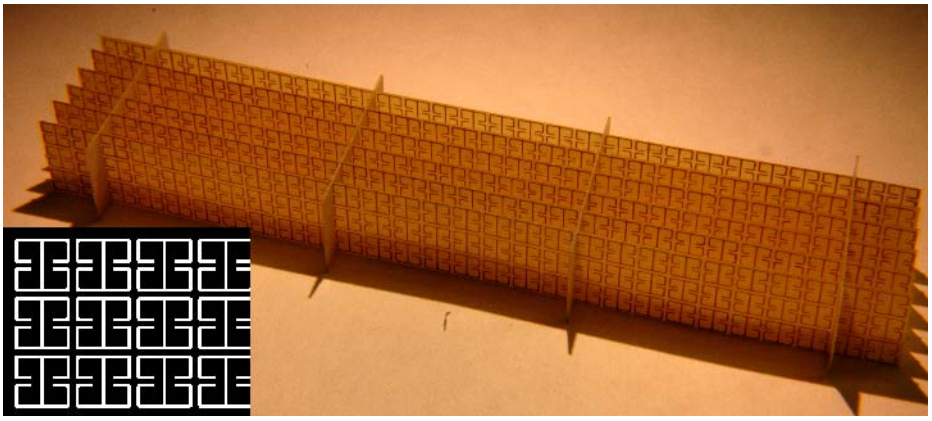

Figure 1.8 Planar gradient metamaterial slabs for millimeter wave and the inset is the magnified view

1.3 Content of this thesis

Chapter 1 provides the introduction of the work and the relevant background for the projects.

Chapter 2 mainly discusses the basic theory background PhCs and metamaterials. Magneto-optic effect, Waveguide theory and Bandgap calculation method are included to understand the control of the guided waves in magnetic-photonic crystal. Optical properties of bulk materials is included to understand the material properties and the numerical background for metamaterials.

Chapter 3 includes the experimental results and computation modeling on one and two dimensionally magnetio-photonic crystals. The fabrication techniques of PhCs and the measurement results of one photonic magneto-optic material Bismuth-Gadolinium-substituted Lutetium Iron Garnet (BiLuIG) are presented and analyzed. These films are fabricated and provided by Vince Fratello and Intergrated Photonics. It specially addresses the magnetically activated switching phenomena in one dimensional magneto-photonic crystals, as well as waveguide mode analysis. It thus extends the analysis beyond the stack model originally used by several authors to include waveguide mode analysis. Some initial results on two dimensional PhCs are also investigated. The experimental results and the computation modeling are discussed.

Chapter 4 demonstrates the simulation technique and numerical method utilized to design photonic metamaterial unit cell and the planar gradient photonic metamaterials and presents the results obtained by these techniques. The simulation and calculation results are presented. The fabrication technique and test possibility are also discussed in this thesis and provides plans for future research.

Chapter 5 summarizes the major achievements of the research and provides plans for future research.

CHAPTER 2

THEORETICAL BACKGROUND

2.1 Magneto-optic effect

A magneto-optic effect is one of a number of phenomena in which an electromagnetic wave propagates through a medium that has been altered by the presence of a quasistatic magnetic field. In such gyrotropic materials, left- and right-rotating elliptical polarizations can propagate at different speeds, leading to a number of important phenomena. When light is transmitted through a layer of magneto-optic material, the plane of polarization can be rotated. This phenomenon is known as the result Faraday Effect. [84]

The properties of the material can be affected by the external field and these phenomena are advantageous in controlling integrated photonic crystal devices. The applied external fields for the optical manipulation include electric field, acoustic field and magnetic field. Potential applications include optical modulator, switch, light deflectors, isolators, amplifiers and radiation detectors. [20]

2.1.1 Magneto-optical iron garnet material system

Single crystal garnet thin films have been shown to be a good materials system for optical waveguides and devices [85]. The garnet material system is promising for device applications exploiting the magneto-optic effect. Among materials exhibiting a magneto-optic effect, iron garnets stand out because they exhibit a high Faraday rotation (FR) and low optical losses in the near infrared region 1.3-5.5μm. Optical absorption coefficients as low as $0.03cm^{-1}$ can be achieved. In this spectral range garnets are the only materials discussed in optical communications to realize nonreciprocal devices such as optical

isolators. This property is very important from the practical point of view, because it is widely used for developing non-reciprocal and other magneto-optical devices [86].

The base crystal system for single crystal garnet technology is yttrium iron garnet, or YIG with the chemical composition $Y_3Fe_2(FeO_4)_3$ or $Y_3Fe_5O_{12}$ [87] YIG which was first discovered in 1957 at Bell Labs [88] is widely used in various microwave and optical-communication devices and other applications mainly due to its suitable magnetic and magneto-optical properties. It shows low absorption of infrared wavelength and large Faraday Effect. [88-91] It has demonstrated such magnetic optic devices as temperature-independent optical isolator, useful for eliminating feedback from laser optical system. [92]

The garnet is characterized by a complex, but basically cubic crystal structure for one single formula unit with three main lattice site categories: tetrahedral sites, two octahedral and three dodecahedral plus oxygen atoms. One single formula unit of YIG contains these three main lattice sites as shown in Fig. 2.1[93]. In the YIG system, the tetrahedral sites and octahedral sites are both occupied by iron ions with +3 valences. The three dodecahedral are occupied by the yttrium ion with a valence of +3 or for a more complex garnet, these sites constrain the rare earth or bismuth ions. [91].

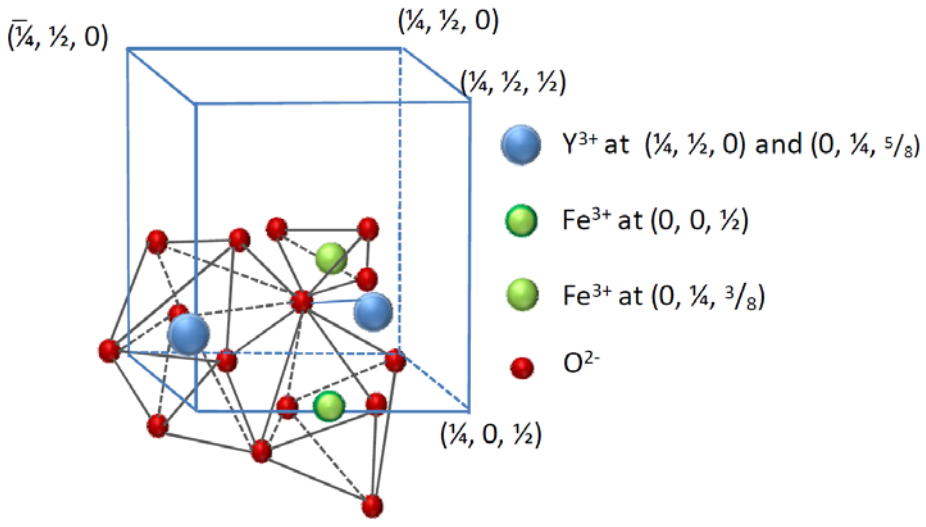

Figure 2.1 Diagram of lattice sites in garnet crystal structure

The pure YIG has fairly low magneto-optic effect in the form of Faraday rotation which degrades the efficiency of the interaction. However, the garnet system is well suited to fine tuning properties by way of varying composition. Those three large and open sites can be easily substituted by other ions [94].

Rare earth elements proved to be ideal for substitution into the crystal sites usually occupied by the yttrium. Bismuth can also substitute into these sites [95]. The substitution of yttrium by bismuth drastically increasing the Faraday rotation was first discovered by Buhrer [96]. The rotation is 7.8°/μm [97] at a wavelength of 633nm if the Yttrium is fully substituted by bismuth while the rotation is 0.084°/μm [98] for YIG. The origin of this effect was identified first by Akselrad [99] and further explained by Wittekoek and Lacklison [89].

They explained that this effect can be caused by the mixing of the 6p orbital of the Bi^{3+} ion with the oxygen orbital as shown in Fig. 2.2[100].

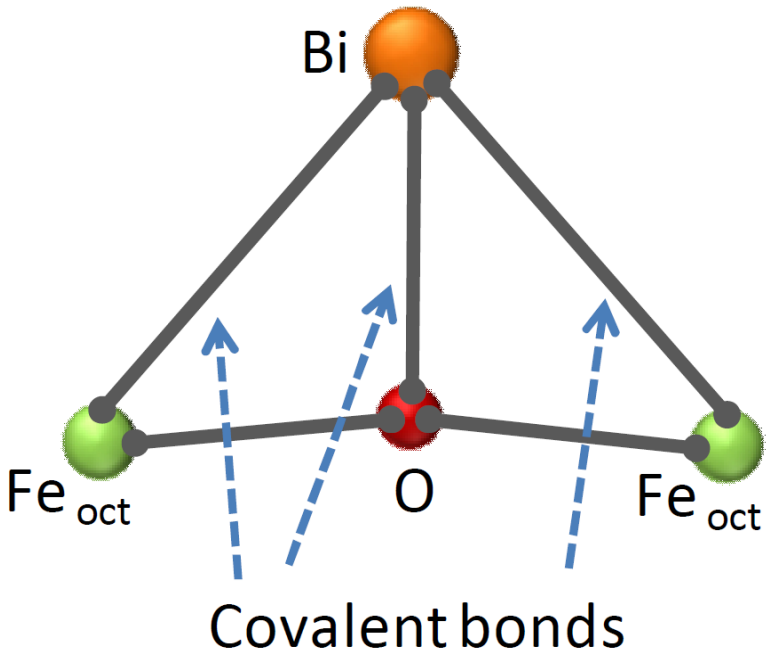

Figure 2.2 Schematic illustration of the iron garnet structure with bismuth enhanced electric dipole transition. Fe atoms replace O atom sites of octahedral and tetrahedral coordination and interact with each other through O [100].

Since the spin-orbit coupling for the 6p electrons of bismuth is about 17000cm-1 for the free ion [89], this mixing leads to a strong increase in the spin-orbit coupling of a 2p electron in O2-. A great strengthening of one or two transitions arising from the tetrahedral iron complex associates with this main effect. As a result, the Fe3+—O2-—Fe3+ interaction might be increased [91].

Lutetium is nonmagnetic as yttrium due to filled outer electron shells. With its smaller atomic size, it can balance out the lattice mismatch that occurs with simple bismuth doped YIG [101]. The bismuth is also nonmagnetic. This results in the iron ions being the only contributor to the magnetization of these films. The iron ions in the two coordination sites, the two octahedral and three tetrahedral sites, exhibit different spins and oppose each other in magnetizations due to super-exchange magnetic interaction. Therefore the net magnetic moments or a ferromagnetism result in the magnetic behavior.

High quality single crystalline YIG or substituted YIG thin film can be produced by liquid phase epitaxy (LPE) or sputtering technology. In this work, bismuth-gadolinum-substituted lutetium iron garnet films are mainly used for our device fabrication which requires low optical loss in the near infrared wavelength region. The films are grown by LPE on a transparent, paramagnetic garnet substrate, (100) gadolinium gallium garnet (GGG), which has a very good lattice match to the rest of the system [102]. The lattice constant for the GGG substrate is 12.383 $\overset{o}{A}$ which is close to pure that of pure YIG. But bismuth ion is much larger than yttrium. The substitution of bismuth into the dodecahedral site results in lattice mismatching. Alternatively, one can reduce the lattice mismatch between YIG and GGG by substituting Y and Fe with Lu and Ga, respectively. The rare material lutetium is used to improve the lattice match. [101]

2.1.2 Faraday Effect overview

Faraday Effect indicates that when light passing through certain materials is exposed to a magnetic field parallel to the propagation direction, the polarization of light rotates. It was first discovered by Michael Faraday in 1845 and was the first experimental evidence that light and electromagnetism are related. [103].

The Faraday Effect occurs as a consequence of the interaction of light and the magnetic field in a dielectric material. The polarization of the light can be changed by the magnetic field depending on the direction and strength of the field. The rotation of the plane of polarization is proportional to the intensity of the component of the applied magnetic field in the direction of the beam of light.

The relationship between the rotation of the ray and magnetic field is given as:

$$\theta = V \cdot H \cdot L \tag{2.1}$$

The angle of rotation of the polarization is proportional to the magnetic field H and the distance L the light travels in a medium along the direction of the field. The rotation is linearly related to the magnetic field by the Verdet constant, defined as the rotation per unit path, per unit field strength. This empirical proportionality constant varies with wavelength and temperature.

The most important property of the Faraday Effect is non-reciprocity. When the magnetic field direction is fixed, the polarization state keeps the same rotation direction. [21,104,105] The Fig. 2.3 shows the mechanism of the Faraday Effect non-reciprocity which is not feasible with the other effects.

The direction of incident light is long the dash line as shown in Fig. 2.3. The magnetic field stays the same direction in both pictures. When the light propagation is the same direction as the magnetic field, the polarization of the light rotates θ clockwisely as shown in Fig. 2.3(a). When the light reflects back, the light beam propagating into the

material has the θ off-set polarization rotation. Even the light travels in the opposite direction to the magnetic field, light still rotates anther θ clockwisely. The final output light is not the same as the original input; instead, it rotates 2θ. Thus, the rotation angle accumulates when the light travels back and forth in the materials if the magnetic field stays the same direction. However, if the light propagates in the same direction, the rotation of polarization can be changed by reversing the magnetic field direction.

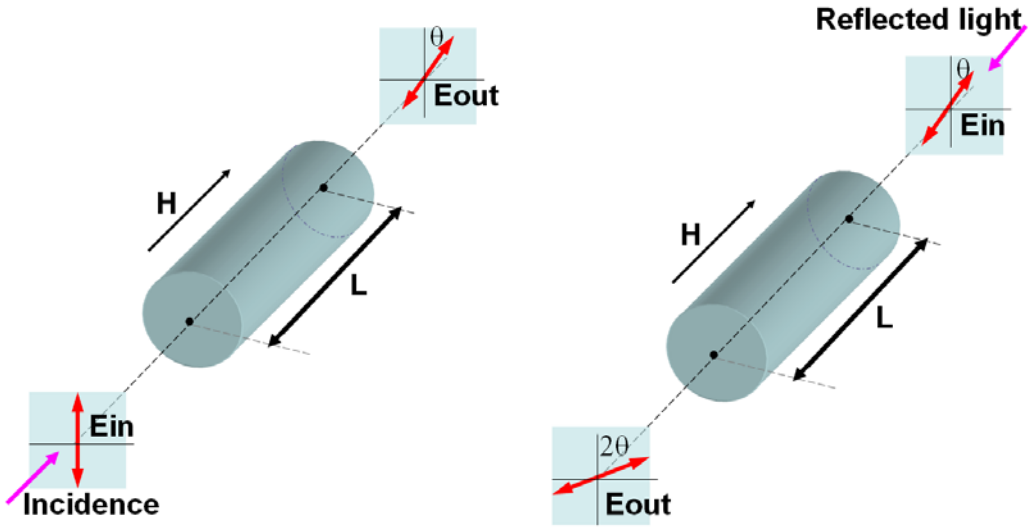

(a) **(b)**

Figure 2.3 Faraday Effect overview (a) Schematic illustration of the Faraday Effect; (b) Non-reciprocity character of the Faraday Effect.

2.1.2.1 Dielectric tensor

The propagation of electromagnetic waves in a material can be characterized by their electric and magnetic permeability tensors ε and μ. The dielectric tensor is the best description for magneto-optical effect and it is the bridge between theory and experiment since it relates the observable quantities, such as refractive index, absorption and FR, etc. When magnetic field is applied along the direction of light wave propagation (z axis), the dielectric tensor can be written as:

$$\boldsymbol{\varepsilon} = \begin{pmatrix} \varepsilon & \varepsilon' & 0 \\ -\varepsilon' & \varepsilon & 0 \\ 0 & 0 & \varepsilon \end{pmatrix} \tag{2.2}$$

The imaginary part of the diagonal elements describes absorption and the real part describes the propagation indicated. Gyrotropic effects, such as magnetic circular birefringence (Faraday Effect), polar Kerr effect and magnetic circular dichroism are described by the imaginary part of the off-diagonal element ε', which is the only element that depends linearly on magnetization. The diagonal elements are related to the normal refractive index n.

In the optical wavelength regime, the permeability of a birefringent uniaxial magnetooptic medium is very close to the permeability of vacuum μ_0, its relative permeability close to unity. The materials we used in our work are transparent to light with optical wavelength. We can assume no absorption of the light in the medium. The diagonal elements are real values. The relative permittivity tensor $\tilde{\varepsilon}$ of the medium for magnetization along the z-axis can be expressed as:

$$\tilde{\varepsilon} = \begin{pmatrix} \varepsilon_{xx} & i\varepsilon_{xy}' & 0 \\ -i\varepsilon_{xy}' & \varepsilon_{yy} & 0 \\ 0 & 0 & \varepsilon_{zz} \end{pmatrix} \tag{2.3}$$

This shows that all components of the relative permittivity are real and $\varepsilon_{xx} = \varepsilon_{yy}$ is not assumed. By solving the wave equation upon normal incidence of a monochromatic plane wave with time dependence $\exp(i\omega t)$ propagating parallel to the z axis on a birefringent magnetooptic medium, one obtains eigenmodes:

$$\boldsymbol{\varepsilon} = \frac{1}{\sqrt{2}} \begin{pmatrix} \cos\alpha \pm \sin\alpha \\ \pm i\cos\alpha - i\sin\alpha \\ 0 \end{pmatrix} \tag{2.4}$$

corresponding to the refractive indices

$$n_{\pm}^2 = \widetilde{\varepsilon} \pm \sqrt{\Delta^2 + \varepsilon_{xy}^2} \tag{2.5}$$

Here, $\widetilde{\varepsilon} = (\varepsilon_{yy} + \varepsilon_{zz})/2$, $\Delta = (\varepsilon_{yy} - \varepsilon_{zz})/2$ and $\tan(2\alpha) = \Delta / \varepsilon_{xy}$

The propagation constant in the medium is defined as: $\beta_{\pm} = \frac{\omega}{c} n_{\pm}$, c is the speed of light in the vacuum [106]

2.1.2.2 Magnetic circular birefringence

For linear electric and magnetic materials, the Maxwell equation wave equation can be expressed as:

$$\nabla^2 \vec{E} - \mu_0 \varepsilon_0 \vec{\varepsilon} \frac{\partial^2 \vec{E}}{\partial t^2} = 0 \tag{2.6}$$

Here, μ_0 and ε_0 are the magnetic and electric permeability of vacuum respectively. $\vec{\varepsilon}$ is the dielectric tensor for the material. Considering the electromagnetic wave propagate in the z direction, we can insert the plane wave expression $\vec{E} = \vec{E}_0 e^{i(\frac{2\pi}{\lambda} nz - \omega t)}$ into the wave equation, the updated wave equation can be expressed without the divergence operator and time derivatives as:

$$-(\frac{2\pi}{\lambda} n)^2 \vec{E} - \mu_0 \varepsilon_0 \vec{\varepsilon} \omega^2 \vec{E} = 0 \tag{2.7}$$

By substituting $\mu_0 \varepsilon_0 \omega^2 = (\frac{2\pi}{\lambda})^2$ into the equation, we obtained $-n^2 \vec{E} + \vec{\varepsilon} \vec{E} = 0$.

Taking dielectric tensor and $\vec{E} = (E_x, E_y, 0)$ into consideration, we can rewrite the wave equation into:

$$(-n^2 + \varepsilon_{xx}) E_x + i \varepsilon_{xy} E_y = 0 \tag{2.8}$$

$$-i \varepsilon_{xy} E_x + (-n^2 + \varepsilon_{xx}) E_y = 0 \tag{2.9}$$

Finally, we get two modes corresponding to right and left circular polarizations.

$$\hat{e}_{\pm} = (\hat{x} \pm i\hat{y})E_0 \exp[i(\frac{2\pi}{\lambda} n_{\pm} z - \omega t)] \tag{2.10}$$

These two modes have different refractive indices. This phenomenon is the effect of magnetic circular birefringence or Faraday Effect. [47]

Faraday rotators are magneto-optic nonreciprocal systems, characterized by two circularly polarized modes having opposite helicities, which is known as circular birefringence. The rays can be considered to re-combine upon emergence from the medium; however, owing to the difference in propagation speed they do so with a net phase offset, resulting in a rotation of the angle of linear polarization. [107].

These normal modes travel at different speeds in the material and their phase difference gives rise to an angular rotation in the polarization of incident linearly polarized light.

The Faraday rotator is magnetized along the direction of propagation, with the magnetization vector pointing either in the forward or backward direction. Considering the effect of magnetic circular birefringence on the transmission of an electromagnetic wave through a magneto-optic material, circular birefringence is exhibited with applying magnetic field parallel to the path of light.

In lossless isotropic material, birefringent materials decompose the incident linearly polarized light into left-hand circular polarized light and right-hand circular polarized (RCP and LCP) light with the same amplitude shown as Fig. 2.4.

Different indices of refraction $n_{\pm}$ exist for the left and right circularly polarized rays. As a result, these rays propagate at different speeds through the medium. The two rays combine at the end, yielding a ray that is offset compared with polarization from the incident ray. This split into opposite-helicity modes traveling at different speeds gives the system its nonreciprocal character, as the magnetization breaks the symmetry between forward and backward propagation.

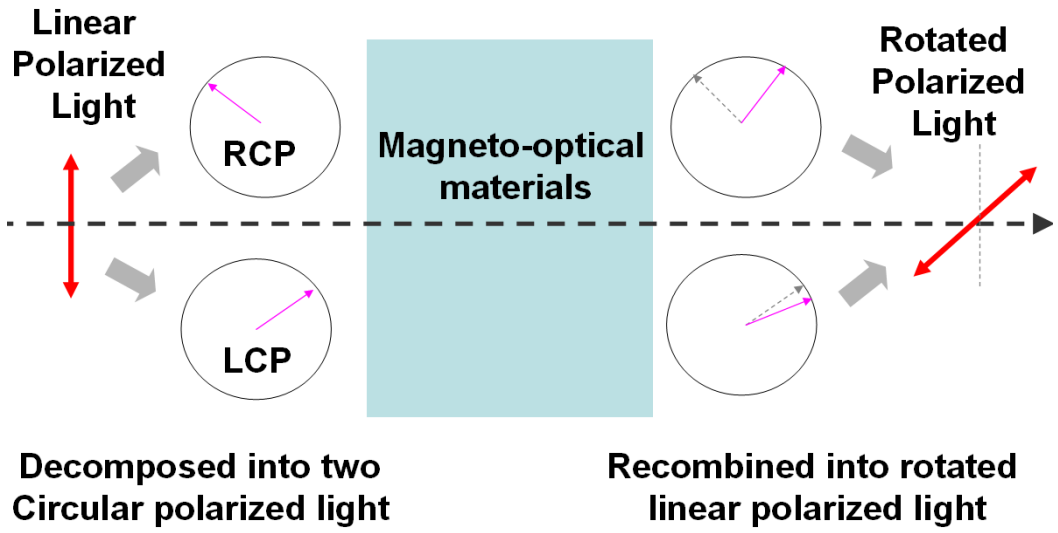

Figure 2.4 Mechanism of Faraday rotation. The diagram of an input linearly-polarized light composed into right- and left-circularly polarized eigenmodes, and its output polarization rotation due to the different experienced speeds of each eigenmodes.

For linearly polarized light passing through a length **L** of the material under the influence of a **B** field, the two circular polarization components suffer different refractive indices and therefore propagate in the medium with different phase shift. The relative phase shift is denoted as:

$$\Delta\phi = \frac{2\pi L(n_+ - n_-)}{\lambda} \tag{2.11}$$

The recombination of these two circular polarized light leads to a polarization rotation which is the rotated angle compared to the incident linear polarization. The Faraday rotation angle will be:

$$\theta_F = \frac{1}{2}\Delta\phi = \frac{\pi L(n_+ - n_-)}{\lambda} \tag{2.12}$$

2.1.2.3 Linear Birefringence

In the waveguide system, the difference of the refractive indices between transverse electric (TE) and transverse magnetic (TM) modes induces a linear birefringence, defined as $\Delta n = n_{TE} - n_{TM}$. There are three types of origins giving rise to the total linear birefringence in epitaxial film waveguides: geometrical or shape birefringence, stress-induced birefringence and growth-induced birefringence. [108] Geometrical birefringence appears when the film thickness is comparable to the wavelength. It is positive and decreases with the increasing of film thickness. There is a different birefringence for each pair of modes in the multimode films. Higher order modes have larger geometrical birefringence. The lattice constant difference between epitaxial film and substrate results in the stress-induced birefringence. Compression or tension in the film leads to negative or positive birefringence respectively. Growth-induced birefringence is observed in garnet bulk crystals and epitaxial films and is introduced during the film growth process. Proper post processing such as high-temperature annealing can reduce this effect to zero.[109] The total linear birefringence can be reduced to zero by carefully balancing the various contributions from geometric (positive value) and stress-induced (negative value) birefringence. [47, 88].

The linear birefringence plays a very important role in the study of the Faraday Effect in waveguide structures utilized in my research. The linear birefringence arises naturally in the fabrication of planar waveguide structure and generates both the preferential direction and ellipticity for light polarization while it is almost negligible effect in stacked films magneto-photonic crystal structures as the light is incident normal to the film plane without asymmetric boundary conditions. The linear birefringence suppresses Faraday rotation and degrades it from linear polarization. The term “polarization rotation” is used to describe the rotation of the semi-major axis of the elliptical polarization as a consequence of the combination of Faraday rotation and linear birefringence.

2.1.2.4 Magnetic elliptical birefringence

Magneto-optic films grown by various deposition techniques and subject to lattice mismatch and differential thermal expansion with the substrate will acquire linear birefringence [42, 110, 111]. In optical channels formed on the film, transverse electric (TE) and transverse magnetic (TM) modes will generally possess different effective or modal refractive indices, hence linear birefringence. The combination of circular and linear birefringence results in elliptically polarized modes. [112].

Birefringent magneto-photonic crystals arise naturally in the fabrication of PhCs in magnetic films for on-chip waveguide applications. A theoretical framework for understanding the polarization response of one-dimensional magneto-photonic crystals in magnetic media possessing simultaneous linear and magnetic circular birefringences is presented. The model elucidates the polarization responses of waveguide magneto-photonic crystals. Analytical expressions for the normal mode vector field amplitudes and their transmittance through the PhCs are obtained. The model predicts a significant nonreciprocal rotation in the presence of linear birefringence levels that would normally suppress the Faraday rotation in ordinary optical channels. [112]

Upon entering a transparent magnetic circular birefringent medium magnetized along the direction of propagation, linearly polarized light breaks up into two counter-rotating circularly polarized modes traveling at different speeds. The phase difference between these modes at the exit point is responsible for the Faraday rotation in the optical signal. In a medium possessing both linear and magnetic circular birefringences, the two components of circular polarization experience different refractive indices, therefore, each emerges from the medium with a different phase and amplitude. The normal modes of the system inside the material are, in fact, no longer circularly polarized but become elliptically polarized. So the material is no longer circularly birefringent but elliptically birefringent. Each elliptical normal mode has a different refractive index and the birefringence. These elliptically polarized modes propagate unchanged through the

medium except for a phase factor but with different refractive indices. [112] The amplitudes of the emergent beams may be denoted by a^+ and a^-, and their phase difference by Δφ, shown as Fig. 2.5.

The optical loss of the iron garnet material used in my work is negligible in the infrared range ~1.5 [113, 114]. The birefringence is the main reason to cause this phenomenon instead of the amplitude variation from the absorption.

Based on the reference [112], how to deduce the normal modes and how they propagate in a birefringence magneto-photonic crystal is discussed in the following section.

In the lossless medium, if Faraday rotation per unit length for the medium and the linear birefringence retardation per unit length are donated by α and β respectively. The x and y coordinates denote the normal mode axes of linear birefringence retardation. The transformation matrix P(z) for propagation of polarized light in medium with combined linear and circular birefringence can be expressed as:

$$P(z) = \exp(-i\frac{2\pi}{\lambda}\bar{n}z)\times\begin{bmatrix}\cos(bz)+i(\beta/2b)\sin(bz) & (\alpha/b)\sin(bz)\\ -(\alpha/b)\sin(bz) & \cos(bz)-i(\beta/2b)\sin(bz)\end{bmatrix} \quad (2.13)$$

Where $b=\sqrt{\alpha^2+\frac{\beta^2}{4}}$.

To obtain the normal modes of the propagation matrix, we solve the eigenvalue equation:

$$\exp(-i\frac{2\pi}{\lambda}\bar{n}z)\begin{bmatrix}\cos(bz)+i(\frac{\beta}{2b})\sin(bz) & (\frac{\alpha}{b})\sin(bz)\\ -(\frac{\alpha}{b})\sin(bz) & \cos(bz)-i(\frac{\beta}{2b})\sin(bz)\end{bmatrix}E(z)$$
$$= \chi\exp(-i\frac{2\pi}{\lambda}\bar{n}z)E(z) \quad (2.14)$$

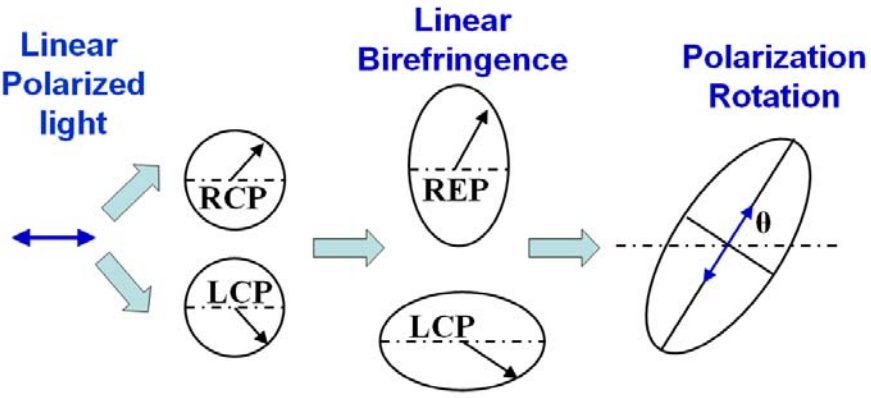

Figure 2.5 Mechanism of polarization rotation. Birefringence of the material causes ellipticity in both eigenmodes. The final output light exhibits a rotated elliptic polarization.

χ is a scalar quantity determined by equating the following determinant to zero:

$$\det\begin{bmatrix} \cos(bz)+i(\frac{\beta}{2b})\sin(bz)-\chi & (\frac{\alpha}{b})\sin(bz) \\ -(\frac{\alpha}{b})\sin(bz) & \cos(bz)-i(\frac{\beta}{2b})\sin(bz)-\chi \end{bmatrix}$$

The solution to the determinant is:

$$\chi = \cos(bz) \pm \sqrt{\cos^2(bz)-1} = \cos(bz) \pm i\sin(bz) = \exp(\pm ibz) \tag{2.15}$$

Thus the phase factors for normal modes are $\exp(-i\frac{2\pi}{\lambda}\bar{n}z \pm ibz)$.

So the elliptical normal modes are characterized by the following relations between there semimajor and semiminor electric field amplitude components.

$$\left(\frac{E_x}{E_y}\right)_{\pm} = i\frac{\alpha}{(\beta/2)\pm\sqrt{\alpha^2+(\beta^2/4)}} \tag{2.16}$$

$$\left(\frac{E_x}{E_y}\right)_{+} = \frac{1}{(E_x/E_y)_{-}} \tag{2.17}$$

Considering the response of the system to an input signal E_{in} linearly polarized along the x direction, we can express input electrical field as:

$$E_z^{in} = \begin{pmatrix} E_0 \\ 0 \end{pmatrix} \tag{2.18}$$

The light travels through the PhCs, the output signal are given as

$$E_z^{out} = \begin{pmatrix} X \\ Y \end{pmatrix} = \begin{pmatrix} \left[\cos(bz)\cos(cz) + \left(\frac{\beta}{2b} \right) \sin(bz)\sin(cz) \right] E_0 \\ -\frac{\alpha}{b} \sin(bz)\cos(cz) E_0 \end{pmatrix} \tag{2.19}$$

Here, $c = \frac{2\pi}{\lambda} n$

$$\cos(cz) = \frac{Y}{E_0} (-\frac{b}{\alpha}) \frac{1}{\sin(bz)} \tag{2.20}$$

The direction θ of the semi-major axis of the output polarization ellipse is given by:

$$\tan 2\theta = \frac{\frac{2b}{\alpha} ctg(bz)}{1 - \frac{1}{\alpha^2} ctg^2(bz)(b^2 + \frac{\beta^2}{4})} = \frac{2\sqrt{1 + \frac{\beta^2}{4}} ctg(bz)}{1 - ctg^2(bz)(1 + \frac{\beta^2}{4\alpha^2})} \tag{2.21}$$

Based on this equation, when input light is horizontally polarized, the polarization rotation can be calculated from the Faraday rotation and linear birefringence. In the following chapters, this equation is used to obtain the plots of polarization rotation as a function of linear birefringence. Thus, we can obtain how many power stays as TE propagation and how many power transfers to TM propagation when light passes through the waveguide with certain distance.

2.2 Waveguide theory

A waveguide is a structure that confines and directs wave propagation, in particular, electromagnetic waves at optical frequencies. According to their geometry, optical waveguides can be classified as planar waveguides, strip waveguides or fiber waveguides. Based on mode structure, it is divided into single-mode and multi-mode waveguide. It can also categorized by refractive index distribution as step or gradient index).

The optical planar waveguide is an optical thin film based structure for carrying the light wave. It has advantage in high density integration and low price mass production [115].Basically, a waveguide contains a region of higher refractive index, compared to surrounding medium. Particularly in a thin film planar waveguide, the thin film is deposited on a transparent dielectric substrate and used as optical waveguide if the film index is higher than the substrate index. Planar waveguide based devices involve new phenomena including birefringence and mode related polarization rotation, which cannot be seen in stacked structure magneto-photonic crystals.

The basic structure contains cladding layer (top), guiding layer (middle), and substrate (below). The waveguide in Fig. 2.6 (a) is called a slab waveguide or 2-D waveguide because light is confined only in the y direction. The waveguide in Fig. 2.6 (b) is called a ridge waveguide or 3-D waveguide because light is transversely confined in the x direction in addition to confinement along y direction. The cladding layer in Fig. 2.6(b) is air. In the slab waveguide, the ray-optical method can be used to introduce basic guided mode concepts. The light beam propagates along the z-direction. The critical angle for total internal reflections at both upper and lower interfaces, are respectively

$$\theta_s = \sin^{-1}\left(\frac{n_s}{n_f}\right), \quad \theta_c = \sin^{-1}\left(\frac{n_c}{n_f}\right) \tag{2.22}$$

The light can be guided only if the index of each layer satisfies the condition: $n_f > n_s$ and $n_f > n_c$. Here: n_f, n_s and n_c are refractive index of guiding layer, substrate and cladding layer respectively. Otherwise, the light leaks into cladding or substrate layer.[116]

The modes of light propagation supported in waveguide structure depend on the dimensions of the waveguiding region and the refractive index contrast defining the waveguiding region. In general, the guided modes can only be confined above a certain film thickness which is defined as cut-off thickness. It happens when the effective index is equal to the index of the substrate. The thickness T of the guiding layer should be larger than the critical thickness. A particular mode of propagation is characterized by "effective" refractive index and is determined by the angle (θ) that the propagation vector makes with the normal to the cladding and waveguide interface. The specific multiple values of θ supported by a particular slab waveguide are determined by the integral relationship that must be maintained between the thickness of the waveguide, T, and the y-component of the mode wave vector ky. The most general waveguide is thus a "multimode" waveguide.

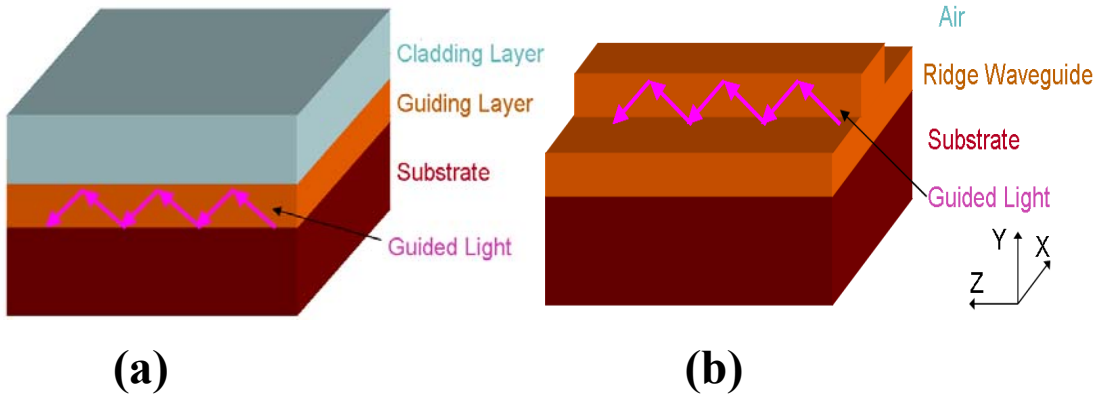

Figure 2.6 Schematic of waveguide structure. (a) slab waveguide; (b) ridge waveguide

Electromagnetic waveguides are analyzed by solving Maxwell's equations, or the electromagnetic wave equation, with boundary conditions determined by the properties of the materials and their interfaces. These equations have multiple solutions, or modes,

which are eigenfunctions of the equation system. Each mode is therefore characterized by an eigenvalue, which corresponds to a cutoff frequency below which the mode cannot exist in the guide. Waveguide propagation modes depend on the operating wavelength and polarization and the shape and size of the guide. The longitudinal mode of a waveguide is a particular standing wave pattern formed by waves confined in the cavity. The transverse modes are classified into different types: TE modes have no electric field in the direction of propagation. TM modes have no magnetic field in the direction of propagation. TEM modes (Transverse Electromagnetic) have no electric or magnetic field in the direction of propagation. Hybrid modes have both electric and magnetic field components in the direction of propagation. [117] In our work, we mainly study the effects from the TE and TM input polarization light.

In an isotropic, lossless dielectric media, Maxwell's equations are [116, 118, 119]:

$$\nabla \times \vec{E} = -\mu_0 \frac{\partial \vec{H}}{\partial t}, \qquad \nabla \times \vec{H} = -\varepsilon_0 n^2 \frac{\partial \vec{H}}{\partial t} \tag{2.23}$$

where n is the refractive index of the media. In the Cartesian (x, y, z) coordinates (see in Fig. 2.6(b), when the plane wave propagates along the z direction with the propagation constant $\boldsymbol{k}$, the solutions for (6) are

$$\vec{E} = E(x,y)e^{i(\omega t - kz)}, \ \vec{H} = H(x,y)e^{i(\omega t - kz)} \tag{2.24}$$

Here, the angular frequency $\omega = 2\pi c / \lambda$.

Two different modes with mutually orthogonal polarization exist in a 2-D slab waveguide [120]. One is TE mode which consists of the field components E_y, H_x, and H_z. The other is TM mode, which has E_x, H_y, and E_z. The propagation characteristics of TE and TM modes are determined by the field solutions and the boundary conditions.

The wave equations of TE and TM mode can be expressed as:
TE mode

$$\frac{\partial^2 E_y}{\partial x^2} + (k_0^2 n^2 - \beta^2) E_y = 0$$

$$H_x = -\frac{\beta}{\omega \mu_0} E_y \tag{2.25}$$

$$H_z = -\frac{1}{i\omega \mu_0} \frac{\partial E_y}{\partial y}$$

TM mode

$$\frac{\partial^2 H_y}{\partial x^2} + (k_0^2 n^2 - \beta^2) H_y = 0$$

$$E_x = -\frac{\beta}{\omega \varepsilon_0 n^2} H_y \tag{2.26}$$

$$E_z = -\frac{1}{i\omega \varepsilon_0 n^2} \frac{\partial H_y}{\partial x}$$

From the boundary conditions, he continuity conditions at the interfaces (x = -T and x =0) should be satisfied. The eigenvalue equations that determine the propagation modes of TE and TM are generated by the field solutions. The two orthogonal TE and TM modes must be distinguished to discuss dispersion characteristics of the guided modes. But the analysis is the same. Here we discuss the analysis for TE mode.

From equation

$$\frac{\partial^2 E_y}{\partial y^2} + (k_0^2 n^2 - \beta^2) E_y = 0) \tag{2.27}$$

The field solutions are written in the as equation (2.24) in different layers.

$$E_y = E_c \exp(-\gamma_c x), (x > 0) \qquad \text{in the cover}$$

$$E_y = E_f cox(k_x x + \varphi_c), (-T < x < 0) \text{ in the guiding layer} \tag{2.28}$$

$$E_y = E_s \exp\{(-\gamma_s (x + T)\}, (x < -T) \text{ in the substrate}$$

Where the propagating constants in x direction are written in terms of the effective index N which is defined as $N = n_f \sin\theta = \frac{\beta}{k_0}$

$k_x = k_o\sqrt{n_f^2 - N^2}$, $\gamma_s = k_o\sqrt{N^2 - n_s^2}$, $\gamma_c = k_o\sqrt{N^2 - n_c^2}$

From the boundary condition, the tangential field components E_y and H_z are also continuous at the interface x=0 and *x =T.* This yields the equations:

$$E_c = E_f \cos\varphi_c \tag{2.29}$$

$$\tan\varphi_c = \frac{\gamma_c}{k_x} \tag{2.30}$$

The eigenvalue equation is generated by eliminating arbitrary. So for TE mode, we have equation

$$k_x T = (m+1)\pi - \tan^{-1}(\frac{k_x}{\gamma_s}) - \tan^{-1}(\frac{k_x}{\gamma_c}) \tag{2.31}$$

Similarly, for TM mode, we have equation:

$$k_x T = (m+1)\pi - \tan^{-1}(\frac{n_s}{n_f})^2(\frac{k_x}{\gamma_s}) - \tan^{-1}(\frac{n_s}{n_c})^2(\frac{k_x}{\gamma_c}) \tag{2.32}$$

Here T is the thickness of the waveguide, *m* is the mode number, equal to 0, 1 2…, and k_y shows that light propagates in the y direction. $N = n_f \sin\theta$ is effective index, $k_0 = \frac{2\pi}{\lambda}$ is a constant known as the free space wave number, θ is the angle of propagation for a supported mode, and λ is the wavelength of the light. γ_s relates the substrate layer to the effective index, γ_c relates the cladding layer to the effective index. N must be discreet values in the range of $n_s<N<n_f$ because the mode number is positive integer. By numerically solving the equations, we can evaluate the dispersion characteristics of guided mode. For a given wavelength and waveguide structure, the number of existed modes is certain. The more modes we can obtain as the film thickness increases. Several propagation mode, indicated as fundamental mode, first order mode,

second order mode and so one corresponding to different m number can coexist in the waveguide.

When the indices of the waveguide material and the guide thickness T are given, ky and the effective index N can be obtained from equation (2.29) and (2.30) for TE and TM modes. There is a minimum thickness for the film to support at least one mode. This point is the cut-off point of the guided modes. However, there is no cut-off thickness for symmetric waveguide with $n_c=n_s$.

The optical electric field and intensity distributions of various waveguide modes are demonstrated in Fig. 2.7 which is simulated by beam propagation method (BPM) using commercial simulation software RSOFT. The dark lines on each pictures are electric filed distributions Ey(x) obtained by equation (2.28).

For a further detailed understanding of light guiding properties, the power P carried by the propagating wave is introduced. The power P carried by a TE mode per unit waveguide width is written as: $P = -\int_{-\infty}^{+\infty} E_y(x) H_x(x) dx$

The power carried by a TM mode per unit waveguide width is written as:

$$P = -\int_{-\infty}^{+\infty} E_x(x) H_y(x) dx \qquad (2.33)$$

TE mode and TM mode can use similar analysis. Considering TE mode situation, the electric field amplitude is normalized so that a unit power is carried by the guided mode.

The preceding power equation can be expressed in the form:

$$P = \frac{1}{2} E_f . H_f . T_{eff} \qquad (2.34)$$

The guided mode is essentially confined to the thickness T_{eff} because it spreads somewhere into the substrate and the cover.

The cladding and substrate indices are different so that the light leaking out at the interfaces exhibits asymmetric exponential decay with distance. This explains that the effective waveguide thickness is larger than the film thickness due to the spreading wave energy into the cladding and substrate layer. The effective thickness is defined as:

$$T_{eff} = T + \frac{1}{\gamma_s} + \frac{1}{\gamma_c} \tag{2.35}$$

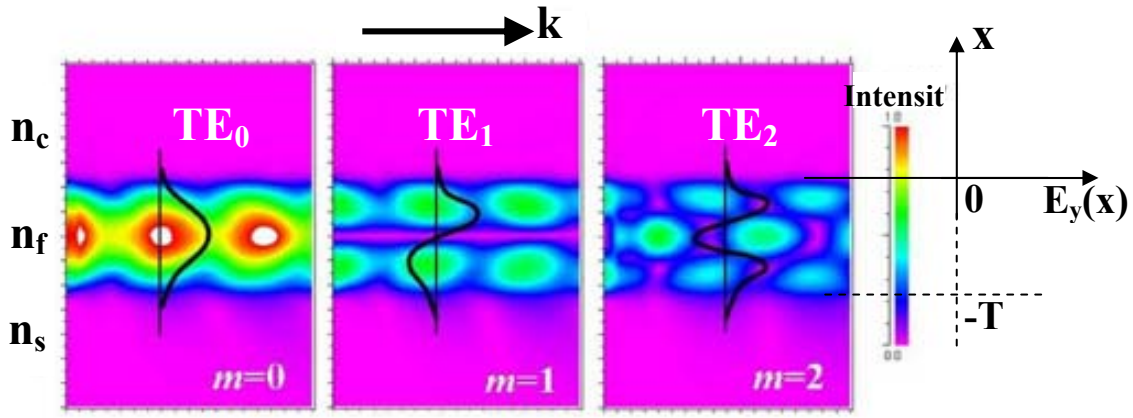

Figure 2.7 The energy distribution of the propagation modes in waveguides.

Here, where $\gamma_{s,c}$ are the optical field decay constants in the substrate and cover, respectively. So $\frac{1}{\gamma_s}$ and $\frac{1}{\gamma_c}$ are the length that wave penetrates to substrate and cladding.

The effective waveguide thickness of the TM guided mode can be obtained in the same analysis as TE mode. It can be expressed as:

$$T_{eff} = T + \frac{1}{q_s \gamma_s} + \frac{1}{q_c \gamma_c} \tag{2.36}$$

Where the quantity q_s and q_c are defined as:

$$q_s = \left(\frac{N}{n_f}\right)^2 + \left(\frac{N}{n_s}\right)^2 - 1 \tag{2.37}$$

$$q_c = \left(\frac{N}{n_f}\right)^2 + \left(\frac{N}{n_c}\right)^2 - 1 \tag{2.38}$$

Overall, the Teff depends upon the mode number. The higher order guided mode has, the larger the effective waveguide thickness is.

For a 3-D waveguide as ridge waveguide, analytical solutions are obtained by approximate analysis. Marcatili's method and the effective index method can be sued for approximate analyses when the guided mode is far from the cut off or the aspect ratio of the ridge waveguide width to thickness is larger than unit. [108, 121] BeamPROB component of RSOFT is used for the study of beam propagation in the ridge waveguide in our work.

2.3 Magneto-Photonic Crystals

When the constitutive materials of photonic crystals are magnetic, the resultant PhCs exhibit very unique optical and magneto-optical properties. Novel functions, such as band Faraday Effect, magnetic super-prism effect and non-reciprocal or magnetically controllable photonic band structure, are predicted to occur theoretically. [122-130]All the unique features of the media arise from the existence of magnetization in media, and hence they are called magneto-photonic crystals providing the spin-dependent nature in PhCs. [122**]** The last decade has witnessed a growing interest in optical propagation and polarization effects in magneto-photonic crystals. [123-131] Nonreciprocity and gyrotropy (Faraday Effect) have been motivating factors for the study of photonic band gap structures in magnetic materials. This activity has generated a number of interesting experimental results and theoretical predictions. Thus, photon trapping in magneto-optic nonreciprocal resonant cavities has been shown to lead to significant Faraday rotation

enhancement. [25, 29 123, 124] Electromagnetic unidirectionality and time-reversal symmetry breaking have also been predicted in nonreciprocal media.[33, 125]

The introduction of crystalline or waveguide-induced anisotropy in magneto-photonic band-gap structures adds a level of complexity and appeal to these systems. Magneto-photonic crystal waveguides and linearly birefringent layers embedded in magneto-optic stacks are examples of such systems. [127-131] Prior work has studied band gap formation and near band-edge polarization rotation in birefringent waveguides, demonstrating strong magneto-optic polarization effects. [126, 128]

Bloch states in birefringent magneto-photonic layered stacks have also been examined theoretically by M.Levy and co-workers.[127-131] This analysis has looked at layered stacks supporting elliptically-birefringent local normal modes, namely elliptically-polarized states with different refractive indices for opposite helicities.[106, 128,131] Different local normal-mode elliptical polarization states characterize adjacent layers. Other work also examined alternating layers with circular and linear birefringence in adjacent layers, a limiting case of the alternating elliptical birefringence. [127, 130]

The coupling of different local normal modes brought about by the boundary conditions at the layer interfaces leads to interesting band gap effects. Bloch states of the system are no longer transverse-electric, transverse-magnetic or circularly polarized. They are rather linear combinations of differently polarized states yielding states with spatially-dependent elliptical polarization.[106, 129-131] The coupling of such Bloch states at points of wave-vector and frequency degeneracy (cross-over points in a band structure plot) can lead to the formation of new types of band gaps.[127-131] Such band gaps, resulting from the hybridization of different Bloch modes, have been theoretically shown to lead to polarization degeneracy at the band edges, and to the rejection of arbitrarily-polarized light.[127] These are called gyrotropic degenerate band gaps.[106, 128, 129]

Although one-dimensional layered magneto-photonic crystals are easily calculated and a widespread modeling structure has been advanced, [110, 124, 127-131] there are important disadvantages to such systems. First of all, to observe the formation of gyrotropic degenerate band gaps in such systems one must use natural anisotropic material with significant anisotropy. There are only few such materials at optical frequencies. Secondly, in order to avoid additional coupling between ordinary and extraordinary waves, one should control the directions of the optic axes in all anisotropic layers with extremely high accuracy. Otherwise the gyrotropic degenerate band gaps will be smoothed over by the appearance of band gaps such as in periodical Šolc filters, where band gap formation is induced by the periodic misalignment of anisotropy axes between adjacent layers. [132] It is hard to create those types of gyrotropic structures by simple sputtering technology because usually the symmetry of the atomic cells is different for anisotropic and magneto-optical materials. All these disadvantages lead to the search for structures where one may control anisotropy properties carefully.

In my research topic, we present an experimental realization of such structures in magneto-optical waveguide photonic crystals. Indeed, waveguide structures already support geometry-induced birefringence between TE and TM polarized waves. Hence natural anisotropy is not required to engender linear birefringence. Also important is that it is possible to prepare these birefringent gyrotropic waveguides from homogeneous magneto-optical materials, thus it is not necessary to stack material layers of different atomic cell symmetry and one may control the direction of the anisotropy axes by controlling the waveguide shape.

Full analytical expression are obtained and analyzed for the dispersion relation and Bloch modes and the conditions for formation of band gap is examined in a one dimensional layered stack PhCs. [131] The approach can also be used analyze the properties of two-dimensional magneto-photonic crystals.

2.3.1 Birefringent periodic stack magneto-photonic crystals

A full analytical formulation for the band structure and Bloch modes in a layered-stack photonic crystal and their properties are analyzed. The model incorporates both the effects of gyrotropy and linear birefringence generally present in magneto-optic thin-film devices. It demonstrates a useful tool in the analysis and design of photonic crystal bandgap systems. [131] It is found that local normal-mode polarization-state differences between adjacent layers lead to mode coupling and affect the wave-vector dispersion and the character of the Bloch states of the system. This coupling produces extra terms in the dispersion relation not present in uniform circularly birefringent magneto-optic stratified media. Normal-mode coupling lifts the degeneracy at frequency band crossover points under certain conditions and induces a magnetization-dependent optical bandgap. This study examines the conditions for bandgap formation in the system. It shows that such a frequency split can be characterized by a simple coupling parameter that depends on the relation between polarization states of local normal modes in adjacent layers. [106]

2.3.1.1 Degenerate Gyrotropic Band Gaps

Gyrotropic degenerate bandgaps have recently been predicted for elliptically birefringent magneto-photonic crystals of the type encountered in magnetic garnet waveguide media by M. Levy, A. M. Merzlikin and A. A. Jalali. [106, 130, 131] The combination of anisotropy, gyrotropy, and periodicity can result in the formation of gyrotropic degenerate band gaps. These band gaps appear inside the Brillouin zone as a result of the Bragg resonance between local normal modes having different polarization states. Elliptical birefringence results from a disparity in refractive indices between elliptically polarized local normal modes, and occurs naturally in planar magneto-photonic crystal waveguides. The possibility to excite different waveguide modes lends added richness to the class of phenomena that can be probed in such systems. Bandgaps have been observed where the Bragg reflection mechanism links forward-going fundamental waveguide modes to high-order backscattered ones. The coupling between different

waveguide modes travelling in opposite directions leads to particularly interesting phenomena. [127, 128]

2.3.1.2 Theoretical Model for periodic stack magneto-photonic crystal

Plane waves are normally incident on a periodic stack structure consisting of alternating elliptically birefringent magneto-optic layers. The basic geometry of the periodic stack model is depicted in Fig. 2.8. $d^{(n)}$ is the thickness of the layer n. This structure captures many of the essential features of the waveguides under consideration. In particular an alternating system of elliptical birefringent states is introduced in adjacent layers. The bloch states for this system can be expressed as a linear combination of local mornal modes. [128]The layers have different average dielectric constants $\bar{\varepsilon}$ and are not assumed to have the same linear birefringence terms Δ, or gyrotropic components ε_{xy}. Here $\bar{\varepsilon} = (\varepsilon_{xx} + \varepsilon_{yy})/2$, $\Delta = (\varepsilon_{yy} - \varepsilon_{xx})/2$.

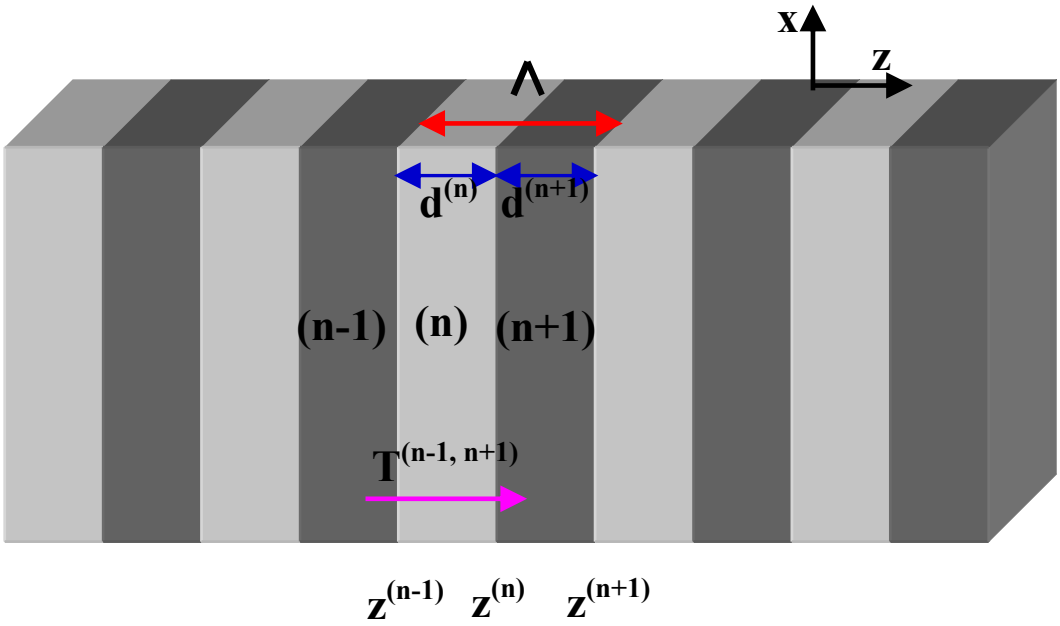

Figure 2.8 Schematic diagram of a one-dimensional birefringent magneto-photonic crystal with period of Λ. The MPCs extends indefinitely in the x and y directions. A plane wave is incident normally to the layered structure. A unit cell spans the region between z^{n-1} and z^{n+1}.

The elliptical birefringence parameters of adjacent layers may differ, but the anisotropy axis are aligned. The Bloch states for this system can be expressed in terms of local normal modes. The use of local normal modes in coupled mode theory is discussed by Dietrich Marcuse in his book on the theory of dielectic optical waveguide [134] Thus in the nth layer the optical electric field a linear combination of the elliptical eigenvectors and can be written as: [106,131]

$$E^{(n)}(z) = (E_{01}^{(n)} e^{i\beta_{+}^{(n)}(z-z_n)} + E_{02}^{(n)} e^{-i\beta_{-}^{(n)}(z-z_n)})\hat{e}_{+}^{(n)} + (E_{03}^{(n)} e^{i\beta_{+}^{(n)}(z-z_n)} + E_{04}^{(n)} e^{-i\beta_{-}^{(n)}(z-z_n)})\hat{e}_{-}^{(n)} \tag{2.39}$$

Here $(E_{0i}^{(n)}(i = 1,...,4)$ are the complex amplitudes of the partial waves corresponding to each normal mode and $\beta_{\pm}^{(n)} = \frac{\omega}{c} n_{\pm}^{(n)}$ are the wave vectors. As described in detail in prior publications by Levy and Jalali [106, 131], it allows the backward-propagating local normal modes to differ in refractive index and polarization state from the forward-travelling modes. Because the satering mechanism responsible for the formation of multiple stropbands in one-dimensional magnetophotinc crystals waveguide, a mechanism that connects different waveguides modes through contradirectional coupling. . [128]

Then the bloch mode in layer n is rewritten as:

$$\begin{aligned} E^{(n)}(z,t) = &[E_{01}^{(n)} \exp(i\frac{\omega}{c} n_{+}^{f}(z-z_n))\hat{e}_{+}^{f} + E_{02}^{(n)} \exp(-i\frac{\omega}{c} n_{+}^{b}(z-z_n))\hat{e}_{+}^{b}]e^{-i\omega t} \\ &+ [E_{03}^{(n)} \exp(i\frac{\omega}{c} n_{-}^{f}(z-z_n))\hat{e}_{-}^{f} + E_{04}^{(n)} \exp(-i\frac{\omega}{c} n_{-}^{b}(z-z_n))\hat{e}_{-}^{b}]e^{-i\omega t} \end{aligned} \tag{2.40}$$

Here f and b strand for forward and backward with propagationg along z- direction.

The Bloch states for this system satisfy the Floquet–Bloch theorem through the following eigenvalue equation:

$$T^{(n-1,n+1)}E = \exp(iK\Lambda) \tag{2.41}$$

Where the transfer matrix $T^{(n-1,n+1)}$ relates the four eigenmode amplitudes E in the second layer of a unit cell which is the region between $z=(n-2)\Lambda$ and $z=(n-1)\Lambda$ to the corresponding amplitudes in the second layer of the adjacent unit cell which is the region between $z=(n-1)\Lambda$ and $z=n\Lambda$. K is the Bloch wave vector, and Λ is the period of the periodic structure. The unit cell transformation matrix $T^{(n-1,n+1)}$ depends on the relative elliptical birefringence parameters and the individual normal mode propagation constants for each layer. When the elliptical birefringence is equal to zero, there is no admixture of the local modes which means that transverse electric (TE) and transverse magnetic TM waves or right- and left- circularly polarized waves remain uncoupled. When there is elliptical birefringence, the Bloch states require an admixture of local normal modes. The strength of the coupling depends on the elliptical birefringence. This elliptical birefringence parameterizes the degree of admixture of the normal modes.

2.3.2 Magneto-photonic crystals on planar waveguides

In planar magneto-photonic crystal waveguides elliptical birefringence occurs naturally. For a one-dimensional ridge waveguide, the band gaps form as a result of the coupling between forward-propagating fundamental modes with backscattered modes of different orders.

The light is back-reflected at stop bands obeying the Bragg condition $\vec{\beta}_{Backward}=\vec{\beta}_{forward}+\vec{K}$, where grating vector $K=\frac{2\pi}{\Lambda}$ and wavevector $\beta=\frac{2\pi}{\lambda}n$, with n equal to the effective index of the corresponding propagating mode. Backward waves correspond to high-order waveguide modes. [133] Fig. 2.9 shows the vector diagram above shows the requirements for the Bragg reflector.

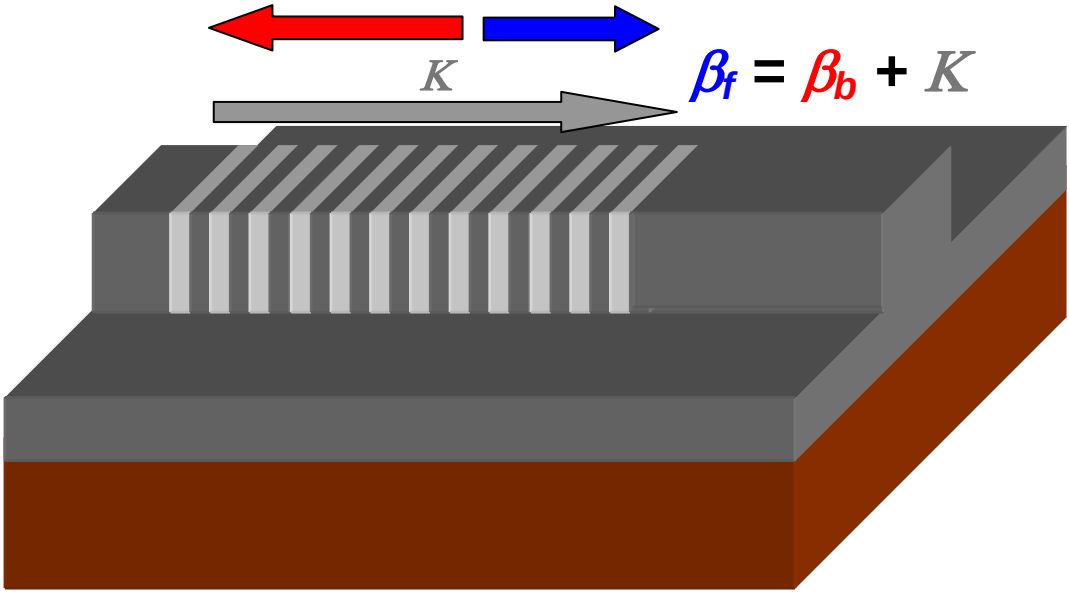

Figure 2.9 The vector diagram above shows the requirements for the Bragg condition for photonic crystals.

In the Bragg reflector, as the incident wave propagates in the forward direction, it encounters many fringes of the grating and each fringe reflects a small fraction of the incident wave. The reflected waves are distributed over the entire grating pattern. As the frequency of incident wave is uniquely determined by grating vector K and backscattering wavevectors β, this frequency is called the "Bragg frequency", which forbids light propagate.

The fundamental modes (TE and TM) have small linear birefringence, and where the higher-order modes have significant birefringence the separation in frequency between different bandgaps in more pronounced for the higher order modes. This is a situation not too different from the case in many of our magneto-photonic crystal waveguides.

2.3.2.1 Gyrotropic bandgap formations in one dimensional grating structures

Considering the phase matching condition for an optical guided wave characterized by a propagation wave-vector $\vec{\beta}$, incident upon a grating region having grating vector $\vec{K}$, where $\left|\vec{K}\right| = \frac{2\pi}{\Lambda}$ and grating period Λ, we see that a space harmonic $\vec{\beta} + q\vec{K}$, for $q = 0,\pm1,\pm2,...$ which is the order of coupling can propagate as a mode as long as $\vec{\beta} + q\vec{K} = \vec{\beta}_m$, for some mode m with wave-vector $\vec{\beta}_m$. The relations can be depited as a wave vector diagram with vectors $\vec{\beta}$, $\vec{\beta}_m$ and K. Such diagrams can be used to determine the combinations of waves involved in the coupling. [116]

The gratings can exhibit wavelength dispersion. The dispersion of a grating in a waveguide structure can be illustrated by using the Brillouin diagram. Fig. 2.10 shows the Brillouin diagram for a waveguide without a grating or photonic crystal structures. There exist no mode couplings. The bold solid curves indicate the guided modes.

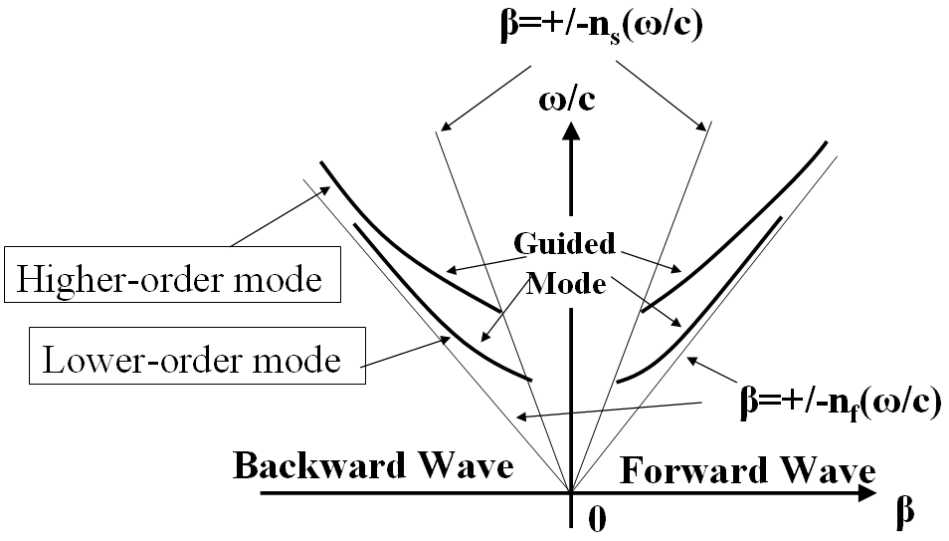

Figure 2.10 Brillouin dispersion diagram for guided modes without a grating structure.

This plot is obtained from the simple dispersion relation for waveguide modes, where one plots frequency versus mode wave-vector. It is taken here from [116]. The curves for the qth order space harmonics yielded by a grating can be obtained by shifting the curves by qK along the β axis. This is a typical plot for TE and TM modes. In the presence of waveguide birefringence the branches for TE and TM modes of a given order are shifted relative to each other but there is no coincidence. The guided mode branches fall between the lines $\frac{\omega}{c} n_f$ and $\frac{\omega}{c} n_s$, where n_f and n_s stand for the film and substrate indices.

In a photonic crystal waveguide the phase-matching condition $\vec{\beta} + q\vec{K} = \vec{\beta}_m$ can be displayed graphically by shifting the dispersion plot by K and looking for the cross-over points. Fig. 2.11 shows the Brillouin diagrams for waveguide grating structures where the interactions are the fundamental order codirectional and contradirectional coupling, respectively. [116]

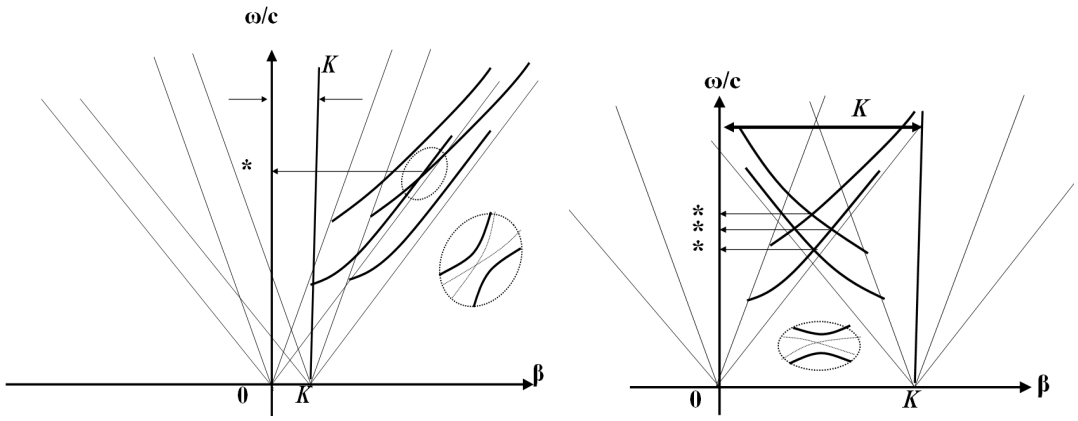

Figure 2.11 Brillion diagrams for guided wave goupling by a grating structure. The coupling occurs at a wavelength corresponding to ω/c indicated by *. (a) is for codirectional coupling; (b) is for contradirectional coupling.

When no couplings occur, the diagrams exactly match the superposition of the curves for the space harmonics. When there are intersections of these curves which are the phase matching points, the dispersion curves are varied by coupling as shown in the enlarged

insets. Panel (a) shows the plot for first order Bragg co-directional coupling. The co-directional coupling yields two normal close β value modes. Coupling can be considered as the interference between the propagation of these two normal modes. Panel (b) in the figure below shows the plot for first-order Bragg contra-directional coupling. The graph is separated into upper and lower curves. The stopband can appear and the wave can not propagate substantially along the z direction. This occurs when K is large enough to allow cross-over between forward and backward propagating guided modes.

In the presence of linear birefringence, i.e. when $\beta_{TE_m} \neq \beta_{TM_m}$ the cross-over between the fundamental mode and mode m looks schematically as follows in Fig. 2.12. This plot has exaggerated the difference between TE and TM branches for the sake of clarity.

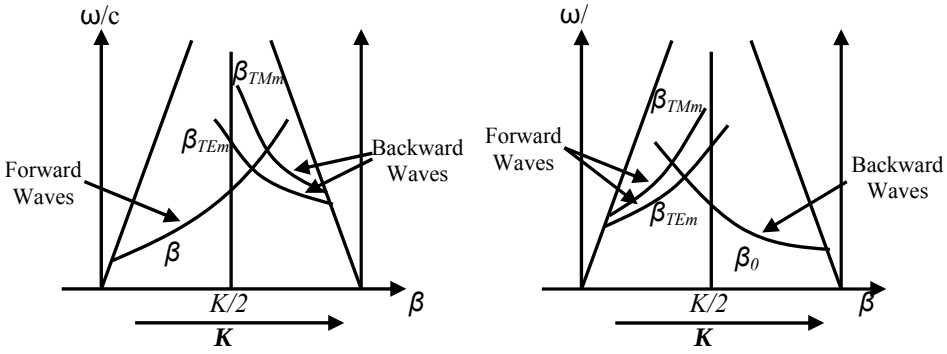

Figure 2.12 Schematic dispersion diagrams for exaggerated TE and TM branches. The difference between TE and TM branches is obvious.

Due to phase matching a band gap opens up at the cross-over points. For fundamental TE or TM modes no band gap would open up at the cross-over with the corresponding high-order orthogonal polarization state. Since TE and TM wave are orthogonal to each other, there are no band gaps for TE to TM cross-over. However, in the presence of gyrotropy, for circularly or elliptically polarized forward modes, a band gap opens up at the cross-over with TE and with TM, or more generally, elliptical backward waves. This is generally true for coupled TE-TM polarized modes which are elliptical modes in non-waveguide configurations. This is shown in Fig. 2.13.

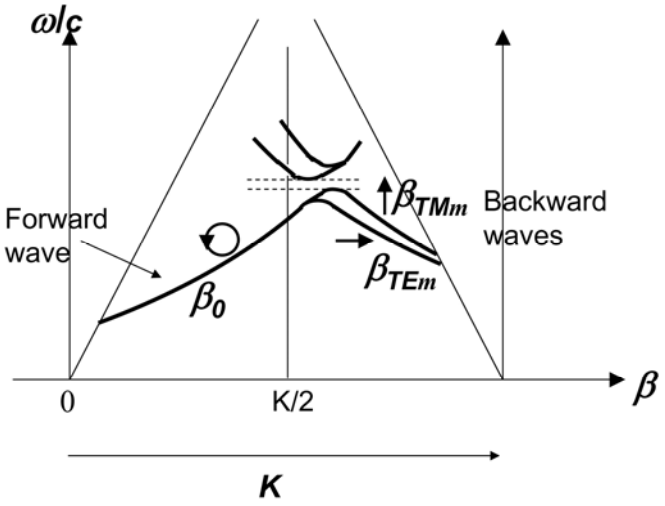

Figure 2.13 Band gap opens up due to the coupling between different elliptically polarized modes traveling in the forward and backward directions.

It should be understood that in the language of waveguide optics, circular or elliptically-polarized modes are described in terms of coupled TE-TM modes. There are two types of coupling. The first type is the coupling due to the gyrotropy. This occurs even in the absence of the photonic crystal and couples TE and TM modes to form circularly- or elliptically-polarized modes. The second type is the coupling that occurs at cross-over points for a PhCs. This type of coupling yields gyrotropic band gaps.

The band gaps away from the Brillouin zone edge correspond to the coupling between elliptically polarized modes travelling in the forward and backward directions. The elliptical forward polarized modes decomposed into quasi-TE and quasi-TM mode and couple with quasi-TE or quasi-TM backward modes, respectively. The reflection of the circularly polarized forward modes into TE backward modes is activated first for increasing frequency or decreasing wavelength as one approaches the band gap from the schematic Fig. 2.13. This means that forwards circular to TE backward modes couple first. It is reasonable to assume that this type of coupling will reflect back some or most of TE component out of the circularly polarized forward wave. What remains from the forward circularly polarized wave is mostly TM component depending on how much TE

is reflected back. Hence the polarization is rotated. TM mode cross over has been shifted away due to linear birefringence.

2.3.2.2 Coupled mode theory

In a lossless waveguide system with uniform structure in propagation direction, various waveguide modes coexist along the propagation direction. These normal eigenmodes are determined by the waveguide structure and its boundary conditions. Each of them propagates independently without mutual coupling. The following analysis for the coupling mode theory is taken from ref. [116]

In perturbed or grated waveguide structure, those normal modes are no longer independent, and become mutually coupled. In order to analyze the optical wave propagation in a pertuerbed waveguide system, we can either use Maxwell equation to compute the normal modes of the waveguide or express the perturbed wave behavior by summation of normal modes in the unperturbed waveguide system. The second gives approximate solutions but more straightforward and simple compared to solving Maxwell equation. This method is known as coupled mode theory.

Under a perturbation, the original normal modes are no longer eigenmodes of the system, and instead, two new normal modes ψ_a and ψ_b couple each other and propagate along a waveguide. ψ_a and ψ_b are expressed as:

$$\begin{aligned} \psi_a(x,y,z,t) &= A(z)\exp(-i\kappa_a z) f_a(x,y) e^{i\omega x} \\ \psi_b(x,y,z,t) &= B(z)\exp(-i\kappa_b z) f_b(x,y) e^{i\omega x} \end{aligned} \tag{2.42}$$

where f_a and f_b are field distribution functions normalized by power flow over a cross section. A and B are mutually dependent:

$$\begin{aligned} \pm\frac{dA(z)}{dz} &= -i\kappa_{ab} B(z)\exp[-i(\kappa_b - \kappa_a)z] \\ \pm\frac{dB(z)}{dz} &= -i\kappa_{ba} A(z)\exp[+i(\kappa_b - \kappa_a)z] \end{aligned} \tag{2.43}$$

where κ_{ab} and κ_{ba} are coupling constant between two modes. When $\kappa_{ab} = \kappa_{ba} = 0$, the solutions reduce to $A(z)=A_0$ (constant) and $B(z)=B_0$, and ψ_a and ψ_b are reduced to the two original waves.

The coupling constant is a measure of the spatial overlap of normal modes over dielectric constant increments $\Delta\varepsilon$ and is calculated by the following integral:

$$\kappa_{ab} = C\int f_a^* \Delta\varepsilon f_b dxdy \tag{2.44}$$

where the integration range is across section of waveguide, and C is a constant related to the normalization of ψ_a and ψ_b. The coupling constant is proportional to the overlap integral between the incident, scattered mode fields and the transversal spatial distribution of the grating refractive index perturbation Δn. When the incident mode is fundamental mode, the forward fundamental mode is able to couple into backscattered higher order modes. The field amplitude distributions of high order modes have higher density near the interfaces than lower order modes. If there are the gratings at the top surface, the higher coupling constant resulted from this larger overlap integral causes stronger backscattering from the coupling between the forward fundamental mode to backward high order modes. [126]

The coupling due to gyrotropy is described in terms of coupled mode equations of the form $\begin{aligned} \frac{dA_{TE}}{dz} &= \kappa_{xy} A_{TM} \exp(iz2\Delta_\beta) \\ \frac{dA_{TM}}{dz} &= \kappa_{yx} A_{TE} \exp(-iz2\Delta_\beta) \end{aligned}$, where $2\Delta_\beta = \beta_{TM} - \beta_{TE}$ is the phase mismatch. These forward propagating waves couple to backward propagating modes satisfying the phase matching condition $\vec{\beta}^f_{TE,TM} + q\vec{K} = \vec{\beta}^b_{TE,TM}$, where the backward waves correspond to high-order waveguide modes. Here $\kappa_{yx} = \kappa_{xy}^*$ is a function of the gyrotropy parameter and equals zero if $\varepsilon_{xy} = 0$. Development of this coupled-mode analysis should yield appropriate waveguide branches for right- and left-circularly or elliptically polarized

waveguide modes. For example the corresponding wave-vectors should look like $\beta_{\pm} = \frac{2\pi}{\lambda} n_{\pm}$, where $n_{\pm}^{\ 2} = \bar{\varepsilon} \pm \sqrt{\Delta^2 + \varepsilon_{xy}^{\ 2}}$.

In this work, we take TE polarization is mostly along the x-direction and TM is mostly along the y-direction.

2.3.2.3 Bandgap calculation method

Given the coupling coefficients κ for a relief grating used in our magneto-photonic crystal waveguides can calculate the power-transfer efficiency and the amplitude of the backward propagating TE and TM waves, which gives us a way of calculating the amplitudes of the reflected and transmitted waves in the photonic crystal.

The expression for the TE-TE and TM-TM coupling coefficient between modes *n* and *m* when the grating groove depth *h* is much smaller than the film thickness *T* is

$$\kappa_{TE_n TE_m} = \frac{4\pi}{\lambda} \frac{\sin(qa\pi)}{q\pi} \frac{h}{\sqrt{T_{eff,n} T_{eff,m}}} \sqrt{\frac{(n_f^2 - N_n^2)(n_f^2 - N_m^2)}{N_n N_m}} \tag{2.45}$$

$$\kappa_{TM_n TM_m} = \frac{2\pi}{\lambda} \frac{\sin(qa\pi)}{q\pi} \frac{h}{\sqrt{T_{eff,n} T_{eff,m}}} \sqrt{\frac{(n_f^2 - N_n^2)(n_f^2 - N_m^2) N_n N_m}{q_{cn} q_{cm}}} \frac{n_c^2}{n_f^2} \left(\frac{1}{n_c^4} + \frac{1}{n_f^4}\right) \tag{2.46}$$

where N_n is the effective index for the mode *n*; n_f is the film index; and T_{eff} are the effective thicknesses. *a* gives the fraction of the period external to the groove in the relief grating (i.e. the ridge of the grating).

The effective thickness is defined as in equation (2.35). The parameter q_{cn} is defined as

$$q_{cn} = \left(\frac{n_n}{n_f}\right)^2 + \left(\frac{n_n}{n_c}\right)^2 - 1 \tag{2.47}$$

The power transfer efficiency between forward and backward propagating modes is a function of the coupling coefficients κ between the specific modes in question and the phase mismatch $\Delta = \beta^b - (\beta^f + qK)$. This power transfer efficiency is given by

$$\eta = \frac{\left|A^b(0)\right|^2}{\left|A^f(0)\right|^2} = \left[1 + \frac{1 - \Delta^2/|\kappa|^2}{\sinh^2\left(\sqrt{|\kappa|^2 - \Delta^2}\,L\right)}\right]^{-1} \tag{2.48}$$

where L is the length of the grating.

We thus have a way of calculating the amplitudes of the reflected and transmitted waves in the PhCs. These equations can be used to calculate the transmittance spectrum discussed in Chapter 3.

2.4 Optical properties of bulk materials

A material is often considered as having some constant value of the permittivity and permeability. However, these material properties are frequency dependent. Several materials models have been constructed to describe the frequency response of materials. For high frequency simulations, different material models are used in order to interpret material properties more precisely. In this thesis, the Drude model is used to describe the properties of the metals for photonic metamaterial design.

2.4.1 Lorentz Oscillator model for dielectrics

One of the most well-know material models is the Lorentz model. It is derived by a description of the electron motion in terms of a driven, damped harmonic oscillator. [48]When a traveling EM wave passes through a medium, its behavior will depend on the properties of the medium and the light. For many materials, including most metals, dielectrics and even plasmas, can describe optical interactions in terms of a simple model

of the material consisting of negatively charged electrons tied to relatively massive positively-charged nuclei through a "spring force" (electrical attraction). Motion of an electron bound to a positively charged nucleus is analogous to the motion of a mass on a spring in many aspects. Fig.2.14 illustrates this concept and compares it to the traditional mechanical model of a spring and damper system.

Provided that the charges are allowed to move in the same direction as the electric field, the Lorentz model describes the temporal response of a component of the polarization field of the medium to the same component of the electric field as:

$$\frac{d^2}{dt^2}P_i + \Gamma_L \frac{d}{dt}P_i + \omega_0^2 P_i = \varepsilon_0 \chi_L E_i \tag{2.49}$$

The terms on the left side of equation account for the acceleration of the charges, the damping mechanisms of the system with damping coefficient Γ_L and the restoring forces with the characteristics frequency $f_0 = \omega_0 / 2\pi$, respectively. The right side of equation is the driving term exhibiting a coupling coefficient χ_L. The response in the frequency domain is expressed as

$$P_i(\omega) = \frac{\chi_L}{-\omega^2 + j\Gamma_L \omega + \omega_0^2} \varepsilon_0 E_i(\omega) \tag{2.50}$$

When the material loss is small, the polarization and the electric fields are related to the electronic susceptibility as

$$\chi_{e,Lorentz}(\omega) = \frac{P_i(\omega)}{\varepsilon_0 E_i(\omega)} = \frac{\chi_L}{-\omega^2 + j\Gamma_L \omega + \omega_0^2} \tag{2.51}$$

The permittivity is obtained as

$$\varepsilon_{Lorentz}(\omega) = \varepsilon_0 [1 + \chi_{e,Lorentz}(\omega)] \tag{2.52}$$

This equation is referred to as the Lorentz model for dielectrics and predicts with surprisingly accurate electromagnetic behavior of bulk materials. The Lorentz model predicts high absorption near resonance and tapering to zero away from resonance. In reality, most of materials exhibits multiple resonances of many types and are best described by a linear sum of Lorentz oscillators.

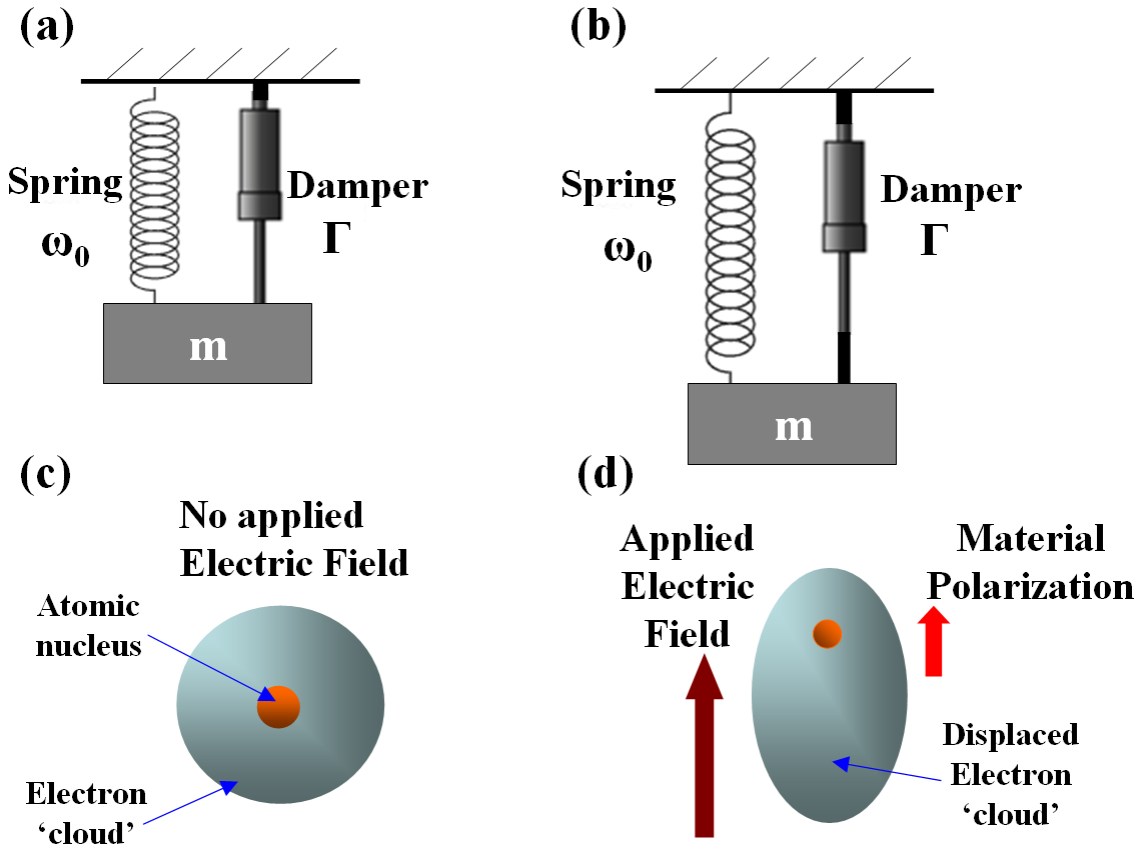

Figure 2.14 Comparisons between traditional mechanical Lorentz oscillator model of a spring and damper system and the motion of electron cloud bound to a positively charged nucleus. (a) and (b) are Lorentz oscillator model under equilibrium and unequilibrium states respectively; (c) and (d) are electron cloud and nucleus system before and after applying electric field; (d) shows electron cloud displacement and exhibit material polarization.

2.4.2 Drude model for metals

The Lorentz model can be extended to metals. As thin metal film shows anomalous optical behavior in the visible spectral region, it is worthwhile to investigate the origin of this behavior for further utilization of metallic nano structures. This is special case for Lorentz model is known as Drude model. The Drude model also provides impressive data fits for the dielectric function measured by Johnson and Christy. The conventional free electron Drude model suitably explains the optical dielectric properties of metals [135]

In metals, the electrons are unbound or 'free', they experience zero restoring force which leads to zero resonance frequency $\omega_0 = 0$ .Then the equation (2.49) and (2.51) can be rewritten as

$$\frac{d^2}{dt^2} P_i + \Gamma_L \frac{d}{dt} P_i = \varepsilon_0 \chi_L E_i \tag{2.53}$$

$$\chi_{e,Lorentz}(\omega) = \frac{\chi_L}{-\omega^2 + j\Gamma_L \omega} \tag{2.54}$$

Here, ω_p is the plasma frequency. It is typically introduced for metals in ultraviolet region. The coupling coefficient is generally represented by the plasma frequency $\chi_D = \omega_p^2$. At frequencies lower than plasma frequency, dielectric constant is mostly imaginary and metals behave like good conductors. Metals are very lossy when they are in the near plasma frequency region due to the large value of real and imaginary parts of the dielectric constant. On the other hand, the imaginary part of the dielectric function is very small above the plasma frequency. This indicates that metals have low absorption. The Drude model can yield a negative real part of the permittivity over a wide spectral range for $\omega < \sqrt{(\omega_p^2 - \Gamma_D^2)}$.

In the similar fashion, the magnetic response models can be obtained. The corresponding magnetization field components M_i and the magnetic susceptibility χ_m equations are

obtained from the polarization and electric susceptibility expressions with the replacements $E_i \rightarrow H_i$, $P_i / \varepsilon_0 \rightarrow M_i$. The permeability is given as:

$$\mu(\omega) = \mu_0[1 + \chi_m(\omega)] \tag{2.55}$$

2.5 Metamaterials

The electromagnetics of metamaterials is a whole branch of modern science. A long period of accumulation of knowledge resulted recently in a large number of publications on metamaterials. The developed concepts of negative refractions, artificial dielectrics, artificial magnetics, and artificial plasma are considered as founders of these directions in applied electromagnetics. [49] Theoretical studies proved that in principle any combinations of ε and μ can be realized if the materials are properly engineered. With the the recent progress in nanofabrication, we are able to fabricate metamaterials for millimeter wave, microwave, infrared and even visible light frequency ranges. In metamaterials, such engineering is considered as metaatoms that substitute natural atoms and molecules. Metaatoms are engineered structures significantly larger than natural atoms but small compared to the wavelength of incoming radiation. Their electric and magnetic properties can be carefully designed and tuned by changing the geometry, size and other characteristics of meta-atoms [136–138].

The history of metamaterials started in 1967 with the visionary speculation on the existence of 'substance with simultaneously negative values of ε and μ' by the Russian physicist Viktor Veselago [50] Left hand materials was used to express the fact that they would allow the propagation of electromagnetic waves with the electric field, the magnetic field and the phase constant vectors building a left handed triad, compared with conventional materials where this triad is know to be right handed. After more than 30 years, the first left handed material was conceived and demonstrated experimentally. An artificial effectively homogeneous structure was proposed by Smith and colleague at university of California, San Diego. This structure was inspired by the pioneering works

of Pendry which introduced the plasmatic-type negative-ε /positive-μ and positive-ε /negative-μ structures shown in Fig. 2.15 [65] which can be designed to have their plasmonic frequency in the microwave range.

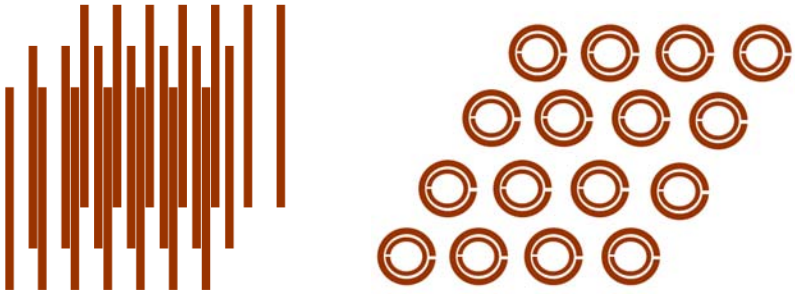

(a) (b)

Figure 2.15 First negative-ε /positive-μ and positive-ε /negative-μ metamaterials which constituted only by standard metals and dielectrics, proposed by Pendry. (a) Thin-wire structure exhibiting negative-ε /positive-μ if E$\parallel$ z; (b) The split-ring resonator (SRR) Structure exhibiting positive-ε /negative-μ if H$\perp$ y [65]

Both of these structures have an average cell size much smaller than the guided wavelength and are effectively homogeneous structure. [49]

2.5.1 Artificial plasma

Artificial plasma, known as a medium with negative permittivity ε has been introduced since 1962 due to works of J. Rotman [139] and J. Brown [140]. The metal thin wire structure as shown in Fig. 2.15 is one artificial plasma presently studied. It is usually a square lattice of thin parallel wires which can be considered at microwaves as perfectly conducting medium. Double and triple wire media were also studied in [139]. Many new interesting features about these lattices have been discovered.

When the wave propagates normally with respect to the wire, the elicitation electric field E is parallel to the axis of the wires (E$\parallel$ z). If the electric field E is perfectly parallel to the axis of the wires, a maximum of effect is obtained. If it is exactly perpendicular to the wires, a situation of cross polarization is obtained which produce no effect. When the

electric field is oblique with respect to the wires, a reduced effect occurs which decreasing with the angle with the wires increases. With the E parallel to the wires, it induces a current along the wires and generates equivalent electric dipole moments; this effective permittivity of the artificial plasma obeys a so-called Drude-model of electric (nonmagnetized) plasma. [49]This metamaterials exhibits a plasmatic-type permittivity frequency function of the form [141]

$$\varepsilon_r(\omega) = 1 - \frac{\omega_{pe}^2}{\omega^2 + j\omega\zeta} = 1 - \frac{\omega_{pe}^2}{\omega^2 + \zeta^2} + j\frac{\zeta\omega_{pe}^2}{\omega(\omega^2 + \zeta^2)} \tag{2.56}$$

Here ω_{pe} is the electric plasma frequency, and ζ is the damping factor due to metal losses. Apparently, when $\omega^2 < \omega_{pe}^2 - \zeta^2$, $\mathrm{Re}(\varepsilon_r) < 0$ is obtained; if $\zeta = 0$ and $\omega < \omega_{pe}$, we get $\varepsilon_r < 0$.

Permeability is simply $\mu = \mu_0$ because no magnetic material is present and no magnetic dipole moment is generated.

2.5.2 Artificial magnetics

Split-ring resonators have been known as a artificial material generating magnetism without magnetic constituents as shown in right picture in Fig. 2.16. This structure can have and positive ε and negative μ. A formular for magnetic polarizability of an individual SRR element indicates the Lorentz frequency behavior of the element. The artificial magnetism is significantly enhanced in the resonant frequency range in lattices of SRRs. Particles with metal loops of various shapes were studied. One single ring in the unit cell produces qualitatively identical effects, but the magnetic activity effective permeability and bandwidth, is enhanced by the presence of a second ring due to larger overall current and slighly different overlapping resonances. So double SRRs shows strong capacitive coupling between loops and more appropriate for the artificial magnetism. The strong coupling of two loops allowed one to obtained the magnetic resonance at lower frequencies which is low enough to consider the lattice of SRRs as a

continuous medium. It is a very practical ways of creating artificial magnetism at microwaves. [49]

If the excitation magnetic field H is perpendicular to the plane of the ring (H $\perp$ y) , it can induce resonating currents in the loop and generate equivalent magnetic dipole moments. Similar to E, if the H is perfectly permendicular to axis of the plane y, a maxium effect is obtained; if the H is parallel to the plane y, we have a situation of a cross polarization, where there is no effect. This metamaterial exhibits a plasmonic-type permeability frequency function of the form [65]

$$\mu_r(\omega) = 1 - \frac{F\omega^2}{\omega^2 - \omega_{0m}^2 + j\omega\zeta} = 1 - \frac{F\omega^2(\omega^2 - \omega_{0m}^2)}{(\omega^2 - \omega_{0m}^2)^2 + (\omega\zeta)^2} + j\frac{F\zeta\omega^2}{(\omega^2 - \omega_{0m}^2)^2 + (\omega\zeta)^2} \tag{2.57}$$

Here, F=$\pi(a/p)^2$, 'a' is the inner radius of the smaller ring and p is the periodicity of the lattice. ω_{0m} is a magnetic resonance frequency. ζ is the damping factor due to metal losses. So SRR structure has a magnetic response despite the fact that it does not include magnetic conducting materials due to the presence of artificial magnetic dipole moments provided by the right resonators. In the lossless situation ($\zeta \neq 0$), when $\omega_{0m} < \omega < \frac{\omega_{0m}}{\sqrt{1-F}} = \omega_{pm}$, it appears that $\mu_r < 0$. Here, ω_{pm} is the magnetic plasma frequency. The resonance of the structure originates from permeability of SRRs. The equivalent circuit of a SRR is shown Fig. 2.16 [49]. For a single ring configuration, the circuit model is the simplest RLC resonator with resonant frequency $\omega_0 = 1/\sqrt{LC}$.

The dimensions of the two rings are very close to each other so that $L_1 \approx L_2 \approx L$ and $C_1 \approx C_2 \approx C$. The double SRR is basically equivalent to the single SRR when mutual coupling is weak. A combined resonance frequency is close to that of a single SRR with the same dimensions but a larger magnetic moment due to higher current density.

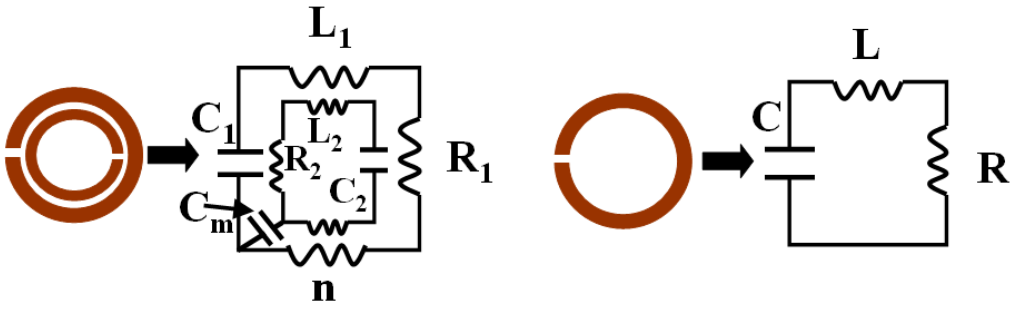

Figure 2.16 Equivalent circuit model of SRRs. Left is a double SRR configuration and right is a single SRR configuration.

Smith et al. combined the thin wire (TW) structure and SRR structures into the composite structure which presented the first experimental LH metamaterials prototype. [138]They designed a TW structure and a SRR structure with overlapping frequency range s of negative permittivity and permeability and combining these two structures into a composite TW-SRR structure. If the launched electromagnetic wave is in the frequency range of interest, the constitutive parameters are simultaneously negative. This structure is widely used in microwave frequency region [49].

2.5.3 Photonic metamaterials

A majority of naturally existing optical materials are non-magnetic. However, it has been recognized for some time that magnetism at optical frequencies may lead to new fundamental physics and novel applications. Metamaterial is one of the most remarkable new classes of materials enabled by bringing magnetism to an optical frequency range. In the last three years several approaches to the realization of optical NIMs structures have been developed by several groups worldwide. One of the first metamaterials with a negative index of refraction at optical frequencies was demonstrated using pairs of metallic nanorods. [142]

A double-periodic array of pairs of parallel gold nanorods is shown to have a negative refractive index in the optical range. Such behavior results from the plasmon resonance in

the pairs of nanorods for both the electric and the magnetic components of light. This resonance can be thought of as a resonance in an optical *LC* circuit, with the metal rods providing the inductance *L* and the dielectric gaps between the rods acting as capacitive elements *C*. [73]

The excitation of the surface waves, known as surface plasmon polaritons on the metal air interface results in the electric resonances of individual nanorods. Such surface plasmon polaritons can be excited in the finite size nanorods not with the plane wave in a semi-infinite medium. The symmetric and anti-symmetric plasmon polariton waves can be supported in a paired nanorod configuration. The electric field parallel to the nanorods induces parallel currents which generate symmetric Plasmon polariton wave in both nanorods, leading to the excitation of a dipole moment. The magnetic field perpendicular to the plane of the nanorods excites antiparallel currents which generates anti-symmetric plasmon polariton wave in the pair of nanorods. Combined with the displacement currents between the nanorods, they induce a resonant magnetic dipole moment. When the wavelength of an incident light is above the resonance, the excited moments are co-directed with the incident field. When wavelengths are below the resonance, the excited moments are counter-directed to the incident fields. The resonant response of the refractive index is originated from the excitation of such plasmon resonances for both the electric and magnetic field component. In particular, the refractive index can become negative at wavelengths below the resonance. [143].

Considering the electromagnetic properties for the nanorods, these metal rods basically conduct current, producing an effect called optical inductance, while a material between the rods produces another effect called optical capacitance. The result is the formation of a very small electromagnetic circuit, but this circuit works in higher frequencies, which include the infrared and visible light. So this structure that works as an optical circuit and interacts effectively with electrical and magnetic field components of light.

A family of coupled nanostrips with varying dimensions is demonstrated exhibiting optical magnetic responses across the whole visible spectrum, from red to blue, which is referred to such a phenomenon as rainbow magnetism. The experimental and analytical studies of such structures provide a universal building block and a general recipe for producing controllable optical magnetism for various practical implementations.[74] The general resonant properties of magnetic metamaterials consisting of arrays of paired thin silver strips. The magnetism in such a structure has been discussed theoretically [76, 77].

The double-wire sandwich structure in which a dielectric layer is sandwiched between two metal films, popularly known as a 'fishnet', has also been demonstrated in optical frequencies. The magnetic response originates from the antiparallel current supported by the wire pairs. When combined with long metal wires shown in Fig. 2.17, this structure is shown to have negative refraction for a particular polarization at optical frequencies. The metamaterial can be viewed as composed of two sets of sub-circuits or "atoms": (i) A coil with inductance L in series with two capacitors with net capacitance C as an LC circuit, providing a magnetic resonance at the LC resonance frequency. (ii) Long metallic wires, acting like a diluted metal below the effective plasma frequency of the arrangement. The negative magnetic permeability from (i) and the negative electric permittivity from (ii) lead to a negative index of refraction. [78]

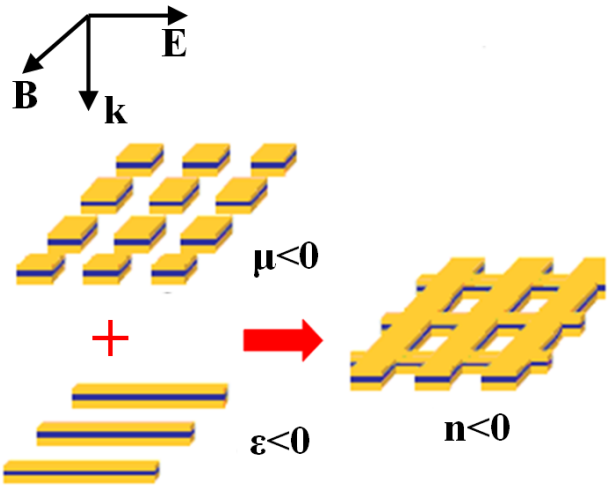

Figure 2.17 Scheme of the metamaterial and polarization configuration.

2.5.4 Gradient index metamaterial

Gradient-index optics is the branch of optics covering optical effects produced by a gradual variation of the refractive index of a material. Mirage of a pool of water appearing on the road on a hot day is a common example of gradient index optics. Because of the weather, hot and less dense air is at surface of the road while the denser cool air is above and the variation in temperature of the air causes a gradient in its refractive index. The light rays are refracted from their normal straight path due to the index gradient. This bending effect is exploited in a gradient-index (GRIN) lens. This is a device with a radially-decreasing refractive index (usually a parabolically shaped index profile). A slab of this material acts like a conventional converging lens, but does not need to be shaped like one, simplifying the mounting of the lens. [144]

For a conventional lens, an incoming light ray is first refracted when an incident light enters the shaped lens surface; the light ray is refracted because of the abrupt change of the refractive index from air to the homogeneous material. It passes the lens material. When it emerges through the exit surface of the lens, it is refracted again because of the abrupt index change from the lens material to air. The reason that the rays can be focused on a spot and to create the image is because a well-defined surface shape of the lens causes. The high precision required for the fabrication of the surfaces of conventional lenses aggravates the miniaturization of the lenses and raises the costs of production. Gradient indexlenses represent an interesting alternative since the lens performance depends on a continuous change of the refractive index within the lens material, instead of complicated shaped surfaces plane optical surfaces. The light rays are continuously bent within the lens until finally they are focused on a spot. The simple geometry allows us a very cost-effective production and simplifies the assembly of your product essentially. Varying the lens length implies an enormous flexibility at hand to fit the lens parameters as, e.g., the focal length and working distance to your special requirements without high research and development efforts and costs. [145]

The most popular production method of the glass-made GRIN lens is ion exchange. Thus the sample obtains a gradient material structure and a corresponding gradient of the refractive index. [49] Metamaterials, known as artificially structured materials give an alternative way to fabricate gradient materials. Recently, most of metamaterials have been constructed from identical element. However, we can also fabricate metamaterials with averaged electromagnetic properties vary as a function of position.

Continuously graded index structures offer a number of advantages over conventional elements with homogeneous and/or step index profile since they offer an additional degree of freedom in the design of the desired characteristics. The gradient index metamaterial use may be anticipated in a wide range of applications, e.g. as an alternative to conventional GRIN lenses and similar passive elements for electromagnetic beam shaping and directing, for high efficiency antireflection structures, etc. [81]

Electromagnetic metamaterials with refractive index continuously varying in space have the graded profiles in a wide frequency range and thus promise increased practical usability in various applications such as lensing and filtering. [76, 77]. Ramakrishna described a spherical perfect lens composed of media with permittivity and permeability graded as ~1/r [146]. Smith et al [80] proposed the use of metamaterial lenses instead of conventional positive index ones for the coupling with radiative elements in high-gain antenna applications because of the reduced geometrical aberration profile in comparison to the conventional ones. Experimental studies of graded index LHM have been reported.

For the situation that index on a planar metamaterial slab varies linearly in a direction perpendicular to incident radiation, a constant gradient metamaterial can be confirmed by observing the deflection of a normal incident beam. To calculate this deflection, two normally incident but offset rays enters a gradient index planar slab of thickness t as shown in Fig. 2.18.

Since the phase fronts are uniform within the material for a thin film, a simplified analysis can be applied strictly to thin samples.

The rays will acquire different phase advances as they propagate through the slab. When the two rays enter at locations x and x+Δx along the slab face and Φ(x) is the phase shift across a slab of arbitrary thickness. The acquired phase difference of the two beams traversing the slab must equal to L which is the phase advance across the path length. This acquired phase difference can be expressed as

$$\Phi(x+\Delta x)-\Phi(x)\sim kt\frac{dn}{dx}\Delta x \tag{2.58}$$

Therefore, we obtain

$$\sin(\theta)\sim t\frac{dn}{dx}=t\frac{dn}{d\omega_r}\frac{d\omega_r}{d\delta}\frac{d\delta}{dx} \tag{2.59}$$

which shows that for a material with a constant spatial gradient in index, the beam is uniformly deflected. Here, δ(x) is the depth of cut as a function of distance along the slab. The phase shift per unit cell is equivalent to the beam deflection that will be produced by a gradient index metamaterial slab one unit cell thick in the propagation direction. [77]

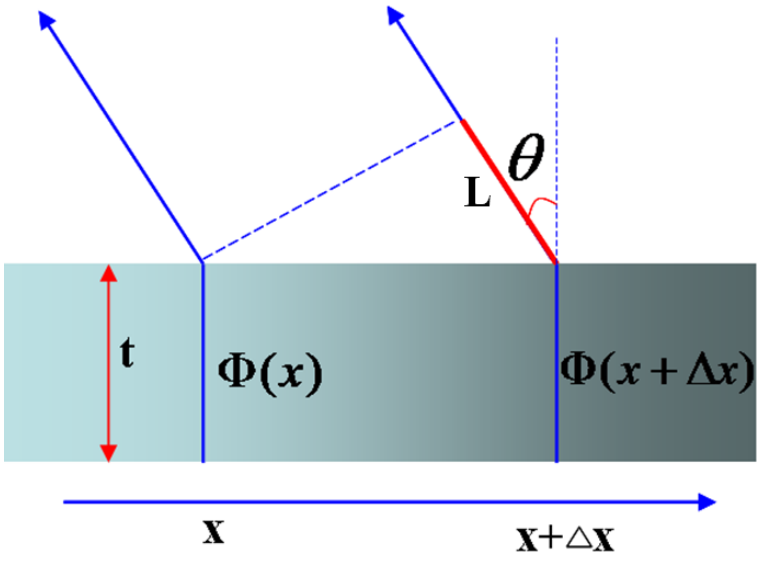

Figure 2.18 Diagram showing the deflection of a wave by a structure whose refractive index possesses a gradient that is constant. [80]

CHAPTER 3

ONE- AND TWO-DIMENSIONAL MAGNETO-PHOTONIC CRYSTALS

Magneto-photonic crystals are spatially periodic dielectric composites with at least one of the constitutive components being a magnetically polarized material. Magnetic polarizations are always associated with nonreciprocal circular birefringence (Faraday rotation). Qualitatively new features are brought to the electrodynamics of photonic crystals due to the Faraday rotation.

Appropriate design and advanced simulation and fabrication technique allow us to demonstrate multifunctional magneto-photonic crystals theoretically and experimentally. In this chapter, one- and two-dimensional magneto-photonic crystals have been investigated. We discuss their patterning on magnetic material bismuth-gadolinium-substituted lutetium iron garnet $Bi_{0.8}$ $Gd_{0.2}$ $Lu_{2.0}$ Fe_5 O_{12} (BiLuIG) thin film. The fabrication process of these two types of photonic crystals is similar.

The following section contains a discussion of the fabrication process of waveguide photonic crystals. Results and analysis of one-dimensional and two-dimensional photonic crystals are discussed respectively after the fabrication section.

3.1. Experiment and setup

3.1.1 Film preparation

Many methods are used to prepare iron garnet films such as liquid phase epitaxy (LPE), pulsed laser deposition (PLD), reactive ion beam sputtering (RIBS), radio-frequency sputtering (RFS), electron cyclotron resonance sputtering (ECRS) and metal organic chemical vapor deposition (MOVCD).[98, 147,148] The bismuth substituted iron garnet

films used in this work are single crystalline films (monocrystals) grown on (100) plane of GGG ($Gd_3Ga_5O_{12}$) substrate by the method of LPE, supplied by H. Dötsch (University fo Osnabruck, Germany) and V. Fratello (Integrated Photonics, Inc, New Jersey).

Liquid phase epitaxy is a commercialized iron-garnet growth method. A single crystal GGG substrate is submerged at certain rotation speed into a supersaturated, metastable melt and a well stoichimetrical monocrystal garnet film is able to be formed on the substrate. [147] The films produced by LPE are single-crystal and of high quality. However, since this growth process occurs under thermodynamic equilibrium, high concentrations for Bi and Ce which can enhance the Faraday rotation significantly and keep the low absorption cannot be incorporated. Meanwhile, the growth rate is relatively high (1μm/min) so that subsequent etching process is needed to adjust the film thickness.

The high-quality films intended for use in this work have the following properties. First, they have high Faraday rotation performance which results from the proper substitution of bismuth. However, doping Bi can also increase the uniaxial anisotropy which makes the magnetization out of plane. The film condition can be properly adjusted by substituting Nd, or Sr and Ga for the position of Y or Fe, respectively in order to result a good planar magnetization for magneto-optical device applications. [116], including intrinsic material absorption, scattering loss, reflection and coupling loss in the final waveguide devices. Last, they have a high refractive index contrast to the substrate. The refractive index of iron garnet film used in my work is n = 2.3095 and its contrast to GGG substrate (n = 1.9375) is generally large enough for photonic crystal applications.

3.1.2 Measurement of film indices and thickness

Prism coupling is an accurate and reliable technique used in this work to measure the refractive indices and thickness of epitaxial films. The background theory was presented by Ulrich and Torge. [149] A Metricon model 2010 prism coupler with ±0.001 for film

index and ±50 $\overset{o}{A}$ for film thickness accuracy was used. The scheme of this method is shown in Fig. 3.1.

Before the fabrication of ridge waveguides, the refractive indices and thickness of the slab waveguides are determined. A Metricon 2010 prism coupler is equipped with He-Ne (632.8 nm) and infrared (1503nm) laser source. The measurement at 632.8 nm give a more accurate thickness, while the modal indices measured at 1503 nm are required for the photonic crystals fabrication. Because the photonic crystals fabricated in my work are functional for infrared electromagnetic wave.

When laser light is incident on a prism and then the sample, reflection occurs at the interface between the prism and the sample. The prism and the sample are mounted to a rotated stage. The incident angle for the laser light changes as the rotation of the stage. The intensity of the light out coming out of the prism is recorded by a photo detector attached to the stage. The light can be coupled into the slab film at a certain angle when the laser light wavevectors are equal to the waveguide wavevectors. Meanwhile, the detector at the other side of the prism senses the sharp intensity drop.

The incident angle corresponds with a waveguide mode can be converted to effective refractive index. The computer can calculate the refractive index and the film thickness directly after one scan by using equations (2.31) and (2.32) for TE and TM mode respectively. .

$$k_x T = (m+1)\pi - \tan^{-1}(\frac{k_x}{\gamma_s}) - \tan^{-1}(\frac{k_x}{\gamma_c})$$

$$k_x T = (m+1)\pi - \tan^{-1}(\frac{n_s}{n_f})^2(\frac{k_x}{\gamma_s}) - \tan^{-1}(\frac{n_s}{n_c})^2(\frac{k_x}{\gamma_c})$$

The refractive indices of TE and TM modes can be obtained by setting the polarization of laser light to TE and TM. In order to obtain both information of index and thickness, the

film must be thick enough to permit propagation of at least two modes in the waveguide. The index contrast of the film to substrate is crucial for fabrication of the photonic crystal structure in the waveguide since the light propagation depends on the selection of path with high index. The photonic crystals fabricated in our lab are using surface relief method which lowers the average effective index in its film section so the light may transmit into the substrate if the effective index becomes lower than the substrate index. Multiple measurements are made to get the average values for effective index for each mode and the film thickness.

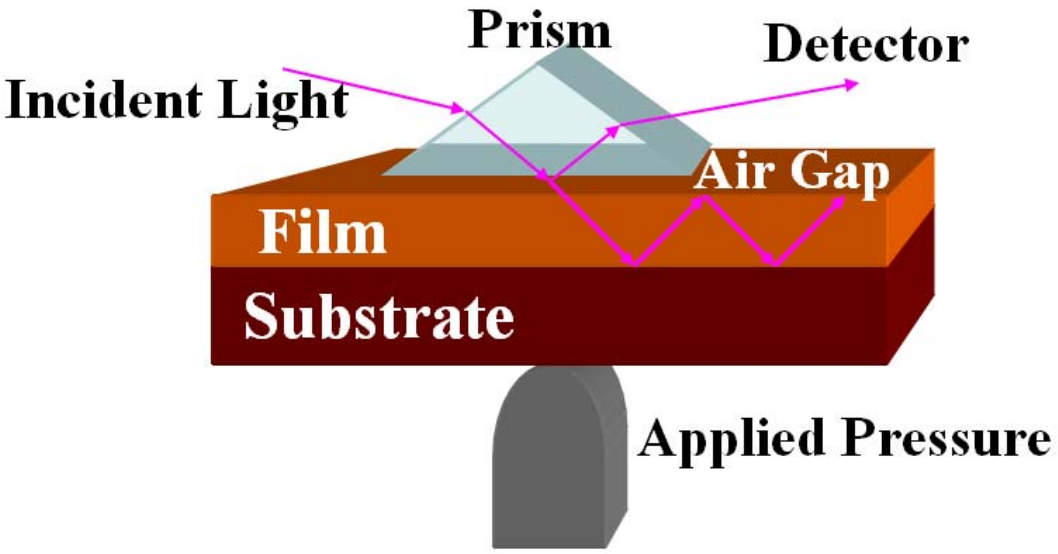

Fig. 3.1 Schematic illustration of the prism coupling method.

3.1.3 Fabrication Process

In this work, one-dimensional periodic gratings and two-dimensional periodic air holes were fabricated on ridge waveguides and slab waveguides respectively on magnetic iron garnet films. Fig. 3.2 shows the top view waveguides fabricated for photonic crystals. For

the two dimensional photonic crystal fabrications, the ridge waveguide is used to guide the light from the laser resources to slab waveguide.

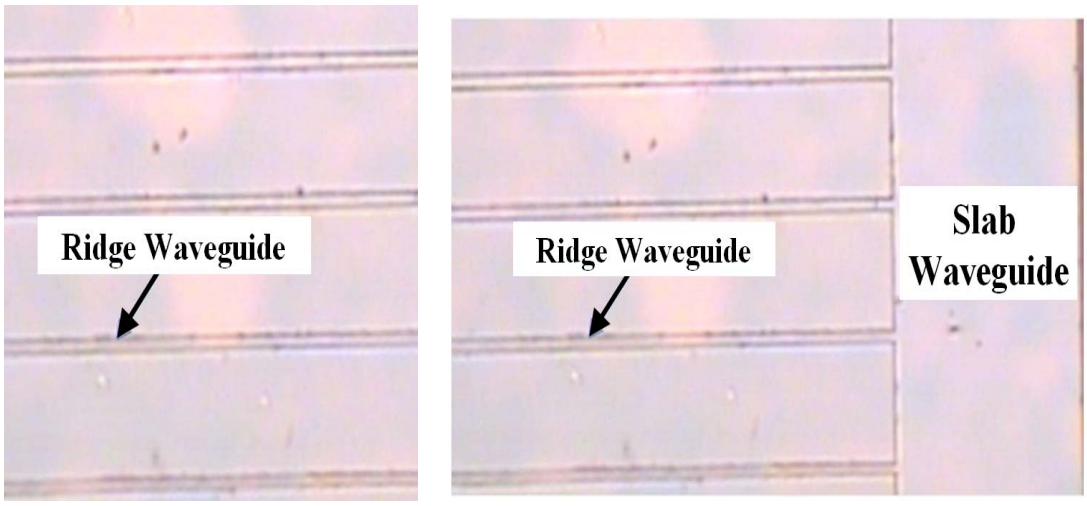

Figure 3.2 This is the top view waveguides before photonic crystal patterning. (a) is ridge waveguides used to fabricate one dimensional grating. (b) is used to fabricate two dimensional air holes. Photonic crystals are patterned on the slab waveguide. Ridge waveguide is used to guide light into slab waveguide.

Fig. 3.3 shows the schematic of the overall structures for our one and two dimensional photonic crystal devices. Waveguides fabricated by photolithography and dry etching. Photonic crystals are patterned using a focused ion beam (FIB) system which has high precision and fast performance.

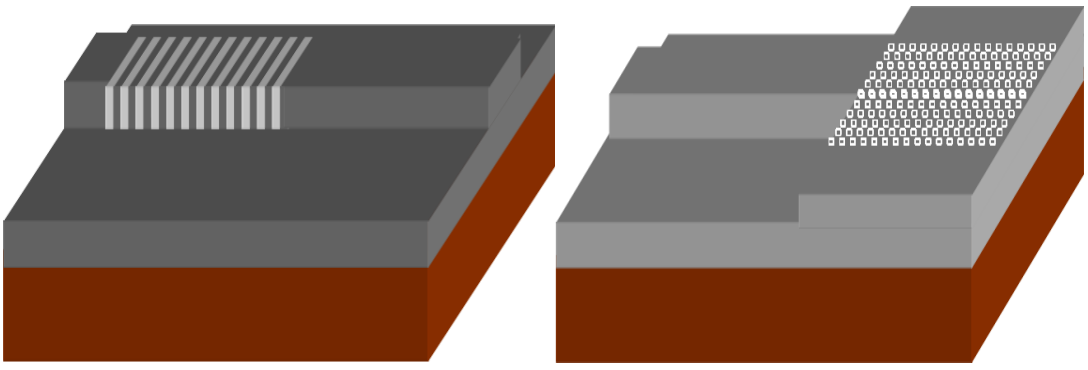

Figure 3.3 Schematics photonic crystals fabricated in this work. (a) One dimensional photonic crystals grating structures fabricated on ridge waveguide; (b) Two dimensional photonic crystal air hole structures fabricated on slab waveguide.

Our major fabrication work is based on this technology now. Mechanical polishing of the facets is used to reduce the loss from waveguide facet and propagation in the slab waveguide.

3.1.3.1 Fabrication of the waveguides

Standard photolithography is used to fabricate the waveguides in our work. Photolithography is the process of transferring geometric shapes on a mask to the surface of a substrate by means of optical illumination in the ultraviolet. The typical steps involved in the photolithographic process are substrate cleaning; photoresist layer formation by spinning; soft baking; mask alignment; exposure; development and hard-baking.

The substrate is soaked in the acetone, methanol, and DI water sequentially in order to remove dust and organic impurities on the surface. Then N_2 is used to blow the H_2O residue.

Positive photoresist S1827 from MicroChem Company is used in this work. It is a type of resist that the region exposed to light dissolve faster in developer. Hexa-methyl-dislizane (HMDS) is spinned on the substrate in order to promote better adhesion of the photoresist to substrate and then photoresist is dispensed on the HMDS with the spinner. The thickness of the photoresist after spinning is normally determined by the spin speed and acceleration. Generally the higher the spin speed the thinner the coating layer. The photoresist-coated substrate is set to hot plate for soft baking at 100 ℃ for 90s in order to dry off the extra solvent.

An EVG 620 aligner is used to expose a 1~2μm thick positive photoresist in 10-15 seconds in order to transfer the structure on the clean chromium mask onto the photoresist layer. Then the substrate is soaked in the developer for some time to remove

the exposed photoresist. All positive photoresist can be removed by alkaline developers such as KOH dissolved in water. MICROPOSIT MF-319 is used in this work. Then the substrate undergoes hard baking for 5-10 minutes at 120 **ºC** to solidify and stabilize the remaining photoresist to better serve as a protecting layer in future plasma etching. S1827 from MicroChem Company is 2.7μm thick at a spin speed of 4000RPM. [127] Fig. 3.4 shows an optical image of photoresist waveguide lines patterned on the BiLuIG slab waveguide sample.

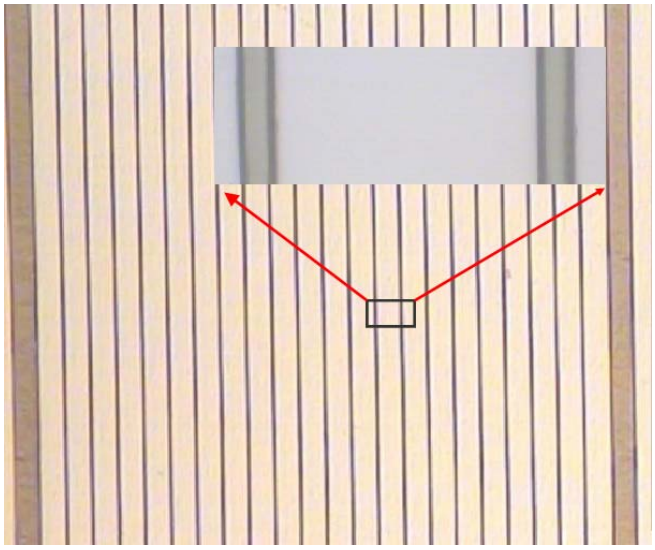

Figure 3.4 Photoresist waveguides patterned using the UV-photolithography process. The inset is the magnified image for the black rectangular region.

Chemically-assisted-ion-beam-etching (CAIBE) is used to remove materials by exposing them to ion bombardment (normally plasma of N, Cl or BCl_3). The waveguide structure is transferred to the substrate by dry etching. A 'RIBETCH 156 ECR LL' dry etching machine is used in this work. Photoresist is utilized as the mask to protect the region from bombardment. There are major three parameters: a) the gaseous ions used for etching, b) the current density of the beam, and c) the accelerating voltage applied to the ions control the etch rates of the samples.

Argon ions are generated from argon gas by the application of microwave power in the presence of a magnetic field using an Electron Resonance (ECR) Source in the CAIBE

plasma chamber. The argon ions are extracted from the plasma by applying the accelerating voltage and are propelled toward the sample. After the application of the accelerating voltage, the plasma density focused on the sample is increased. Dry etching using the ECR source is preferred over the DC and RF sources because of higher ion and free radical densities [150].

The plasma current densities vary with Argon flow rates. When the Argon flow rate is decreased from 20 SCCM to 5 SCCM, the current densities raise significantly from170 $\mu A/cm^2$ to 290$\mu A/cm^2$. [151]A flow rate of 10 to 15 SCCM is used in my work. Due to the high current density at lower flow rates, the temperature of the sample rapidly rises and often charring of the photoresist is observed.

First, the sample is bonded onto a mounting fixture using Apiezon high vacuum grease and is loaded into the loadlock chamber. The grease also serves as a thermal contact for the heat dissipation. After attaining vacuum levels of ~ 10^{-6} Torr, the sample is transferred into the main chamber and is locked onto a Peltiercooled table during the dry etching process, since the BiLuIG film used in our work are stable at several hundreds of degrees but the photoresist cannot sustain at temperature higher than 100^{o}C. This cooling system allows the sample to cool down without overheating the photoresist. The sample is tilted normal to the plasma source and Argon plasma is ignited at a flow rate of 10-15 SCCM, with vacuum stabilizing at pressures of ~ 10^{-4} Torr. The stage is set to rotate during etching to give us uniform etching results. Fig. 3.5 [151] shows the etch rates of various samples used in the research laboratory.

After waveguide fabrication, the sample is cut by diamond saw dicing to suitable size for further FIB milling. The mechanical polish is used to polish both input and output facet to small roughness which is good for optical coupling and reducing losses.

A MultiPrep semi-automatic polishing machine with 30μm, 15 μm, 9 μm, 3 um, 1 μm diamond lapping films is used to polish facets of the samples. The lapping films are used

from larger to smaller particle size in order. Polishing with the subsequent lapping films is done to remove the material in microns at least twice the grit size of the preceding diamond lapping. The samples are examined under an optical microscope to ensure consistency in polishing after polishing with each lapping. After polishing, the surface and facets of the sample are thoroughly cleaned using cotton swabs in acetone, IPA and DI water. The ridge waveguide with polished facet can be seen in Fig. 3.7.

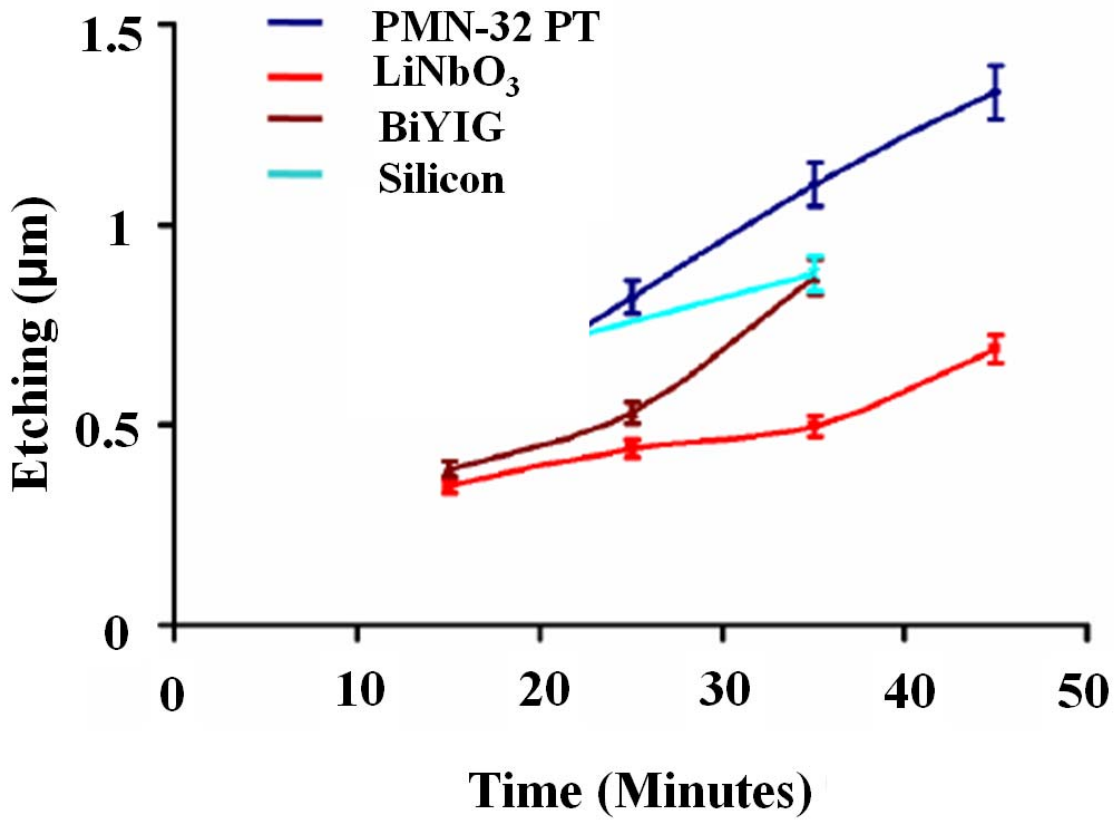

Figure 3.5 Etch rates of various samples using the dry etching machine (CAIBE). This result is taken out by colleague Raghav.

The overall view of standard photolithographic and plasma etching process to make ridge waveguides is shown in Fig. 3.6.

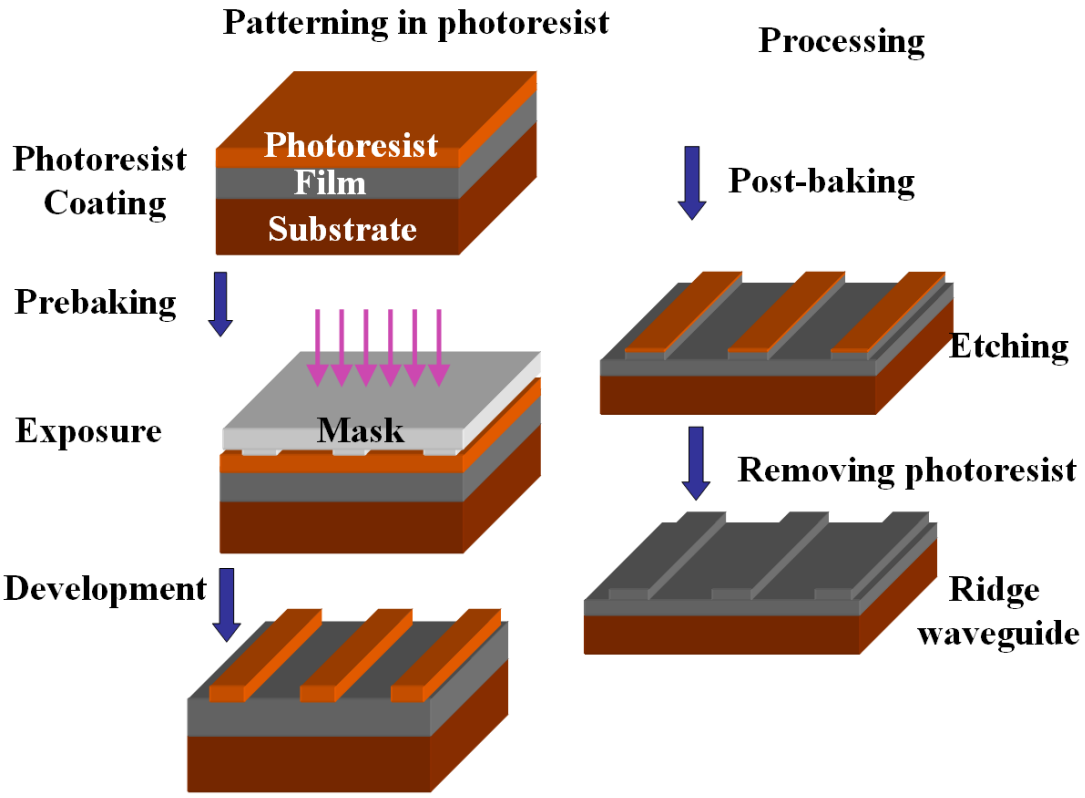

Figure 3.6 Photolithographic processes to make ridge waveguides.

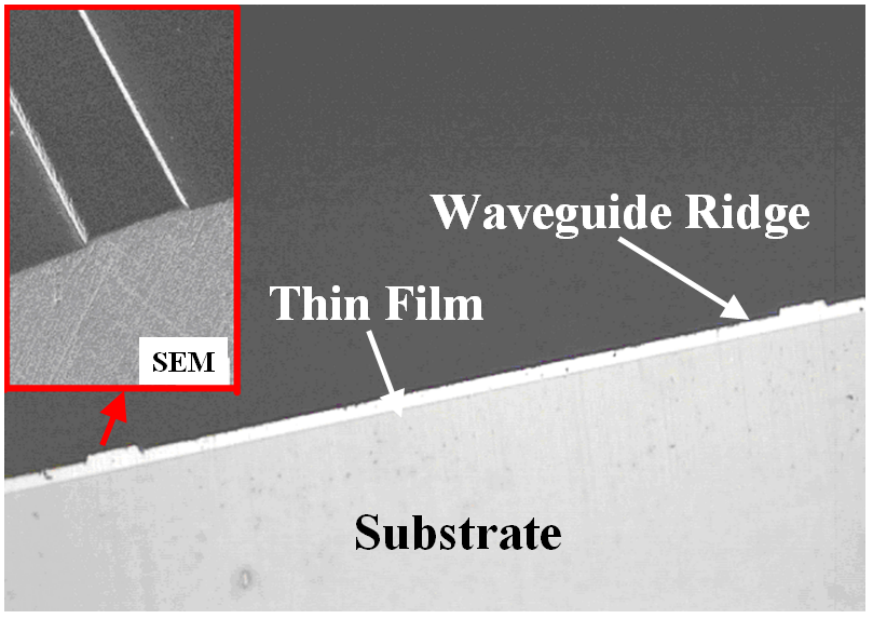

Figure 3.7 Optical microscope picture of the polished facet and the inset is the SEM image for a ridge waveguide.

3.1.3.2 Fabrication of Photonic Crystals

Focused ion beam milling, mainly used in this work for photonic crystals fabrication, performs a mask-free, high precision, friendly interface and efficient milling/deposition processes. A Hitachi FB-2000A system is used for scanning the surface topography and the pattern process. Unlike Scanning Electronic Microscope (SEM) for topography which uses the collected electron signal to display image, gallium ions are the source in FIB. Gallium is commonly used as the energy source due to its low melting point which is 29.8 °C, low volatile nature leading to longer source life and its superior mechanical, electrical and vacuum characteristics. The ion beam is characterized with brightness in the order of 10^6 A/cm^2/Sr, current densities greater than 10 A/cm^2 and a beam diameter of less than 10 nm [152].

A focused beam of Ga ions is accelerated to an energy of 5-50keV by an accelerating voltage 30keV. The gallium beam scans and rasters over the sample to create nanoscale patterns. The aperture controls the gallium beam current and the spot size. The beam diameters and beam current densities are varied through apertures with diameters ranging from 6-500μm. The interaction of the ion beam with the sample results in ejection of atoms from the surface. The production of secondary electrons and ions enables us to observe the image of the surface and fabricate the structures as designed. 500 $\overset{o}{A}$ high resolutions is obtained. Fig. 3.8 [153] shows the detailed FIB configuration.

There are several operation mode settings in the FIB. According to the balance among the process time, milling depth and the pattern dimensions listed in Table 3.1, M1 and M0 are the two beam modes usually used in our patterning process.

M1 is working beam mode for patterning and M0 is observation beam mode for imaging. The typical milling time for the grating and air hole structures used in my research is at least 40 minutes. The beam is required to be stable to guarantee the uniformity of the photonic crystals. Based on the balance between the milling time and desired depth, we

choose M1-100 for milling beam. M0-50 is used for imaging and examination the structure considering the clarity of the image and less demagnification on the sample surface.

Table 3.1
Standard beam current for each aperture and beam diameter

	Beam Mode M1		Beam Mode M2	
Aperture (μm)	**Beam Current (nA)**	**Beam diameter (nm)**	**Beam current (nA)**	**Beam Diameter (nm)**
6	0.001-0.005	35	0-0.002	10
20	0.015-0.004	35	0.004-0.01	20
50	0.1-0.3	40	0.02-0.05	60
100	0.4-0.8	60	0.1-0.3	250
200	2-3.5	120	0.4-0.8	800
300	4-8	250		
500	11-15	1000		

The Hitachi FB 2000A is equipped with onboard CAD software. However, the resolution of the patterns created using this software is not sufficient for the nano size photonic crystal pattern. The Nano Pattern Generation System (NPGS) from J. C. Nabity Company controlling the single-ion beam was connected to our FIB system is utilized as the finer software control for the design and fabrication of the nano size patterns.

The depths of milling structure can be adjusted by different milling parameters: line dose, beam current, line width. The characterization of the relationship of the milling depth and the line dose of ion beam on different films with 100nm CAD-designing groove width is shown in the Fig. 3.9 [20], which was done by the previous group members Rong Li, Xiaoyue Huang and Ziyou Zhou. The method has been developed and used in experiments to calibrate the depths through FIB and SEM by pattern the grooves on the edge of the polished facets. We can measure the groove depth under SEM by observing

the facet views of the samples. The plot is obtain by experiments. Different materials may have specific trend. The depth begins to saturate at high line dose due to the substantial redeposition and backscattering the Ga ions to the side walls of the narrow grooves or holes. However, if multiple beams scan the thin films in the horizontal and vertical direction alternatively, re-deposition effect can be reduced and grooves can be deeper and straighter down. [153]

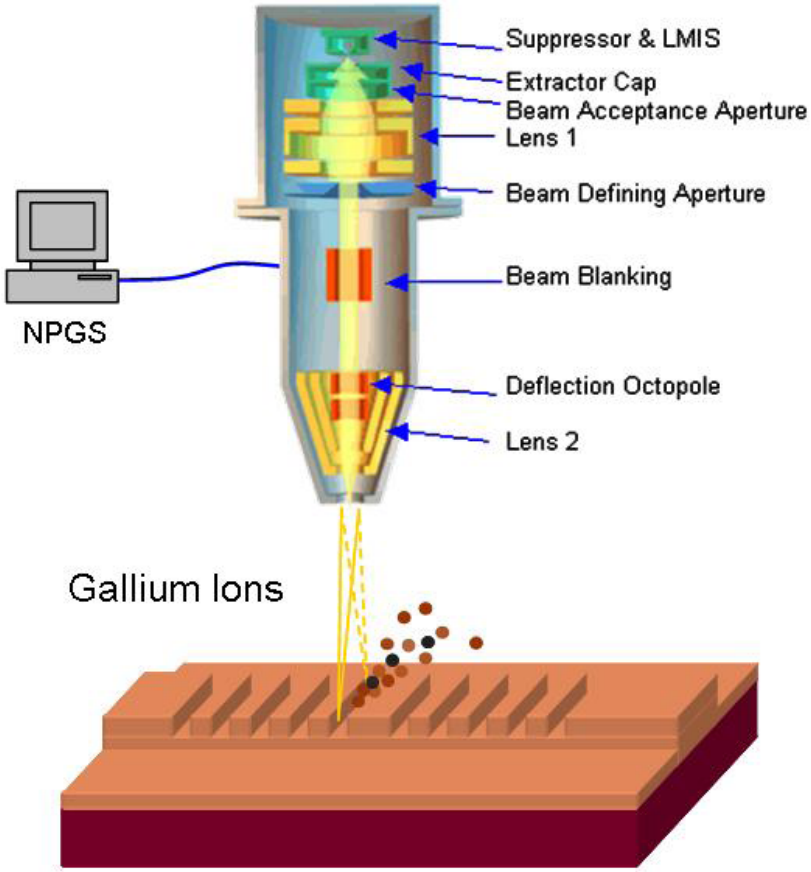

Figure 3.8 Schematic illustration of a single beam FIB model configuration with NPGS system. See Appendix A for documentation of permission to republish this material. Copyright permitted by Xiaoyue Huang

Since surface implantation and redeposition occur due to the ion milling, acid post-treatment is used to remove the residue which can reduce the optical scattering loss. In this work, the fabricated sample is soaked in a solution of orthophosphoric acid maintained at 75°C for 10~15 seconds.

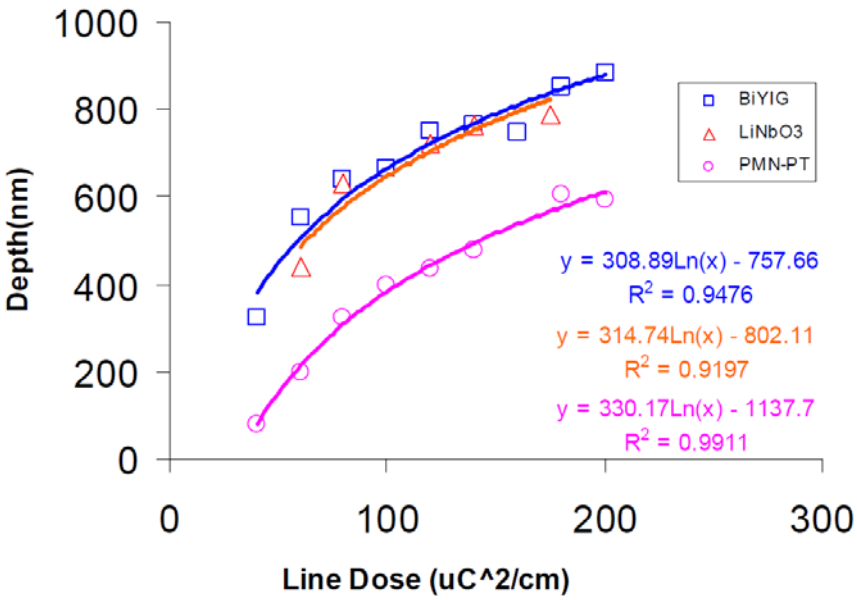

Figure 3.9 The characterization of FIB milling depth and line dose. This result is taken out by colleague Ziyou Zhou.

Fig. 3.10 and Fig. 3.11 show SEM images for one dimensional grating and two dimensional air holes fabricated on a ridge waveguide and a slab waveguide respectively by FIB milling system.

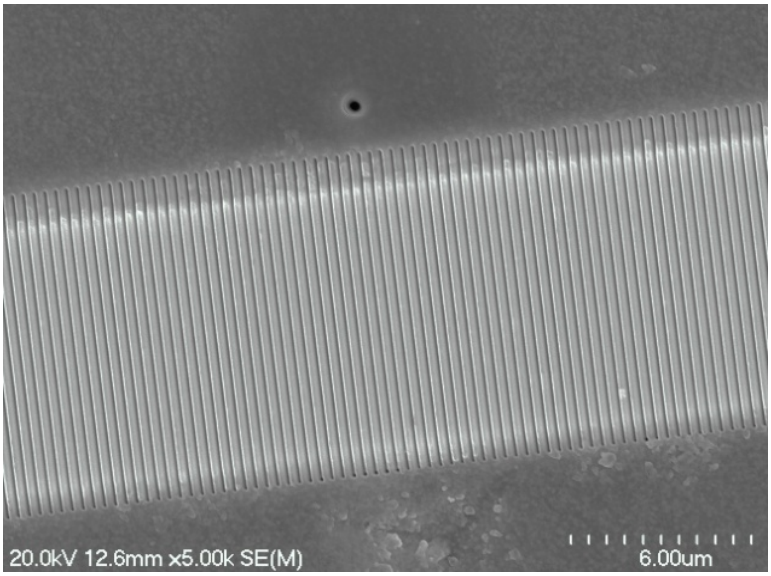

Figure 3.10 The SEM image of one dimensional photonic crystals on a ridge waveguide.

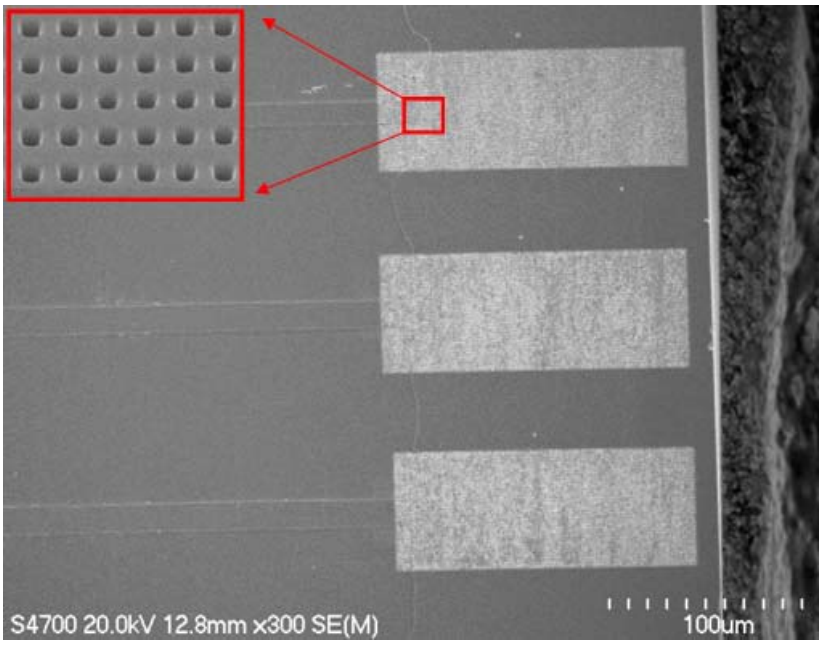

Figure 3.11 The SEM image for the overall topography of two dimensional photonic crystals on a slab waveguide. The inset is the magnified image of the square air holes.

3.1.4 Optical measurement setup

The sample undergoes optical test after fabrication. The optical response of the system including transmittance spectrum, beam spot profile and Faraday rotation of magneto-photonic crystals are measured by end-fire fiber coupling from a 1480nm-1540nm tunable laser source. The setup of the optical test is set on a free space bench-top to prevent possible variation as illustrated as Fig. 3.12 [153].

The input optical beam is generated from a tunable laser source (Ando AQ4321A) with wavelength range from 1480nm-1540nm. The step size is adjustable with 0.001 nm wavelength resolution, 7.9mW (9dBm) maximum, 0.079mW (-11dBm) minimum output power. The light from laser is guided to a polarization controller (Agilent 11896A) through fiber and the polarization of the light is adjusted to transverse electric or transverse magnetic polarization light. Then the polarized light is coupled into sample

through single mode lensed fiber with diameter about 3.3μm. The sample is placed on a stage with x, y, and z controls and light coupling into the waveguide is achieved by carefully adjusting the x, y, z stage controls. The output laser beam from the waveguide is focused by a 10 × microscope objective and goes through an aperture to reduce the background light. A 50 % non-polarizing beam splitter is used to divides the beam into two halves. One beam is used for intensity detection. The record of output intensity is synchronized with the laser wavelength. The other beam is used to monitor the beam profile and check the shape of output light. As the wavelength of input light is tuned, the optical intensity through the waveguide is simultaneously recorded over a fixed duration to obtain the transmission spectrum as a function of the wavelength. When the motor-controlled polarizer (Newport Universal motion controller, Model ESP100) is inserted and rotates 360^{o} with constant speed, the spatial intensity spectrum of the output light polarization can be plotted. The intensity in terms of angle can be calculated. The polarization rotation angle is determined by taking the angular difference between the directions of the semi-minor axes of the polarization spatial spectra for opposite directions of applied magnetic field and dividing by two. The schematic illustration of the optical measurement setup is shown in Fig. 3.13 [153].

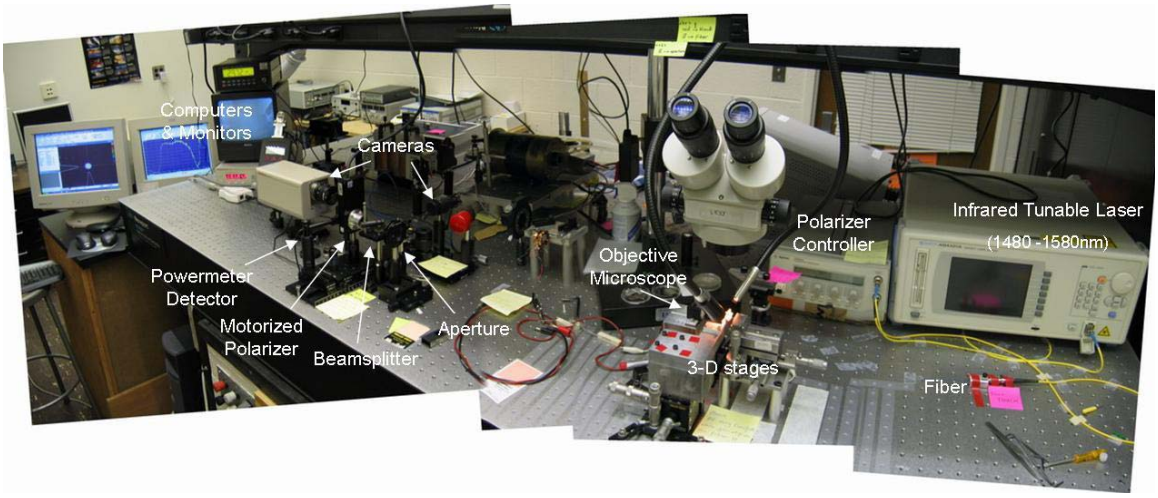

Figure 3.12 Optical setup for the transmission and Faraday rotation measurements. See Appendix A for documentation of permission to republish this material. Copyright permitted by Xiaoyue Huang.

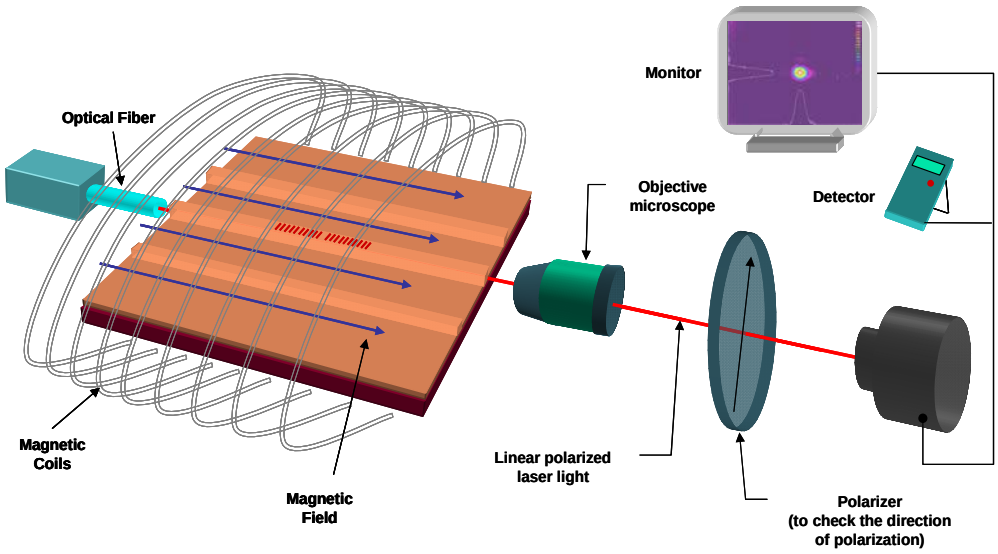

Figure 3.13 Schematic of the optics bench setup for the end-fire measurements. See Appendix A for documentation of permission to republish this material. Copyright permitted by Xiaoyue Huang.

3.2 Waveguides Loss

Losses in optical waveguide are important criteria affecting the performance of the optical waveguide based devices. The major reasons for the losses in the waveguide are intrinsic material absorption, scattering loss, reflection loss and coupling loss. Absorption losses arise due to light absorption phenomena occurring due to interband absorption, carrier absorption, material absorption etc. Scattering losses can also arise due to imperfections in the waveguide structure. These losses can be reduced by improving the fabrication processes such as reducing the surface roughness, reducing the sidewall roughness etc. Mode conversion losses arise due to the conversion of an excited mode to other modes. Radiation losses arise due to out-of-plane scattering and in-plane scattering. [151]

3.2.1 Absorption Loss

Magnetic garnets have very low optical absorption in the infrared window between 1.2 and 5 μm wavelengths. The garnet films grown by LPE show a rather strong additional

absorption due to impurity ions like Pb^{2+}, Pb^{4+} and Pt^{4+} incorporated into the film, which can be explained by the mechanism of Verwey conductivity involved with non-three-valent ions. The electron is excited first to a higher energetic level and then falls back to any one of the different centers with an equal probability. Because of the 'photodetachment', the non-three-valent ions such as Fe^{2+} are the origin of the photon absorption. The absorption properties of doped crystals are determined by The probability of the photons absorbed by an Fe^{2+} center and the population distribution of the centers on different octahedral sites [147, 154, 155] A very low optical absorption film can be obtained by a charge compensation controlling these impurity ions during growth process. [156]

3.2.2 Surface Scattering Loss

Subsurface scattering (SSS) is a mechanism of light transport in which light penetrates the surface of a translucent object, is scattered by interacting with the material, and exits the surface at a different point.[157]Surface scattering takes place on the border surface between two different homogeneous media. Tien has derived an expression for scattering loss due to surface roughness. [158]

In our final waveguide structures, the scattering loss includes the surface roughness and sidewall effect resulted from the fabrication process. The appropriate etching process is used to reduce the scattering loss by removing the residue and smoothing the surfaces.

The details about the etching process to improve waveguides and photonic crystals will be given in the section fabrication process.

3.2.3 Reflection and Coupling Losses

Reflection and coupling losses happen when the light is coupled from the fiber to the waveguide. It is the ratio of the power guided in the waveguide over the total power emitted from the fiber.

Both reflection and refraction of the light occur when light moves between media of different refractive indices. The reflection of light that the equations predict is known as Fresnel reflection. When light moves as near-normal incidence to the interface from a medium of a given refractive index n_1 into a second medium with refractive index n_2, the reflection coefficient are given by:

$$L_f = 10 \cdot \log\left(\frac{n_1 - n_2}{n_1 + n_2}\right)^2 dB \tag{3.1}$$

For the film with refractive index equal to 2.3095 used in our work, the reflection loss is about -8.05dB.

The coupling loss mainly results from the waveguide geometry and the mismatch between fiber and waveguide in our study. This study was done by colleague Rong Li through Rsoft simulation [127]. When the output spot from the fiber is comparable to the waveguide profile, the loss takes place at beginning and the power tends to reach a stable value which is about 0.7 times of the input power. This loss results from the geometry mismatch. So the coupling loss is 10log (0.7) = -1.55dB to the input power. [127]

3.3 One dimensional magnetically-activated gyrotropic photonic crystals

This section concerns band gap tunability in magneto-photonic-crystal multi-mode waveguides. It reports the formation of magnetically-controlled band gaps in one-dimensional magneto-photonic crystal waveguides fabricated on bismuth-gadolinium-

substituted lutetium iron garnet films ($Bi_{0.8}Gd_{0.2}Lu_{2.0}Fe_5O_{12}$). Specifically, it addresses the magneto-optic response of one-dimensional photonic crystals. Magnetic activation of new band gaps and polarization selectivity are demonstrated. These band gaps form as a result of the coupling between forward-propagating fundamental waveguide modes with backscattered modes of different orders. Hybridization of counter-propagating modes of different gyrotropy-induced polarization states is established by the magneto-photonic crystal. A rich field of phenomena opens up by the simultaneous introduction of periodicity, gyrotropy and modal birefringence in multi-mode waveguides. In the absence of gyrotropy transverse-electric and transverse-magnetic modes do not couple. But the introduction of gyrotropy in birefringent waveguides enables the hybridization of differently polarized counter-propagating waves, carrying different polarization ellipticities and consisting of a superposition of out-of-phase TE and TM modes. Stop-band widening and the selective transmission of various partial-wave components in the gap is predicted and observed.

3.3.1 Introduction

The present work examines the coupling between Bloch modes with spatially-dependent elliptical polarization and their magnetization dependence. These modes are formed by the activation of TE-TM mode coupling in birefringent gyrotropic systems upon longitudinal magnetization. [127-131] Partial back-reflection of these modes is observed experimentally and reported on. Band structure analysis in waveguide geometry is advanced to analyze the response of fabricated crystals. The coupling of different elliptically-polarized waves leading to gyrotropic band gap formation is observed and discussed.

This section is devoted to a theoretical and experimental investigation of band gaps in one-dimensional magneto-photonic crystals with elliptical birefringence in waveguide geometries. The existence of high-order waveguide modes in addition to the fundamental mode results in a rich complex of dispersion curves and qualitative changes in band gap

formation. The character and polarization response of these band gaps is analyzed, as well as their dependence on magnetization direction. This analysis goes beyond the stack model predictions discussed in prior work, experimentally studying the optical response of these systems and incorporating waveguide mode band structure and magnetization dependence calculations. [128-130] We show that the multi-mode regime, a regime not encountered in layered stacks, plays an important role in the system under consideration, partially breaking the gyrotropic degeneracy reported by Merzlikin and co-workers [127] and leading to wave-vector and frequency splitting for each fundamental to high-order mode scattering process. This particular type of splitting permits magnetically-controlled transmittance and the possibility of magneto-photonic-crystal-based magnetic switches and filters.

3.3.2 Experimental Background

3.3.2.1 Sample preparation

In this section, epitaxial bismuth and gadolinium substituted lutetium iron garnet BiLuIG planar thin films grown on (100) oriented gadolinium gallium garnet $Gd_3Ga_5O_{12}$ substrates by liquid phase epitaxy is used in our experiments. These films are grown commercially. The lattice parameter is matched to within $\pm 0.001\ \mathring{A}$. The films are grown from a small melt and so may have a fair number of defects. In terms of composition and properties the thin planar films used are all approximately equal. The saturation induction 4π Ms is 1800G. The Gd reduces it some and the Bi increases it some by increasing the Curie temperature so they balance. The actual in-plane anisotropy is difficult to measure with the saturation magnetization so high. But the extrapolated perpendicular saturating field is similar the saturation magnetization. The films are grown from a small melt and so may have a fair number of defects. Additional cleaning is necessary before film characterization and further fabrication.

Magneto-photonic crystals are fabricated in multi-mode waveguides. The slab waveguide film is 2.75 ± 0.05 μm thick with a composition $Bi_{0.8}$ $Gd_{0.2}$ $Lu_{2.0}$ Fe_5 O_{12} and a measured specific Faraday rotation of 83°/mm at 1510 nm. The specific Faraday rotation in the film was determined by measuring the polarization rotation across the film thickness. The Faraday measurement is done by a standard rotating polarizer method, [128] correcting for the diamagnetic contribution to the rotation imparted by the substrate. It is the referential Faraday rotation per unit length as measured perpendicular to the film to avoid linear birefringence induced distortions in the measurements. The rotation spectra measured from waveguide structures include the combination effect from Faraday rotation and birefringence. This film is grown by LPE on a (100) GGG substrate, with planar magnetic anisotropy and in-plane coercivity of a few Oe. [47, 158] The measured refractive index of GGG substrate in my samples is 1.9357, which is used for further confirmation and calculation of effective indices of waveguide modes on BiLuIG thin film. The dielectric tensor in the film at 1510 nm wavelength, excluding absorption, is given by

$$\tilde{\varepsilon} = \begin{pmatrix} 5.3384 & 0.00165i & 0 \\ -0.00165i & 5.3338 & 0 \\ 0 & 0 & 5.3361 \end{pmatrix}$$

There is a small stress-induced birefringence caused by lattice mismatch between the film and the underlying GGG substrate. The stress birefringence is extracted from the prism-coupler data of refractive indices in the un-patterned slab waveguide.

The dielectric tensor $\vec{\varepsilon}$ for the material now contains non-zero ε_{xy} and ε_{yx} off-diagonal components given by $\pm i\lambda\theta_F\bar{n}/\pi$. Here $\bar{n}$ is the average refractive index $\frac{1}{2}(n_{TE}+n_{TM})$, θ_F is the specific Faraday rotation and λ is the wavelength in vacuum. At wavelength λ =1510 nm, the off-diagnal components of the dielectric tensor can be obtained by substituting θ_F =83°/mm and $\bar{n}$ =2.3095. Absorption effects introduce a neglectable imaginary contribution to the diagonal components.

The dispersion of the waveguide modes is characterized by prism coupling and by analyzing the wavelength dependence of the stop bands induced by the photonic crystal. Four TE and TM modes are allowed in the slab waveguide for transverse magnetization (in-plane perpendicular to the waveguide ridge axis).

Waveguide ridges are patterned on the film by standard photolithography procedure and plasma etching. An EVG620 aligner is used to expose a 1~2 um thick positive photorestist S1827 in 10 to 15 second. Chemical assisted ion beam etching is used to create waveguide structure on the film with a ridge height varies depending on Ar-ion beam etching parameters setup. Table 3.2 shows the major CAIBE etching process parameters used to fabricate ridge waveguide on the thin film. For BiLuIG materials, under the same etching parameter setups, the ridge height varies from 0.5um to 1.2um depending mainly on the etching time. Fig. 3.14 shows the etch rate of the CAIBE on the BiLuIG sample. The height of the ridge waveguides used to fabricate photonic crystals is 600 nm which takes about 35 minutes in plasma etching process.

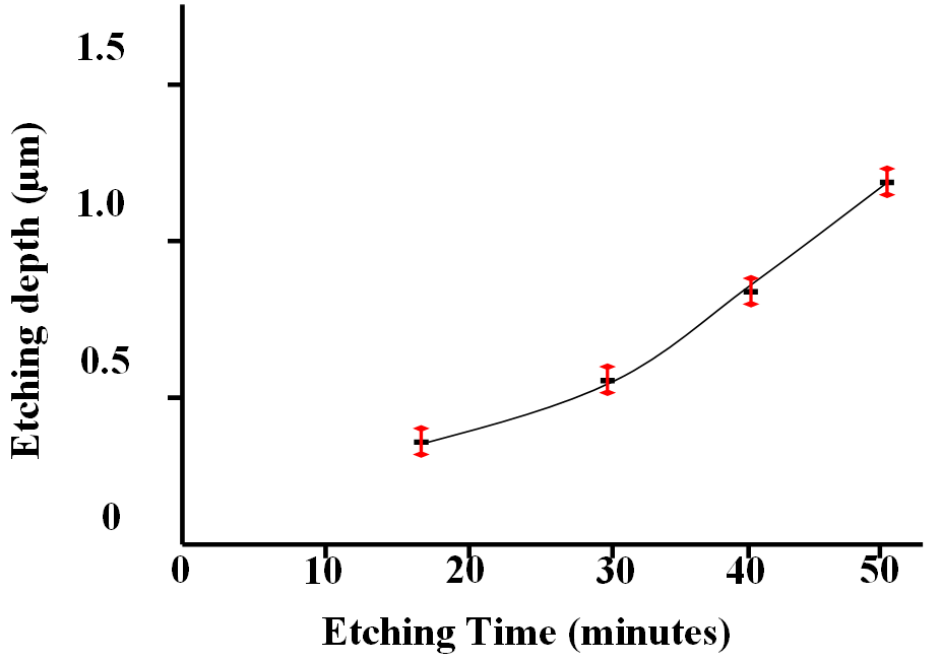

Figure 3.14 The etch rate of the BiLuIG in the dry etching machine.

BiLuIG samples are non-conductive so samples need to be coated with conductive layers to prevent any charging effect. A proper charge dissipation is accomplished by sputter coating the samples with 100nm Cr and 100nm Au using a Hummer sputtering machine. The coating of Cr and Au is the necessary conductive layer during the ion milling. The coated waveguide samples are ready for FIB processing. A one-dimensional photonic crystal is formed by FIB milling followed by a 75°C 10sec bath in orthophosphoric acid to remove sidewall damage.

Table 3.2
The CAIBE etching process parameters

Process parameters	Set Value
Accelerating voltage(V)	80
Beam Voltage (V)	70
Microwave (W)	410
Magenet (G)	1200
Argon (SCCM)	15
Current Density (μA/cm2)	180-200
Chamber Pressure (Torr)	10^{-4}
Base chamber pressure (Torr)	2×10^{-7}

For the one-dimensional photonic crystals, all the tested samples are fabricated under similar conditions. The parameter setups are the same for FIB. The M1-100 milling beam is chosen for sample milling. The line dose affects the depth of grooves. And directly influences the strength of photonic crystals. It is very important to be able to precisely control this milling depth parameter. The characterization of the relationship of the milling depth and the line dose of ion beam on BiLuIG film with 100nm CAD-designing groove width is shown in the Fig. 3.15.

The depth increases by increasing the line dose. When ion milling happens deeper into the grooves, substantial backscattering ions redeposit on the groove side walls. The groove depth can not be deeper. 120 μC/cm line dose is used to fabricate one dimensional photonic crystals. The grating grooves on the samples used for further characterization are 720 ± 25 nm-deep.

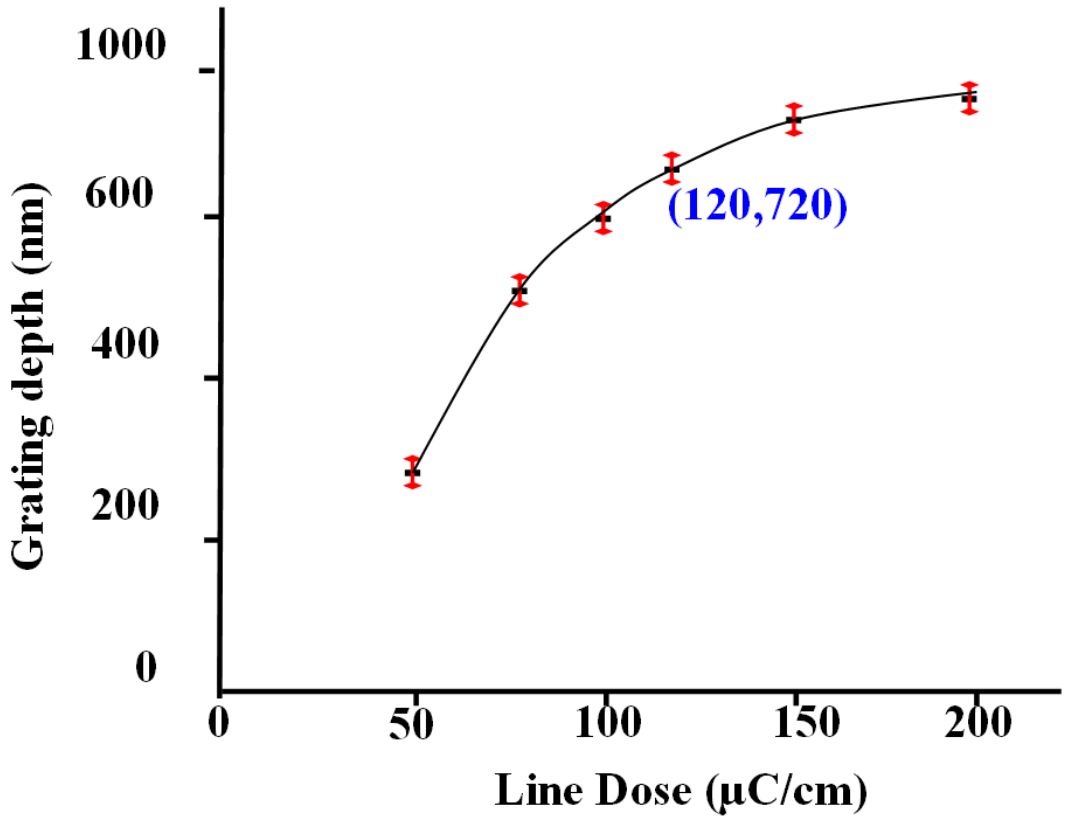

Figure 3.15 The dependence of groove depth with line dose based on BiLuIG thin film. The point (120, 720) shows the line dose used to fabricate 720 nm deep grooves.

The scanning electron micrographs of the top view and the cross section of the one dimensional grating structure on ridge waveguide are shown in Fig. 3.16 and Fig. 3.17 respectively.

The cross sectional images of the grooves show narrowing down structure with depth increament. The grating period is 343.4 ± 0.3 nm corresponding to fundamental and higher order mode stopbands in the wavelength range from 1480 to 1540 nm.

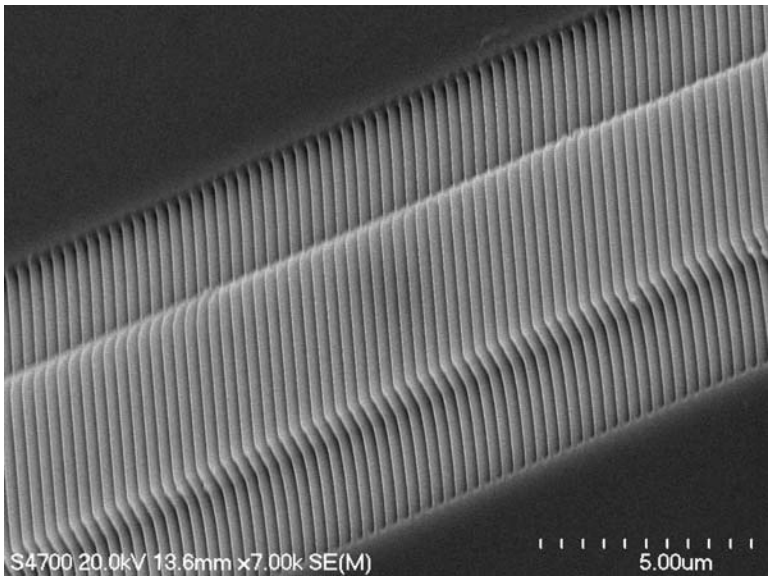

Figure 3.16 The SEM image of topview for the one dimensional photonic crystal on a 5 μm wide BiLuIG ridge waveguide.

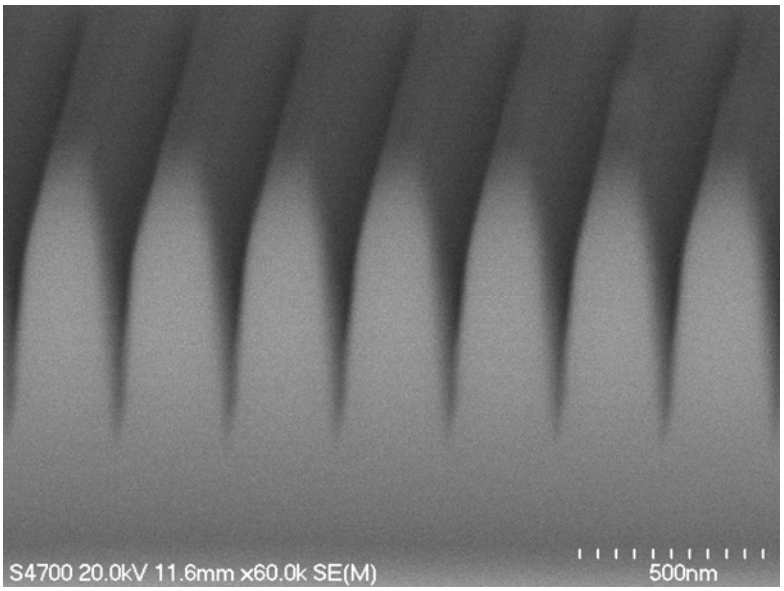

Figure 3.17 The SEM image of cross section for grating grooves patterned on the BiLuIG ridge waveguide.

The thickness of the film at the tip of the grating ridges is reduced by about 100nm due to overlap milling shown in Fig. 3.18.

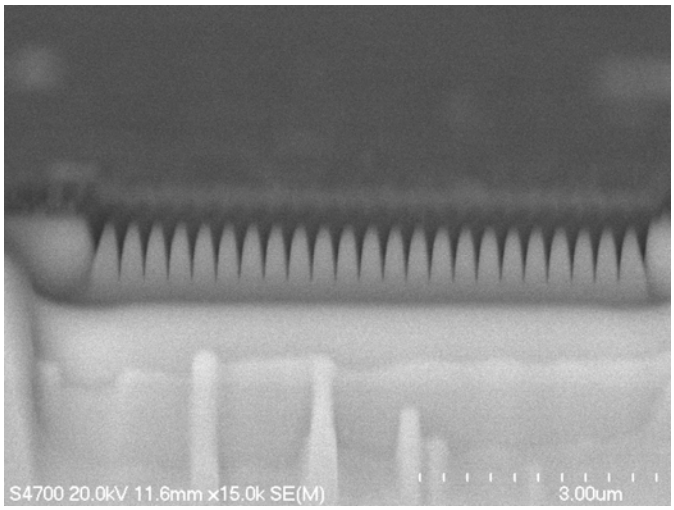

Figure 3.18 Scaniing-electron-micrograph (SEM) image showing overlapping milling. This overlapping milling reduces the thickness in the grating region.

So the effective mode indices on the grating region are different from the effective indices on the ridge waveguide without grating. Both these mode indices can be calculated by the Beam propagation component in Rsoft. Ridge waveguides are 1.2 mm-long with the photonic crystal structure (200 μm in length) positioned 100 μm away from one of the facets. The latter are prepared by polishing both input and output ends of the waveguide. A schematic depiction of the structures the ridge waveguide with photonic crystal near one facet is shown in Fig. 3.19.

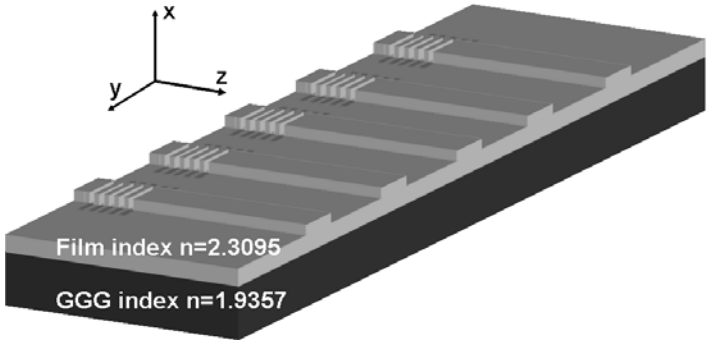

Figure 3.19 A schematic description for one-dimensional magneto-photonic crystal structures on BiLuIG ridge waveguides.

3.3.2.2 Transverse and longitudinal magnetization

Waveguide modes in the structure are characterized by analyzing the wavelength dependence of the stop bands induced by the photonic crystal. In a nonmagnetized state, the slab waveguide supports four TE and TM modes. Patterning of the ridge waveguide and photonic crystal slightly modifies the character and effective indices of the waveguide modes. The resulting modes are quasi-TE and quasi-TM with dominant in-plane (quasi-TE) or out-of-plane (quasi-TM) polarization for transverse magnetization. Confinement of the light beam in the asymmetric optical channel generates a geometry-induced birefringence, not arising from natural anisotropy of the material.

An interesting point about the magnetic response is that waveguide birefringence causes quasi-TE and quasi-TM modes to resonate at different wavelengths, thus engendering different stop bands. This is clearly seen for the case of transverse magnetic field, i.e., magnetic field applied perpendicular to the direction of propagation. In that case there is no magneto-optic coupling between TE and TM modes and the stopbands corresponding to light polarized in the vertical and horizontal directions (relative to the plane of the film) occur at different wavelengths.

Let us consider mode dispersion in transverse magnetization, along the y-direction in Fig. 3.19. The patterning of a ridge structure on the slab slightly modifies the effective index and character of the allowed waveguide modes, resulting in modes with dominant in-plane (quasi-TE) or out-of-plane (quasi-TM) polarizations. When the magnetization points in the transverse planar direction, perpendicular to the ridge axis, vertically- (quasi-TM) or horizontally- (quasi-TE) polarized light remain in their original polarization state. The input polarization does not rotate as there is no coupling between TE and TM modes. At the same time TE-TE coupling (or respectively TM-TM coupling) between modes of different orders is brought about by the grating at those wavelengths satisfying the Bragg condition.

Upon a change of magnetization direction to collinear with the waveguide axis the stopbands reconfigure as a result of the coupling between quasi-TE and quasi-TM modes.

Activation of the gyrotropy (Faraday Effect) upon longitudinal magnetization along the ridge waveguide axis (z-direction in Fig. 3.19) couples the quasi-TE and quasi-TM modes. This coupling yields elliptically polarized Bloch modes with spatially-dependent elliptical polarization in the photonic crystal region. Thus a magnetic field along the waveguide axis induces the opening up of a TM bandgap for light originally launched as TE, and vice-versa. The magneto-optic response of the system engenders the formation of a new bandgap where none existed before for transverse magnetic fields.Thus light coupled into the far-end facet to the grating (from right to left in Fig. 3.19) undergoes significant polarization rotation upon longitudinal magnetization before reaching the photonic crystal structure. The 0.9 mm-long region before light enters the photonic crystal is referred to here as a feeder section. Based on the polarization rotation equations discussed in Chapter 2.3, we can obtain the polarization rotation as a function of birefringence before entering the photonic crystal region, shown in Fig. 3.20. The propagation light rotates about 76^{o} in the feeder section before entering photonic crystal with the linear birefringence 0.0005.

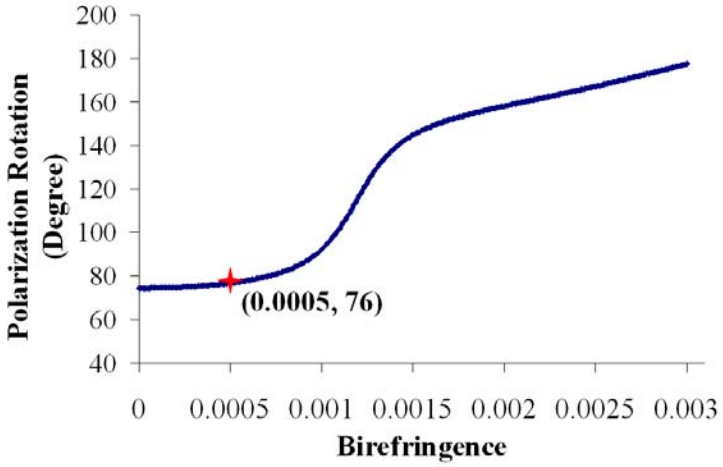

Figure 3.20 Polarization rotation before light enters the photonic crystal from the far-end feeder section as a function of birefringence. The point marked in the plot is the rotation for the approximated birefringence 0.0005 in our structure.

3.3.2.3 Transmittance measurements

Vertical and horizontal linearly-polarized light is inserted through the input facet by end-fire coupling from a lensed fiber. The light has a beam waist diameter of 2 μm at the focal point, and the working distance between fiber tip and waveguide facet is adjusted for maximum insertion power. Fig. 3.21 shows the light output from a typical 5μm wide ridge waveguide. We can only observe fundamental mode from the experiments.

There are four modes that can propagate in the ridge waveguide geometry in this work. Rsoft is used to simulate these mode profiles in the waveguide. The mode profiles fro the fundamental, first, second and third order modes are illustrated in Fig. 3.22.

When the light is launched into the waveguide, the total power distributes itself into different modes. In our experiments, the output light we detect with an infrared camera has the mode-shape of the fundamental mode. Power distribution into different modes is calculated by beam-propagation (BeamPROP) simulation by Rsoft, which has been a commercial available photonic and network design software since 1994. BeamPROP is the industry-leading design tool based on the Beam Propagation Method (BPM) for the design and simulation of integrated and fiber-optic waveguide devices and circuits.

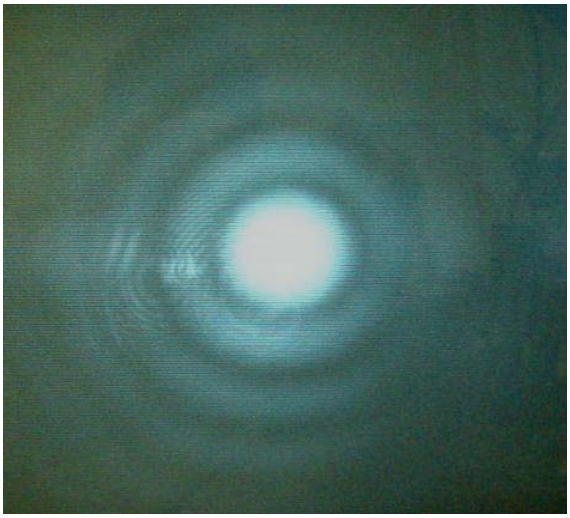

Figure 3.21 Image of the light output from ridge waveguide.

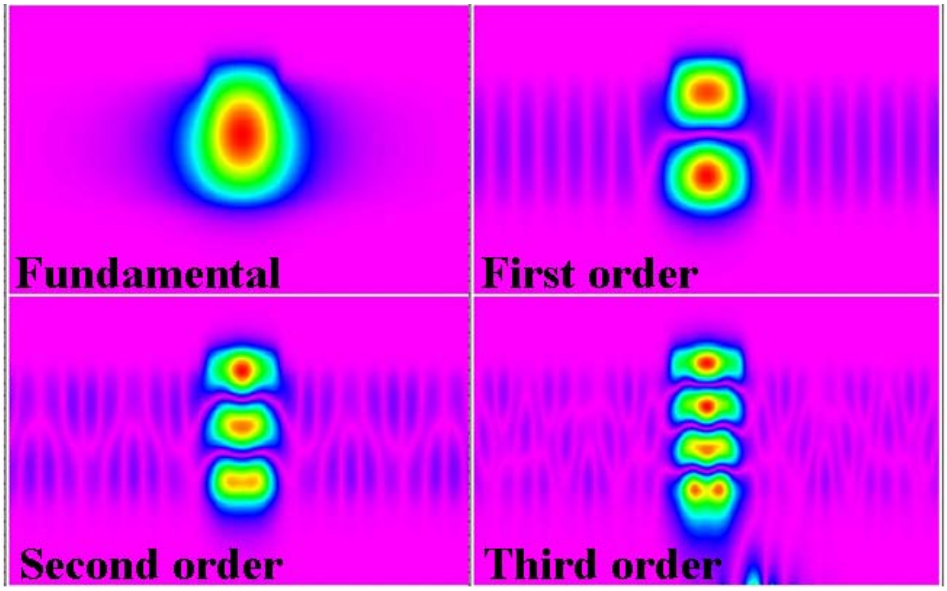

Figure 3.22 The simulated mode profiles for fundamental, first, second and third order modes in a ridge waveguide.

As the experiment measurement setup, the input light is coupled into the center of ridge waveguide. Fig. 3.23 shows the beam distribution profile.

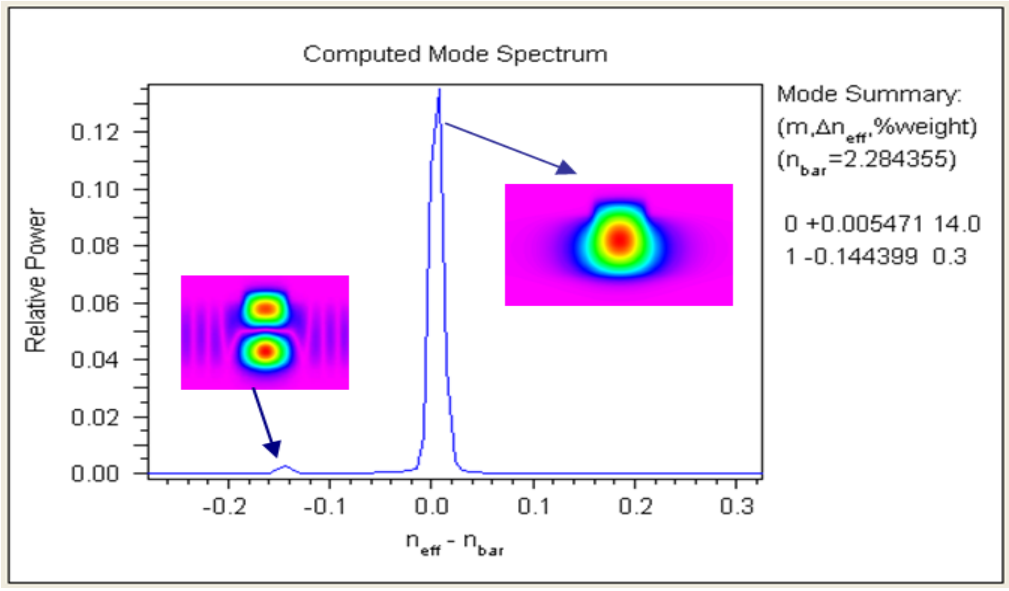

Figure 3.23 The beam distribution profile. The relative power of fundamental mode is 14 while the first order mode is 0.3. Forward propagation light mainly stays as fundamental mode.

When linearly polarized light is launched into the ridge waveguide centered on the input facet, the relative power into the fundamental waveguide mode is 97.9% as the first order mode is 2.1% calculated by the BeamPROP. No higher order modes appear in the computed mode spectrum. Thus, more than 95% of the power that propagates in the guide in the forward direction resides in the fundamental mode.

Transmittance spectra are recorded by scanning the wavelength with a tunable Ando laser source between 1480 nm and 1540 nm for both input polarizations. Data are acquired for optical insertion from both input facets, at the near- and far-ends from the photonic crystal. An average insertion loss of 4.4 dB is measured between the optical fiber output and the photonic crystal waveguide output away from the stop bands. The power coming out from fiber directly is about 180um and the power after the light propagating through photonic crystal waveguide is about 65um. By using the insertion loss equation

$$\text{Insertion Loss (dB)} = 10\log_{10}\left(\frac{P_{in}}{P_{out}}\right) \tag{3.2}$$

Here P_{in} and P_{out} are the power from the fiber directly and the power after light passing through photonic crystal waveguide.

Transmittance from the near-end facet corresponds to insertion polarization into the grating close to the input quasi-TE or quasi-TM for longitudinal magnetization. Based on the calculations on the polarization rotation as a function of birefringence, the Fig.3.24 shows the polarization when the light travels in the feeder section for 100 μm. Since the Faraday Effect (modulated by waveguide birefringence) has only rotated the electric component of the field by 8.28° at the point of insertion into the photonic crystal.

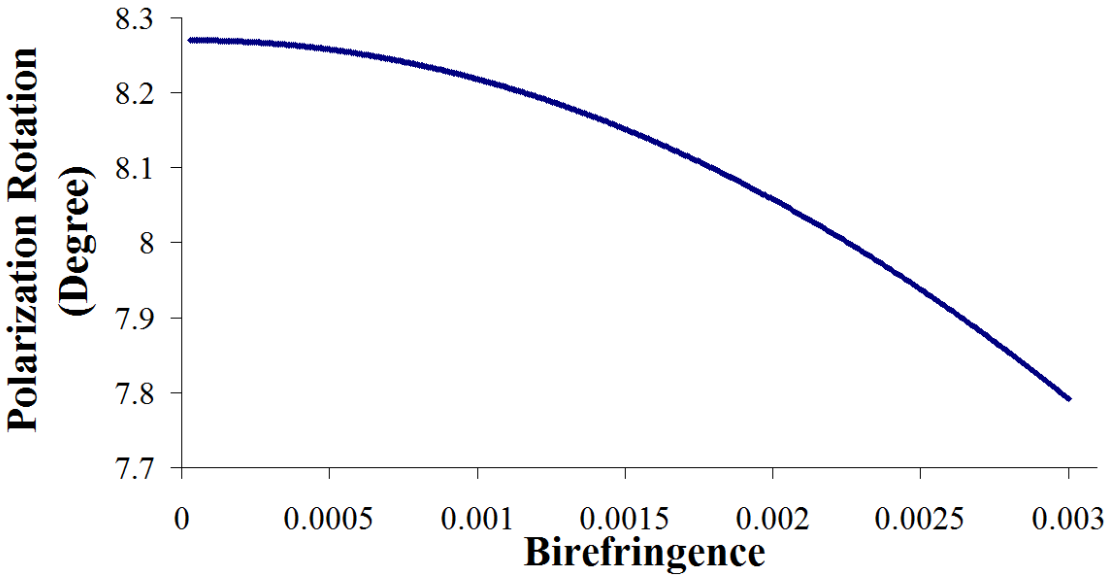

Figure 3.24 The polarization rotation before light enters the photonic crystal from the near- end feeder section as a function of birefringence. The point marked in the plot is the rotation for the approximated birefringence 0.0005 in our structure.

Experimentally measured transmittance spectra for transverse magnetization are shown in Fig. 3.25. Gray is for horizontal and black is for vertical input polarization. The spectra are normalized to the output power of a ridge waveguide without photonic crystal pattern. Notice that the quasi-TE and quasi-TM stop bands are shifted relative to each other for high-order backscattering. The spectra correspond to two different waveguides on the same sample.

However, transmittance from the far-end corresponds to more strongly rotated polarization having significant quasi-TE and quasi-TM components at the point of insertion into the photonic crystal. From the polarization rotation equation discussion in Chapter 2.3, we can also obtain the plots of the power of quasi-TE and quasi-TM components at the point into the photonic crystals as a function of birefringence as shown in Fig. 3.26. Here the feeder section is 900 μm long.

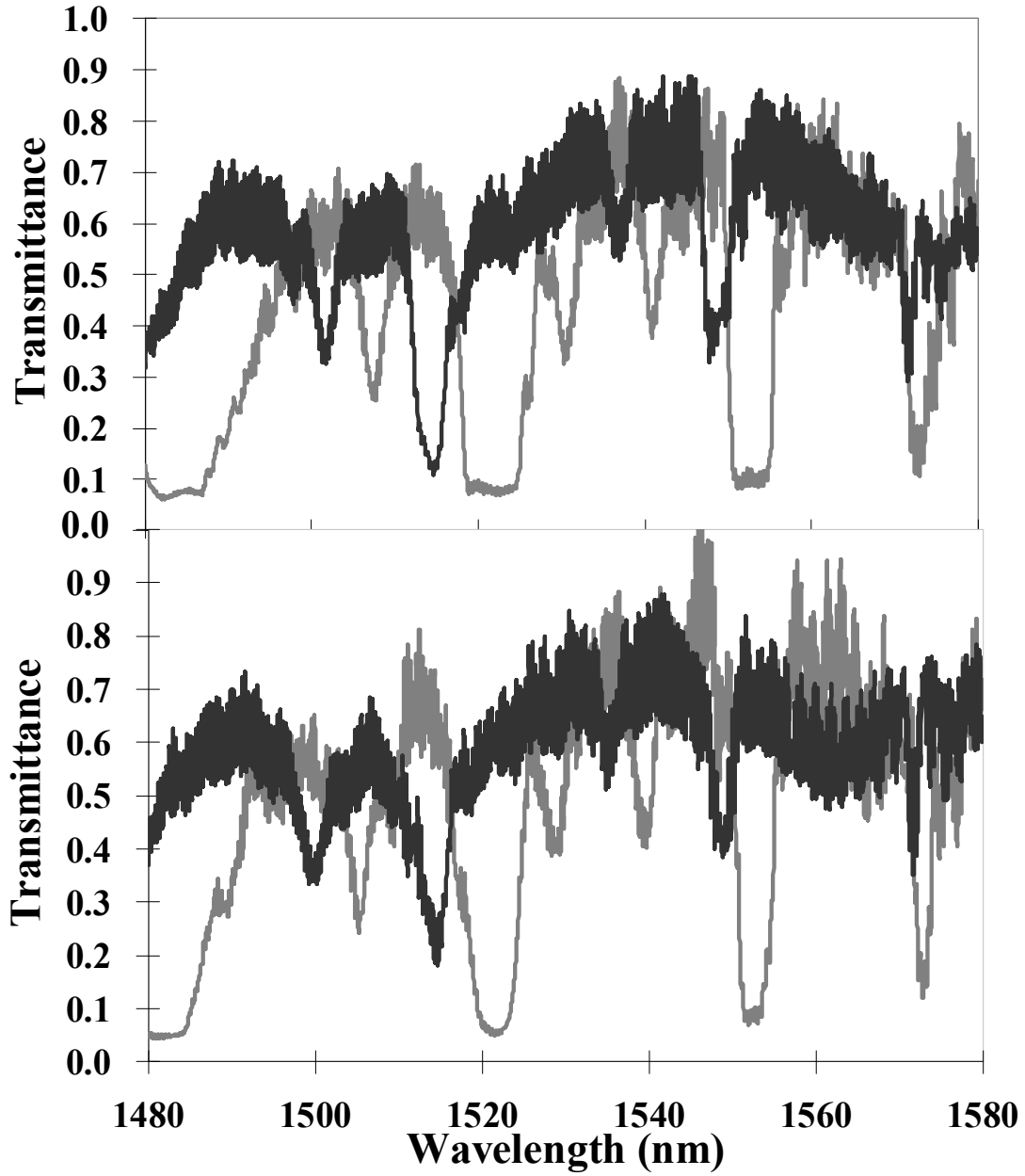

Figure 3.25 Transmission spectra for transverse magnetization. The gray and black spectra are corresponding to horizontal and vertical input polarization. Here are the spectra for two different waveguides on the same samples.

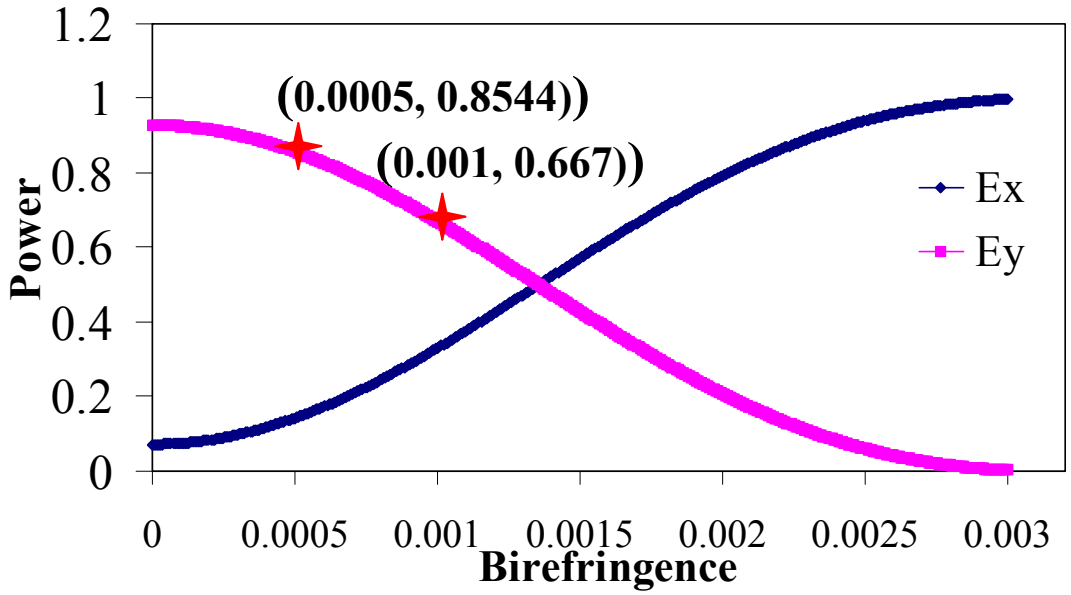

Figure 3.26 Power distributions of quasi-TE and quasi-TM components at the point into the photonic crystals as a function of birefringence. The points marked in the plot are the quasi-TM power for the approximated birefringence 0.0005 and 0.001.

Thus when the birefringence is relatively small (<0.001)for the fundamental mode, we can estimate that for a longitudinal magnetization the power transfer from quasi-TE to quasi-TM mode is more than 65% in the 900 μm waveguide feeder section before entering the photonic crystal. Especially the birefringence in the feeder section is 0.0005 for our film; the transferred power from quasi-TE to quasi-TM is about 85%. Data were collected for 10 different photonic crystal waveguides in three different samples, with similar results. Fig. 3.27 shows stopband spectra obtained experimentally for transverse magnetization (gray) and longitudinal (black) magnetization for horizontal input polarization. The spectra correspond to two different waveguides on the same sample. The opening up of a quasi-TM bandgap for light originally launched as horizontal polarization.

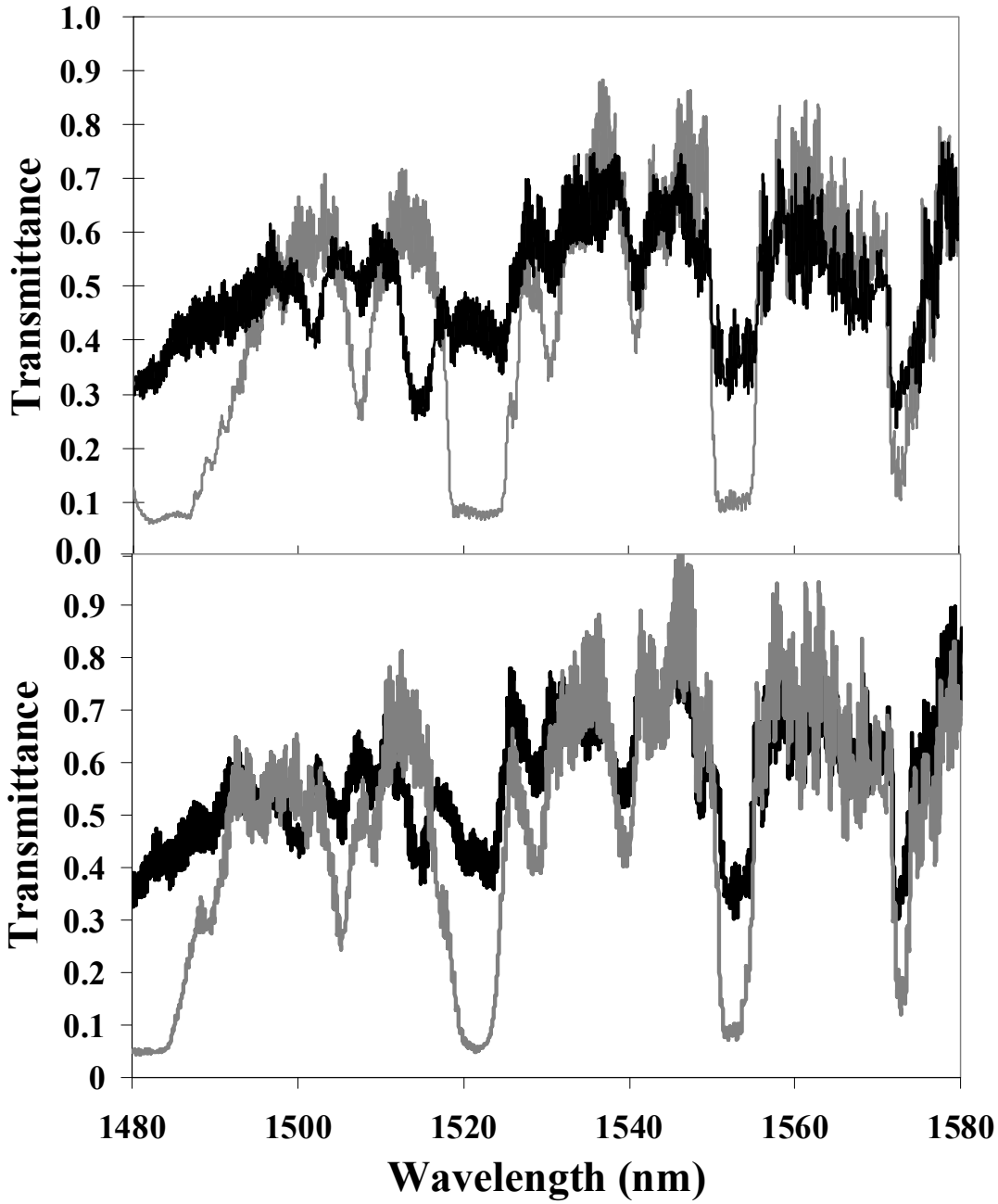

Figure 3.27 Transmission spectra for horizontal input polarization. The gray and black spectra are corresponding to transverse magnetization and longitudinal magnetization respectively. Here are the spectra for two different waveguides on the same sample.

3.3.3 Effective mode indices analysis

The patterning of a ridge structure on the slab slightly modifies the effective index and character of the allowed waveguide modes. Focused Ion Beam milling of the grating on the waveguide ridge reduces the average thickness of the optical channel and further modifies the mode indices. The mode index is the average quantity depending on the grooves depth, height of ridge waveguide and the film thickness for the grating region. The index is not a simple linear average of the film index and the air index; instead, it is very complicated to calculate for the exact value for the gratings especially with the V shape cross section. For approximation, the average thickness the grating area is used to calculate the effective indices for the region. The average grating region thickness is the film thickness with modification from the FIB overlapped milling deducting a half of the grooves depth.

Effective indices of the quasi-TE and quasi-TM modes in the grating region are determined by numerical simulation in conjunction with Bragg-reflection data analysis. Cross-comparison with the transverse-magnetization stop band spectrum Fig. 3.25 is exploited for this purpose.

3.3.3.1 Stopband spectral analysis

Wave-vector and frequency degeneracy occur upon phase matching between counter-propagating waves in different polarization states. Considering the phase matching condition for an optical guided wave characterized by a propagation wave-vector $\vec{\beta}$, with $\left|\vec{\beta}\right| = \frac{2\pi}{\lambda} n$ incident on a grating region having grating vector $\vec{K}$, where $\left|\vec{K}\right| = \frac{2\pi}{\Lambda}$ and grating period Λ. In the grating, a space harmonic $\vec{\beta} + m\vec{K}$, for $m = 0, \pm 1, \pm 2$ and etc. can exist. We see that waves with wave-vector $\vec{\beta} - \vec{K}$ will be coupled by the grating. These can propagate as a mode as long as $\vec{\beta} - \vec{K} = \vec{\beta}_m$, for some mode m with wave-vector $\vec{\beta}_m$.

Considering counter propagating wave coupling, the phase matching condition can be written as

$$\vec{\beta}_b = \vec{\beta}_f + m\vec{K} \tag{3.3}$$

Here $\beta_b = \frac{2\pi n_b}{\lambda}$ and $\beta_f = \frac{2\pi n_f}{\lambda}$. This equation describes the coupling of the forward propagating incident mode and the backward propagating mode in Bragg gratings. In the case of m=-1, the equation changed to

$$\lambda = \Lambda(n_f + n_b) \tag{3.4}$$

Due to the grating scattering, the light propagating in the forward fundamental mode can be coupled into fundamental or higher order modes in the backward direction. The stop band positions depend on the Bragg conditions. The Bragg conditions:

$$\lambda = (n_f{}^{TE} + n_b{}^{TE})\Lambda \tag{3.5}$$

$$\lambda = (n_f{}^{TM} + n_b{}^{TM})\Lambda \tag{3.6}$$

where n_f^{TE} and n_f^{TM} are the mode indices of the forward propagating light and $n_b{}^{TE}$ and $n_b{}^{TM}$, the mode indices of the backscattered light for quasi-TE and quasi-TM polarizations, respectively.

The indices can be obtained by the experimental results and the equation above. There are four stop-bands for quasi-TE and quasi-TM transmittance respectively in Fig. 3.24. The center wavelength positions of the first three stop bands clearly show within 1480nm to 1580 nm range. They are listed in Table 3.3.

Table 3.3
The center positions of stopbands for Quasi-TE and Quasi-TM transmittance spectra

	Fundamental λ_0 (nm)	**First-order λ_1 (nm)**	**Second-order λ_2 (nm)**
Quasi-TE	1572.09	1552.06	1521.6
Quasi-TM	1570.16	1547.97	1512.34

Considering the forward fundamental mode stop-band first couples with high order backscattering mode, the Bragg conditions for each stop bands can be expresses as the following equations.

For quasi-TE:

$$\begin{aligned} \lambda_0{}^{TE} &= (n_0{}^{TE} + n_0{}^{TE})\Lambda \\ \lambda_1{}^{TE} &= (n_0{}^{TE} + n_1{}^{TE})\Lambda \\ \lambda_2{}^{TE} &= (n_0{}^{TE} + n_2{}^{TE})\Lambda \end{aligned} \tag{3.7}$$

Substituting the data in table 3.3, we obtain the effective indices for quasi-TE fundamental, first and second order modes are 2.289, 2.2309 and 2.141.

For Quasi-TM:

$$\begin{aligned} \lambda_0{}^{TM} &= (n_0{}^{TM} + n_0{}^{TM})\Lambda \\ \lambda_1{}^{TM} &= (n_0{}^{TM} + n_1{}^{TM})\Lambda \\ \lambda_2{}^{TM} &= (n_0{}^{TM} + n_2{}^{TM})\Lambda \end{aligned} \tag{3.8}$$

Substituting the data in Table 3.3, we obtain the effective indices for quasi-TE fundamental, first and second order modes are 2.2862, 2.2215 and 2.1148. These indices are obtained by the experimental results.

3.3.3.2 Mode indices calculation

Mode indices are computed by beam-propagation analysis of a simulated ridge waveguide having the same width, average grating thickness, ridge height and material index as the fabricated structure.

In these calculations the average grating thickness is allowed to range within the experimentally determined uncertainty in measured thickness. Account is also taken of the grating groove-depth and its uncertainty since this also impacts the average film thickness in the grating region. The material film indices for TE and TM waves are determined by prism-coupler measurements on the un-patterned slab waveguide film. However an adjustment of 0.9% in their value is allowed to fit the measured stop band spectrum. This is within the experimental uncertainty in the prism-coupler data. The simulation makes use of the correlation method to extract mode indices, comparing the calculated propagating field amplitude against the input field. Minor adjustments to the measured average grating thickness and ridge height (within experimental uncertainty) are made to fit the experimentally measured stop band spectrum.

The mode indices in the ridge waveguide section outside the grating region are calculated. By the same correlation method, the ridge waveguide height is modified to match the average film thickness for the grating area in order to approximate the effective mode indices for the grating region. The ridge width, height and TE, TM material film indices are those of the fabricated ridge waveguide.

Fig. 3.28 shows the geometry of the ridge waveguide structure. W, H and T_f are the final simulated data for the ridge width, ridge height and the thickness of the film respectively. Table 3.4 lists the properties of the ridge waveguides. These parameters are used in the beam propagation simulation to calculate the effective mode indices for both waveguide region and photonic crystal region. From the dielectric tensor of the film, the refractive indices for TE and TM mode are 2.31049 and 2.3095 respectively. The effective index for GGG substrate is 1.9357. They are the same for both geometries. The pure waveguide region with grating is referred to here as a feeder section.

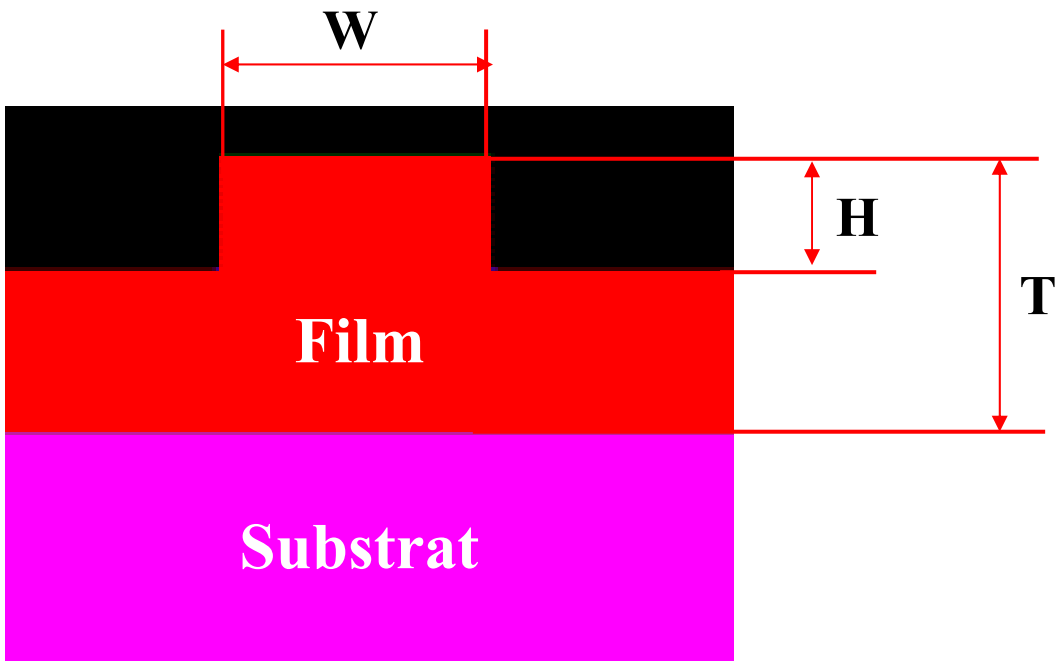

Figure 3.28 The geometry for ridge waveguide

The Fig. 3.29 Contour map and the computed fundamental mode profile of the waveguide geometry of feeder section at 1550 nm. The Fig. 3.30 Contour map and the computed mode profile of the waveguide geometry of the photonic crystal region at 1550 nm.

Table 3.4
Ridge waveguide dimensions

	Ridge Width W(μm)	**Ridge Height H (μm)**	**Film thickness T_f (μm)**
Photonic crystal	5	0.6	2.33
Feeder	5	0.6	2.75

Table 3.5 and 3.6 show refractive indices for the different waveguide modes in the photonic-crystal region and feeder sections for transverse magnetization at 1550 nm wavelength.

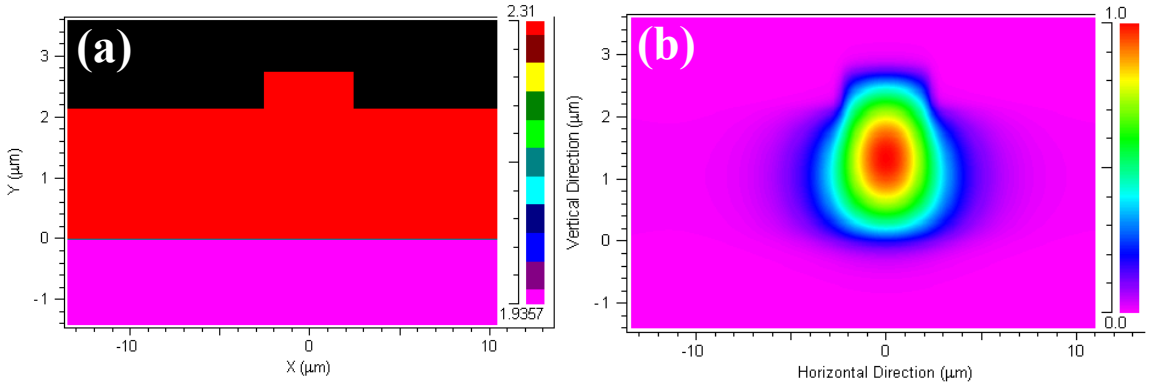

Figure 3.29 Beam Propagation analyses for ridge waveguide for feeder section. (a) Contour map of transverse index profile; (b) Computed transverse fundamental mode profile.

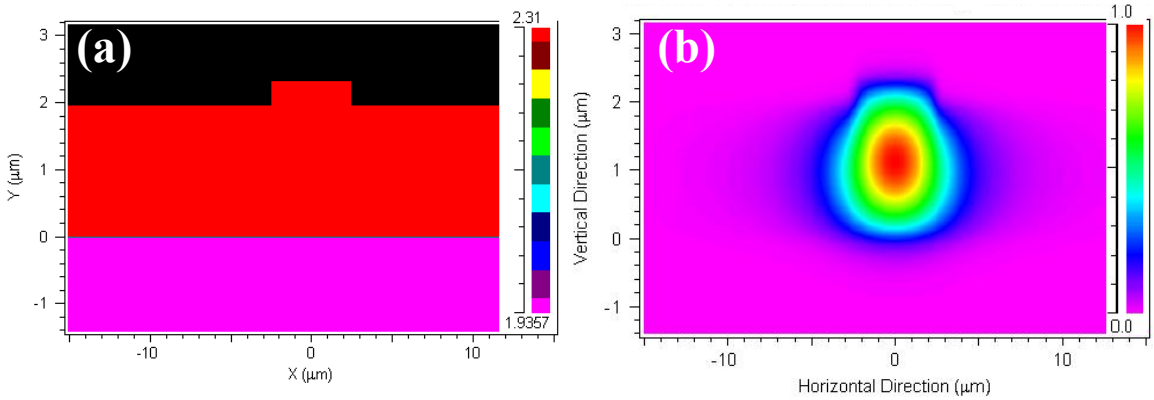

Figure 3.30 Beam Propagation analyses for ridge waveguide for photonic crystal region. (a) Contour map of transverse index profile; (b) Computed transverse fundamental mode profile.

Table 3.5

Refractive indices for the different waveguide modes in the photonic crystals

Mode order	Fundamental	First	Second	Third
Quasi-TE mode index	2.2877	2.2301	2.1336	1.9989
Quasi-TM mode index	2.2863	2.2219	2.1145	1.9720
Linear Birefringence	0.0014	0.0082	0.0191	0.0269

Table 3.6
Refractive indices for the different waveguide modes in feeder sections

Mode order	Fundamental	First	Second	Third
Quasi-TE mode index	2.2930	2.2497	2.1781	2.0765
Quasi-TM mode index	2.2925	2.2450	2.1661	2.0555
Linear Birefringence	0.0005	0.0047	0.0120	0.0210

These calculated effective indices show very good agreement with those obtained from Bragg condition equations based on the experimental results. It appears that the discrepancy in the calculated experimental and theoretical effective indices increases with mode order in the comparison. But these differences are still within experimental uncertainty.

The fundamental mode has low linear birefringence in the feeder section and is hence susceptible to TE-TM mode coupling due to the gyrotropy of the magneto-optic film. Fundamental mode linear birefringence in the ridge waveguide region outside the photonic crystal pattern is 0.0005. Thus light coupled into the far-end facet to the grating undergoes significant polarization rotation upon longitudinal magnetization before reaching the photonic crystal structure. From Fig. 3.26, we can estimate that for a longitudinal magnetization the power transfer from quasi-TE to quasi-TM mode is 85% in the 900 μm waveguide feeder section before entering the photonic crystal. For higher orders the large linear birefringence strongly suppresses TE-TM coupling, although the modes are no longer the same quasi-TE and quasi-TM as for transverse magnetization but are rather elliptically polarized.

3.3.4 Results and Analysis

Previous work has analyzed theoretically the band structure of layered stacks. [153-155] It is shown there that alternating gyrotropic layers with different elliptical birefringence

in adjacent layers can lead to the formation of band gaps arising from the coupling of Bloch modes of opposite helicities. This point is significant because unlike circularly-polarized waves, where opposite helicity modes are orthogonal and do not couple, the model predicts that spatially-dependent elliptically polarized modes of opposite helicities do couple, leading to the formation of new types of band gaps. These band gaps form away from the Brillouin zone edge ($K\Lambda \neq \pm\pi$, where K is the Bloch wave-vector), and can be made to reject arbitrarily-polarized light. [127] Levy *et. al.* extended this theoretical model to allow linear combinations of elliptically-polarized modes having different elliptical polarizations in opposite propagation directions, but still within a layered-stack framework.[128] The model predicts the formation of nearly-degenerate pairs of gyrotropic band gaps away from the Brillouin zone edge.[128]

The present study looks at this type of band gap formation in waveguide geometries in elliptically birefringent systems. The structure of these band gaps and the effect of magnetization direction on the gyrotropic band gaps are analyzed. These waveguide structures constitute a physical realization of the model where oppositely traveling elliptically-birefringence waves correspond to waveguide modes of different order. The study demonstrates the existence of nearly-degenerate gyrotropic band gaps, formed by elliptically polarized Bloch modes. These gyrotropic band gaps are realized by the hybridization of elliptically polarized waveguide modes of different order. Band gap activation in response to an applied magnetic field is also demonstrated.

In a photonic crystal waveguide the phase-matching condition $\vec{\beta} - \vec{K} = \vec{\beta}_m$, where m is the mode order and $\left|\vec{K}\right| = \frac{2\pi}{\Lambda}$ for grating period Λ, can be displayed graphically by shifting the dispersion plot by K and looking for the cross-over points. Due to phase matching a band gap opens up at the cross-over points. For fundamental quasi-TE or quasi-TM modes no band gap opens up at the cross-over with the corresponding high-order orthogonal polarization state. However, in the presence of gyrotropy, for circularly

or elliptically polarized forward modes, quasi-TE modes (or quasi-TM modes) acquire quasi-TM (or quasi-TE) components, partially activating the latter band gaps.

This band structure is calculated using beam-propagation simulation to find the effective indices for a ridge waveguide with an effective ridge height equal to the average thickness in the presence of the grating grooves. The mode effective indices for each wavelength are calculated. The selected values for the mode indices for quasi-TE and quasi-TM for different wavelength are listed in Table 3.7. 'WL' in the table stands for wavelength.

Fig. 3.31 plots frequency versus waveguide-mode wave-vector for quasi-TE and quasi-TM bands computed for ridge waveguides of the same ridge width, ridge height, thickness and material refractive indices as the fabricated one used in our experiments. For the forward propagation waves, wavevector is β_0^f and the x axis values can be expressed as $\beta_0^f \Lambda$; for the backward propagation waves, due to the space harmonic requirement for light to propagate in the grating region, the wavevectors are $K - \beta_n^b$ and the x axis values can be expressed as $(K - \beta_n^b)\Lambda$. Here n is equal to 1, 2, 3 and etc for higher order modes.

Fig. 3.31 shows the band structures for both quasi-TE and quasi-TM bands. Cross-over points between these bands show that waveguide modes of different order become degenerate at specific wavelengths and can couple. This coupling satisfies the phase matching condition and leads to band gap formation. Due to the very small birefringence between quasi-TE and quasi-TM fundamental modes, the band structures for fundamental forward and backward quasi-TE and quasi-TM are very close to each other. The inset is an example of forward fundamental band couple with backward second order bands. When we apply transverse magnetization, we only obtain either TE or TM band gaps as

the left figure in the inset. When we apply longitudinal magnetization, previous TE and TM bands are transformed into elliptical bands. Two additional bandgaps opened up due to the rotational modes coupling.

Table 3.7
Calculated quasi-TE and quasi-TM mode indices for different wavelength

WL (nm)	TE_0	TE_1	TE_2	TE_3	TM_0	TM_1	TM_2	TM_3
1480	2.2894	2.2369	2.1475	2.0228	2.2883	2.2292	2.1306	1.9973
1482	2.2893	2.2362	2.1471	2.0220	2.2882	2.2290	2.1302	1.9965
1485	2.2893	2.2359	2.1465	2.0210	2.2882	2.2287	2.1295	1.9955
1490	2.2892	2.2355	2.1455	2.0193	2.2880	2.2281	2.1283	1.9937
1500	2.2889	2.2346	2.1435	2.0157	2.2877	2.2273	2.1260	1.9902
1474	2.2886	2.2333	2.1407	2.0108	2.2873	2.2256	2.1228	1.9848
1476	2.2885	2.2331	2.1403	2.0103	2.2873	2.2254	2.1224	1.9841
1480	2.2884	2.2328	2.1396	2.0089	2.2872	2.2250	2.1215	1.9826
1482	2.2884	2.2326	2.1391	2.0082	2.2871	2.2248	2.1210	1.9819
1485	2.2883	2.2323	2.1385	2.0072	2.2870	2.2246	2.1202	1.9810
1495	2.2880	2.2314	2.1366	2.0037	2.2867	2.2234	2.1180	1.9773
1505	2.2878	2.2305	2.1346	2.0003	2.2864	2.2223	2.1152	1.9736
1508	2.2877	2.2302	2.1339	1.9992	2.2864	2.2220	2.1147	1.9725
1510	2.2877	2.2301	2.1335	1.9988	2.2863	2.2218	2.1145	1.9719
1512	2.2876	2.2299	2.1331	1.9979	2.2862	2.2215	2.1142	1.9710
1515	2.2875	2.2296	2.1325	1.9968	2.2861	2.2213	2.1132	1.9702
1525	2.2873	2.2287	2.1305	1.9934	2.2859	2.2202	2.1109	1.9665
1530	2.2872	2.2282	2.1295	1.9916	2.2857	2.2196	2.1098	1.9647
1531	2.2871	2.2281	2.1293	1.9920	2.2852	2.2197	2.1095	1.9644
1532	2.2871	2.2280	2.1291	1.9910	2.2856	2.2195	2.1093	1.9642
1533	2.2871	2.2279	2.1289	1.9912	2.2856	2.2193	2.1091	1.9638
1540	2.2869	2.2273	2.1274	1.9883	2.2854	2.2186	2.1075	1.9613

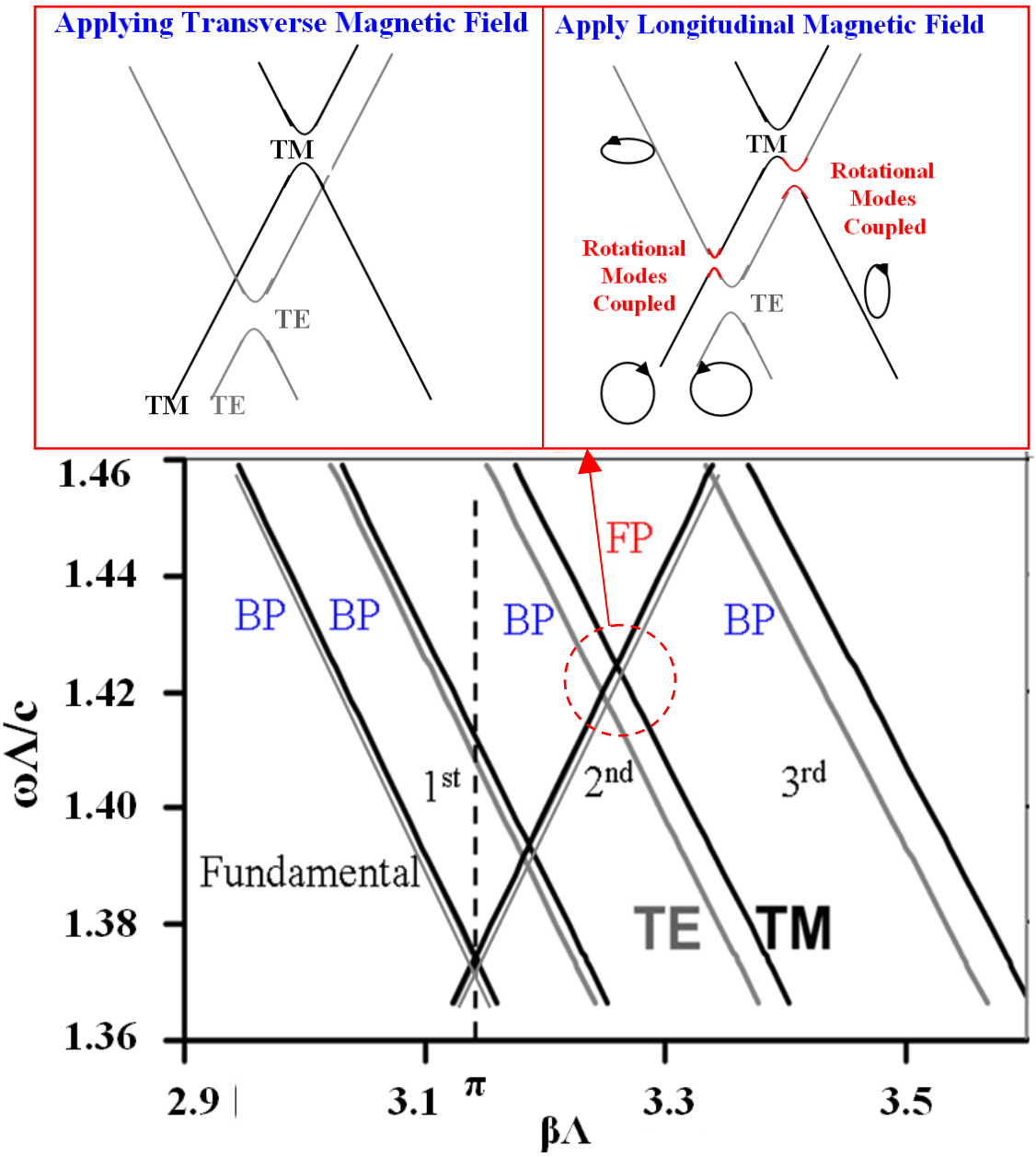

Figure 3.31 Band structure of the magneto-photonic crystal for transverse magnetization. The inset is an example of forward fundamental band couple with backward second order bands.

This band structure is calculated for transverse magnetization by numerical simulation. Mode indices are computed on the basis of the correlation method for propagating modes and plotted against frequency. These indices are evaluated as a function of wavelength

for a ridge waveguide structure of the same dimensions as our fabricated waveguides with 600 nm-waveguide ridge step and 5μm-ridge-width for all waveguide modes. The film height is determined from scanning-electron micrographs of the ridge waveguide cross section for an average film top near the mid-point between a grating groove ridge tip and trough. Excellent correspondence is obtained between the measured mid-point values of TE and TM stop bands for all waveguide modes and the cross-over points of fundamental and backscattered mode bands. The calculated mid-band wavelengths are obtained from the plot, listed in Table 3.8.

Table 3.8
Rsoft calculation of mid-band wavelengths

	Fundamental λ_0 (nm)	**First-order λ_1 (nm)**	**Second-order λ_2 (nm)**
Quasi-TE	1572.5	1552.3	1520.8
Quasi-TM	1570.3	1548.1	1513.8

Very good agreement with the experimentally measured spectra is obtained as can be seen by comparing compared to experimental data listed in Table 3.3and 3.7. The differences are within the experimental uncertainty. The accuracy of the calculated cross-over wavelengths as compared to the measured mid-band wavelengths equals $\pm\frac{1}{10}$ of the experimental bandwidth for TE stop bands and $\pm\frac{1}{5}$ for TM stop bands. The experimental bandwidth scale is taken to be the width of the stop band centered at 1522 nm for TE gaps and at 1515 nm for TM gaps.

For the samples used in this work, the grating groove depth h=720nm is much smaller than the film thickness d =2.7μm. According to equations 2.45 and 2.46, the TE-TE and TM-TM coupling coefficient between modes n and m for first-order Bragg reflection can be calculated.

Given the coupling coefficients κ for a relief grating used in our magneto-photonic crystal waveguides corresponding to different modes coupling, we compute the power-transfer efficiency and the amplitude of the backward propagating TE and TM waves.

The power transfer efficiency between forward and backward propagating modes is a function of the coupling coefficients κ between the specific modes in question and the phase mismatch $\Delta = \beta^b - (\beta^f + K)$ according to equation 2.48. Calculated stopbands for both TE and TM coupling between different-order are shown in Fig. 3.32. Very good agreement with the experimentally measured spectra is obtained as can be seen by comparing Fig. 3.25 and Fig. 3.32.

The accuracy of the calculated cross-over as compared to the measured mid-band wavelengths equals ±0.48 nm for the TE stop bands and ±0.2 nm for TM stop bands.

Fig. 3.25 shows the experimental transmittance for vertical and horizontal input polarizations for a transverse magnetic field. Notice that for high-order mode backscattering quasi-TE and quasi-TM bands form spectrally separate depending on the input polarization. The activation of Faraday rotation gyrotropy by switching the magnetization to the longitudinal direction induces a polarization rotation and band gap activation. Thus, for a TE input, for example, the TM stop band is accessible for longitudinal magnetic fields due to TE-TM mode coupling. These results show that quasi-TE and quasi-TM stop bands can be activated by enabling or disabling gyrotropic mode coupling through magnetic field control.

The band structure depicted in Fig. 3.31 shows that for the present photonic crystal waveguides, gyrotropic band gaps form between asymmetrically coupled forward and backscattered modes. Moreover, gyrotropic mode splitting leads to degeneracy lifting of the band gap edges. The gyrotropic degenerate bandgaps predicted in [128] are thus partially split in the present configuration leading to a widening of the band gaps for elliptically-polarized Bloch modes upon longitudinal magnetization, as observed in Fig. 3.27.

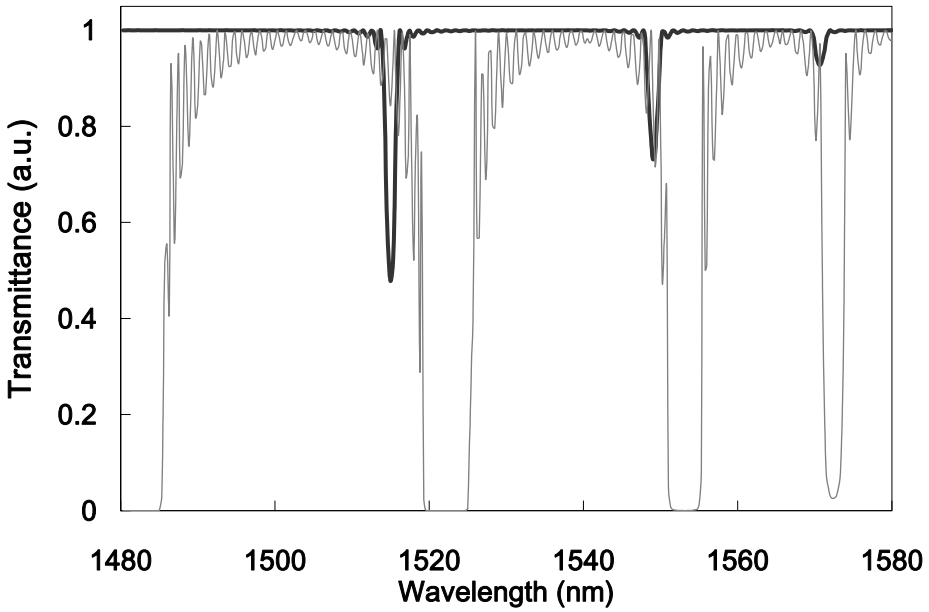

Figure 3.32 Calculated stop bands for both TE and TM coupling between different-orders. Gray color shows TE stop bands, black shows TM stop bands.

Polarization-degenerate band gaps of the type predicted by Merzlikin *et.al.*, [128] that is, band gaps that reflect arbitrarily-polarized light suffer the following transformation in the waveguide system investigated here. First the quasi-TE and quasi-TM component-mode gaps appear in adjacent and possibly overlapping spectral regions, as displayed for first- and second-order mode back-reflection in Fig. 3.27. Thus, upon longitudinal magnetization the stop bands become wider, as they now encompass back-reflection of both types of polarization states (quasi-TE and quasi-TM). Secondly, the optical power is only partially reflected inside the gap, depending on the power distribution between different polarization components incident on the photonic crystal. Hence gyrotropic degenerate band gaps become gyrotropic quasi-degenerate band gaps, since arbitrary polarization is back-reflected but only partially (Fig. 3.27) or in adjacent but not fully overlapping spectral regions. This is the waveguide manifestation of gyrotropic degenerate band gaps.

3.3.5 Application: gyrotropic photonic crystal waveguide switches

Functional photonic crystals fabricated in iron garnet films are shown to provide magnetically-controllable optical switching. Transverse-electric and transverse-magnetic stop band separation in conjunction with optical gyrotropy are utilized to selectively block and transmit near-infrared light in waveguide geometries. Geometrical birefringence allows the simultaneous low- and high-birefringence in different modes necessary to create band gap separation and effective magneto-optic gyrotropy in a single device. This section introduces magneto-photonic crystal optical switches fabricated on chip in $Bi_{0.8}Gd_{0.2}Lu_{2.0}Fe_5O_{12}$ films with a specific Faraday rotation of 83°/mm at 1510 nm.

To produce the optical switches, one-dimensional magneto-photonic crystals are fabricated into multimode waveguides can be considered as a functional optical switch. This design was discussed in the last section. Single-mode waveguides are not required. Rather, the devices work best in a multimode configuration.

The switch consists of a feeder section, 900 μm in length, followed by the photonic crystal, as shown in Fig. 3.33. The waveguide feeder acts as a magnetically-activated polarization rotator, as the fundamental mode in this section has very low linear birefringence.

The optical switch operates as follows. Light is coupled into the fundamental mode from the input facet on the far side to the photonic crystal to allow for sufficient polarization rotation due to TE-TM mode coupling upon longitudinal magnetization. No TE-TM coupling occurs for transverse magnetization. Ideally the device should impart 90° of Faraday rotation in the feeder section, without any linear birefringence. Birefringence-free Faraday rotator waveguides have already been demonstrated in magnetic garnet films. End-fire coupling centered on the input facet delivers better than 95% of the

guided power into the fundamental mode in the multimode waveguide. Power distribution into different modes is calculated by beam-propagation simulation.

Based on the Table 3.5 and 3.6, it is the large linear birefringence of the non-fundamental modes that enables the selective transmission and reflection required for optical switching in this device, as quasi-TE and quasi-TM band gaps are spectrally separate. The mode indices and birefringence in the feeder are different from the photonic crystal region due to the lower effective thickness of the grating section as compared to that of the feeder.

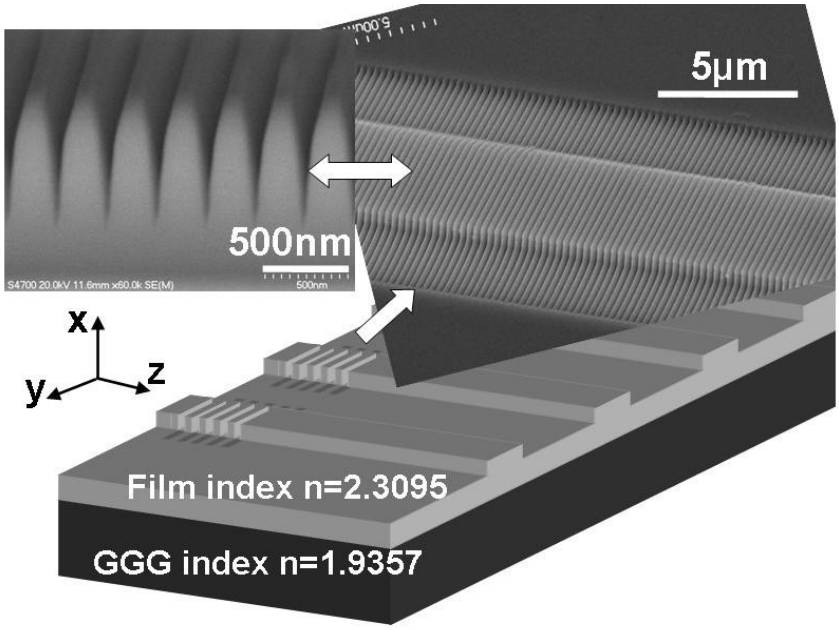

Figure 3.33 Schematic depiction of gyrotropic waveguide-switch with one dimensional magneto-photonic crystal. A magneto-optic feeder section precedes the band gap structure. A scanning-electron micrograph of the magneto-photonic crystal on the ridge waveguide is also shown.

It is well known that anisotropy may suppress the magneto-optic rotation.[104] But in our case the fundamental mode birefringence parameter $\vec{n}\Delta n$ in the feeder section is smaller than the magnitude of the off-diagonal component of the dielectric tensor $\lambda\theta_F\vec{n}/\pi$

because the small stress birefringence is of opposite sign to the geometrical birefringence and lowers the fundamental mode birefringence Δn to 0.0005 ± 0.0003 in the feeder. This allows for effective quasi-TE to quasi-TM coupling (Faraday rotation) for longitudinal magnetization along the ridge waveguide axis. Here $\bar{n}$ is the average refractive index $\frac{1}{2}(n_{TE} + n_{TM})$, $\Delta n = n_{TE} - n_{TM}$ and θ_F is the specific Faraday rotation.

A comparison of the mode birefringence parameter $(\pi / \lambda)\Delta n$ with the specific Faraday rotation 0.00145 radians/μm shows that TE-TM mode coupling operates for the fundamental mode, with $(\pi / \lambda)\Delta n$ equal to 0.00105 per μm at 1550 nm wavelength, and is progressively suppressed at higher-order modes with $(\pi / \lambda)\Delta n$ =0.0097, 0.0244, and 0.0426 per μm for first, second, and third-order modes, respectively.

The top picture in Fig. 3.34 shows the transmittance spectrum for transverse magnetization for a vertical and horizontal polarization inputs, evincing that quasi-TE and quasi-TM stop bands are separate in high-order back reflection. The bottom picture in Fig. 3.34 displays the measured transmittance of a typical device for transverse in-plane (gray spectrum) and longitudinal (black spectrum) magnetization for horizontal (in-plane) input polarization. Longitudinal magnetization is collinear with the waveguide axis.

In all cases most of the forward propagating power is in the fundamental waveguide mode. The spectra are normalized to the output power of a ridge waveguide (magnetized in the corresponding direction) without a photonic-crystal pattern, of the same ridge-width on the same sample.

Notice that the quasi-TE (horizontal-polarization input) and quasi-TM (vertical-polarization input) stop bands occur at different wavelengths for high-order backscatter modes. Hence quasi-TE light will be transmitted efficiently at the quasi-TM stop band and vice-versa. Fig. 3.35 shows the output image for longitudinal (a) and transverse (b)

magnetization at 1522.8 nm wavelength for a horizontally-polarized input. A small electromagnet pictured in Fig. 3.36 is used to switch the magnetization.

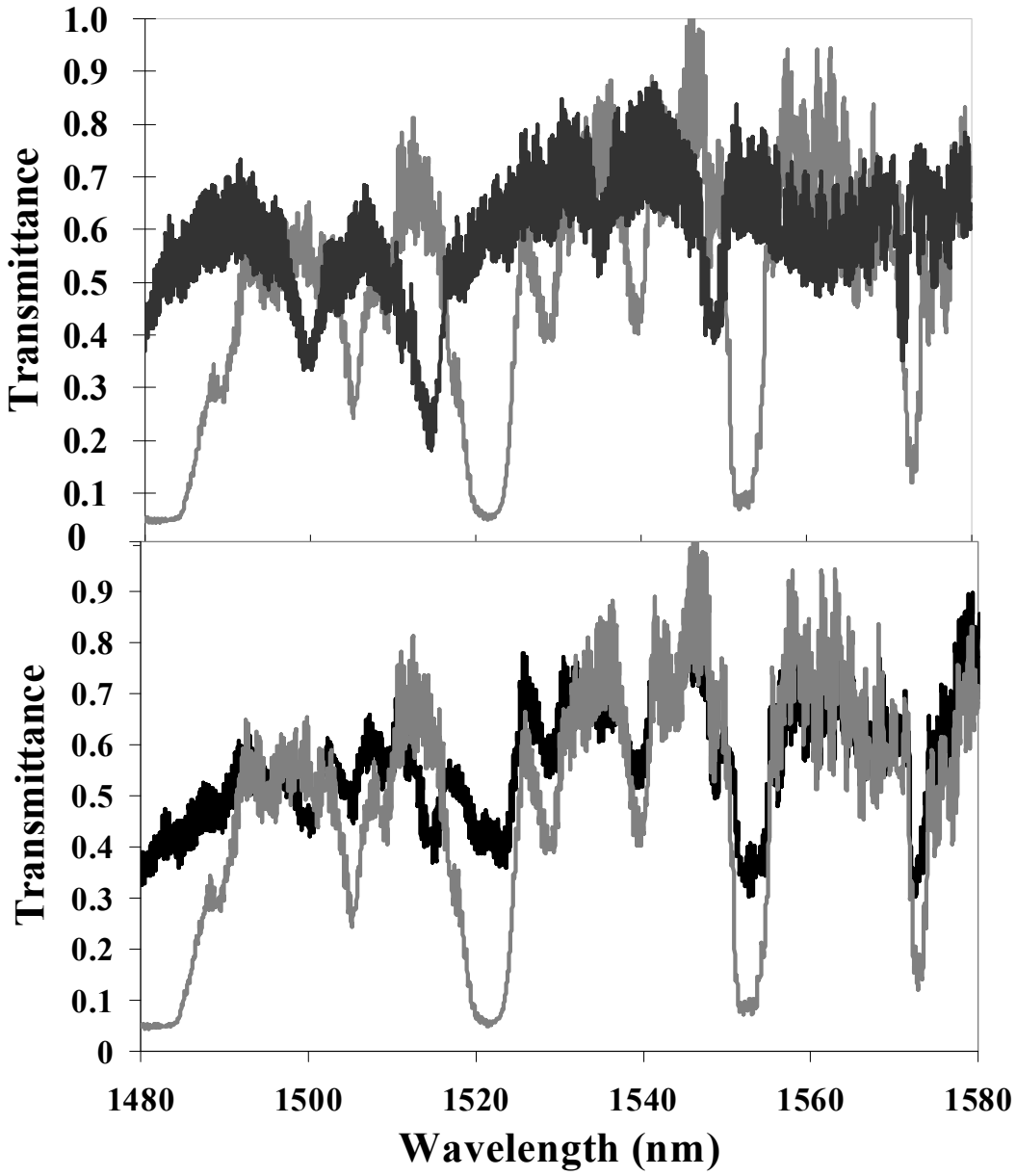

Figure 3.34 Transmittance spectra for transverse (gray) and longitudinal (black) magnetization for horizontally polarized input. The top picture displays transmittance spectra for transverse magnetization and vertical input (quasi-TM) and horizontal input (quasi-TE), showing separation of the corresponding stop bands. The spectra are normalized to the transmittance of a ridge waveguide without photonic crystal pattern.

The magnetic field is generated and controlled by a set of homemade magnetic coils equipped on the sample stage. Both longitudinal and transversal magnetic field can be generated by applying current through different sets of copper coils. A programmable power supply (Instek PSM-3004) is used to generate a self-stabilized step current with 1mA precision. Tests on ten different magneto-photonic crystal devices fabricated on three different samples exhibit similar spectra.

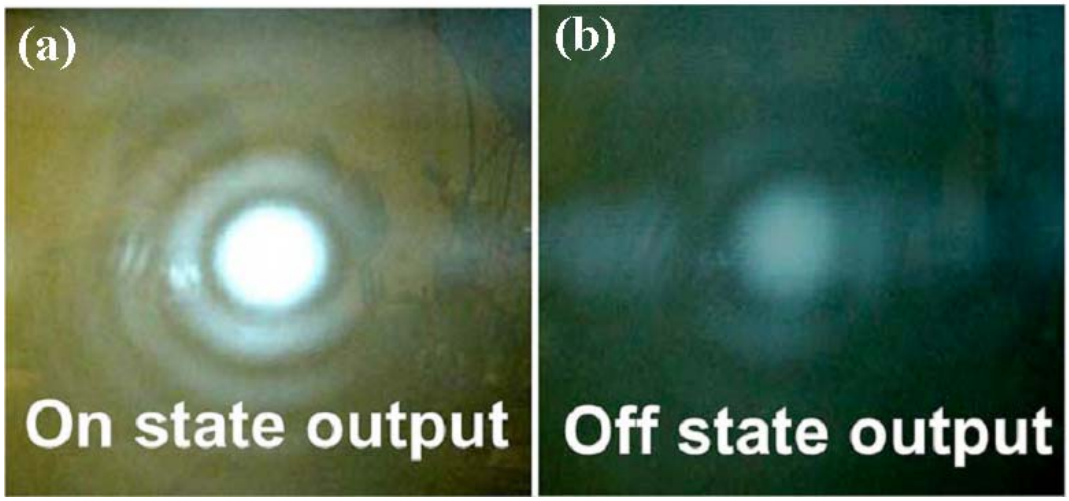

Figure 3.35 Transmitted light through the magneto-photonic crystal optical switch at 1482.8 nm wavelength. The input polarization is horizontal. (a) is for longitudinal magnetization; (b) is for transverse magnetization.

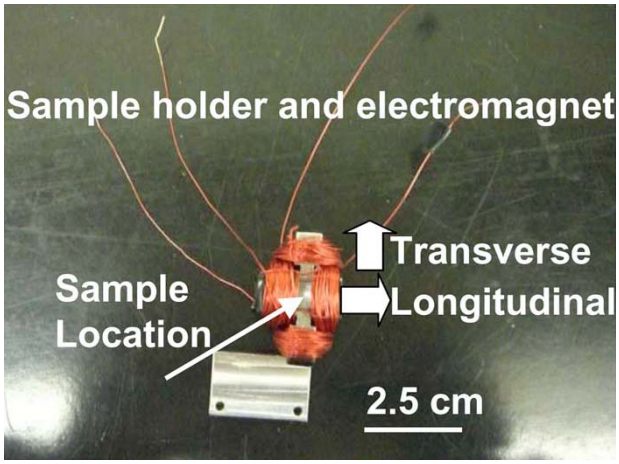

Figure 3.36 The electromagnet on sample holder used to switch the applied magnetic field from collinear to transverse relative to the ridge waveguide axis.

For a TE input and longitudinal magnetization the optical power transmitted at the quasi-TE stop bands is significantly higher than for transverse magnetization, due to the polarization rotation induced by the gyrotropy. We estimate that for a longitudinal magnetization the power transfer to the quasi-TM mode is 85% in the 900 μm waveguide feeder section before entering the photonic crystal. This rotation activates the optical transmission through the quasi-TE stop band, corresponding approximately to the observed transmittance in the band.

Both quasi-TE and quasi-TM light are back-reflected at the Bragg condition for the corresponding modes. For a horizontal-polarization input and transverse-magnetization, optical transmission is blocked with 11.5 dB efficiency in the fabricated devices at the quasi-TE stop bands, excluding losses in the grating section. This provides a measure of the dark-state of the switch. Grating losses are about 1 dB at 1530 nm. Upon switching to a longitudinal magnetization direction the optical polarization rotates as a result of the Faraday effect modified by the linear birefringence since forward propagating light is in fundamental mode, with low linear birefringence. Upon Faraday rotation the forward propagating mode passes through the quasi-TE stop band for a transmission state. Fig. 3.35 shows light and dark images obtained upon switching the magnetization from longitudinal to transverse directions at a wavelength of 1522.8 nm, corresponding to fundamental to second-order backscattering.

The overall efficiency of the device can be characterized by the ratio of transmitted power in the “on” and “off” states. We estimate this number to be about nine at 1522.8 nm. Improvements can be achieved by better tuning the birefringence to zero in the fundamental mode, adjusting the length of the waveguide feed section to achieve full TE to TM conversion in the longitudinal-field configuration before the light enters the photonic crystal, and enhancing the grating coupling constant for stronger light rejection at extinction. The insertion loss of a typical device in transmission is estimated at 5.4 dB.

This figure includes Fresnel reflection, absorption and grating losses and radiation losses due to fiber to ridge waveguide mode mismatch.

3.3.6 Transmission measurement and analysis on additional samples

According to the previous data and analysis, functional magnetically-controllable optical switches can be fabricated. The stop band positions depend on the Bragg condition, which means the periodicity of the photonic crystal has also a major effect on the bandgap positions. Besides the controllability through the magnetic field, we can also fabricate photonic crystals on the magnetic thin film with different periodicities to control the stopband positions. In this way, the same switching phenomena can be observed on these samples at different frequencies. We can design and fabricate magnetically controlled photonic crystals switches according to frequency switching requirement. In the following paragraphs, transmittance analysis for grating structures with different periods is demonstrated.

Magneto-photonic crystals were fabricated in multi-mode waveguides with the same conditions as the sample used in the previous demonstrations. The slab waveguide film is 2.75 ± 0.05 μm thick with a composition $Bi_{0.8}\ Gd_{0.2}\ Lu_{2.0}\ Fe_5\ O_{12}$.Waveguide ridges with 600 nm ridge height are patterned on the film by standard photolithography and plasma etching. A one-dimensional photonic crystal is formed by focused ion beam milling with grating grooves are 720 ± 25 nm-deep. Ridge waveguides are 1.2 mm-long with the photonic crystal structure (200 μm in length) positioned 100 μm away from one of the facets. Thus the feeder section and photonic crystal region have the same refractive index parameters as listed in Table 3.5 and 3.6. However, the one dimensional magneto-photonic crystals used for the following transmittance measurement have different periodicities.

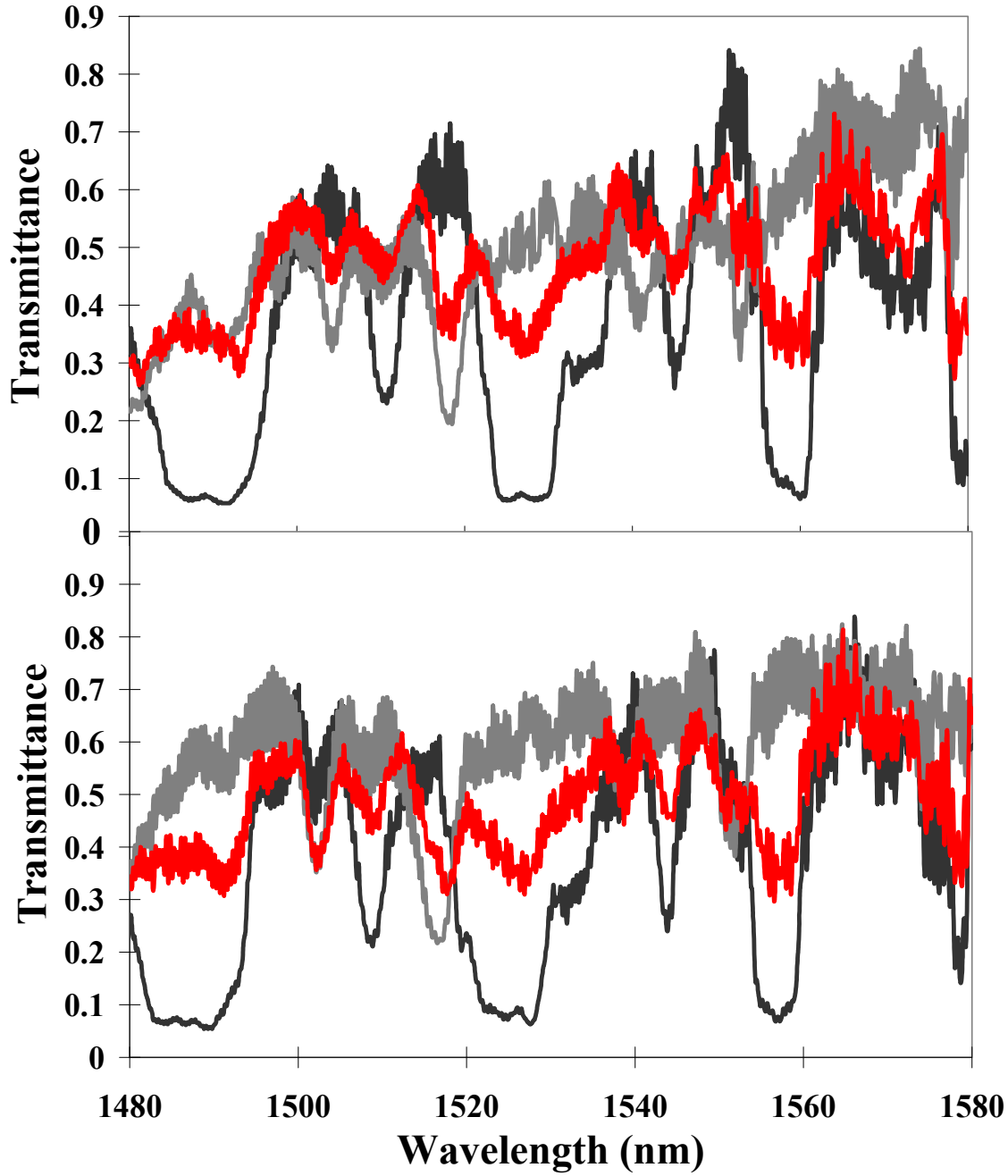

Figure 3.37 Stop band spectra obtained experimentally for both transverse and longitudinal magnetization on the photonic crystal with a period of 345 ± 0.3 nm. With transverse magnetization, black is for horizontal and gray is for vertical input polarization. With horizontal input polarization, black is for transverse magnetization and the red is for longitudinal magnetization. The spectra correspond to two different waveguides on the same sample.

When the grating has a period of 345.15 ± 0.3 nm, multiple transmittance spectra are measured under different conditions, as shown in Fig. 3.37. Experimentally measured transmittance spectra for transverse magnetization are shown as gray and black spectra in Fig. 3.37. Black is for horizontal and gray is for vertical input polarization. The spectra are normalized to the output power of a ridge waveguide without photonic crystal pattern. Notice that the quasi-TE and quasi-TM stop bands are shifted relative to each other for high-order backscattering.

Fig. 3.37 also evinces stopband spectra obtained experimentally for transverse magnetization (black) and longitudinal (red) magnetization for horizontal input polarization. The spectra correspond to two different waveguides on the same sample. The opening up of a quasi-TM bandgap for light originally launched as horizontal polarization is observed at different frequencies.

When the grating has a period of 347.45 ± 0.3 nm, multiple transmittance spectra are measured under different conditions, as shown in Fig. 3.38. The opening up of a quasi-TM bandgap for light originally launched as horizontal polarization is observed at different frequencies.

The center-wavelengths of the stopbands for quasi-TE and quasi-TM transmittance on these two photonic crystals with different periods are different from previous data. According to Fig. 3.37 and 3.38, the center wavelength positions of the stop bands clearly shown within 1480nm to 1580 nm range are listed in Table 3.9 and Table 3.10 respectively.

Table 3.9
The center positions of stopbands for Quasi-TE and Quasi-TM transmittance spectra

	Fundamental λ_0 (nm)	**First-order λ_1 (nm)**	**Second-order λ_2 (nm)**
Quasi-TE	1579.2	1559.1	1526.2
Quasi-TM	1578.23	1523.5	1518.61

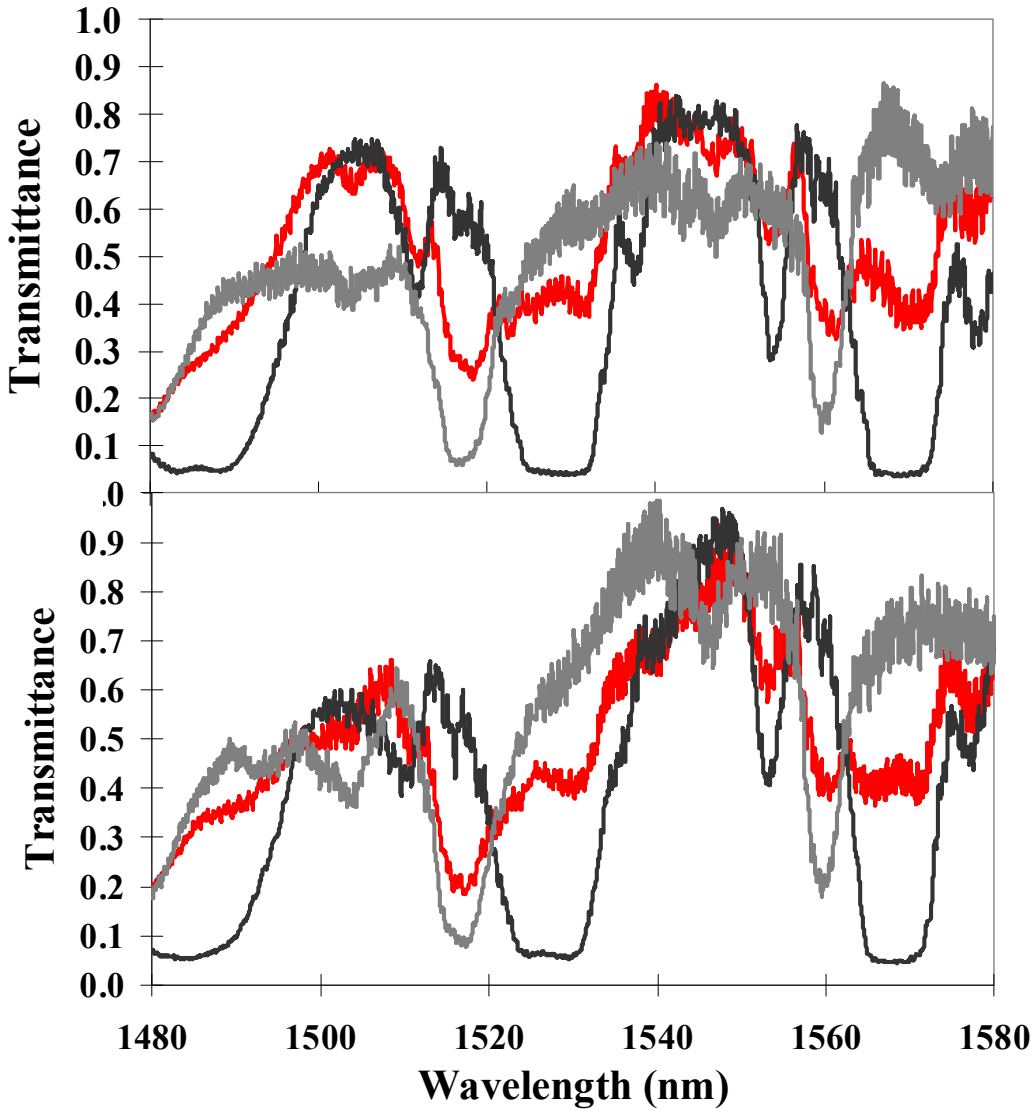

Figure 3.38 Stop band spectra obtained experimentally for both transverse and longitudinal magnetization on the photonic crystal with a period of 347.45 ± 0.3 nm. With transverse magnetization, black is for horizontal and gray is for vertical input polarization. With horizontal input polarization, black is for transverse magnetization and the red is for longitudinal magnetization. The spectra correspond to two different waveguides on the same sample.

Table 3.10
The center positions of stopbands for Quasi-TE and Quasi-TM transmittance spectra

	First-order λ_1 (nm)	Second-order λ_2 (nm)	Third-order λ_3 (nm)
Quasi-TE	1569.48	1528.63	1487.27
Quasi-TM	1559.54	1516.59	N/A

The same analysis as discussed in section 3.3.3 can be applied. These experimental results also show good agreement with the Bragg condition and calculated effective indices. Discrepancies fall within the experimental uncertainty. The opening up of a quasi-TM bandgap for light originally launched as horizontal polarization can be observed at different frequencies.

The purpose of this section is to demonstrate the period dependence of the photonic bandgaps and the on-off switching phenomena. The functional magnetically controlled optical switches can be used to control the on and off state of light propagation at different frequencies based on the period of the structures.

3.3.7 Conclusion

In conclusion, the multi-stopbands in transmission spectrum of a MPC on the waveguide are observed, according the Bragg condition of forward fundamental mode coupled to backward fundamental and higher order waveguide modes. The number of stopbands corresponds with the number of modes supported by the waveguide. This character is not present in the stack model. The waveguide mode indices for different wavelength are calculated by BeamPROP simulation. The band structures are plotted based on these data. The corresponding wavelength of intersection points for forward and backward bands have good agreement with the mid-bandgap positions from experiments.

This section also studies and analyzes the magnetic control of band gap activation in one-dimensional photonic crystals. Different forward-propagating waveguide modes are built up by enabling or disabling the gyrotropic coupling between quasi-TE and quasi-TM polarization states. These forward propagating waves hybridize with high-order backscattered modes at different wavelengths satisfying the Bragg condition for asymmetric coupling. The band gaps thus formed reject or partially allow the transmission of different polarization states depending on the direction of the applied magnetic field. Geometrical birefringence plays an important role in the magneto-optic response of these photonic crystals partially breaking the gyrotropic degeneracy reported for stacked gyrotropic photonic crystals. [128]

A magnetically controlled optical switch based on TE/TM band gap separation in magneto-photonic crystal waveguides has been demonstrated. Fundamental mode Faraday rotation upon longitudinal magnetization together with back-scattering into high-birefringence non-fundamental modes for transverse magnetization is shown to selectively block and transmit infrared light. Functional photonic crystals fabricated in iron garnet films are shown to provide magnetically-controllable optical switching. According the different periodicities for the structure, this switching property can be demonstrated at different frequencies.

3.4 Two dimensional magneto-photonic crystals

Most early works dealing with magneto-photonic crystals have been either devoted to study of one dimensional structures [24, 25] or quasi-one-dimensional models [150]. The potential impact of magneto-optical activity in two- or three-dimensional periodic systems remains rather unexplored. [159, 160] The purpose of this project is to initiate an investigation and begin to fill in the gap in understanding of the basic properties of two-dimensional magneto-photonic crystals (MPC). Two-dimensional MPC structures were successfully fabricated as part of the work reported here through FIB milling technology

on the substituted iron garnet waveguide. Some initial work such as optical transmission and Faraday rotation response has been tested on the samples. Obvious multi-stopbands and enhancement of Faraday rotation effect are observed experimentally. In this section we present a simulation study to analyze band structures for two dimensional magneto photonic crystals on slab waveguide as well as the results of fabrication and testing structures.

3.4.1 Experimental background

Epitaxial bismuth and gadolinium substituted lutetium iron garnet BiLuIG planar thin films grown on (100) oriented gadolinium gallium garnet $Gd_3Ga_5O_{12}$ substrates by liquid phase epitaxy is used in these experiments. In terms of composition and properties the thin planar films used are all approximately similar to the ones used for one dimensional photonic crystal fabrication. The approximate composition is $Bi_{0.8}Gd_{0.2}Lu_{2.0}Fe_5O_{12}$. We characterize the BiLuIG planar thin film by prism coupler measurement. The film thickness is 2.77μm and film index is 2.315. Prism-coupling measurements on the slab before surface patterning reveal modal indices 2.301, 2.26066, 2.19108 and 1.965 for the fundamental, first-, and second-, third-, forth-order TE modes, at 1503nm wavelength, respectively. And the modal indices are 2.346, 2.258, 2.1825, 2.0741 and 1.94 for the fundamental, first-, and second-, third-, forth-order TM modes, at 1503nm wavelength, respectively. The Faraday rotation per unit length in the material is about 137°/mm.

The most straightforward design is to simply fabricate a 2d-periodic crystal on a slab waveguide. A schematic depiction of the design is shown in Fig. 3.39. The two dimensional photonic crystals are periodic along x and z directions. This crystal can have photonic bandgaps in the xz plane. Unlike one-dimensional photonic crystals, this two dimensional photonic crystal strcuture can prevent light from propagating in any direction within the plane. Such a structure can confine light vertically within the slab via index guiding, a generalization of total internal reflection—this mechanism is the source of several new tradeoffs and behaviors of slab systems compared to their 2D analogues.

Ridge waveguides on the magnetic iron garnet films which is used to guide light from laser source into slab waveguide are fabricated by photolithography and dry etching. Photonic crystals are patterned on the slab waveguide by focused ion beam milling. Fig. 3.40 is an SEM image of two dimensional photonic crystal patterns fabricated on magnetic garnet slab waveguides. Mechanical polishing is used to polish the output facet close to photonic crystal region in order to reduce the scattering loss from facet roughness and the propagation loss in the slab waveguide.

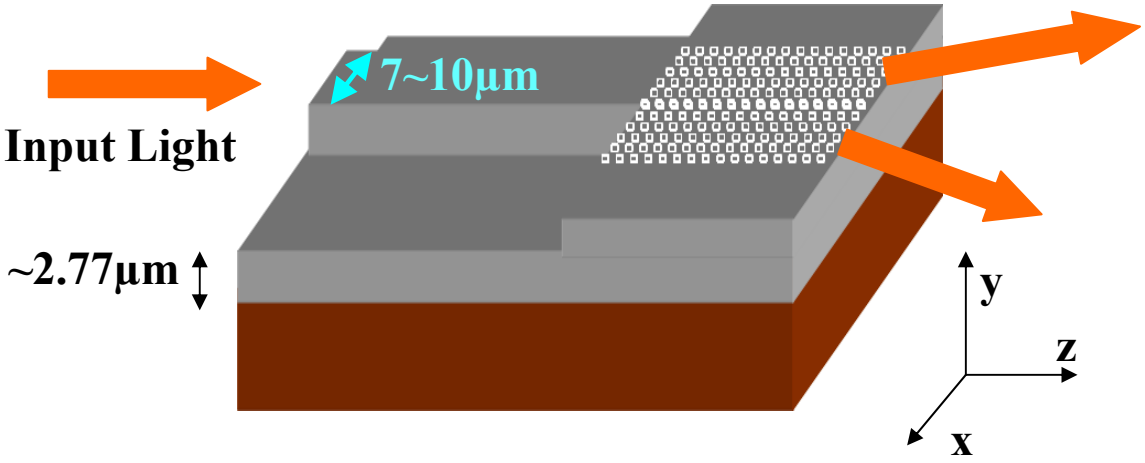

Figure 3.39 Sketch of the mechanism for design.

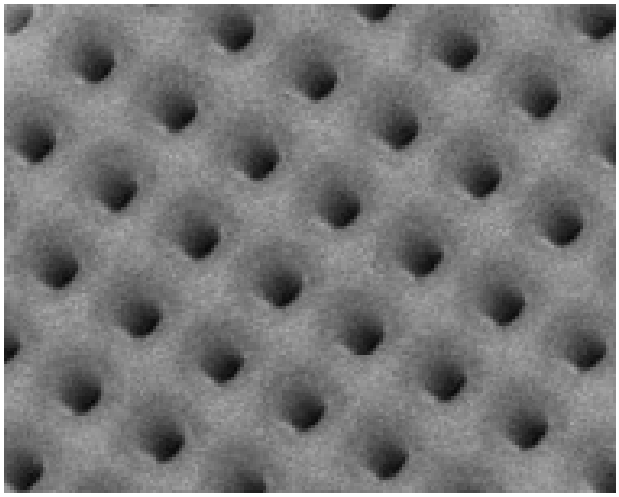

Figure 3.40 Top view of two dimensional photonic crystal on slab waveguide.

The input light travels through a ridge waveguide of width from 7μm to 10μm and length around 1mm. Then the light couples into the two-dimensional photonic crystal. The photonic crystal interacts with the light and controls the light propagation. Output light can be detected by the optical setup and precise measurements of transmittance and Faraday rotation can be effected.

A top view of the structure is shown in Fig. 3.41. The red dots are square air holes with adjustable side length. The orange arrows show the light scattered in the photonic crystal structure. The total dimensions of the structure are determined by light scattering after the ridge waveguide in order to make sure the light can propagate in the photonic crystal structures in the slab waveguide. The approximated dimensions can be calculated. For approximation, λ=1.5μm is used which is within the wavelength used in the optical test.

$$\tan\alpha = \frac{\lambda}{W_1} = \frac{W_2 - W_1}{2L} \tag{3.9}$$

Here, W_1 is the width of ridge waveguide. W_2 and L are the width and length of the photonic crystal respectively. Using this equation, the approximated size of the photonic crystals can be decided.

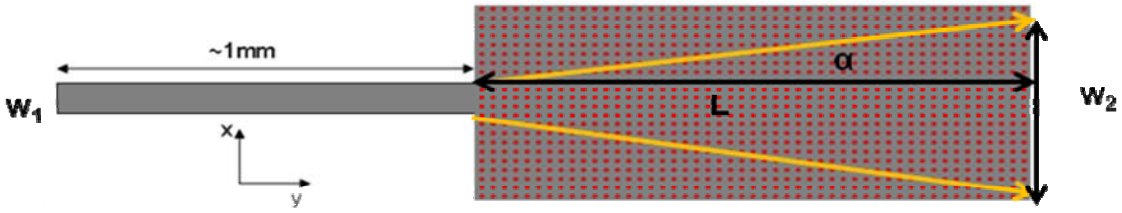

Figure 3.41 Schematic top view of design 2D structure.

3.4.2 Measurement results and analysis

We initiated actual measurements of transmittance and polarization rotation on these two -dimensional photonic crystals. The multi-stopbands and Faraday rotation responses are observed in the magneto-photonic crystals.

In order to make sure the response is coming from the MPC structures instead of slab waveguide itself a null test was performed. Fig. 3.42 shows the transmittance (black) and polarization rotation (gray) for light passing through a 6 um waveguide without the two-dimensional photonic crystal at the end. In other words, this is a null test. It shows no stopbands and no special polarization rotation features, except for fringes.

The polarization rotation is defined as the position of the semi-major axis of the polarization ellipse at the output. The rotation is magneto-optically active in the sense that it reverses sign when the magnetic field is reversed (all these data are taken with a magnetic field in the direction of propagation or opposite to it). The reversal is not always perfectly symmetrical: The data in the presence of the photonic crystals below give the rotation for both magnetization directions. The input polarization is linear and oriented at zero degrees to the horizontal (TE).

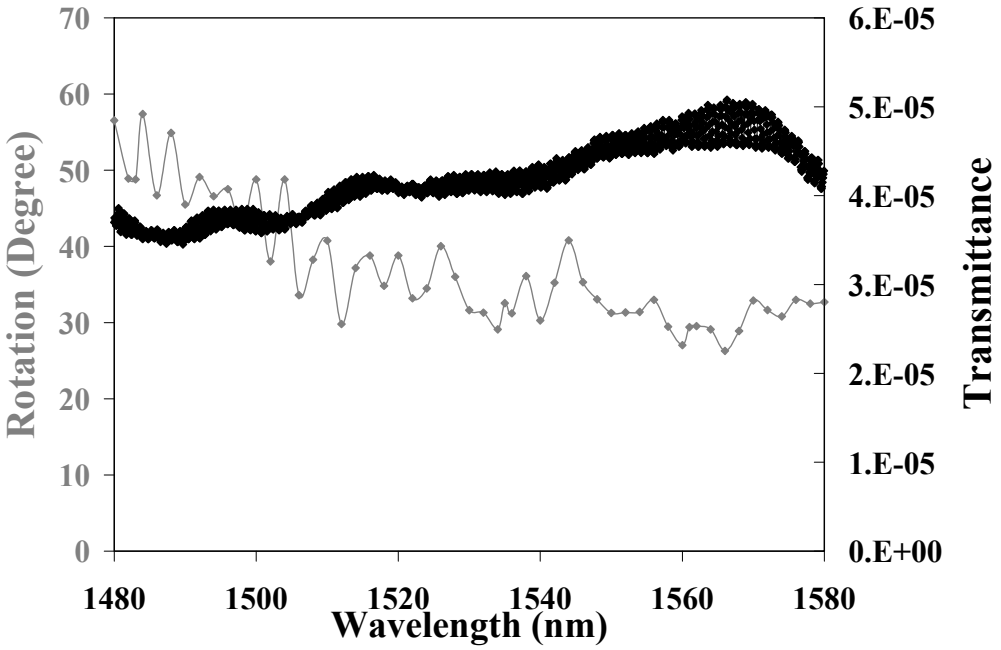

Figure 3.42 Transmittance spectrum and Polarization rotation response for pure waveguide. The gray line is for Polarization rotation and the black curve is transmittance spectrum.

Tests on two-dimensional magneto-photonic crystals were carried out on three photonic crystal structures with slightly different dimensions. Multi-stopbands are present on all these samples.

Similarly to the analysis done for one-dimensional photonic crystals, the patterning on the slab slightly modifies the effective index and character of the allowed waveguide modes. Focused-ion-beam milling of the holes on the waveguide reduces the average thickness of the optical channel and further modifies the mode indices. The mode index is the average quantity depending on the hole-depth and film thickness for the patterned region. Approximately the average thickness the photonic crystal area is used to calculate the effective indices for the region. The average thickness is the film thickness as modified by the FIB milling. By the same correlation method, the slab waveguide height is modified to match the average film thickness for the grating area in order to approximate the effective mode indices for the grating region.

Effective thickness and effective indices for the TE modes in the photonic crystal region are determined by numerical simulation in conjunction with Bragg-reflection data analysis. Mode indices are computed by beam-propagation analysis of a simulated slab waveguide having the effective film thickness and material index as the fabricated structure.

Considering the hole depth, the average effective thickness is allowed to range within the experimentally determined uncertainty in measured thickness. Since the hole-depth could be vary from 300 nm to 1000nm. The effective thickness of the film on the photonic crystal region can be varied from 2.27 μm to 2.52 μm. Minor adjustments in the thickness values are allowed to fit the experimentally measured stop band.

3.4.2.1 Test and analysis on one 2D MPC

Fig. 3.43 shows normalized transmittance spectra on a two-dimensional photonic crystal. The light is launched from an 8μm wide ridge waveguide. The size of the square air hole is 250 nm X 250nm. Normalization is to the output of a waveguide without photonic crystals.

Mode indices and band structure are calculated using beam-propagation simulation to find the effective indices for a slab waveguide with the same material index and an effective slab height equal to the average thickness in the presence of the photonic crystals. In these calculations the average thickness is allowed to range within the experimentally determined uncertainty in measured thickness. For a better agreement between experimental and simulated data, cross-comparison with the transverse-magnetization stop band spectrum shown in Fig. 3.43 is used to determine the average thickness of photonic crystal region and the real period of the structure. The effective film thickness is chosen to be 2.27 um which is within the effective thickness variation.

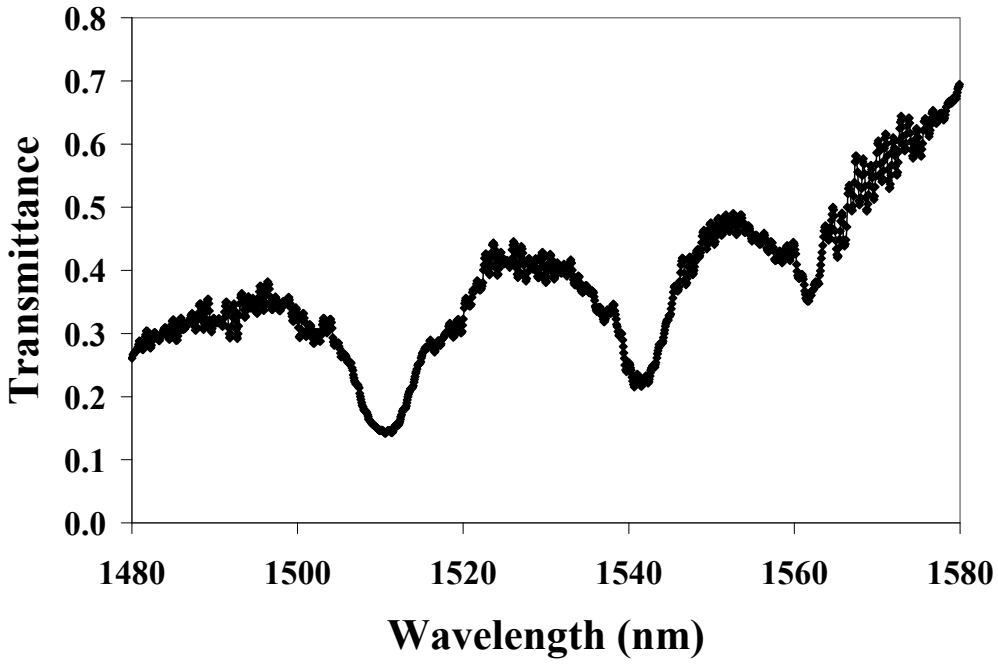

Figure 3.43 Normalized transmittance spectra for the first sample.

The mode effective indices for each wavelength are calculated. The selected values for the mode indices for TE and different wavelength are listed in Table 3.11. The band structures for TE bands from simulation are shown in Fig. 3.44. Cross-over points between these bands show that waveguide modes of different order become degenerate at specific wavelengths and can couple. This coupling satisfies the phase matching condition and leads to band gap formation. The period for photonic crystal in the propagation direction is 340.92 nm.

Table 3.11
Calculated TE mode indices for different wavelength

WL (nm)	TE_0	TE_1	TE_2	TE_3
1480	2.291818	2.237394	2.145284	2.015257
1490	2.2916	2.236521	2.143301	2.01213
1500	2.291381	2.235644	2.14131	2.008651
1505	2.291271	2.235205	2.140307	2.006636
1510	2.291161	2.234764	2.139309	2.005272
1520	2.290941	2.23388	2.137304	2.001815
1530	2.290719	2.232992	2.135273	1.998542
1535	2.290607	2.232547	2.13426	1.996361
1540	2.290496	2.2321	2.133243	1.994789
1545	2.290384	2.231654	2.13223	1.993521
1550	2.290272	2.231205	2.131206	1.991521
1555	2.29016	2.230756	2.130188	1.989846
1560	2.290047	2.230306	2.129166	1.988149
1565	2.289935	2.229855	2.128141	1.986267

Both Fig. 3.43 and Fig. 3.44 display three discernible stopbands. The center wavelengths of the first three stop bands clearly show within 1480nm to 1540 nm range. They are listed in Table 3.12.

Table 3.12
The center positions of stopbands for experimental and calculated data.

TE	Fundamental λ_0 (nm)	First-order λ_1 (nm)	Second-order λ_2 (nm)
Experimental	1561.61	1542.06	1510.61
Calculation	1561.5	1542.3	1510.2
Difference	0.11	0.24	0.41

Very good agreement with the experimentally measured spectra is obtained. The accuracy of the calculated cross-over as compared to the measured mid-band wavelengths equals $\pm\frac{1}{10}$ of the experimental bandwidth 5.53nm. This experimental bandwidth scale is taken to be the width of the stop band centered at 1510.61 nm. For better comparison, the transmittance and rotation are plotted together in Fig. 3.45. The gray is transmittance spectrum. Pink and red lines are polarization rotation tested applying a magnetic field in opposite directions.

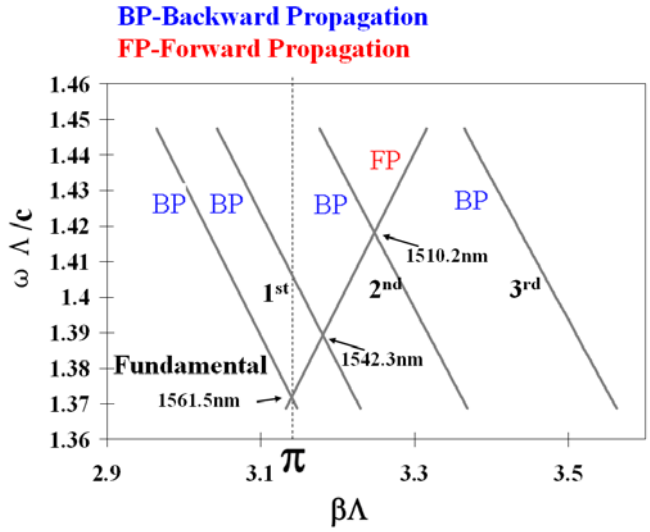

Figure 3.44 Band structure of the magneto-photonic crystal for transverse magnetization. The intersection points of bands are the mid-bandbap positions.

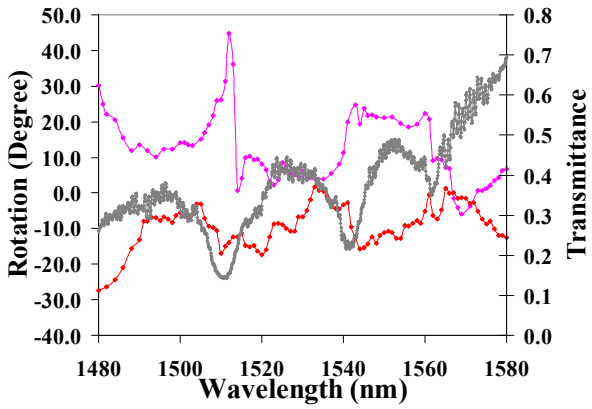

Figure 3.45 Transmittance spectra and Polarization rotation with different magnetic field directions.

3.4.2.2 Test and analysis on more 2D MPCs

Two dimensional photonic crystals of different sizes were fabricated in order to study how the size of the air hole affects width of the stopbands. The sample has the side length of the square air holes 280nm and the width of guiding ridge waveguide is 10μm. Fig. 3.46 shows the normalized transmittance spectra on this two-dimensional photonic crystals. For better comparison, the rotation spectra are plotted together in this figure. The gray is transmittance spectrum. Pink and red lines are polarization rotation tested applying magnetic field in opposite directions. The band width of this structure is slightly larger than that of the last sample. The largest rotation at the peak is around 20 degrees bigger than those outside stopband.

From the cross-comparison analysis, the effective thickness of photonic crystal region is the same as the first sample 2.27 μm. The band structures for TE bands from simulation are shown in Fig. 3.47. Cross-over points between these bands show that forward and backward waveguide modes coupling satisfy the phase matching condition and lead to band gap formation. The period for photonic crystal in the propagation direction is 340.23 nm.

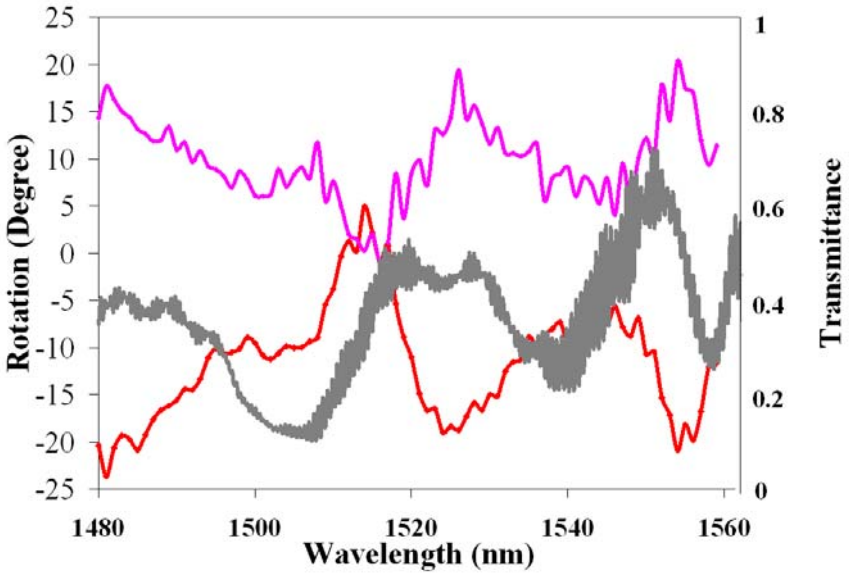

Figure 3.46 Transmittance spectra and Faraday rotation with different magnetic field directions.

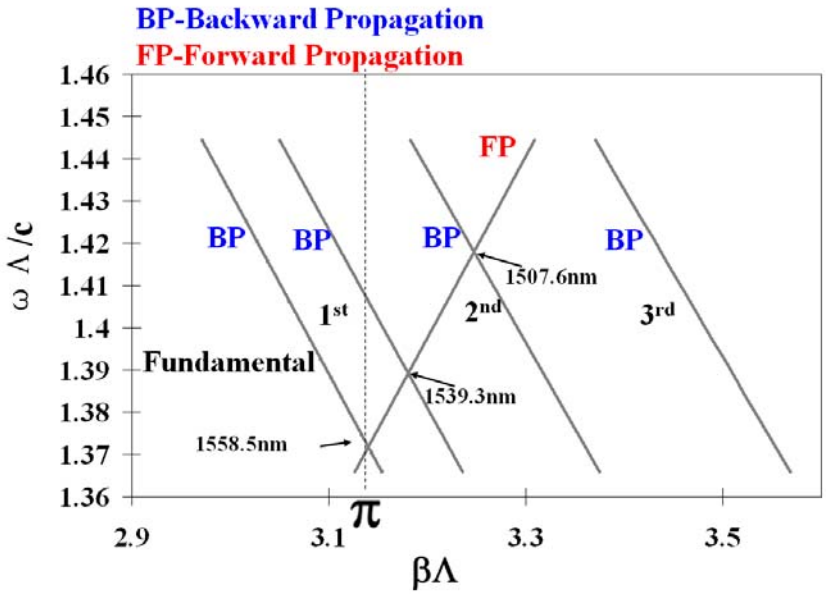

Figure 3.47 Band structure of the magneto-photonic crystal for transverse magnetization. The intersection points of bands are the mid-bandbap positions.

Both Fig. 3.46 and Fig. 3.47 display three discernible stopbands. The center wavelength positions of the first three stop bands clearly show within 1480nm to 1540 nm range. They are listed in Table 3.13.

Table 3.13
The center positions of stopbands for experimental and calculated data

TE	Fundamental λ_0 (nm)	First-order λ_1 (nm)	Second-order λ_2 (nm)
Experimental	1558.78	1539.73	1507.23
Calculation	1558.5	1539.3	1507.6
Difference	0.28	0.43	0.37

Very good agreement with the experimentally measured spectra is again obtained. The accuracy of the calculated cross-over as compared to the measured mid-band wavelengths equals $\pm\frac{1}{20}$ of the experimental bandwidth 12.06nm. This experimental bandwidth scale is taken to be the width of the stop band centered at 1507.23 nm.

Another two dimensional photonic crystal was fabricated using a lower line dose as compared to the previous two samples. The side length for the square air hole is 250nm. The ridge waveguide to launch light is 7μm wide. Fig. 3.48 shows normalized transmittance spectra on this two dimensional photonic crystals together with rotation spectra. The gray is transmittance spectrum. Pink and red lines are polarization rotation tested applying magnetic field in opposite directions. The Faraday rotation appears almost symmetrically spectrum with different magnetic field directions and the largest at the peak is about 20 degrees bigger compared to that outside the stopband.

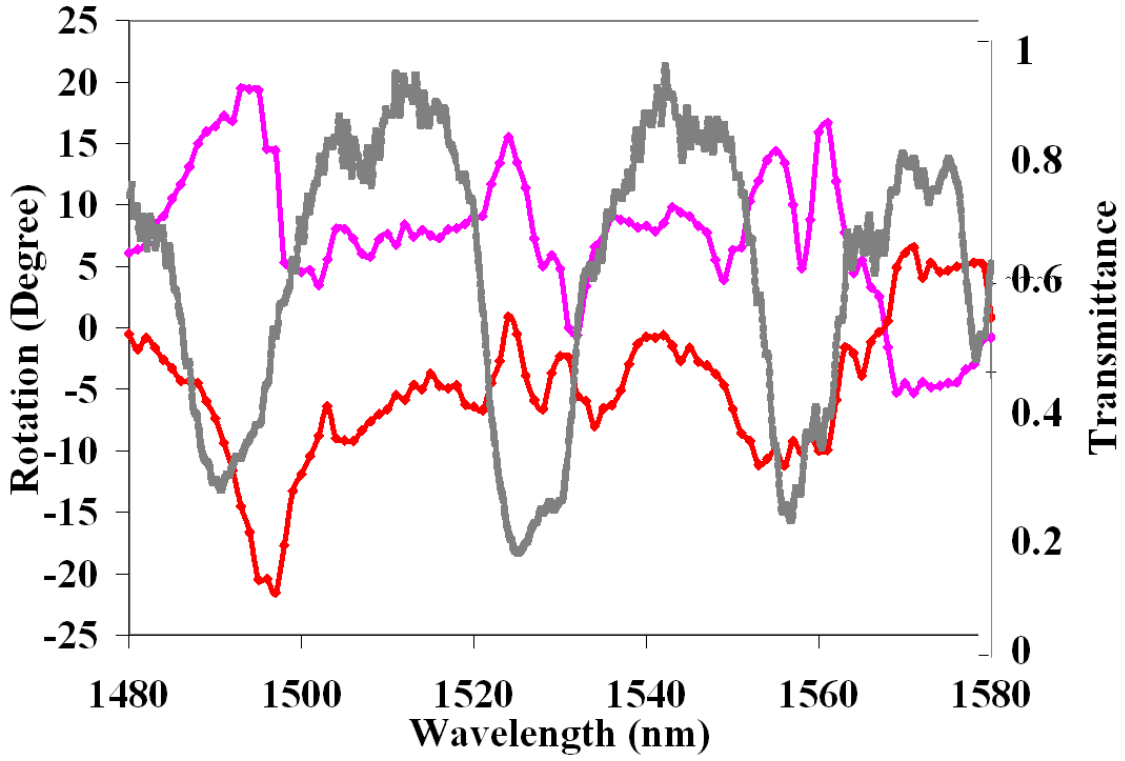

Figure 3.48 Transmittance spectra and Faraday rotation with different magnetic field directions.

From the cross-comparison analysis, the effective thickness of photonic crystal region is the same as the first sample 2.50 μm. This is reasonable. Because with less line dose, the thickness reduced by overlapped milling and the hole depth are less than those with larger line dose, the overall effective thickness should be larger. The mode effective indices for

each wavelength are calculated. The selected values for the mode indices for TE and different wavelength are listed in Table 3.14.

Table 3.14
Calculated TE mode indices for different wavelength

WL (nm)	TE_0	TE_1	TE_2	TE_3
1485	2.294558	2.248457	2.170489	2.059633
1490	2.294465	2.248084	2.169642	2.058098
1495	2.294372	2.247711	2.168794	2.056695
1505	2.294185	2.246962	2.167091	2.053534
1520	2.293902	2.245832	2.16452	2.048996
1525	2.293807	2.245454	2.16366	2.04745
1530	2.293713	2.245075	2.162796	2.046029
1535	2.293618	2.244695	2.161929	2.044379
1545	2.293427	2.243934	2.16019	2.041384
1555	2.293235	2.243169	2.158444	2.038042
1560	2.293139	2.242785	2.157571	2.036747
1570	2.292947	2.242015	2.155817	2.033682
1575	2.29285	2.241629	2.154939	2.032002
1580	2.292753	2.241242	2.154058	2.030506

The band structures for TE bands from simulation are shown in Fig. 3.49. The period for photonic crystal in the propagation direction is 343.7 nm.

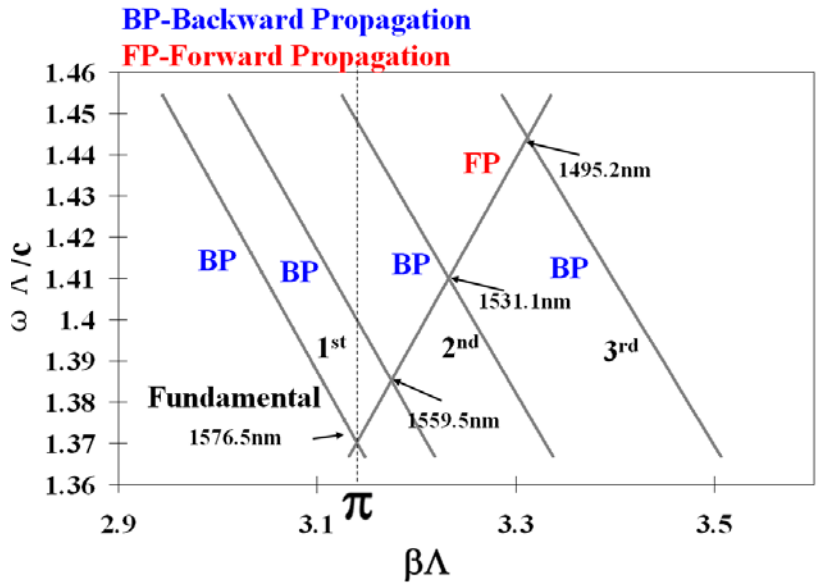

Figure 3.49 Band structure of the magneto-photonic crystal for transverse magnetization. The intersection points of bands are the mid-bandbap positions.

Both Fig. 3.48 and Fig. 3.49 display four discernible stopbands. The center wavelength positions of the first three stop bands clearly show within 1480nm to 1540 nm range. They are listed in Table 3.15.

Table 3.15
The center positions of stopbands for experimental and calculated data.

TE	Fundamental λ_0 (nm)	First-order λ_1 (nm)	Second-order λ_2 (nm)	Third-order λ_3 (nm)
Experimental	1577.13	1559.06	1528.73	1494.2
Calculation	1576.5	1559.5	1531.1	1495.2
Difference	0.63	0.44	2.37	1

Again very good agreement with the experimentally measured spectra is obtained. The accuracy of the calculated cross-over as compared to the measured mid-band wavelengths equals $\pm\frac{1}{6}$ of the experimental bandwidth 13 nm. This experimental bandwidth scale is taken to be the width of the stop band centered at 1494.2 nm.

3.4.3 Conclusions and possible improvement in fabrication and future work

Two dimensional MPC structures in the substituted iron garnet waveguide have been successfully fabricated through FIB milling technology. The optical measurements including optical transmission and Faraday rotation response have been tested. Obvious multi-stopbands and enhancement of Faraday rotation effect are observed experimentally. The observation of multi-stopband in different sample makes sure photonic crystals play the role of modifying the propagation of light in the slab waveguide. The origin of the multi-stopbands is the couplings between forward and backward waveguide modes. The Bragg condition is used to analysis the stopband positions. Very good agreement for the stopband positions between experimental and simulation is obtained.

Experimentally, the method of launching the light into the hole-array pattern can be improved. For the work I have done so far, 7μm to 10μm wide ridge waveguides are used to launch the beam onto a two-dimensional hole-array patterned on BiLuIG slab waveguides. There exist diffraction effects after the light leaves the ridge waveguide and strikes the photonic crystals. Considering the diffraction into the theoretical analysis, presents additional complications. If a planar collimated beam is launched, the analysis can be simplified. In order to launch a planar collimated beam in the slab and measure transmittance and polarization response, an adiabatic taper can be patterned by photolithography on the slab to collimate the beam. The beam can be collimated by adiabatically tapering out a waveguide to avoid lateral multi-modes. Design of an adiabatic taper has been done by taper simulation which is available in commercial optical simulation software. Fig. 3.50 shows how light propagates in such a taper. Fig. 3.51 shows the light intensity of light propagation through taper structure and keep collimated after coupling into space.

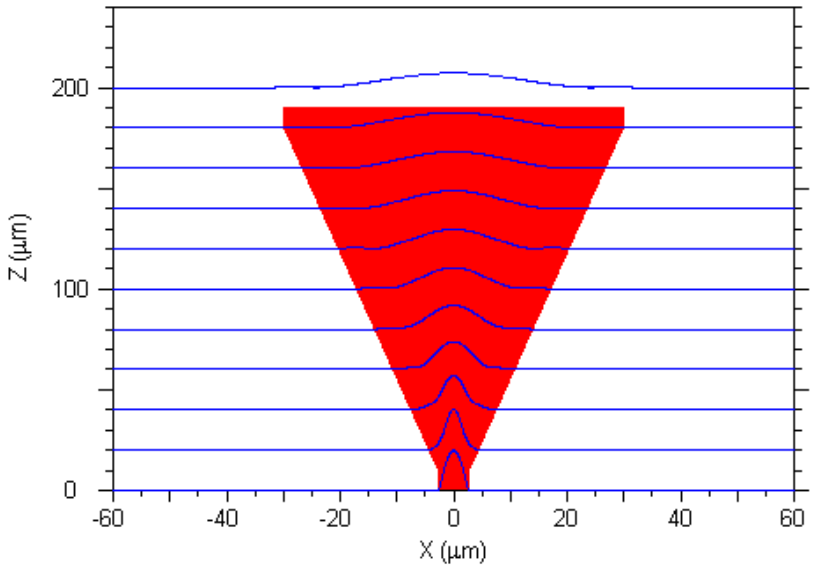

Figure 3.50 Light propagation in the taper simulated in Rsoft.

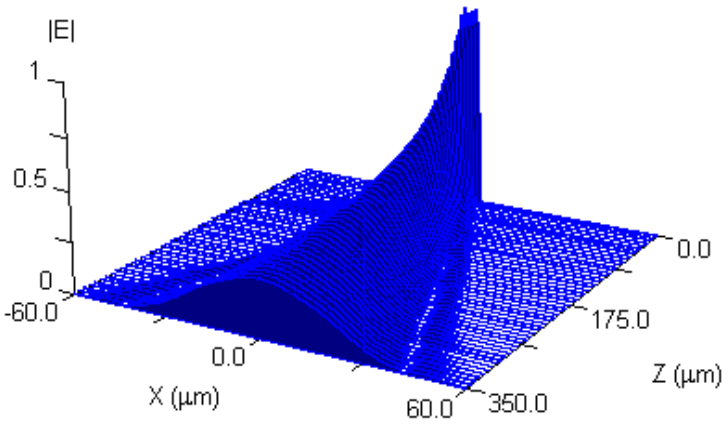

Figure 3.51 The light intensity of light propagation through taper.

Based on simulation results, there are several taper structures which can launch a planar collimated beam in the slab waveguide. Fig. 3.52 and Table 3.16 display the designs.

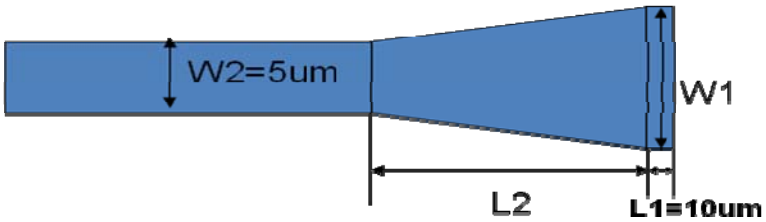

Figure 3.52 Schematic of taper structure

Table 3.16 Parameters of Taper dimensions

W_1(μm)	40	40	40	50	50	50	50	60	60	60	60
L_2(μm)	190	210	240	190	210	230	250	190	200	230	240

A mask with all these taper structures has been designed and prepared by this project. In future experimental work, adiabatically taper can be fabricated on a planar magnetic thin film first. This step can reduce the uncertainty introduced by the diffraction of light after ridge waveguide into slab waveguide with photonic crystals.

Theoretically, both the transmittance, ellipticity and polarization rotation (a mixture effect of Faraday rotation and birefringence) spectra have been carefully studied and

examined for one dimensional magneto-photonic grating structure. The MPC structure highly increases the polarization rotation within stopbands in spite of a reduction in polarization linearity and spectra distortion (with appearance of doublets or offsets) due to the presence of linear birefringence.

Some initial work such as optical transmission and Faraday rotation response has been tested on two dimensional magneto-photonic crystals. Obvious multi-stopbands and enhancement of Faraday rotation effect are observed experimentally. In order to study the properties two-dimensional magneto-photonic crystals, there are more features needed to be analyzed such as the tunability of the bands; the dimensionality of the polarization response; the bandwidth of the polarization rotation, transmittance in the bandgaps, photonic crystals with central magnetic optical defect and how different design affects these properties.

CHAPTER 4

PLANAR GRADIENT PHOTONIC METAMATERIALS

Metamaterials operating at optical frequencies, referred as optical metamaterials or photonic metamaterials, require the feature fabricated at subwavelength scale from 50 nm to 1000nm. Planar gradient index metamaterials are designed and demonstrated in the optical frequencies by numerical simulation through finite-difference time domain method in conjunction with electromagnetic retrieval technique. We confirm the gradient by simulating the deflection of a light beam by multilayer silver (Ag) and magnesium fluoride (MgF_2) slab featured with specially designed nano rectangular holes. The planar gradient index optical metamaterial we propose can be fabricated by available nano-fabrication technologies. Optical tests can be performed since the designs are also based on the consideration of frequency range available for evaluation.

In this section, we discuss how we combine gradient concept with the fishnet structure for the purpose of extending gradient index metamaterials into optical frequencies. We design the fishnet unit cell with optimum refractive index range by tuning the unit cell dimension. A commercial software package CST MICROWAVE STUDIO (CST), the specialized tool for the fast, accurate simulation of high-frequency problems, is mainly used to calculate transmission and reflection coefficients, known as S-parameters. A standard material parameter retrieval algorithm is developed to determine effective refractive index from transmission and reflection coefficients [161, 162]. Refractive indices as a function of unit cell geometry are used to the map index profile to the variation of unit cells. The electric field mapping simulation shows the beam forming mechanism. The light beam deflection from planar gradient metamaterial consisting of a multilayer Ag-MgF_2-Ag sandwich slab featured with specially designed and arranged fishnet unit cells is demonstrated. Unlike most of previous metamaterial gradient index

designs, first, this is designed to operate in positive index regime away from resonance to minimize losses; second, all of the patterned elements are planar which does not require volumetric unit cell; third, it is for optical frequencies.

4.1 Simulation techniques

A variety of theoretical and numerical methods have been employed to study the propagation of electromagnetic waves in LH materials. These numerical modeling tools are utilized to calculate the transmission properties of finite LH slabs and help gain better understanding of the engineered material behavior in the optical wavelengths. A background in suitable numerical methods is helpful.

4.1.1 General Considerations for Numerical Modeling

For electromagnetic simulations, finite-element methods and finite-difference methods are attractive, particularly when metals are incorporated. Finite Element Method cuts a structure into several elements (pieces of the structure, and then reconnects elements at "nodes" as if nodes were pins or drops of glue that hold elements together. It uses the concept of piecewise polynomial interpolation. By connecting elements together, the field quantity becomes interpolated over the entire structure in piecewise fashion. . In the finite-element method, a distributed physical system is often divided into a large number of discrete elements. The complete system may be complex and irregularly shaped, but the individual elements are easy to analyze. This process results in a set of simultaneous algebraic equations. [163]

For 2D simulations, the finite-difference frequency-domain (FDFD) method is accurate, simple to implement, and excellent for modeling complex structures of finite size [164]. The transfer matrix method [165] is popular for 2D and 3D structures, especially when they contain metals.

The main power of this method is its ability to calculate the stationary scattering properties such as the complex transmission and reflection amplitudes of finite slabs of LH materials. However, this method requires the discretization of the unit cell which introduces some numerical artifacts and some constraints into the shape and size of the components inside the unit cell.

Finite-difference time-domain (FDTD) [166, 167] is a very powerful tool for modeling finite sized devices, large scale structures, and characterizing devices over very broad frequency range. It is excellent for the study of transmission through finite slabs since it can model almost arbitrary materials combinations and microstructure configuration. It has been used in many systems containing dielectric or metallic components.

4.1.2 Scattering Parameters

S-parameters or scattering are measured by sending a *single* frequency signal into the network or “black box” and detecting what waves exit from each port. The term 'scattering' is more common to optical engineering than RF engineering, referring to the effect observed when a plane electromagnetic wave is incident on an obstruction or passes across dissimilar dielectric media. S-parameters change with the measurement frequency so this must be included for any S-parameter measurements stated, in addition to the characteristic impedance or system impedance. [168] S-parameters are complex. They have magnitude and angle because both the magnitude and phase of the input signal are changed by the network, frequency, load impedance and source impedance.

Two ports S parameters are defined by considering a set of incident wave propagating through a system. They are defined and measured with the ports terminated in characteristic reference impedance. A portion of wave is transmitted through the system and a portion is reflected back toward to the source, shown in Fig. 4.1.For a wave incident on Port 1, some part of this signal reflects back out of that port and some portion

of the signal exits other ports. S_{11} refers to the signal reflected at Port 1 for the signal incident at Port 1.

S_{21} refers to the signal exiting at Port 2 for the signal incident at Port 1. S_{11} is the reflection coefficient and S_{21} describes the forward transmission coefficient responding port 1. Generally, the transmitted and the reflected wave have the same frequency as the incident wave. However, the amplitude and phase of the transmitted and reflected wave are changed compared with the incident wave.

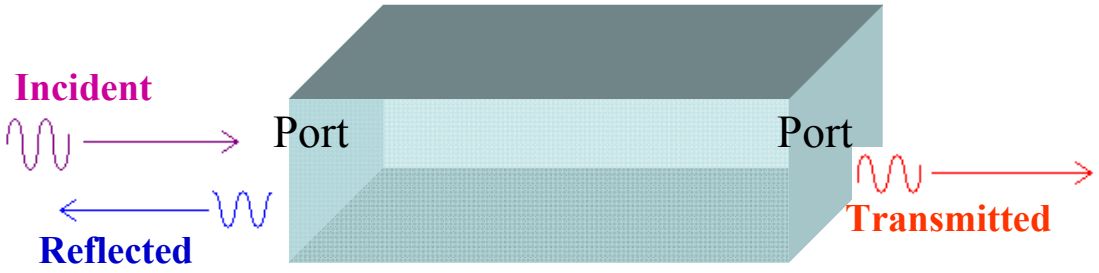

Figure 4.1 The mechanism of S parameter.

4.1.3 Preliminary simulations by Finite Element Method (HFSS, COMSOL)

HFSS™, a commercial finite element method solver for electromagnetic structures from Ansoft Corporation. The acronym originally stood for high frequency structural simulator. It is one of the most popular and powerful applications used for antenna design, and the design of complex RF electronic circuit elements including filters, transmission lines, and packaging.[169]

It is the industry-standard simulation tool for 3D full-wave electromagnetic field simulation. HFSS provides- and H-fields, currents, S-parameters and near and far radiated field results. Fig. 4.2 shows the design flowchart. [170] Since metamaterials are periodic structure, I only need to design and simulate unit cell structures. First, solution types are chosen based on the purpose of our design. Second, the geometry and material parameters are chosen. After boundary conditions are applied to the model and the source

ports are excited, we set up solutions and run simulations. By looking into the simulation results, we can adjust the set up to optimize the results and designs

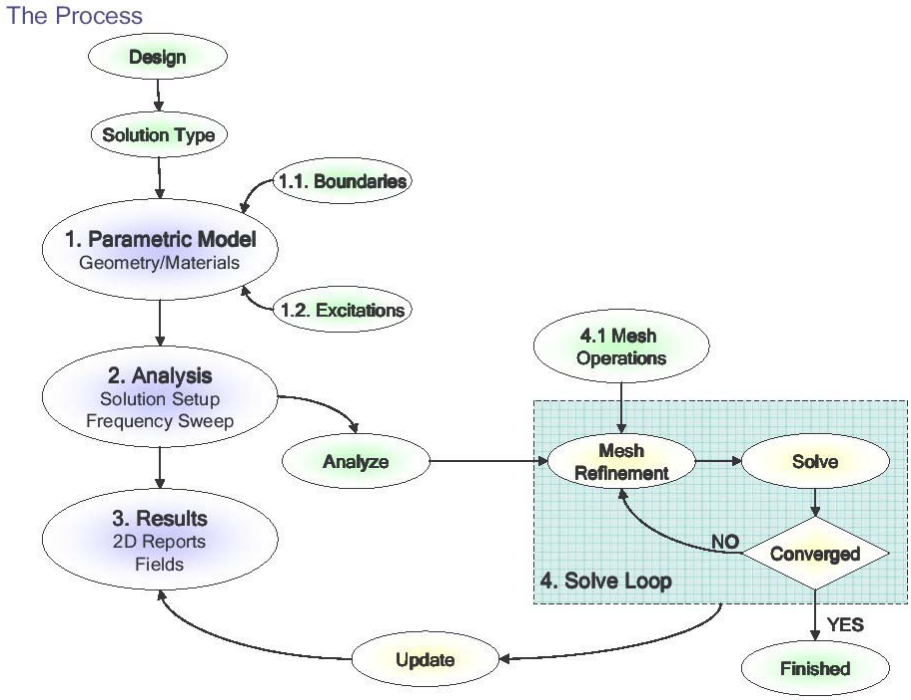

Figure 4.2 Design flow chart for HFSS simulation

Previously, in order to simulate periodic structures for millimeter wave and microwave, a combination of PEC (Perfect Electric Conductor or Perfect E) and PMC (Perfect Magnetic Conductor or Perfect H) boundary conditions is used to create a waveguide that will force the incident wave on the unit cell to be a plane wave. As shown in Fig. 4.3, it is the setup for transmission simulation with unit cell of the periodic structures. The front and back of the waveguide are set to be perfect magnetic conduct boundaries; the left and right sides are set to be perfect electric conductor boundary conditions; the top and bottom are set to be wave ports. By using PEC and PMC boundaries in this manner, the unit cell is effectively "mirrored" to create an infinite array due to the mirroring effect of perfect conductors. Once the boundary conditions are setup the model can be excited by using waveports. This method works well for millimeter and microwave frequencies.

However, when the structure scales down the structure in to nano size structure which works in optical frequencies, the software gives meshing errors and aborts simulations.

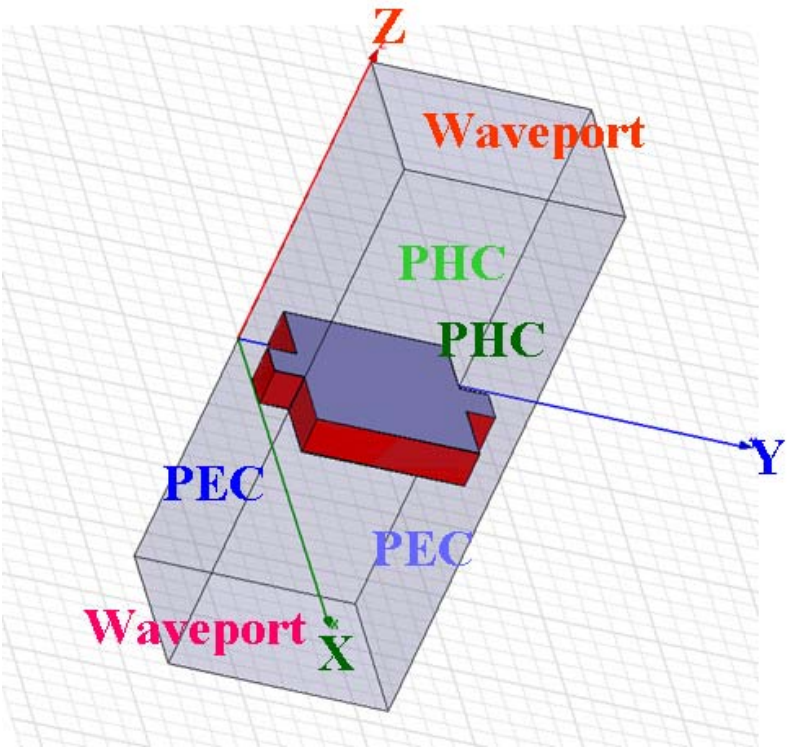

Figure 4.3 The set up for Waveport method with perfect E and H boundary condition

To overcome this issue, a Floquet port in HFSS is exclusively used with planar periodic structure and is also suitable for nano-scale simulations. Floquet modes are plane waves with propagation direction set by the frequency, phasing and geometry of the periodic structure. The analysis of the infinite structure is accomplished by analyzing a unit cell. Unit cells for frequency selective surface (FSS) simulations may be constructed using Master/Slave boundaries and two Floquet ports, with one port above the plane of the structure and one port below as shown in Fig. 4.4. The reflection and transmission coefficient known as S-parameters are direct results. Both magnitude and phase of the transmission and reflection coefficients are obtained. References [171, 172] give detail steps and examples about how to use Floquet mode.

For the millimeter and micrometer dimension structures, both Waveport method and Floquet mode method can give accurate results. When it comes to nano size unit cell geometry, waveport is not functional. Here is an example of S-parameter calculation for a nano-size fishnet structure by Floquet port in HFSS. Fig. 4.5 is the fishnet unit cell geometry. The periods in the *x*- and *y*-directions are $a_x = a_y = 860$nm, the cut-wire pair length is Wx = 565nm and the wire width is Wy = 265nm. The structure consists of alternating layers of 30nm silver and 50nm alumina. Fig. 4.6 is the transmission and reflection coefficients calculated for this structure. The inset is the unit cell dimension.

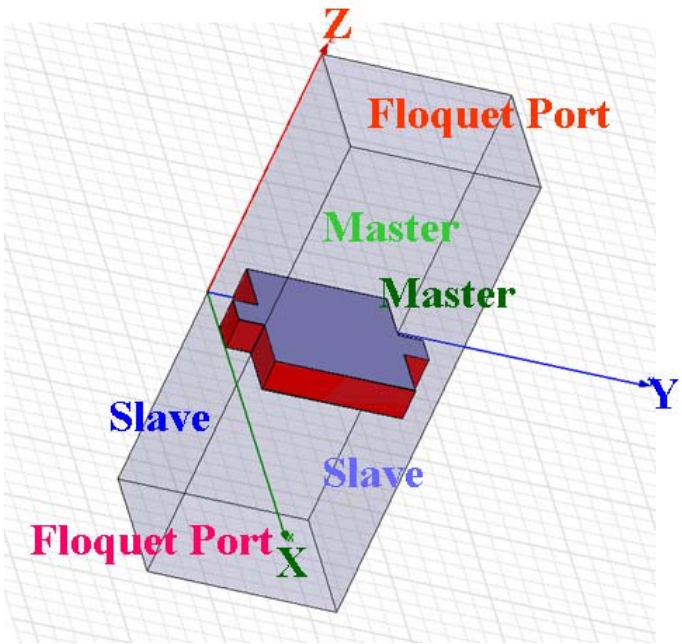

Figure 4.4 The set up for Floquet simulation method

Even though HFSS has optical application note, it has some limitations. First, fast frequency sweep is not supported in this application note. Interpolating sweep is mostly used for frequency information. Second, for optical frequency, the electromagnetic properties for metal are no longer the same as bulk metal. We need to set the suitable permittivity and permeability for metal. There is no in-built optical material model such as Drude-model in HFSS. We are able to find mathematic equations for different material

model, but it takes extra efforts to do this while these models are already available in simulation software like CST.

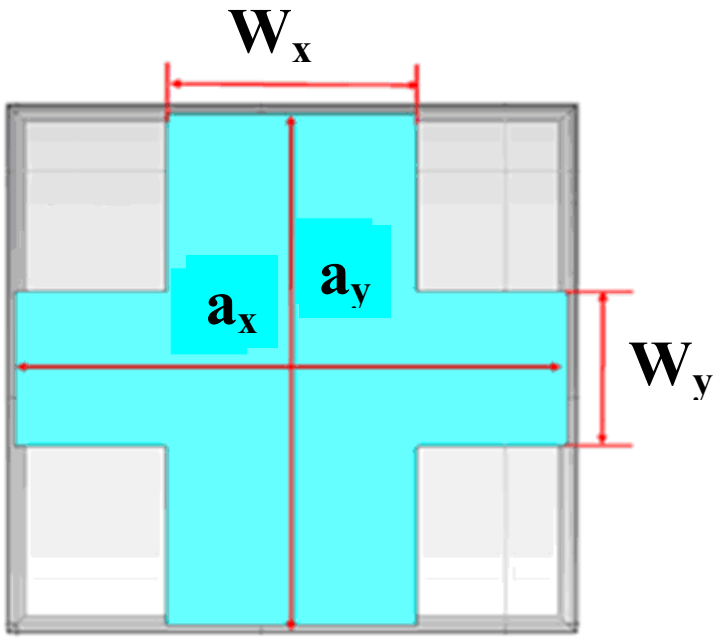

Figure 4.5 Fishnet unit cell dimension description. a_x and a_y are the period in x and y direction. Wx and Wy are the cure wire length and width.

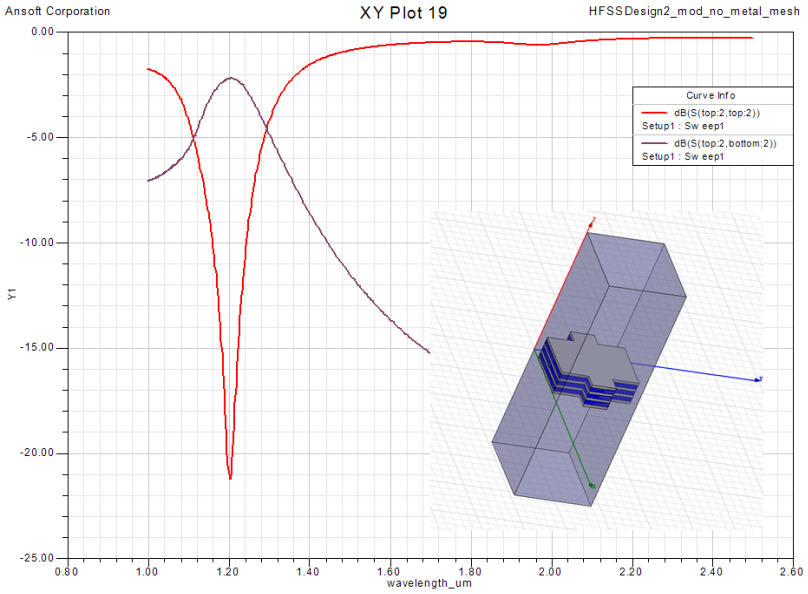

Figure 4.6 S-parameters simulated by Floquet port in HFSS.

Modeling periodic nanostructures with COMSOL multiphysics is widely applied, as one can see from the large number of COMSOL-based papers [173] COMSOL is used to calculate reflection, transmission and absorption spectra of periodic perforated nano-film in 3D using S-parameters. We can set up a simulation with periodic "Floquet" boundary conditions to calculate normalized reflectance, transmittance and absorbance for periodic structure. Electromagnetic wave application mode in RF module is used. S-parameters can be obtained by following the instructions. But overall, more complicated steps are involved in order to get the unit cell geometry, set boundaries and ports, plot the results and all other settings and it is not as convenient to use as HFSS and CST.

4.1.4 Electromagnetic simulation by Finite Different Time Domain (CST)

CST MICROWAVE STUDIO, the specialized tool for the fast, accurate simulation of high-frequency problems. CST MWS It enables the fast and accurate analysis of high frequency (HF) devices such as antennas, filters, couplers, planar and multi-layer structures and SI and EMC effects. It quickly gives you an insight into the EM behavior of your high frequency designs. It is exceptionally user friendly and has very flexible way to create the shape in the CAD design interface. Many different options exist to create the desired models. CST currently offers different kinds of solver modules.[174] Frequency Domain solver and Transient Solver are mainly used for planar metamaterial unit cell design and full gradient structure design, respectively.

Frequency domain solver delivers electromagnetic near and farfields as well as S-Parameters, the main task for the frequency domain solver module on my research is to calculate S-parameters. It features a special periodic boundary implementation, which automatically creates the boundaries for arbitrarily shaped unit cells. The ports are equipped with Floquet-mode solvers for highly accurate and fast simulation, and the easy analysis of polarization and mode type. [175]

Once unit cell geometry is created in the CAD window, unit cell boundary conditions are set to combine with open boundary conditions in the z-direction; the open boundaries will be automatically realized by a Floquet port that allows excitation of a plane wave. The list of ports and modes to excite then contains the Floquet ports "Zmin" and "Zmax" as well as the names of the Floquet modes, such as "TE (0, 0)" and "TM (0, 0)" for the plane waves. Frequency range is set up for the frequency sweep. The list of frequency samples allows you to easily define the number, interval, and sampling method of frequency domain solver simulation points by entering values in the corresponding columns. Frequency domain calculation starts and the 1-D and 2 or 3 D plot results can be found from the navigation tree.

In order to study the same structure with different parameter sets, a higher level parameter study or optimization can be performed by using parameter sweep component in CST. All the S-parameter with different unit cell dimensions. All these S-parameter data: magnitude and phase with different unit cell dimensions are calculated and saved for retrieval effective index.

The Transient Solver of CST MWS is a general purpose 3D EM simulator. Real time domain simulation is particularly interesting to study the field propagating through a component. It transient Solver is a very flexible time domain simulation. Electromagnetic field distributions at various frequencies for the full gradient structure and nano-prism structure shown in Fig. 4.7 are monitored by transient solver. It stimulates the structure at a previously defined port using a broadband signal.

Broadband stimulation enables to receive the S-parameters for entire desired frequency range and, optionally, the electromagnetic field patterns at various desired frequencies from only one calculation run. Additional information on the electromagnetic field distribution inside structure is obtained. Open boundary conditions are set on each side wall and the lower boundary in z direction is set as waveguide port which allows

excitation of a plane wave. The number of modes to excite can be defined such as "TE (0, 0)" and "TM (0, 0)" for the plane waves.

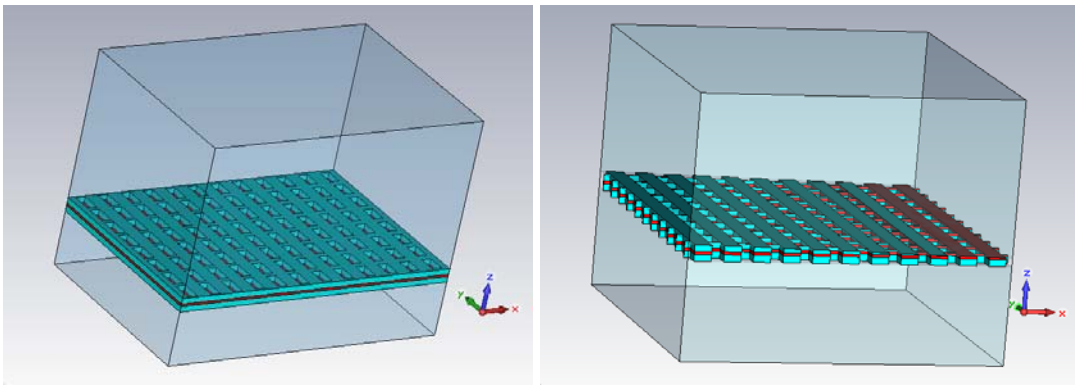

(a) **(b)**

Figure 4.7 Light beam deflection setups in the CST. (a) Simulation setup for planar gradient structure; (b) Simulation setup for nano-prism made from photonic metamaterials

After a calculation, you can observe electric field monitors by selecting them in the navigation tree and visualize the field mapping results.

4.2 Retrieving the constitutive effective parameters of metamaterials

The effective refractive index n and impedance z can be obtained by S parameters calculated from a wave incident normally on a slab of metamaterial. The slab of the metamaterials is characterized as an effective homogeneous slab. The permittivity ε and permeability μ are then directly calculated from $\mu = nz$ and $\varepsilon = n/z$. This retrieval process may fail under certain circumstances, for instance, when the thickness of the effective slab exhibits bulk properties and is not accurately estimated or when reflection S_{11} and transmission S_{21} data are very small in magnitude [161, 176,177].

An improved method to retrieve the effective constitutive parameters (permittivity and permeability) of a slab of metamaterial from the measurement of *S* parameters has ben proposed in ref. [162]

The effectiveness and robustness has been proved by applying to various metamaterials and successful retrieval results.

When a plane wave incident normally on a homogeneous slab, we can retrieve the permittivity and permeability from the reflection S_{11} and transmission S_{21} data. When a slab is thickness *d*, S_{11} is equal to the reflection coefficient and S_{21}, is related to the transmission coefficient *T can be expressed as* by $S21=Te^{ik0d}$, where *k*0 denotes the wave number of the incident wave in free space. The *S* parameters are related to refractive index *n* and impedance *z* by [178, 179]

$$S_{11} = \frac{R_{01}(1-e^{i2nk_0d})}{1-R_{01}^2 e^{i2nk_0d}} \tag{4.1}$$

$$S_{21} = \frac{(1-R_{01}^2)e^{i2nk_0d}}{1-R_{01}^2 e^{i2nk_0d}} \tag{4.2}$$

where $R_{01} = (z-1)/(z+1)$

Combining the relations $\mu = nz$ and $\varepsilon = n/z$, the refractive index *n* and the impedance *z* are calculated from inverting Eqs. (4.1) and (4.2):

$$z = \pm\sqrt{\frac{(1+S_{11})^2 - S_{21}^2}{(1-S_{11})^2 - S_{21}^2}} \tag{4.3}$$

$$e^{ink_0d} = X \pm i\sqrt{1-X^2} \tag{4.4}$$

where $X = 1/2S_{21}(1-S_{11}^2+S_{21}^2)$

The signs in Eqs. (4.3) and (4.4) are determined by the requirement:

$$\left|\mathrm{Re}(z)\right| \geq 0 \tag{4.5}$$

$$\left|\mathrm{Im}(n)\right| < 0 \tag{4.6}$$

The value of refractive index n can be determined from Eq. (4.4) as

$$n = \frac{1}{k_0 d}\{[\mathrm{Im}[In(e^{ink_0 d})] + 2m\pi] - i\,\mathrm{Re}[In(e^{ink_0 d})]\} \tag{4.7}$$

Here m is an integer related to the branch index of *Re(n)*. The imaginary part of n is uniquely determined, but the real part is complicated by the branches of the logarithm function.

The impedance of a homogeneous slab of material does not depend on its thickness. If the boundaries of the slab are well defined and the S parameters are accurately known, we can use Equations (4.3) and (4.4) to obtain the impendence and effective index directly. However, a metamaterial is not homogeneous; two issues need to be carefully addressed. First, the location of the two boundaries of the effective slab needs to be determined to ensure constant impedance for various slab thicknesses. Second, the numerically calculated and experimentally measured S parameters are noisy. This can cause the retrieval method to fail, especially at those frequencies where z and n are sensitive to small variations of S_{11} and S_{21}.

When a plane wave is incident on metamaterial, currents will be induced on the metals creating a scattered field. The field produced by the induced currents is not uniform. It is strongest around the metal and decay at a certain distance. The first effective boundary is located where the reflected wave behaves like a plane wave. It has to be determined in order to obtain accurate data for reflection S_{11} and transmission S_{21}.

When Re(*z)* and Im*(n)* are close to zero, a little perturbation of S_{11} and S_{21} from experimental measurements or numerical simulations, may change the sign of Re(*z)* and Im(n), making it unreliable to apply the requirement of Eqs. (4.5) and (4.6) as discussed in Ref. [16]. However, we can use the relation between z and n to determine the signs in

Eqs.(4.3) and (4.4). When $|\mathrm{Re}(z)| \geq \delta_z$, where δ_z is a positive number, we apply Eq. (4.5). In the other hand, when $|\mathrm{Re}(z)| < \delta_z$ the sign of z is determined so that the corresponding refractive index n has a non-negative imaginary part, where n is derived from Eqs. (1a) and (4.2):

$$e^{ink_0 d} = \frac{S_{21}}{1 - S_{11}\dfrac{z-1}{z+1}} \tag{4.8}$$

Based on the method mention above, we can calculate effective refractive index from the S parameters obtained from CST simulations.

4.3 Result and analysis

Two major achievements have been reached in this work. First, a pioneering achievement is correctly simulating the metamaterials on optical frequencies and obtaining the relations between the effective refractive index and dimension of unit cell structure. Second, a further and extensive study has been carried on the subject of achieving the electric beam deflection by planar gradient photonic metamaterial structure to achieve the electric beam deflection.

4.3.1 Theoretical background and simulations

Fig. 4.8 shows the fishnet structure with the polarization configuration. The incident light is polarized along one of the gratings. The fishnet metamaterial can be considered as composed of pairs of short slabs with continuous wires which are physically connected. A capacitance formed by a pair of finite width metal stripes parallel to the direction of magnetic field separated by a dielectric layer. The magnetic response originates from this antiparallel current metal pair which leads to the negative permeability. The array of thin metallic wires along the direction of electrical field is physically connected with the continuous metal stripes that provide the plasmonic electric response which results in the negative electric permittivity. This fishnet structure is shown to have negative refraction

for a particular polarization at optical frequencies. [161, 171-173] Silver is chosen as the metal layer because it is known to introduce low losses in optical frequencies. The optical material parameter refractive index of dielectric layer MgF_2 is taken as 1.38. The electromagnetic properties for metals in optical frequencies are no longer the same as bulk metals. The Drude model is sufficient to describe actual silver optical properties by setting the plasma frequency equal to 1.37×10^{16}/s and damping or collision frequency equal to 9×10^{13}/s at the frequencies of interest here. [174].

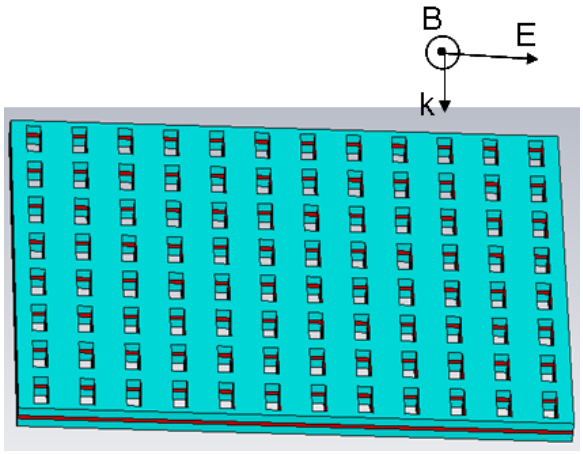

Figure 4.8 Scheme of the fishnet metamaterial and polarization configuration.

The transmission simulations with normal incident wave have been performed using the finite integration technique, employed through the commercial software CST. The reflection and transmission coefficients are direct results. In this paper, Frequency Domain solver and Transient Solver are used for the planar metamaterial unit cell design and the full gradient structure design, respectively.

Frequency domain solver is employed to calculate S-parameters. Once the unit cell geometry is created, unit cell boundary conditions are set to combine with open boundary conditions in the z-direction and periodic boundary conditions along the lateral directions. The open boundary will be automatically realized by a Floquet port that allows excitation of a plane wave. Transient Solver is used to map the electric beam deflection. Electromagnetic field distributions at various frequencies for the full gradient structure

are monitored. Broadband stimulation enables to receive the S-parameters for entire desired frequency range and the electromagnetic field patterns at various desired frequencies. The information on the electromagnetic field distribution inside structure is obtained. Fig. 4.9 (a) is S-parameter simulation setup. Plane waves are excited from Floquet ports 'Zmin' and 'Zmax' and the fishnet structure is realized by periodic boundary condition which allows to create infinite array of unit cell structure in x and y direction. (b) is the fishnet unit cell geometry with parameter indicated. The periodicity in the *x*- and *y*-directions is 'a', the grating length along the magnetic field direction is Wx and the grating length along the electric field direction is Wy.

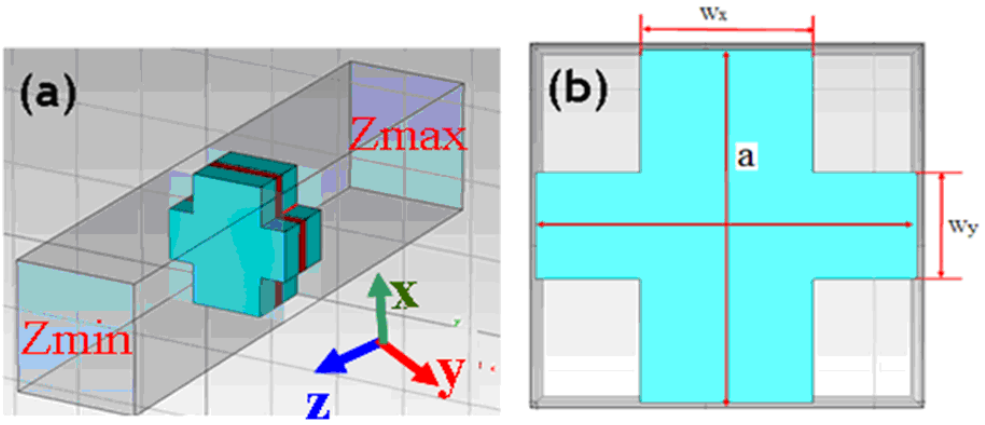

Figure 4.9 Unit cell simulation in CST. (a) The fishnet unit cell with simulation setup; (b) Top view of the unit cell with geometrical parameters indicated.

Fig. 4.10 shows the simulation setup for the transient solver. Open boundary conditions are set on each side wall and the lower boundary in z direction is set as waveguide port which allows excitation of a plane wave.

In order to design gradient structure, we vary the unit cell geometrical dimensions and simulate S-parameters corresponding to each design. All these S-parameter data: magnitude and phase are saved to be used for retrieval effective index. Refractive index versus geometry function is used to map index profile to variation of unit cell. The unit cell designs with optimum effective refractive indices range are chosen to be utilized for gradient metamaterial design.

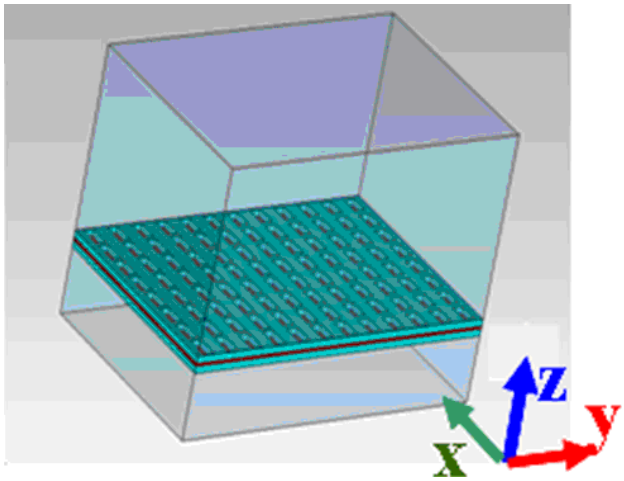

Figure 4.10 Transient solver simulation setup for the planar gradient metamaterial design.

Researchers have been working on retrieving their effective permittivity and permeability to better characterize metamaterials [161,175,176]. From *S* parameters calculated from a wave incident normally on a slab of metamaterials, the effective refractive index *n* and impedance *z* are first obtained [162, 177]. A robust method for extraction effective parameters: impedance and effective refractive index of a slab of metamaterials from transmission and reflection data is implemented. The real and imaginary parts of refractive indices are retrieved based on this algorithm [170].

We first investigate the fishnet structure with geometrical parameters indicated as: lattice constant a = 300 nm, Wx = 102 nm, Wy = 68 nm, t = 40 nm, s = 17 nm. Here, t is the thickness of Ag and s is the thickness of MgF_2. The simulations are executed in optical frequency from 350 THz to 430 THz. The periodic structure in the x-y plane is with the scales comparable to the wavelength. The dimension of the metamaterials in the z-direction is just the physical thickness of the three layers 97nm. Fig. 4.11 shows calculated S-parameters for a three layer fishnet structure and corresponding refractive indices retrieval results based on the geometry.

Parameter sweep is used to calculate the S-parameter with different unit cell dimensions. Fig. 4.12 shows the simulated transmission reflection spectra with different grating width along the direction of electric field Wy while all other parameters are the same as those used to calculate Fig. 4.11. The transmission decreases as Wy becomes larger due to metal polarizer effects. When Wy is small, the resonance is characterized by a dip in the transmission. With increasing of Wy, a peak in the transmittance can be formed. All these S-parameter data: magnitude and phase are going to be used for retrieval effective index. This gradient metamaterial is designed to operate in positive index regime away from resonance to minimize losses. The real part of refractive indices is what we concern.

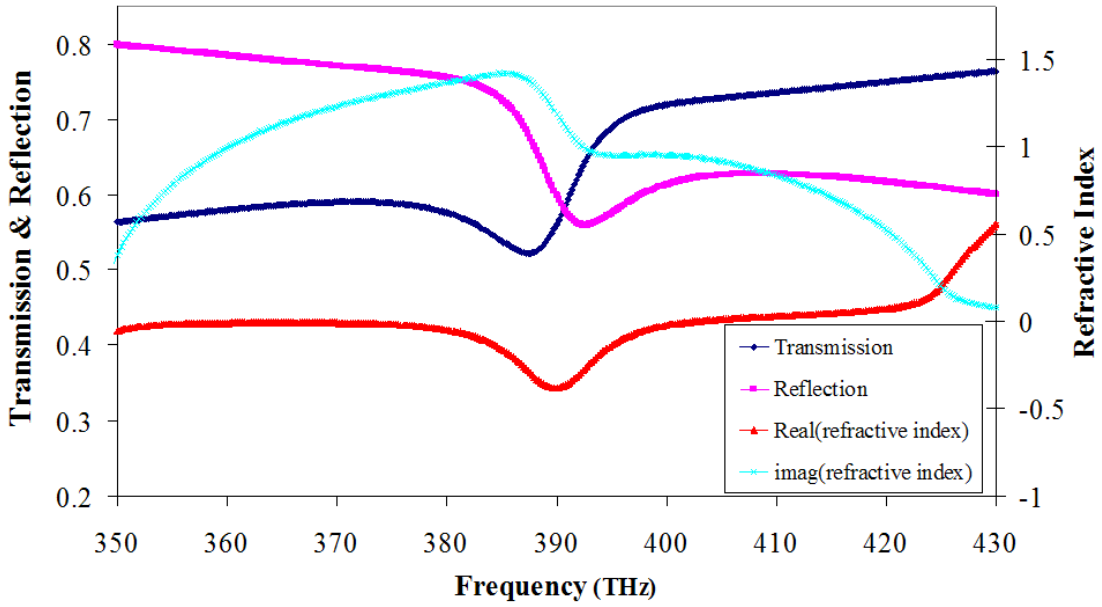

Figure 4.11 S-parameters calculated from CST and the corresponding real and imaginary parts of effective refractive indices.

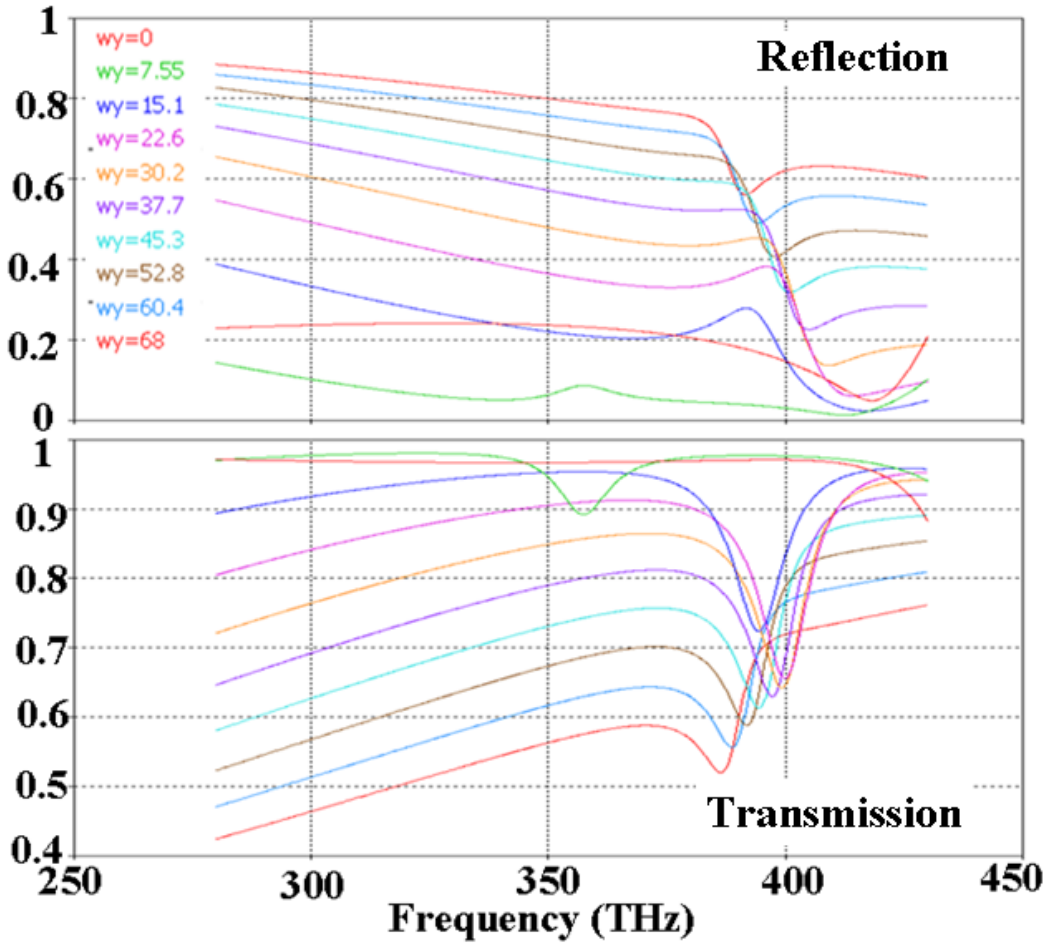

Figure 4.12 Transmission and reflection spectra with different Wy from 0 nm to 68 nm.

To retrieve the effective refractive index from the reflection and transmission coefficients, we obtain refractive index as a function of frequency. For a certain structure, the refractive index goes up and down dependent on wavelength, especially changes trend near the resonance. Fig. 4.13 demonstrates the refractive index as functions of frequency for different unit cell dimensions. The grating along the electric field direction Wy varies from 8nm to 38nm. The other parameters for simulation are the same as those used in Fig. 4.11. In order to make reliable gradient design, we need to operate the design within the frequency range which the refractive index has the same increasing or decreasing

tendency. We can tune and design the unit cell dimensions based on the desired operating frequency.

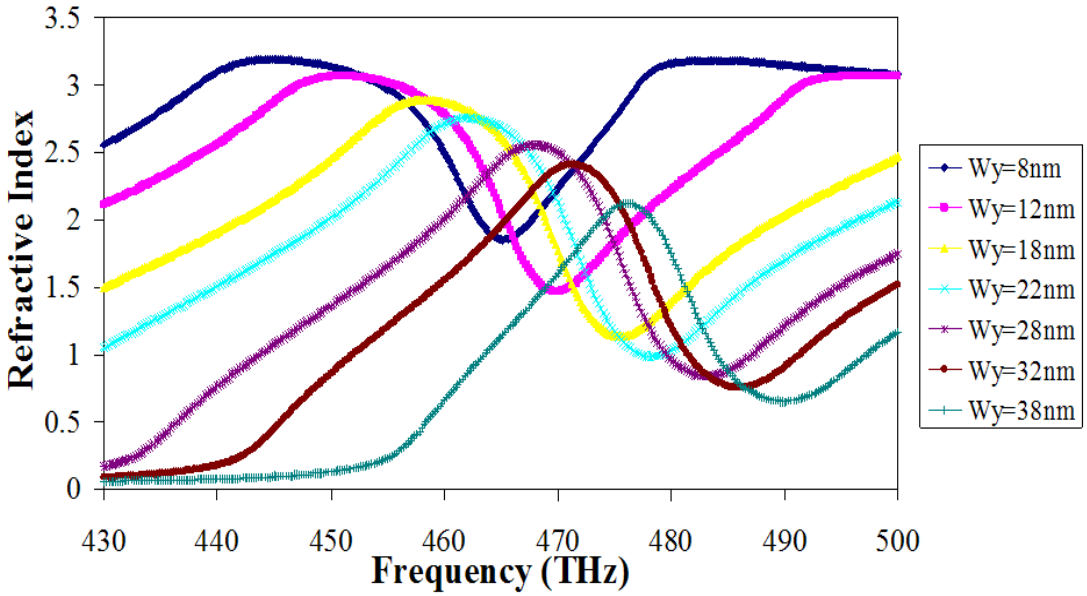

Figure 4.13 Effective refractive index is a function of frequency with different unit cell dimensions.

4.3.2 Analysis and gradient index structure design

Refractive index versus geometry function is used to map index profile to the variation of unit cell. An index gradient can be introduced by continuous tuning of a single parameter in the metamaterial element. Refractive index as functions of different unit cell geometry elements is demonstrated. Planar gradient photonic matamaterial are designed by varying fishnet unit cell dimensions along a certain direction on the Ag-MgF_2-Ag slab.

The chosen wavelengths for parameter retrieval are away from resonance to reduce the metamaterial losses and also within the laser range available in the lab which gives us future optical test possibility. We have different methods to play around with the geometrical dimension of the unit cell to map the function of refractive index versus a single parameter of the unit cell at certain frequencies.

When the geometry parameters are lattice constant a=175nm; Wx = 102nm; t = 40nm; s = 17 nm, we can obtain the plot of refractive index profile to the variation of Wy at wavelength equal to 698 nm and 750 nm, shown in Fig.4.14. The insets demonstrate the schematic varied unit cells and enlarged view for refractive index profile with Wy in the range from 20nm to 60 nm. When Wy is smaller than 20nm, refractive index decreases rapidly with Wy. When Wy is lager than 20nm, refractive index decreases slightly with the increasing of Wy. The operating range of changing Wy is narrow, less than 20nm. It is also a fabrication challenge to obtain grating size less than 20nm. We increase the periodicity a of the unit cell to make the design available for the current fabrication technique. When the geometry parameters are lattice constant a=300nm and the rest parameters are the same as those used for Fig. 4.14, we can obtain the plot of refractive index profile to the variation of Wy at wavelength equal to 669nm, shown in Fig. 4.15. Refractive index decreases with increasing Wy from 18nm and 88nm obviously. This design gives wide range to tune Wy to obtain the refractive index profile. It is possible to fabricate with larger Wy.

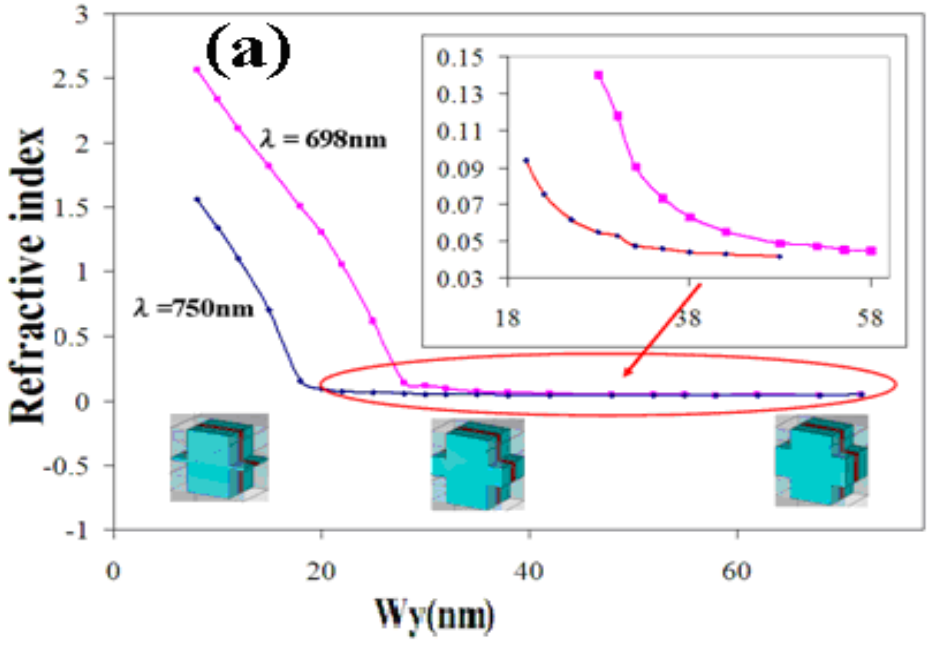

Figure 4.14 Refractive index as a function of grating length Wy with the periodicity equal to 175nm.

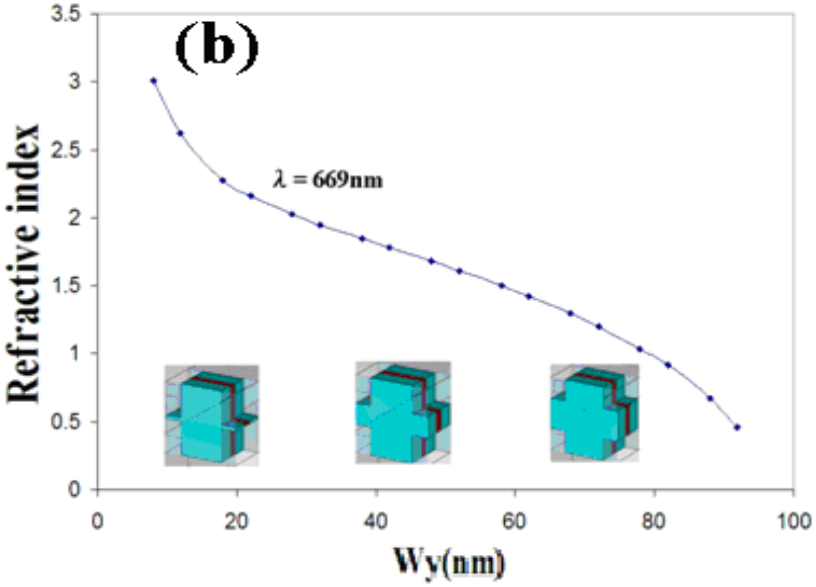

Figure 4.15 Refractive index as a function of grating length Wy with the periodicity equal to 300nm.

Refractive index can be also presented as a function of periodicity of the unit cell. Fig. 4.16 and 4.17 show two designs based on the variation of periodicity.

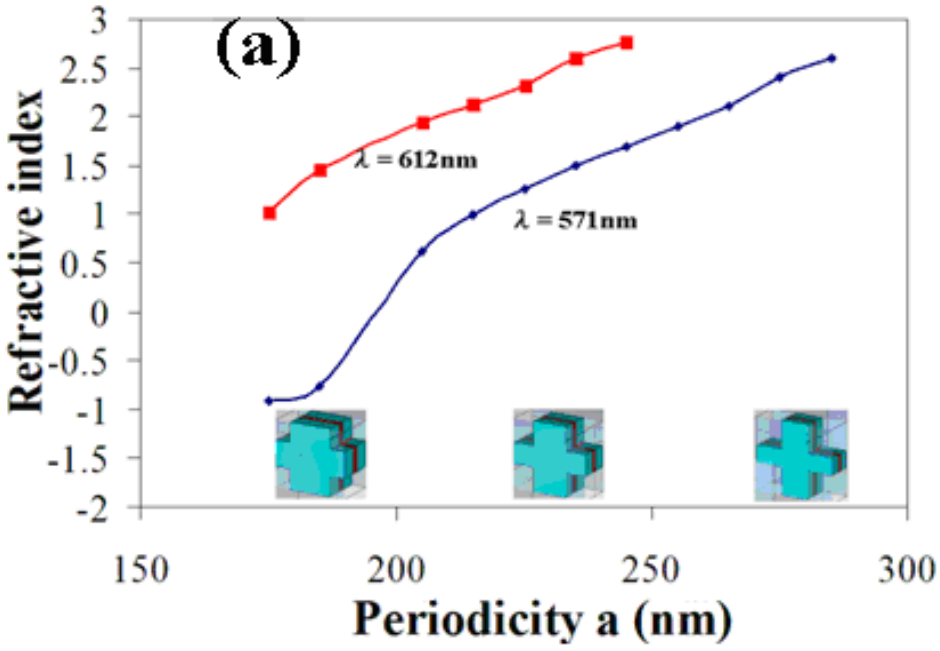

Figure 4.16 Refractive index is a function of periodicity with fixed Wx, Wy and the slab thickness.

In the Fig. 4.16, geometrical parameters are Wx=102, Wy=68nm, s=17nm and t=40nm. The refractive index decreases while periodicity increases at wavelength equal to 698nm and 667 nm. The fishnet structure is periodical and it can be interpreted as a multilayer slab with rectangular holes, shown in Fig. 4.17, the size of the holes is fixed with 232 nm in x direction and 198 nm in y direction. By increasing the periodicity, the refractive index decreases at wavelength equal to 612 nm and 571 nm. The insets show the varied unit cell geometries.

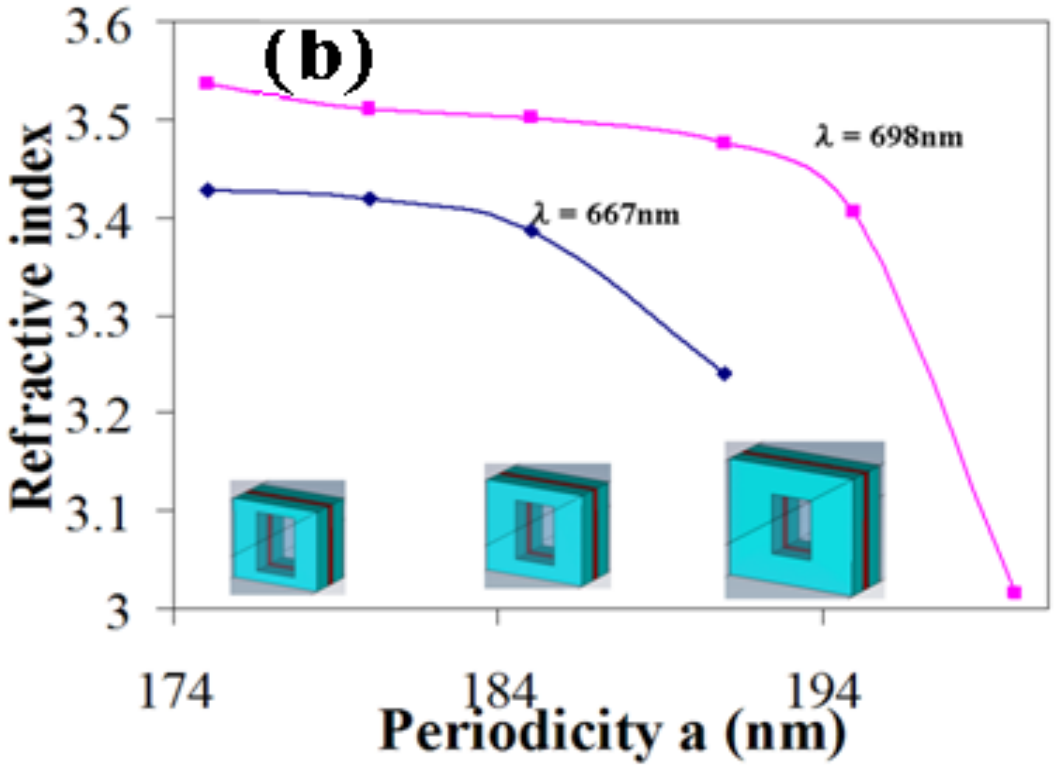

Figure 4.17 Refractive index is a function of periodicity with fixed rectangular hole size and the slab thickness.

The planar gradient photonic metamaterial is designed to be a Ag-MgF2-Ag multilayer slab with fishnets structure with different unit cell along one direction. In this way, the slab consists of the photonic metamaterials with gradually changed refractive index which makes the slab able to deflect the light beam in the propagation direction. Fig. 4.18

is the display of slab design by varying Wy in the x direction. From the refractive index profile to the variation of Wy, the refractive index of the slab decrease along electric field direction due the increasing of Wy. The inset is the top view which clearly shows the size of Wy decreasing along x direction.

Information on the electromagnetic field distribution inside structures at various frequencies is monitored in order to understand how light beam passing through different structured slabs. Electric field mapping of four different slab layouts were studied.

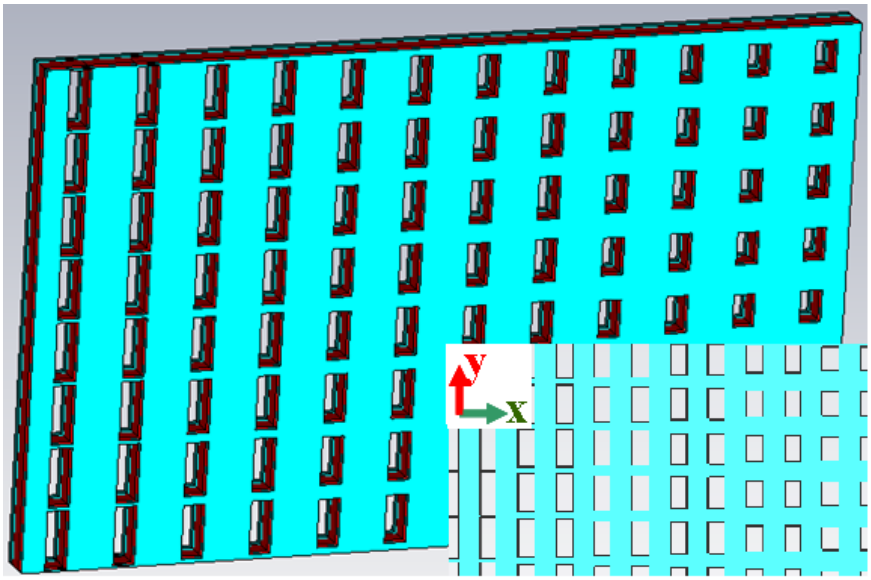

Figure 4.18 Display of gradient slab design with Wy decreasing along the electric field x direction. The inset is the topview of the design.

Fig. 4.19 shows two structures which do not deflect light beam when light passes though the structure. (a) is solid either a dielectric or a metal slab with holes with different sizes. (c) is the fishnet structure without varying unit cell dimensions. When normal incident light passes these two structures, there is no beam deflection for these two structures. This result is what we expect, since the light can not sense the phase different across the slab to produce the deflection.

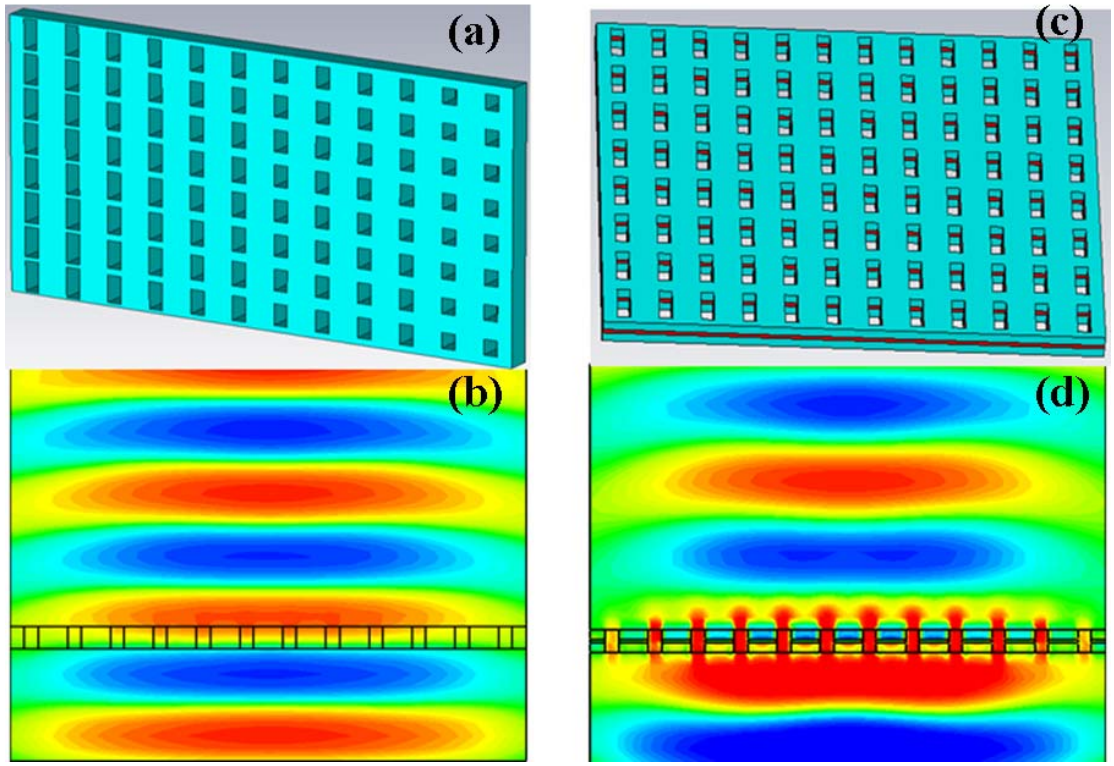

Figure 4.19 Structures without beam deflection simulations. (a) and (b) show a solid slab with different rectangular hole dimensions and its corresponding electric field mapping result; (c) and (d) shows a fishnet structure with the same unit cell geometry on the slab and its corresponding electric field mapping result

Comparison of 2-D Electric Field Map Results between metamaterial gradient slab and nano-prism are demonstrated in Fig. 4.20. (a) is a multilayer slab with fishnet structures with varying Wy along x direction. The sizes of the holes are the same as those used in Fig. 4.19 (a). (c) is nano-prism made from a fishnet structure with the same unit cell dimension as Fig. 4.19 (c). When normal incident light passes through these structures, for gradient matematerial slab, the gradient introduce a phase difference across slab which results in deflection of incident beam; for nano-prism, the prism geometry leads to the bend. The refraction angle depends on the phase gradient that light beam experiences when refracted from angled output surface, appropriate to Snell's law. The mechanism for how the fishnet naso-prism works can be found in Ref. 2.

Metamaterials with gradient show beam deflection are comparable to metamaterial nano-prism structure. Gradient index represent an interesting alternative light deflection phenomena depends on a continuous change of the refractive index within the planar slab, instead of shaped optical surfaces.

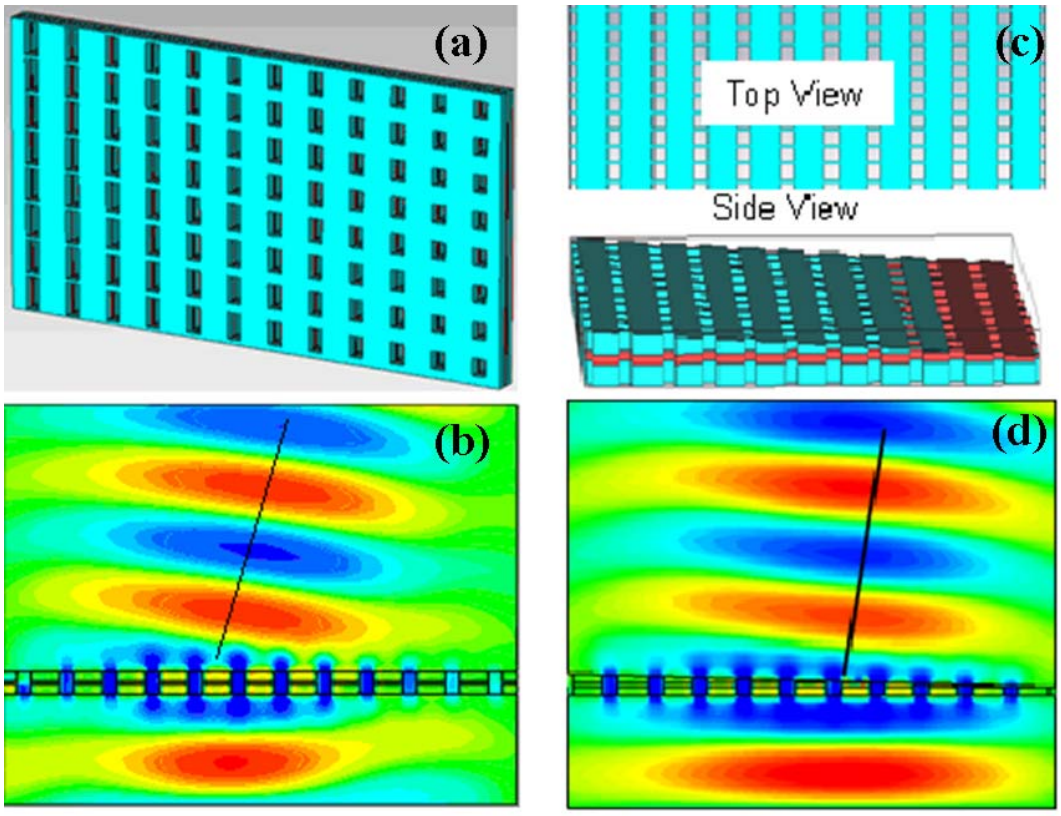

Figure 4.20 Structures with beam deflection simulations. (a) and (b) show a fishnet structure with varying unit cell dimensions along the x direction on the slab and its corresponding electric field mapping result; (c) and (d) show a metamaterial nano-prism and its corresponding electric field mapping result. The black lines on the electric field mapping plots approximately show the light beam propagation direction.

4.4 Conclusions and discussions

In conclusion, this chapter discuss the metamaterial design goes beyond previous work on gradient metamaterials since we design and demonstrate the planar structure in the high optical frequency. This work systematically studies the effects of varying the

geometry of the fishnet unit cell on the refractive index in optical frequency. Planar gradient index photonic metamaterials which can deflect light beam are designed and demonstrated. By tuning a single parameter of fishnet unit cell, the refractive index varies as a function of this parameter. The fishnet structures with different dimensions are specially designed on a planar slab to realize the gradient refractive index along a certain direction. The proposed gradient metamaterals include a few nanometers to few hundred nanometers size structure so that it can be fabricated by available nano-fabrication technologies. Electron beam evaporation system can be applied to produce multilayer metal-dielectric stacks. The role of material deposition rate in the performance of optical plasmonic metamaterials is studied. A lower deposition rate results in a better quality metallic surface and a lower loss experimentally. [178] Focused ion beam system can be used to fabricate the fishnet structure on multilayer samples with capability to mill spot size in order of nanometers. Field Emission Scanning Electron Microscopy can be used to study the hole size and help refine the feature variation from fabrication.

CHAPTER 5

CONCLUSIONS AND FUTURE WORK

5.1 Conclusions

A magnetically controlled optical switch based on one-dimensional magneto-photonic crystal waveguides has been successfully fabricated and tested. According the different periodicities for the structure, this switching property can be demonstrated at different frequencies. Functional photonic crystals fabricated in iron garnet films are shown to provide magnetically-controllable optical switching. The band gaps formed reject or partially allow the transmission of different polarization states depending on the direction of the applied magnetic field.

We also successfully fabricated two- dimensional MPC structures in the substituted iron garnet slab waveguide through FIB milling technology for the first time. The optical measurements including optical transmission and Faraday rotation response have been tested. Obvious multi-stopbands and enhancement of Faraday rotation effect are observed experimentally. The multi-stopbands in transmission spetra on these MPC is because the forward propagating wave hybridizes with high-order backscattered modes at different wavelengths satisfying the Bragg condition.

We developed a waveguide mode analysis. It gives good agreement between simulation and experimental results and explains the multi-stopbands in transmission spectra. It is beyond multilayer stack model and can be applied to one-and two- dimensional photonic crystals on waveguide structures.

For the second major aspect of the dissertation, planar gradient index photonic metamaterials which can deflect light beam are designed and demonstrated for the first time. This work involved carefully engineering and optimizing fishnet unit cell

dimensions and a thorough understanding of the planar gradient metamaterial design by using a commercial software CST modeling with FDTD method. The robust method to retrieve the constitutive effective parameters of metamaterials is successfully utilized to obtain the refractive indices of photonic metamaterials. The fishnet structures with different dimensions are specially designed on a planar slab to realize the gradient refractive index along a certain direction.

5.2 Future work

This dissertation succeeds several goals but it also raises further questions. More projects especially in two- dimensional photonic crystals and photonic metamaterials fabrication can be investigated.

A. In order to study the properties two-dimensional magneto-photonic crystals, there are more features needed to be analyzed such as the tunability of the bands; the dimensionality of the polarization response; the bandwidth of the polarization rotation, transmittance in the bandgaps, photonic crystals with central magnetic optical defect and how different design affects these properties.

B. The proposed gradient metamaterals include a few nanometers to few hundred nanometers size structure so that it can be fabricated by available nano-fabrication technologies. Electron beam evaporation system can be applied to produce multilayer metal-dielectric stacks. The role of material deposition rate in the performance of optical plasmonic metamaterials is studied. A lower deposition rate results in a better quality metallic surface and a lower loss experimentally. Focused Ion Beam System can be used to fabricate the fishnet structure on multilayer samples with capability to mill spot size in order of nanometers. Field Emission Scanning Electron Microscopy can be used to study the hole size and help refine the feature variation from fabrication. We can use the

techniques mentioned above to fabricate the planar gradient photonic metamaterials and investigate how to set up the optical test.

REFERENCS

1. D. R. Smith, J. B. Pendry, M. C. K. Wiltshire. Metamaterials and Negative Refractive Index. *Science* 6; Vol. 305. no. 5685, pp. 788 – 792(2004).

2. J.D. Joannopoulos, R.D. Meade, J.N.Winn, Photonic Crystals: Molding the Flow of Light, Princeton University Press, Princeton, NJ, (1995).

3. C.M. Soukoulis (Ed.), Photonic Crystals and Light Localization in the 21st Century, Kluwer, Dortrecht, (2000).

4. John S.. Strong localization of photons in certain disordered dielectric superlattices. Phys. Rev. Lett.; 58(23):2486-2489(1987).

5. Eli Yablonovitch. Inhibited Spontaneous Emission in Solid-State Physics and Electronics. Phys. Rev. Lett.; 58: 2059(1987).

6. Information of photonics, http://www.rp-photonics.com/index.html.

7. Information of photonic crystals, http://ab-initio.mit.edu/photons/.

8. U. Grüning, V. Lehmann, S. Ottow, and K. Busch. Macroporous silicon with a complete two-dimensional photonic band gap centered at 5 μm. Appl. Phys. Lett.; 68: 747(1996).

9. Albert Birner, Ralf B. Wehrspohn, Ulrich M. Gösele, and Kurt Busch. Silicon-Based Photonic Crystals. Adv. Mater.; 13: 377(2001)

10. Ho K.M., Chan C.T., Soukoulis C.M.. Existence of a photonic gap in periodic dielectric structures. Phys. Rev. Lett.; 65: 3152(1990).

11. G. Feiertag, W. Ehrfeld, H. Freimuth, H. Kolle, H. Lehr, and M. Schmidt. Fabrication of photonic crystals by deep X-ray lithography. Appl. Phys. Lett.; 71: 1441(1997).

12. E. Özbay, A. Abeyta, G. Tuttle, M. Tringides, R. Biswas, C. T. Chan, C. M. Soukoulis, and K. M. Ho. Measurement of a three-dimensional photonic band gap in a crystal structure made of dielectric rods. Phys. Rev.; B 50: 1945-1948(1994).

13. Susumu Noda, Alongkarn Chutinan & Masahiro Imada. Trapping and emission of photons by a single defect in a photonic bandgap structure. Nature; 407: 608(2000).

14. Johnson S. G., Joannopoulos J. D. "Introduction to Photonic Crystals: Bloch's Theorem, Band Diagrams, and Gaps (But no Defects)," Pamphlet. http://ab-initio.mit.edu/photons/tutorial/ (2003).

15.

16. Johnson S. G., Joannopoulos J. D. Photonic Crystals: The Road from Theory to Practice. Boston: Kluwer Academic Publishers. (2002).

17. W. Jiang and R. T. Chen. Multichannel optical add-drop process in symmetrical waveguide-resonator systems. Phys. Rev. Lett.; vol. 91, 213901(2003).

18. Y. Jiang, W. Jiang, L. Gu, X. Chen, R. T. Chen. 80-micron interaction length silicon photonic crystal waveguide modulator. Appl. Phys. Lett.; 87, 221105(2005).

19. W. Jiang, R. T. Chen, and X. Lu. Theory of light refraction at the surface of a photonic crystal. Physical Review.; B 71, 245115(2005).

20. http://en.wikipedia.org/wiki/Photonic_crystal

21. Ziyou Zhou, Metal-oxide film and photonic structures for integrated device applications, PhD. dissertation, (2009).

22. A. G. Gurevich, G. A. Melkov. Magnetization Oscillations and Waves. Boca Raton: CRC Press, (1996).

23. M. Inoue, K. Isamoto, T. Yamamoto and T. Fujii, J. Appl. Phys. 79(3), 1611 (1996).

24. M. Inoue and T. Fujii, J. Appl. Phys. 81(8), (1997).

25. M. Inoue and K. Arai, T. Fujii and M. Abe, J. Appl. Phys., 83(11), 6768 (1998).

26. M. Inoue, K. Arai, T. Fujii, M. Abe, J. Appl. Phys., 85 (8), 5768 (1999).

27. E. Takeda, N. Todoroki, Y. Kitamoto, M. Abe, M. Inoue, T. Fujii and K. Arai, J. Appl. Phys. 87, 6782 (2000).

28. H. Kato, T. Matsushita, A. Takayama, et al. Optics Communications, 219, 271 (2003).

29. H. Kato, T. Matsushita, A. Takayama, et al. J. Appl. Phys., 93, 3906 (2003).

30. S. Kahl and A.M. Grishin, Appl. Phys. Lett. 84, 1438 (2004).

31. H. Kato and M. Inoue, J. Appl. Phys. 91, 7017 (2002).

32. H. Kato, T.Matsushita, A. Takayama, M. Egawa, K. Nishimura and M. Inoue, IEEE Trans. Magn., 38, 3246 (2002).

33. I. L. Lyubchanskii, N. N. Dadoenkova, M. I. Lyubchanskii, E. A. Shapovalov, and T. Rashing, J. Phys. D. 36, 277, (2003).

34. A. Figotin, I. Vitebskiy, Phys. Rev. B, 67, 165210, (2003).

35. C. Kee, J. Kim, H. Park, I. Park, H. Lim, Phys. Rev. B 61, 15523(2000).

36. M. Salib, L. Liao, and et al. “Silicon photonics”, Vol. 8, Issue 2, (2004).

37. M. Levy, R. Li, Appl. Phys. Lett. 89, 121113, (2006).

38. M. Levy, “Magneto-photonic crystal isolators”, US patent 6952300(2005).

39. R. Li, X. Huang, M. Levy, and H. C. Yang, Mater. Res. Soc. Symp. Proc. J1.7 Vol. 834 (2004).

40. M. Levy, X. Huang, R. Li, H.C. Yang and H. Bakhru, Proc. SPIE Int. Soc. Opt. Eng. 5515, 30 (2004).

41. R. Li, M. Levy, Appl. Phys. Lett. 86, 251102-1(2005).

42. R. Li, M. Levy, Appl. Phys. Lett. 87, 269901 (2005).

43. X. Huang, R. Li, H.C. Yang, M. Levy, J. Magn. Mag. Materials, Vol. 300, Issue 1, 112-116(2006).

44. T. Izuhara, M. Levy, and R. M. Osgood, Jr. Appl. Phys. Lett. 76, 1261-1263 (2000).

45. S.Y. Sung, N.H. Kim, B.J.H. Stadler, Mat. Res. Soc. Symp. Proc. Vol.768, G4.6.1, MRS (2003).

46. M. Levy, J. Appl. Phys. 99, 073104(2006).

47. M. Levy, R. Li, A. A. Jalali and X. Huang, J. of the Magnetics Society of Japan 30, No. 6-2, 561-566(2006).

48. R. Li, "Fabrication and characterization of planar magneto-photonic crystals", PhD. Thesis (2006).

49. Nader Engheta, Richard W.Ziolkowski. Metamaterials: Physics and Engineering Explorations. John Wiley & Sons, Inc (2006)

50. Christophe Caloz, Tatsuo Itoh. Electromagnetic Metamaterials: Transmission line theory and Microwave applications.John Wiley & Sons, Inc (2006)

51. V.G. Veselago, 'The electrodynamics of substances with simultaneously negative values of epsiv; and mu' Soviet Physics-Uspekhi 10(4), 509-514(1968)

52. Pendry, J.B. Phys. Rev. Lett., 85,3966 (2000).

53. V.G. Veselago, Sov. Phys. Uspekhi 10, 509 (1968).

54. H.J. Lezec, J.A. Dionne, and H.A. Atwater, Science 316,430 (2007).

55. B.T. Schwartz and R. Piestun, J. Opt. Soc. Am. B 20, 2448(2003).

56. J. Li and N. Engheta, Phys. Rev. B 74, 115125 (2006).

57. N. Engheta, Science 317, 1698 (2007).

58. M.G. Silveirinha and N. Engheta, Phys. Rev. B 76, 245109(2007).

59. A. Ourir, A. de Lustrac, and J.-M. Lourtioz, Appl. Phys.Lett. 88, 084103 (2006).

60. V.A. Fedotov, P.L. Mladyonov, S.L. Prosvirnin, and N.I.Zheludev, Phys. Rev. E 72, 056613 (2005).

61. J.B. Pendry, D. Schurig, and D.R. Smith, Science 312, 1780(2006).

62. U. Leonhardt, Science 312, 1777 (2006).

63. D. Schurig, J.J. Mock, B.J. Justice, S.A. Cummer, J.B.Pendry, A.F. Starr, and D.R. Smith, Science 314, 977 (2006).

64. S.A. Cummer and D. Schurig, New J. Phys. 9, 45 (2007).

65. W. Cai, U.K. Chettiar, A.V. Kildishev, and V.M. Shalaev,Nature Photonics 1, 224 (2007).

66. J. B. Pendry, A. J. Holden, D. J. Robbins, and W. J. Stewart, "Magnetism from Conductors and Enhanced Nonlinear Phenomena," IEEE Trans. Microw. Theory Tech. 47(11), 2075–2084 (1999).

67. D. R. Smith, W. J. Padilla, D. C. Vier, S. C. Nemat-Nasser, and S. Schultz, "Composite medium with simultaneously negative permeability and permittivity," Phys. Rev. Lett. 84(18), 4184–4187 (2000).

68. R.A. Shelby, D.R. Smith, S. Schultz. Experimental Verification of a Negative Index of of Refraction, Science v. 292, 6 (2001).

69. http://en.wikipedia.org/wiki/Photonic_metamaterials

70. S. Zhang, W. Fan, N.C. Panoiu, K. J. Malloy, R.M. Osgood, and S.R.J. Brueck, "Experimental demonstation of near-infrared negative-index metamaterials," Physical review Letters 95(13), 137404-137401(2005)

71. S. Zhang, , W. Fan, B.K Minhas, A. Frauenglass, K. J. Malloy, and S.R.J. Brueck, "Midinfrared resonant magnetic nanostructures exhibiting a negative permeability,' Physical review Letters 94(3), 037402-037401(2005)

72. J. Zhou, T. Koschny, M. Kafesaki, E. N. Economou, J. B. Pendry, and C. M. Soukoulis, "Saturation of the magnetic response of split-ring resonators at optical frequencies," Phys. Rev. Lett. 95(22), 223902 (2005).

73. V. M. Shalaev, "Optical negative-index metamaterials," Nat. Photonics 1(1), 41–48 (2007).

74. V.M. Shalaevetzetz, 'Negative index of refraction in optical metamaterials', Optics Lettes, v. 30, 3356(2005).

75. W. Cai etc, 'Optical magnetism: from Red to Blue', OPTICS EXPRESS ; Vol. 15, No.6, 3333 (2007)

76. Jason Valentine, Shuang Zhang, Thomas Zentgraf, Erick Ulin-Avila, Dentcho A. Genov, Guy Barta, Xiang Zhang, 'Three dimensional optical metameterial with neagitive refractive index', *Nature* 455, 376-379 (2008).

77. A. V. Kildishev, W. Cai, U. K. Chettiar, H.-K. Yuan, A. K. Sarychev, V. P. Drachev, and V. M. Shalaev, 'Negative refractive index in optics of metal-dielectric composites', J. Opt. Soc. Am. B 23, 423 (2006).

78. G. Shvets and Y. A. Urzhumov, 'Negative index meta-materials based on two-dimensional metallic structures', J. Opt. A 8, S122 (2006).

79. G. Dolling, M. Wegener, C. M. Soukoulis, S. Linden, 'Negative-index metamaterialat 780 nm wavelength', OL, 39(2007)

80. Peter H. Berning, "Use of Equivalent films in the design of infrared multilayer antireflection coatings", J. Opt. Soc. Am.,Vol. 52(4), pp. 431-436(1962).

81. D.R. Smith, J.J. Mock, A.F. Starr, D. Schurig, "Gradient index metamaterials", Physical Review E, 71, 036617(2005).

82. Milan Maksimović1, Zoran Jakšić2, Nils Dalarsson3, Transmission Properties of Gradient Index Metamaterial Slabs, Proc. XL Internet. Scientific Conf. ICEST 2005, Niš, Serbia, Vol. 1, pp. 195-198(2005).

83. B.J. Justice, B.N. Nguyen, S. H. Yonak, J. Kim, and D. R. Smith, 'electric-field-couple metamaterials for microwave beam formation,' in IEEE Antennas and Propagation Society International Symposium, pp. 2566-2569(2007).

84. B.N. Nguyen, S. H. Yonak and D. R. Smith, 'millimeter-wave artificial dielectric gradient index lenses', 3rd European Conference on Antennas and Propagation(2009)

85. http://en.wikipedia.org/wiki/Magneto-optic_effect

86. P.K. Tien, R.J. Martin, S.L. Blank,S .H. Wempalend L .J. Varnerin, A ppl. Phys.Lett. vol. 21, pp. 207-209(1972).

87. S. Keutebneuerm A, Geubtucg. J. Appl.Phys. 99.08M704 (2006)

88. A.H. Eschenfelder, Magnetic BubbleTechnology, Springe Brerlin (1981).

89. H. C. Yang, "RF-sputter fabrication of magnetic garnet thin films and simulation modeling for 1-D magnetic photonic crystal waveguide devices", PhD. thesis (2005).

90. A. D. McLay, M. F. Crawford, Phys. Rev. 44, 986 (1993).

91. G. F. Dionne and G.A. Allen, J. Appl. Phys. 75, 6372 (1994).

92. M. A. Gilleo, “Ferromagnetic insulators: garnets”, Ferromagnetic Materials, Vol. 2, North-Holland Pub (1980).

93. K. Matsuda,H . Minemoto, O. Kamadaand, S. Ishizuka, IEEE Trans. Magn. Vol. MAG-23p, p. 3479-3481(1987).

94. N. Bilaniuk, D.D. Stancil and S.H. Talisa, J. Appl. Phys. vol. 67, pp. 508-510 (1990).

95. S. Geller: Zeits. Kristall., 123, 1 (1967)

96. G.B. Scott and D.E. Lacklison, IEEET rans. Magn.v ol. MAG-12p, p .292-311 (1976).

97. C.F Buhrer, J. Appl. Phys. 40, 4500 (1969)

98. P. Hansen and J. P. Krumme, Thin Solid Films, 114, 69(1984).

99. N.Adachi, V. P. Denysenkov, S. I. Khartesev, A. M. Grishin, and T. Okuda, j. Appl. Phys. 88, 5(2000).

100. A. Akselrad, AIP Conf. Proc. 5, 249(1971).

101. P. HansenC, .-P. Klages,J . Schuldta ndK . Witter, Phys.Rev.B vol. 31, pp. 5858-5864(1985).

102. E.A. Giess,J .D. Kuptsisa ndE .A.D.White, J. Cryst. Growth vol. 16, pp. 36-42 (1972).

103. G. F. Dionne, G.A. Allen, P. R. Haddad, C. A. Ross and B. Lax, Lincoln Lab. J. 15, 2(2005).

104. http://en.wikipedia.org/wiki/Faraday_effect

105. A. K. Zvezdin, V. A. Kotov, “Modern Magneto-Optics and Magneto-Optical Materials”, Bristol: IOP(1997).

106. L. D. Landau, E. M. Lifshitz, “Electrodynamics of Continuous Media”, Oxford: Pergamon (1984).

107. Amir A. Jalali and Miguel Levy, “Local normal mode coupling and energy band splitting in elliptically birefringent 1D magnetophotonic crystals,” Journal of the Optical Society of America B 25, 119-125 (2008).

108. http://en.wikipedia.org/wiki/Faraday_effect

109. R. Wolfe, V. J. Fratello, and M. McGlashan-Powell, J. Appl. Phys. 63(8), 3099 (1988).

110. M. Mcglashan-Powell, R. Wolfe, J. F. Dillon, Jr., and V. J. Fratello, J. Apple. Phys. 66, 3343 (1989).

111. M. Steel, M. Levy, and R. M. Osgood, "Photonic bandgaps with defects and the enhancement of Faraday rotation," J. Lightwave Technol. 18, 1297–1308 (2000).

112. H. Yang, M. Levy, R. Li, P. Moran, C. Gutierrez, and A. Bandyopadhyay, "Linear birefringence control and magnetization in sputter-deposited magnetic garnet films," IEEE Trans. Magn. 40, 3533–3537 (2004).

113. M. Levy, "Normal modes and birefringent magnetophotonic crystals," J. Appl. Phys. 99, 073104 (2006).

114. J.F. Dillon, Jr. J. Phys, Radium, 20, 374 (1959)

115. S. Sugano, N. Kojima, 'Magneto-Optics', Springer, German (2000)

116. "Planar Waveguide Circuits Global Market Forecast", published by ElectroniCast Corp(2009).

117. H. Nishihara, M. Haruna, T. Suhara, "Optical Integrated Circuits", McGraw-Hill, New York, (1987)

118. http://en.wikipedia.org/wiki/Waveguide_(electromagnetism).

119. Okamoto, Katsunari, Fundamentals of optical waveguides, Elsevier Inc. 2nd ed. (1949).

120. María L. Calvo, Vasudevan Lakshminarayanan, .Optical waveguides: from theory to applied technologies, Technology & Engineering (2007).

121. A.P. Vinogradov, S. G. Erokhin, A.B. Granovsky and M. Inoue, J. Cm. Tech. Elect.,9, 88 (2004).

122. W.K. Burns and A. F. Milton, IEEE J. Quant. Electron., QE-11(1), 32 (1975).

123. M Inoue, R Fujikawa, A Baryshev, A Khanikaev, P B Lim, Magnetophotonic crystals, M Inoue et al J. Phys. D: Appl. Phys. 39 R151(2006).

124. S. Sakaguchi and N. Sugimoto, J. Lightwave Technol. 17, 1087 (1999).

125. M. J. Steel, M. Levy, and R. M. Osgood Jr., IEEE Photonics Technol. Lett. 12, 1171 (2000).

126. F. D. M. Haldane and S. Raghu, "Possible Realization of Directional Optical Waveguides in Photonic Crystals with Broken Time-Reversal Symmetry," Phys. Rev. Lett. PRL 100, 013904 (2008)

127. M. Levy and R. Li, "Polarization rotation enhancement and scattering mechanisms in waveguide magnetophotonic crystals," Appl. Phys. Lett. 89, 121113(2006).

128. A.M. Merzlikin, M. Levy, A. A. Jalali and A.P. Vinogradov, "Polarization degeneracy at Bragg reflectance in magnetized photonic crystals," Physical Review B 79, 195103(2009).

129. Miguel Levy, Amir A. Jalali, Ziyou Zhou and Neluka Dissanayake, "Bandgap formation and selective suppression of Bloch states in birefringent gyrotropic Bragg waveguides," Optics Express 16, 13421- 13430(2008).

130. Fei Wang and Akhlesh Lakhtakia, "Intra-Brillouin-zone bandgaps due to periodic misalignment in one-dimensional magnetophotonic crystals, Appl. Phys. Lett. 92, 011115 (2008).

131. A.M. Merzlikin, A.P. Vinogradov, A.V. Dorofeenko, M. Inoue, M. Levy and A.B. Granovsky, "Controllable Tamm states in magnetophotonic crystal," Physica B: Condensed Matter 394, Issue 2, 277-280, 15 (2007).

132. Miguel Levy and Amir A. Jalali, "Band structure and Bloch states in birefringent 1D magnetophotonic crystals: An analytical approach," Journal of the Optical Society of America B 24, 1603-1609(2007).

133. I. Šolc, Czech. J. Phys., Sect. A 4, 65 (1954), P. Yeh, J. Opt. Soc. Am. 69, 742 (1979)

134. Rong Li and Miguel Levy, "Bragg Grating Magnetic Photonic Crystal Waveguides," Appl. Phys. Lett. 86, No. 25, 251102(2005).

135. Dietrich Marcuse, Theory of Dielectric Optical Waveguides, Chaper 3, Academic Press (1991).

136. Jeong Su Yang, Seung Gol Lee, Se-Geun Park, El-Hang Lee and Beom-Hoan O, Drude Model for the Optical Properties of a Nano-Scale Thin Metal Film Revisted, Journal of the Korean Physical Society, Vol. 55, No. 6, December, pp. 2552_2555(2009).

137. I.V. Shadrivov, S.K. Morrison, and Y.S. Kivshar, Opt. Express 14, 9344 (2006).

138. D.H. Werner, D.-H. Kwon, I.-C. Khoo, A.V. Kildishev, and V.M. Shalaev, Opt. Express 15, 3342 (2007).

139. A. Degiron, J.J. Mock, and D.R. Smith, Opt. Express 15, 1115 (2007).

140. W. Rotman, IRE Trans. Antennas Propagat., 82 (1962).

141. J. B. Pendry, A. J. Holden, W. J. Stewart, and I. Youngs. " Extremely low frequency plasmons in metallic mesostructure, " Phys. Rev. Lett., vol. 76, no. 25, pp. 4773-4776, june 1996.

142. *N.M.* Litchinitser*,* V.M. Shalaev*,* Photonic metamaterials, Laser Phys. Lett. 5, No. 6, 411–420 (2008) / DOI 10.1002/lapl.200810015

143. R.A. Depine and A. Lakhtakia, Microwave Opt. Technol. Lett. 41, 315 (2004).

144. http://en.wikipedia.org/wiki/Gradient-index_optics

145. http://www.grintech.de/e_main_grin.htm

146. S.A. Ramakrishna, J.B.Pendry, "Spherical perfect lens: Solutions of Maxwell's equations for spherical geometry", *Phys. Rev. B*, vol. 69 (11), pp. 1151151-1151157, (2004)

147. R. C. Linares, J. Cryst. Growth, 3-4, 443, (1968).

148. S. Mino, M. Matsuoka, A. Shibukawa, and K. Ono, Jpn. J. Appl. Phys. 29, L1823, (1990).

149. R. Wolfe, V. J. Fratello, and M. McGlashan-Powell, Appl. Phys. Lett. 51 (16), 19, (1987).

150. Spanninga, S., Development of ion beam etching of PZN-PT for fabrication of optical wave guides. MS Thesis, Michigan Technological University, 2004.

151. Raghav Vanga, "Relaxor piezoelectric film actuators, waveguides and photonic crystals: fabrication and characterization" PhD dissertation, 2008

152. Giannuzzi, L.A. and F.A. Stevie, Introduction to focused ion beams: instrumentation, theory, techniques, and practice. 2005, New York: Springer. xiv, 357 p.

153. Xiaoyue Huang, "Dimensional effects on the magnetic domains in planar magnetophotonic crystal waveguide" , PhD dissertation(2007).

154. U. Enz, H. Van Der Heide, Solid St. Commun. , 347, (1968)

155. F. Lucari, C. Mastrogiuseppe, and G. Tomassetti, J. Phys. C: Solid State Phys. 10, 4869, (1977).

156. H. Dotsch, P. Hertel, B. Luhrmann, S. Sure, H. P. Winkler, and M. Ye, IEEE Trans, Magn. 2979, (1992)

157. http://en.wikipedia.org/wiki/Subsurface_scattering

158. Hunsperger, Robert G. Integrated optics, theory and technology, Springer-Verlag/Sci-Tech/Trade.

159. A.Jalali, A. Friberg, Optics Communications 253 (2005) 145-150

160. A. Jalali, A. Friberg, Optics letters,Vol. 30, No. 10

161. D. R. Smith, S. Schultz, P. Markos, and C. S. Soukoulis, 'Determination of effective permittivity and permeability of metamaterial from reflection and transmission coefficients', Phys. Rev. B, vol. 65, 2002, 195104.

162. Xudong Chen, Tomasz M.G, etc., 'Robust method to retrieve the consititutive effective parameters of metameaterials', physical review E 70, 016608 (2004)

163. http://web.mit.edu/16.810/www/16.810_L4_CAE.pdf

164. S. Wu and N. Glytsis, "Finite-number-of-periods holographic gratings with finite-widthincident beams: analysis using the finite-difference frequency-domain method," *J. Opt. Soc. Am. A*, vol. 19, pp. 2018-2029, 2002.

165. J. B. Pendry, "Photonic band structures," *J. Mod. Opt.*, vol. 41, pp. 209-229, 1994.

166. D. M. Sullivan, *Electromagnetic Simulation Using the FDTD Method*. Piscataway, NJ: IEEE Press, 2000.

167. A. Taflove and S. C. Hagness, *Computational Electrodynamics: the Finite-Difference Time-Domain Method, 2nd Edition*. Norwood, MA: Artech House, Inc., 2000.

168. http://en.wikipedia.org/wiki/S-parameters

169. http://en.wikipedia.org/wiki/HFSS

170. http://www.ansoft.com/products/hf/hfss/

171. Frequency Selective Surfaces Analyzed with Floquet Ports, Revision date: April 6, 2007

172. HFSS, User manual Ver. 11, Getting Started with HFSS: Floquet Ports.

173. http://comsol.com/academic/papers/?freetext=plasmonic

174. http://www.cst

175. http://www.cst.com/Content/Products/MWS/FrequencyDomainSolver.asx. com/Content/Products/MWS/Overview.aspx

176. R. W. Ziolkowshi, IEEE Trans. Antennas Propag. 51, 1516(2003).

177. A. M. Nicolson and G. F. Ross, IEEE Trans. Instrum. Meas. 19, 377 (1970).

178. J. A. Kong, *Electromagnetic Wave Theory* (EMW, Cambridge, MA, 2000).

179. J. A. Kong, Prog. Electromagn. Res. 35, 1 (2002).

PUBLICATIONS/PATENT APPLICATIONS

1. Z. Wu, Miguel Levy, V. J. Fratello, and A. M. Merzlikin, "Gyrotropic photonic crystal waveguide switches", Appl. Phys. Lett. 96. 051125. (2009)

2. A.M. Merzlikin, M. Levy, A.P. Vinogradov, Z. Wu, A.A. Jalali, "Band gaps in periodically magnetized homogeneous anisotropic media", Opt. Commun.05.068. (2010)

3. Z. Zhou, X. Huang, R. Vanga, Zhuoyuan Wu, "Enhanced photonic bandgap in ion-implanted lithium niobate waveguides by improving index contrast JOSA B, Vol. 27, Issue 7, pp. 1425-1429. (2010)

4. Patent pending on Planar Gradient Index Optical Metamaterials. (2009)

5. Miguel Levy, Zhuoyuan Wu, V. J. Fratello, A. M. Merzlikin, and M. J. Steel, "Magnetically-Activated Gyrotropic Band Gaps in One-Dimensional Photonic Crystals". In preparation.

6. Zhuoyuan Wu, and Serdar Yonak, 'Planar gradient index photonic metamaterials'. Submitted to Optics Express. (2010)

APPENDIX A

Permissions from Authors/Companies to use their figures for this dissertation

Figure 1.6

From Millner, Delois <DMilln@osa.org>
Sent: 07/09/2010 12:44 PM
Dear Zhuoyuan Wu:
The Optical Society of America considers this requested use of its copyrighted material to be Fair Use under United States Copyright Law. It is requested that a complete citation be included in any publication.
MS. DELOIS MILLNER July 9, 2010
Authorized Agent

The Optical Society
2010 Massachusetts Ave., NW
Washington, DC 20036 USA
Direct:+1.202.416.1920 Fax: +1.202.416.6129
Email: dmilln@osa.org

Figure 1.7

From Millner, Delois <DMilln@osa.org>
Sent: 07/12/2010 01:51 PM
Dear Dr. Wu:
The Optical Society of America considers this requested use of its copyrighted material to be Fair Use under United States Copyright Law. It is requested that a complete citation be included in any publication.
MS. DELOIS MILLNER July 12, 2010
Authorized Agent

The Optical Society
2010 Massachusetts Ave., NW
Washington, DC 20036 USA
Direct:+1.202.416.1920 Fax: +1.202.416.6129
Email: dmilln@osa.org

Figure 3.8, Figure 3.12 and Figure 3.13:

From Xiaoyue Huang <xiaoyue.huang@seagate.com>
Sent: 07/08/2010 03:24 PM
Sure. You can use them.

Best Regards,
Xiaoyue (Phillip) Huang, *PhD*
Seagate Technology
7801 Computer Avenue South
Mailstop: NRW102
Bloomington, MN, 55435
Tel: 952.402.7687
Fax: 952.402.8721